Anomalous Heat Transport in Low-Dimensional Quantum Spin Systems

Inaugural-Dissertation
zur
Erlangung des Doktorgrades
der Mathematisch-Naturwissenschaftlichen Fakultät
der Universität zu Köln

vorgelegt von

Michael Hofmann

aus Bretten (Baden)

Köln 2002

Berichterstatter:	Prof. Dr. A. Freimuth Priv.-Doz. Dr. G.S. Uhrig
Vorsitzender der Prüfungskommission:	Prof. Dr. L. Bohatý
Tag der mündlichen Prüfung:	07. Januar 2002

Contents

1 Introduction **1**

2 The Physics of Low-Dimensional Systems **5**
2.1 Quasi-One-Dimensional Conductors 5
2.1.1 Peierls Instability and the CDW Groundstate 6
2.1.2 The SDW Transition 12
2.2 One-Dimensional Antiferromagnets 13
2.2.1 The Spin-Peierls Systems in Magnetic Fields 15
2.2.2 Magnetic Frustration 17

3 Thermal Transport in Solids **19**
3.1 Heat Transport by Phonons 19
3.2 Heat Transport by Electrons 21
3.3 Heat Transport by Magnetic Excitations 22

4 Experimental **27**
4.1 Thermal Conductivity 27
4.1.1 Sample Insert and Cryostat 29
4.1.2 Calibration 31
4.1.3 Contacting the Samples 37
4.2 Electrical Resistivity 41

5 $SrCu_2(BO_3)_2$ **43**
5.1 Structure and Magnetism 43
5.2 Experimental Results of the Thermal Conductivity 50
5.3 Scattering Mechanisms and Modeling of the Data 54
5.3.1 Scattering on Elastic Deformations 54
5.3.2 Resonant Scattering 56
5.3.3 Resonant Scattering Rates 59
5.3.4 Summary 73

6 $CuGeO_3$ **75**
6.1 Structure and Magnetic Exchange 75
6.2 The Spin-Peierls Transition in $CuGeO_3$ 78
6.3 Magnetic Excitation Spectrum and Spin-Phonon Coupling 79
6.4 Thermodynamic Properties of $CuGeO_3$ 81
6.4.1 Specific Heat and Thermal Expansion 81

6.4.2 Pressure Dependencies and Magnetic Frustration 82
6.4.3 H-T Phase Diagram 84
6.5 Thermal Conductivity of $CuGeO_3$ 86
6.5.1 Previous Thermal Conductivity Measurements on $CuGeO_3$ 86
6.5.2 Our Experimental Thermal Conductivity Results 87
6.5.3 Discussion 91
6.6 Thermal Conductivity of Doped $CuGeO_3$ 105
6.6.1 Introduction 105
6.6.2 Experimental Results 107
6.6.3 Discussion 112

7 The Bechgaard Salts **117**
7.1 Structure and Basic Electronic Properties 117
7.2 Experimental Results 120
7.2.1 $(TMTTF)_2PF_6$ 120
7.2.2 $(TMTSF)_2PF_6$ 121
7.2.3 $(TMTSF)_2ClO_4$ 124
7.3 Discussion 127

8 The Insulating Cuprate $Sr_2CuO_2Cl_2$ **137**
8.1 Introduction 137
8.2 Experimental Results 138
8.3 Discussion 139

9 Summary **145**

References **150**

Chapter 1

Introduction

Low-dimensional systems show unusual, rich, and fascinating physical properties. A well-known example for the peculiar physics in one dimension, predicted by Peierls already in 1955, is the Peierls instability of one-dimensional metals. This instability leads to a metal-insulator transition with an insulating so-called charge density wave (CDW) groundstate, consisting of a periodic charge density modulation accompanied by a periodic lattice distortion. Another possible groundstate is the spin density wave (SDW) state. In one-dimensional antiferromagnets an analogous instability, the so-called spin-Peierls transition, may occur with a non-magnetic groundstate of singlet pairs and an energy gap for spin excitations.

An important aspect of the physics in low dimensions is the presence of quantum-fluctuations. For example, a one-dimensional Heisenberg antiferromagnet does not show magnetic ordering even at zero temperature; both, the groundstate and the excitation spectrum are determined by strong quantum fluctuations. Another example is the physics of one-dimensional metals with electron-electron interactions. It is believed that these systems cannot be described by the usual Fermi liquid picture involving well defined quasiparticle excitations, common to the description of conventional metals and semiconductors. Instead, more exotic scenarios like the Tomonaga-Luttinger liquid are believed to be appropriate with fascinating properties, as for example, spin/charge separation, where independent spin and charge excitations with different velocities are formed. In two dimensions the influence of strong quantum fluctuations is also of much current interest and strongly debated, since it is directly related to the physics of the high-temperature superconductors, which are obtained by doping a two-dimensional Heisenberg antiferromagnet with mobile charge carriers.

A fresh impetus to the field of low-dimensional systems has been given by the discovery of a variety of materials in the last few years, in which such low-dimensional structures are realized. For example, a number of cuprates and vanadates with low-dimensional spin structures – spin chains, spin-ladders, as well as various planar spin arrangements – are now available as good single crystals. Also, various one-dimensional conductors are known, most notably the organic conductors and among those the so-called Bechgaard salts. These systems are, to some researchers, the most interesting and fascinating materials ever discovered. Their physics displays the complete set of unusual phenomena typical for low-dimensional materials, including unconventional superconductivity, spin/charge separation, spin-Peierls, CDW-, and SDW-transitions as well as a plethora of effects driven by magnetic fields like a field

induced spin density wave state with quantized Hall-resistance.

The groundstate, the excitation spectrum as well as various thermodynamic properties, such as the specific heat and the magnetic susceptibility of many low-dimensional spin systems have been studied quite intensively in the last few years. In contrast, much less is known about the dynamics of magnetic excitations, e.g., the microscopic understanding of how they transport energy, and their coupling to the lattice degrees of freedom. Nevertheless, such studies appear to be quite promising, as, for example, magnetic excitations are expected to move without dissipation in a spin 1/2 Heisenberg chain with nearest neighbor coupling.

A valuable tool for the study of the dynamics of magnetic excitations and of their coupling to the lattice is provided by measurements of the thermal conductivity as a function of temperature, magnetic field and doping. The challenge of this thesis was therefore a systematic experimental study of the thermal conductivity of low-dimensional spin systems in a wide range of temperature, magnetic field and in various materials with different magnetic properties. Our results are indeed very remarkable and promising: First, a sizeable magnetic contribution to the heat current may occur in systems with large magnetic coupling and it may even dominate the total thermal conductivity at rather high temperatures of a few hundred Kelvin. To our knowledge these cases provide the first class of insulators, in which the dominant mechanism of heat transport at high temperatures is non-phononic. Second, the phonon heat current is strongly influenced by the presence of magnetic excitations, as signaled, e.g., by a strong damping and by a magnetic field dependence of the phononic thermal conductivity.

The course of this thesis is the following: In chapter 2 an introduction to low-dimensional systems is given. The basic ideas of heat transport in solids are sketched out in chapter 3. A detailed description of the experimental setup and of the calibration procedure, necessary to conduct high resolution heat transport measurements is given in chapter 4.

Chapter 5 deals with the thermal conductivity of the 2-d spin liquid system $SrCu_2(BO_3)_2$. Among the 2-d spin 1/2 systems $SrCu_2(BO_3)_2$ is an intriguing compound with fascinating physical properties. The spin structure realizes the Shastry-Sutherland model which was studied theoretically 20 years ago. One finds a spin dimer ground state with extremely localized magnetic excitations. Furthermore, quantized magnetization plateaus can be observed in striking contrast to classical spin systems where the magnetization increases monotonically. The heat transport parallel and perpendicular to the 2-d spin system is studied and compared to analytical results. It turns out that the interplay between phonons and magnetic excitations plays a central role for the heat transport. We will suggest a consistent interpretation of the thermal conductivity data in terms of resonant scattering of phonons by magnetic excitations, worked out with the collaboration of G.S. Uhrig.

Chapter 6 is devoted to the quasi 1-d spin-Peierls system $CuGeO_3$. Before the discovery of $CuGeO_3$ all known systems exhibiting a spin-Peierls transition were organic compounds, e.g., $(TMTTF)_2PF_6$. The discovery of $CuGeO_3$, the first inorganic spin-Peierls compound, has renewed the interest in studying this phenomenon as large crystals of high quality have been synthesized allowing, e.g., precise neutron scattering experiments. A systematic study of the thermal conductivity as a function of temperature and as a function of the magnetic field along all three crystallographic directions is presented for pure $CuGeO_3$. Anomalous

temperature dependence of the thermal conductivity along two crystallographic directions is found. In addition, κ depends strongly on the applied magnetic field. A discussion of the experimental results, including numerical calculations of possible magnetic contributions to the heat current and anisotropy considerations, is presented subsequently. Thermal conductivity data of Zn and Mg doped $CuGeO_3$ accomplish the experimental investigations on $CuGeO_3$.

In chapter 7 a systematic study of the heat transport as a function of temperature and of the magnetic field in the Bechgaard salts is presented. To our knowledge, these measurements provide the first systematic study of heat transport in these materials at high and low temperatures. We find an anomalous magnetic field and temperature dependence of κ, irrespective of whether the systems are metallic or insulating. We will see that the Luttinger liquid picture and in particular the scenario of spin/charge separation, discussed for these materials, may be an appropriate picture for an understanding of the findings. A detailed discussion and model calculations for the heat transport complete this chapter.

Chapter 8 deals briefly with the heat transport in $Sr_2CuO_2Cl_2$. This compound is isostructural to La_2CuO_4, the parent compound of the high-temperature superconductors. The thermal conductivity of La_2CuO_4 is known to be anomalous, but its interpretation is still under debate [1]. This stems from lattice instabilities making different thermal conductivity scenarios possible. $Sr_2CuO_2Cl_2$ is free from these complications which facilitates the interpretation of the thermal conductivity results. A discussion of our findings and a comparision to the previously obtained thermal conductivity data of La_2CuO_4 and of $YBa_2Cu_3O_6$ are presented [1,2].

Chapter 2

The Physics of Low-Dimensional Systems

Over several decades low-dimensional systems have attracted considerable interest since they are well-suited to investigate the properties of strongly interacting electron systems with a variety of possible groundstates. Besides charge density wave (CDW) or spin density wave (SDW) groundstates, superconductivity can also be observed. Thus it is argued that low-dimensional model systems help towards a better understanding of the superconducting state. As the field is relatively large, I will focus my attention on the instabilities and particularities in quasi-one-dimensional systems. I start from low-dimensional conductors discussing the Peierls-transition, the CDW groundstate and SDW transition. Finally, the spin-Peierls transition will be presented.

2.1 Quasi-One-Dimensional Conductors

Loosely speaking, low-dimensional conductors are materials with strongly anisotropic electrical conductivity. Hence, for a perfectly one-dimensional conductor we would expect a finite electrical conductivity along one direction and no electronic transport along the other two directions. The highly anisotropic electronic transport is closely related to the anisotropic nature of the crystal structure. Atoms form linear chains where the orbitals strongly overlap. This is for example seen in the so-called perylene radical cation salts (e.g. $(PE)_2PF_6 \times 2/3$ THF), where the building blocks are planar molecules arranged in such a way that a strong overlap of the orbitals occurs only perpendicular to these planes [3, 4]. In the molecule planes the overlap between the orbitals are much weaker or possibly zero. Hence, for certain electron configurations a one-dimensional conduction band along the chain direction is formed where the delocalization of the electrons results in a relatively large electrical conductivity along the chains. Perpendicular to the chains the electrons are localized and little or none electrical conductivity is expected.
However, in nature there are no perfect one-dimensional conductors. The conducting chains are embedded in a three-dimensional lattice and very often the interchain overlap cannot be completely neglected. Thus we speak of quasi-one-dimensional conductors.

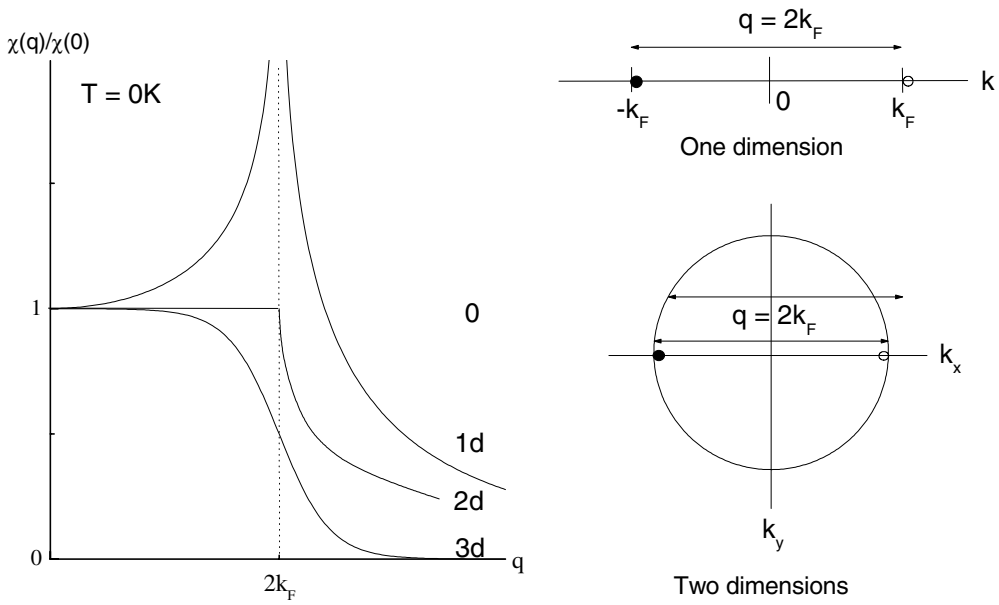

Figure 2.1: Left: Polarisation function $\chi(q)$ for the one-, two- and three-dimensional case at T = 0. Right: Fermi surface in one (1-d) and two dimensions. According to Kagoshima et al. [5].

2.1.1 Peierls Instability and the CDW Groundstate

A salient feature of quasi-one-dimensional metals is the Peierls transition in conjunction with an insulating ground state [5]. This so called charge density wave (CDW) ground state is a consequence of the properties of the density response function $\chi(q)$ of a one-dimensional electron gas

$$\chi(q) \propto \frac{1}{q} \ln \left| \frac{q + 2k_F}{q - 2k_F} \right| \ . \tag{2.1}$$

Fig. 2.2 shows $\chi(q)$ for a one-, two- and three-dimensional free electron gas [5]. In one dimension a logarithmic divergency occurs, while for the other two dimensions $\chi(q)$ remains finite.

The different response functions arise from the different dimensionality of the Fermi surfaces. The right panel of Fig. 2.2 shows the Fermi surfaces of an ideal one- and two-dimensional Fermi surface. In one dimension the Fermi surface consists of two points at $\pm k_F$. In the two dimensional case the surface is a circle.
Let us now discuss what this means for the electron system. The Pauli exclusion principle states that electrons can be scattered into empty states only. As the energies of the phonons are very small ($\simeq k_B T$) compared to the energies of the electrons, only electrons in the vicinity of the Fermi surface can participate in scattering processes. For a one-dimensional Fermi surface there are thus two processes to consider. First, the scattering of electrons by phonons with wave vectors $q \approx 0$, i.e., energy and momentum of the electrons are approximately conserved. Second, processes where phonons with wave vectors $q \approx 2k_F$ are absorbed or emitted, changing the wavevector of the electrons from $k \approx \pm k_F$ to $k \approx \mp k_F$, i.e., the electrons are scattered from one side of the Fermi surface to the other (see Fig. 2.1). Thus if a phonon wants to change the electron momentum it must have the wavevector $2k_F$. In other words, one phonon mode ($2k_F$) interacts virtually with all electrons for which the scattering is allowed. In the one-dimensional case $\chi(q)$ diverges at $q = 2k_F$. This is sometimes called

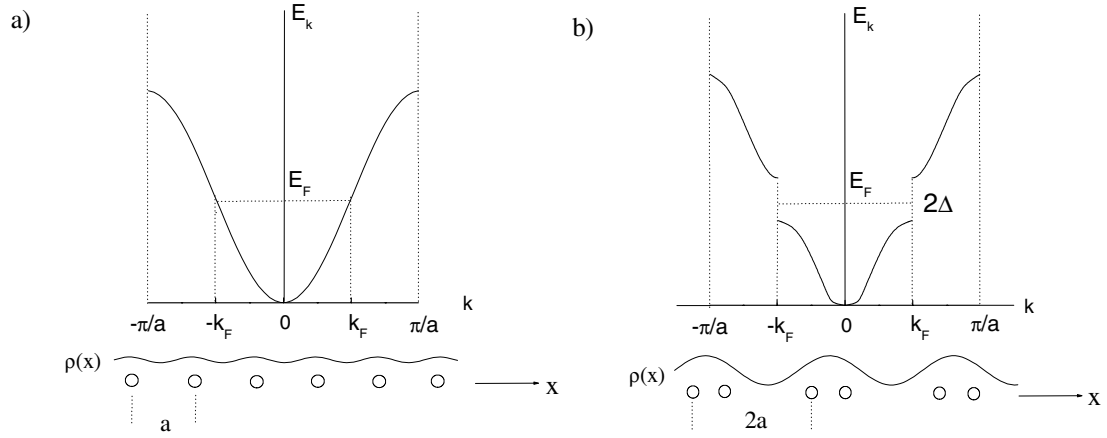

Figure 2.2: Peierls transition illustrated on the basis of a one-dimensional model. The half-filled conduction band and the electron density $\rho(x)$ are outlined for the undistorted chain (a). The electron density smoothly varies with the lattice periodicity. Insulating CDW ground state (b) with a static lattice distortion. The electron density is modulated with a periodicity of $2k_F$. The lattice constant is denoted by a.

"perfect nesting". The pairs of states, one full and one empty, differing by $2k_F$ and having the same energy, give a divergent contribution to $\chi(q)$. In higher dimensions the number of such states is strongly reduced, indicated by the upper $2k_F$ wavevector of the 2-d case in Fig. 2.1(left). This leads to the reduction of the singularity of $\chi(q)$ at $2k_F$.
However, Peierls instabilities are not restricted to one-dimensional systems only. If the energy spectrum meets certain conditions the transition occurs also in higher dimensions, e.g., in the layered transition metal oxides $NbSe_2$ and TaS_2 [6].

To illustrate the Peierls transition we start with the simple situation of a one-dimensional metal (Fig. 2.2 a) with equidistant atoms. First, the situation of a half-filled conduction band is considered. In the nearly free electron approximation, the electron wave functions are the well known Bloch states where the electron density $\rho(x)$ smoothly varies with the lattice periodicity [7]. Let us now shift the atoms from the equilibrium positions according to $u = u_0 \cdot cos(2k_F x)$, as illustrated in Fig. 2.2 b). This leads to a doubling of the unit cell. Hence, the reciprocal lattice vector changes from $2\pi/a$ to π/a. The border of the first Brillouin zone is now at the Fermi wavevector k_F. Consequently, an energy gap opens at the Fermi level where all states below the gap are filled and the states above are empty. The former metal has transformed into a semiconductor with a gap. The electron density $\rho(x)$ is now modulated with a periodicity of $2k_F$.

Is the CDW state energetically favourable? To answer this, we must consider the balance between the gain of electronic energy δE_{el} (due to the lowering of the occupied states) and the loss of elastic energy δE_{dis}, resulting from the distortion of the lattice.
The change of the total energy was calculated by Kagoshima [5]

$$\delta E = \delta E_{el} + \delta E_{dis} \approx -\Delta^2 \left(\chi(q,T) - \frac{\kappa}{2g^2} \right) , \tag{2.2}$$

where g denotes the electron-phonon coupling constant and κ denotes the elastic constant. The polarisation function $\chi(q,T)$ diverges with $T \to 0$ and $q = 2k_F$, while the elastic constant is finite. Hence, for finite g the Peierls transition takes place at finite temperature[1]. The transition temperature follows from $\delta E(T = T_P) = 0$ and is given by

$$k_B T_P^{MF} = 1.1 E_F exp\,(-1/\lambda_0) \text{ with } \lambda_0 = \frac{|g^2 D(E_F)|}{\hbar\omega_{2k_F}} \tag{2.3}$$

where λ_0 the dimensionless electron-phonon coupling constant, ω_{2k_F} the high-temperature phonon frequency leading to the Peierls instability and $D(E_F)$ is the density of states at the Fermi level.

Some Theoretical Results

The formation of the CDW and the Peierls transition are two sides of the same coin. To elucidate this one has to take a closer look at the Fröhlich Hamiltonian in momentum space describing a one-dimensional system consisting of electrons and phonons [8].

$$\mathcal{H} = \sum_{k,\sigma} \epsilon(k) \hat{c}^\dagger_{k,\sigma} \hat{c}_{k,\sigma} + \sum_q \omega_q \left(\hat{b}^\dagger_q \hat{b}_q + \frac{1}{2} \right) + \sum_{k,\sigma} \sum_q g(q) \hat{c}^\dagger_{k+q,\sigma} \hat{c}_{k,\sigma} \left(\hat{b}^\dagger_{-q} + \hat{b}_q \right) \tag{2.4}$$

The first term describes the electron system with Bloch eigenstates. The corresponding electron energies are measured with respect to the chemical potential. The second term represents the phonon energy, where the simplest case with only one acoustical phonon branch is considered. Finally, the electron-phonon interaction is given by the last term with the coupling constant g(q) [8]. This expression can be interpreted in terms of scattering electrons from a state $|k>$ to a state $|k \pm q>$ by absorbing/emitting a phonon with wavevector q (-q).

I want to consider the mean field results now [9]. One should keep in mind that fluctuation effects which are neglected by the mean field theory are particularly important in one-dimensional systems. Here, they are so strong that no long range order occurs at finite temperatures. However, the always present three-dimensional coupling between the chains in real systems allows the formation of a Peierls phase for temperatures above $T = 0$. For further reading about fluctuation effects at the Peierls transition, please refer to the following references [10–14].

Subsequently, I will show on a basic level how the CDW state follows from the Fröhlich Hamiltonian. The transition to the CDW state is related to the "vanishing" of the $2k_F$ phonon mode, i.e., a static lattice distortion occurs for $T \leq T_P$. Thus, the associated mean values $< b_{\pm 2k_F} >$ are different from zero.
In the first step one keeps in the interaction term only the terms with $q = \pm 2k_F$. Next, the operators $\hat{b}_{\pm 2k_F}$ are replaced by their mean values $< b_{\pm 2k_F} >:= b$. Retaining only these terms we find

$$\mathcal{H} = \sum_{k,\sigma} \epsilon(k) \hat{c}^\dagger_{k,\sigma} \hat{c}_{k,\sigma} + \sum_{k,\sigma} g(2k_F) \hat{c}_{k \pm 2k^\dagger_F} \hat{c}_k \cdot 2b + \omega(2k_F) b^2 \ . \tag{2.5}$$

[1] Note, that according to the Mermin-Wagner theorem, ordering in strictly one-dimensional systems does not take place even for T→ 0.

From Eq. 2.5 the average energy $E =< \mathcal{H} >$ can be obtained and reads

$$E = E_0 + g(2k_F)\langle \sum_{k,\sigma} \hat{c}^{\dagger}_{k\pm 2k_F,\sigma}\hat{c}_k\rangle \cdot 2b + \omega(2k_F)b^2 \ , \tag{2.6}$$

where E_0 is the expectation value of the first term in Eq. 2.5. A minimization of E with respect to b yields

$$b = -\frac{g}{\omega} < \sum_{k,\sigma} \hat{c}_{k\pm 2k^{\dagger}_F}\hat{c}_k > \ . \tag{2.7}$$

The righthand side of Eq. 2.7 is not zero as $b \neq 0$. Eq. 2.7 can now be related to the average electron density which is given by

$$\hat{\rho}(x) = \sum_q \rho_q e^{iqx} \tag{2.8}$$

and its q-th component by the Fourier transform

$$\hat{\rho}_q = \sum_{k,\sigma} \hat{c}^{\dagger}_{k\pm q,\sigma}\hat{c}_{k,\sigma} \ . \tag{2.9}$$

the average number density is therefore equal to the righthand side of Eq. 2.7. In the metallic state only $< \hat{c}^{\dagger}_k\hat{c}_k > \neq 0 \Rightarrow < \hat{c}^{\dagger}_{k-q}\hat{c}_k >= \rho_0\delta(q)$. Thus, together with Eq. 2.8 one gets $< \rho(x) >= \rho_0 = constant$. In the CDW ground state, however, one has in addition $< \hat{c}^{\dagger}_{k-2k_F}\hat{c}_k >= \rho_1\delta(q-2k_F)$. Thus the average density is given by

$$< \rho(x) >= \rho_0 + \rho_1 e^{i2k_F x} \tag{2.10}$$

which implies a modulation of the CDW with a period of $2k_F$. Eqs. 2.7-2.10 show the close relationship between the distortion of the lattice and the CDW groundstate. The CDW and the lattice distortion with wavevector $2k_F$ are proportional to each other and have the same periodicity. It should be noted here that this is also the case for a conventional metal, where the Bloch waves are modulated with the periodicity of the lattice. The crucial difference is the collective formation of the CDW ground state, where the $2k_F$ component of $\rho(x)$ dominates all others.

The results obtained by a much more rigorous treatment on the mean field level are summarized below [8, 9].
The modulation of the charge density wave reads

$$\rho(x) = \rho_0 + \rho_1 \cos(2k_F x + \phi) \qquad \rho_1 = \frac{\rho_0\Delta}{\lambda_0\hbar v_F k_F} \ , \tag{2.11}$$

where λ_0 is the dimensionless electron phonon coupling constant, v_F the Fermi velocity, k_F the Fermi wave vector and ϕ the phase. The corresponding displacement at site n is given by

$$u_n = \sqrt{\frac{2}{\omega_{2k_F}}}\frac{\Delta}{g}\cos(2k_F na + \phi) \ . \tag{2.12}$$

Both $\rho(x)$ and u_n are related to a complex order parameter

$$\hat{\Delta} = \Delta e^{(i\phi)} \tag{2.13}$$

describing the phase transition. The energy gap is given by

$$1 = \lambda_0 \int_0^{E_F} \frac{1}{\sqrt{\epsilon^2 + (\Delta(T))^2}} \tanh\left(\frac{\sqrt{\epsilon^2 + (\Delta(T))^2}}{2k_B T}\right) d\epsilon \tag{2.14}$$

and

$$\Delta(0) = 1.76 k_B T_{MF} \tag{2.15}$$

which is formally equivalent to the temperature dependence of the gap of BCS-superconductors.

For a priori soft phonons a strong renormalisation of the phonon spectrum occurs in the vicinity of $2k_F$ (Kohn anomaly). The new phonon frequencies are

$$\Omega_q^2 = \omega_q^2 \left(1 - \frac{2g^2}{\hbar\omega_q}\chi(q,T)\right) \leq \omega_q^2 \tag{2.16}$$

with the unrenormalised phonon frequency ω_q [9]. The temperature dependency of the $2k_F$ mode reads

$$\Omega_{2k_F}^2 = \lambda_0 \omega_{2k_F}^2 \ln(T/T_P^{MF}) \tag{2.17}$$

where λ_0 and T_{MF} denote the electron-phonon coupling constant and the transition temperature in mean field theory respectively. That is the formation of a static lattice deformation arises with $T \to T_{MF}$. Below the transition temperature, the phonon dispersion relation also changes substantially due to the change in the size of the Brillouin zone [5]. This implies that the degenerate phonon branch splits into an optical and an acoustical phonon branch. It can be shown that these branches correspond to the elementary excitations of the CDW, the so-called A_- and A_+ modes [5]. The A_+ mode corresponds to a modulation of the amplitude (amplitudons) of the CDW and the A_- to a phase modulation (phasons). While the amplitudons are gapped, the phason modes are gapless excitations which may be regarded as a sliding of the CDW along the chain, requiring no energy for $q \to 0$.
The sliding without resistance is only possible if the CDW is incommensurate to the lattice, i.e., the ratio of the wavelength of the CDW and the periodicity of the lattice is irrational[2]. However, the translation invariance of the Fröhlich Hamiltonian is broken when the ratio of the wavelength of the CDW and the periodicity of the lattice is rational (commensurable), when impurities in the lattice interact with the CDW or when the CDWs on the 1-d chains interact with each other. In these cases the sliding motion of the CDW is suppressed. One often speaks of this as the "pinning of the CDW". The sliding charge density waves can contribute to the electrical conductivity in a large frequency range [15]. Moreover, the sliding of the CDW is related to extraordinary transport phenomena, e.g., nonlinear conduction, current oscillations and interference effects [16–19].

Experimental Indication of the CDW

The Peierls transition can be identified by dc-conductivity or X-ray measurements. The CDW can be observed by measuring, e.g., the microwave conductivity. In Fig. 2.3 a measurement

[2] Actually, the irrationality requirement is too strong, because commensurability effects are only important for ratios of, e.g., 1/2 or 2/3. For "higher" ratios, e.g. 1/4, 1/8, etc., commensurability effects become weaker [5].

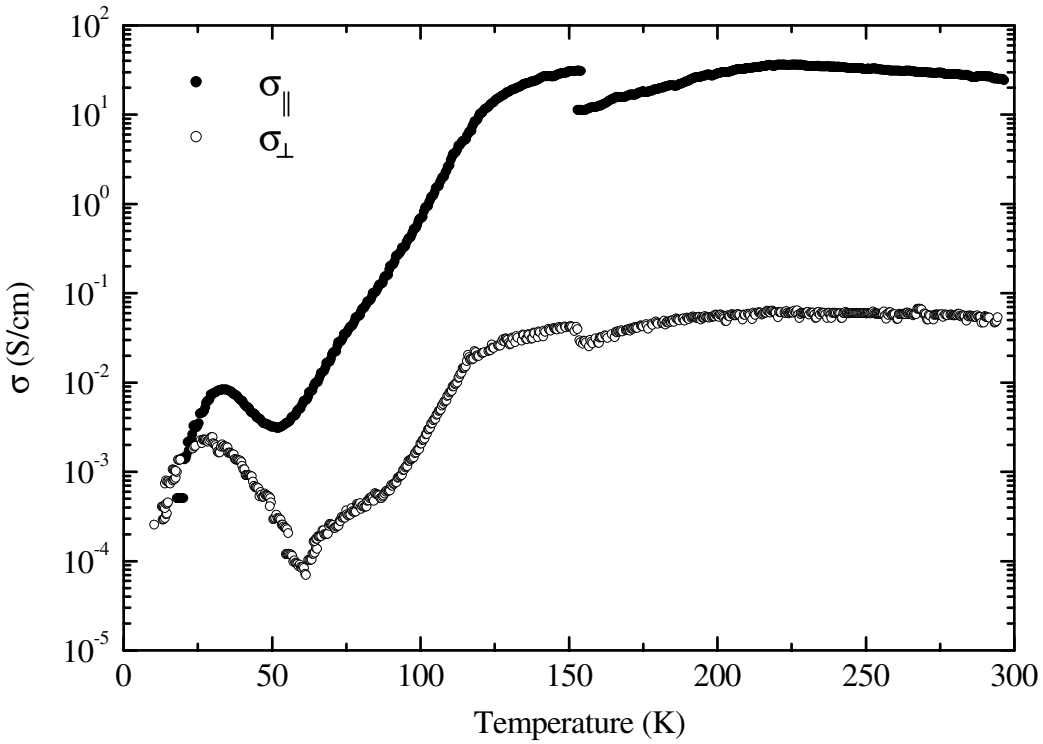

Figure 2.3: Longitudinal (•) and transversal (◦) microwave conductivity of the perylene radical cation salt $(PE)_2PF_6 \times 2/3$ THF.

along and perpendicular to the highly conducting chains of the quasi-one-dimensional conductor $(PE)_2PF_6 \times 2/3$ THF is shown[3]. The system belongs to the so-called perylene radical cation salts. Compared to a conventional metal, the absolute value of $\sigma_{||}$ is rather low. As the transverse conductivity is three orders of magnitude smaller than $\sigma_{||}$, the system is proved to be a quasi-one-dimensional conductor. The low absolute value of σ is attributed to domain walls hampering the electrical conductivity.
The Peierls transition takes place at around 118 K resulting in an activated behavior of the conductivity. Note that the conductivity drops by about four orders of magnitude in a relatively narrow temperature range.
Due to impurities in the lattice the CDW is pinned and no additional contribution to the dc-conductivity is expected. However, the CDW contribution to σ is frequency dependent ($\sigma(\omega) \propto ne^2\delta(\omega - \omega_0)$), where $\omega_0 \approx 10$ GHz is the resonance frequency of the CDW. This results in an enhancement of $\sigma(\omega)$ [4]. The local maximum in σ at 30 K is an indication of charge density waves as a similar effect is not detected in the dc-conductivity [4].
The temperature dependence of $\sigma_{||}$ above the transition reflects the strong influence of structural phase transitions on the electrical conductivity. At 151 K the stack molecules rotate and the anions are shifted out of their original positions, indicated by a step in $\sigma_{||}$. It is believed that the system becomes higher dimensional which partly suppresses the lattice fluctuations. This results in a reduction of the electron scattering and therefore in an increase of $\sigma_{||}$ below 151 K.

[3]The measurements were conducted in a 10.2 GHz resonant cavity during my diploma thesis at II. Physikalisches Institut of the University of Karlsruhe [3].

At 213 K a splitting in two kinds of domains, where the stack molecules are turned into different directions, takes place. This leads to additional electron scattering and therefore to a decrease of $\sigma_{||}$ towards lower temperatures. The transverse electrical conductivity strongly resembles $\sigma_{||}$. However, the step in $\sigma_{\perp}$ at 151 K is smaller that that found in $\sigma_{||}$ and the splitting of the crystal into two domains at 213 K is almost not visible.

2.1.2 The SDW Transition

The electron-electron interaction can have drastic consequences on the ground state of a one-dimensional metal. The simplest possible Hamiltonian describing such an interaction is given by

$$H = t \sum_{<i,j>,\sigma} \hat{c}^{\dagger}_{i,\sigma} \hat{c}_{j,\sigma} + U \sum_{i} \hat{n}_{i,\uparrow} \hat{n}_{i,\downarrow} \tag{2.18}$$

where $\hat{n}_{i,\sigma} = \hat{c}^{\dagger}_{i,\sigma} \hat{c}_{j,\sigma}$ [19]. This is the so-called Hubbard model, given here in coordinate space. The first term describes the kinetic energy of the electrons and the second stands for on-site Coulomb interaction. No electron-phonon interaction is taken into account. The radical limitation to short range interaction is rather severe but the model has proven to be a powerful tool in understanding magnetism and metal-insulator transitions [20].
The spin density wave ground state is thought to arise from electron-electron interaction. This was shown by Overhauser through a mean field approach [21]. As in the case of the CDW state, a gap opens up at the Fermi level and a metal-insulator transition occurs. But in contrast to the CDW state, no lattice distortion takes place. This can be clarified by viewing the SDW as a superposition of two charge density waves – one for the "spin up" and one for the "spin down" subbands which are shifted against each other by $\phi = \pi$ resulting in a cancellation of the charge density modulations, as sketched in Fig. 2.4. The spatial spin modulation is given by

$$< S >= 2S \cos(2k_F x + \phi) \tag{2.19}$$

where S is the amplitude and ϕ is the phase of the spin density modulation. Spin rotational and translation symmetries are broken in the SDW state. The reason why the symmetry breaks is the gain in energy by pushing the occupied states down while raising the empty states.

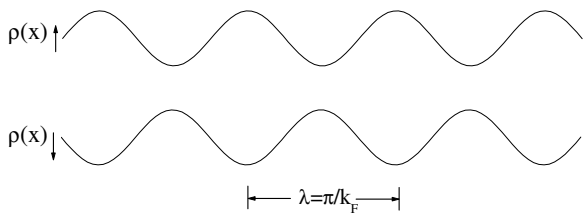

Figure 2.4: Charge and spin density modulation for the two spin subbands in the spin density ground state

As a lattice distortion is absent, the SDW state cannot be observed by structural experiments (e.g., X-ray). However, the transition can be observed by, e.g., measuring the electrical conductivity (see chapter 7) or by applying nuclear magnetic resonance and muon spin rotation techniques [22].

2.2 One-Dimensional Antiferromagnets

The insulating compound $CuGeO_3$, intensively studied in this thesis, belongs to the class of so-called quasi-one-dimensional antiferromagnets where the magnetic coupling is strongly direction dependent. For quasi-one-dimensional spin-1/2 systems with Heisenberg or XY-magnetic exchange, which also exhibit a large magneto-elastic coupling, the spin-Peierls transition is proposed. This transition is driven by the spin system. A spontaneous breaking of the translation symmetry of the spin system leading to a dimerized ground state causes a gain in magnetic energy. While the spin chains are coupled to the lattice, the singlet formation is tied to a lattice distortion, leading to a loss in elastic energy that has to be overcompensated by the magnetic energy gain to force the transition.
In order to see how the spin-phonon coupling comes into play one may consider the following Hamiltonian

$$\mathcal{H} = \sum_i J(i,i+1)\hat{s}_i\hat{s}_{i+1} + \sum_{\mathbf{q},j} \hbar\omega_0(\mathbf{q},j)\left(\hat{b}^\dagger_{\mathbf{q},j}\hat{b}_{\mathbf{q},j} + \frac{1}{2}\right) \ . \tag{2.20}$$

The phonons described by noninteracting bosons are given by the second term where $\mathbf{q}$ and j denote the wavenumber and the phonon branch, respectively. A detailed discussion about the spin-Peierls active phonon modes is given by Braden et al. [23]. The interaction between the phonons and the spin system stems from the influence of a local lattice displacement on the electronic transition matrix elements and hence on the magnetic exchange. To introduce the spin-phonon coupling, J is expanded into a power series of the lattice displacement $\mathbf{u}(i)$. One obtains

$$J(i,i+1) = J + \sum_i \left(\mathbf{u}(i) - \mathbf{u}(i+1)\right)\cdot\nabla_i J(i,i+1) + \dots \ . \tag{2.21}$$

For small phonon displacements it is sufficient to retain the linear term of the expansion only.

The spin-Peierls transition is closely related to the Peierls transition of quasi-one-dimensional metals. As discussed in section 2.1.1, metals with half filling are featured by an instability tending towards dimerisation. It can be shown that for the XY-model the spin operators can be mapped via a Jordan-Wigner-Transformation onto the model of noninteracting spinless fermions (pseudo fermion representation), i.e., one obtains for the pseudo fermions the bandstructure of a Peierls metal [24]. Thus the spin-Peierls transition can be discussed in the same framework as the Peierls transition. The ground state of the spin-Peierls system is a nonmagnetic singlet state separated by an energy gap Δ from the excited triplet states.

A brief overview of the theoretical results will be given now. I want to point out that approximations concerning, e.g., the phonon system and the so-called four-fermion-terms resulting from the Jordan-Wigner-Transformation are necessary in order to obtain the following relations. For further reading on this subject, there are numerous references [24–31].

The transition temperature in the weak coupling regime ($T \ll J$) is given by

$$T_{\mathrm{SP}} = 0.83pJ\exp\left(\frac{-1}{p\lambda}\right) \quad \text{with} \quad \lambda = \frac{4\tilde{g}^2}{\omega_0^2\pi J} \ , \tag{2.22}$$

where $\tilde{g} = \tilde{g}(2k_F)$ is the linearized spin-phonon coupling constant and $\omega_0 = \omega_0(2k_F)$ the unrenormalized frequency of the spin-Peierls active phonon mode. The renormalisation constant p resulting from a Hartree-Fock approximation of the four-fermion-terms is within the

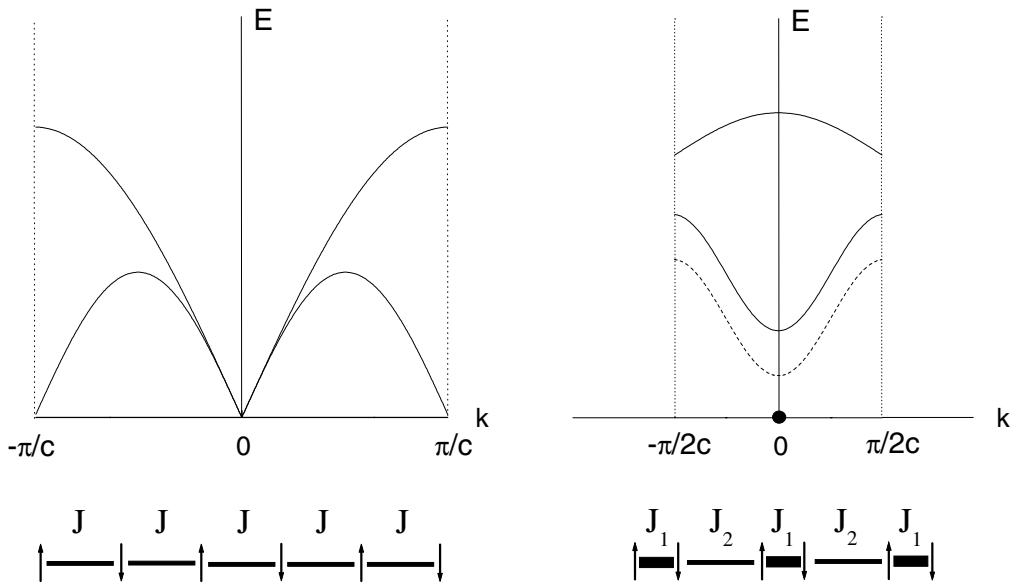

Figure 2.5: Schematic representation of the excitation spectra for the uniform (left) and dimerized (right) antiferromagnetic Heisenberg chain. The long-dashed curve represents the magnon dispersion. The continuum is found between the two solid lines.

weak coupling limit $\simeq 1.64$. As for Peierls systems, a BCS-like energy gap is predicted with $\Delta(T=0) = 1.765\ k_B T_{\mathrm{SP}}$. The dimerisation δ in the D-phase leads to a magnetic energy gain of $E_m \propto \delta^2 \ln \delta$ [29] and is related to the energy gap via

$$J_{1,2} = J\ (1 \pm \delta(T)) \quad \text{and} \quad \delta(T) = \frac{\Delta(T)}{pJ}\ . \tag{2.23}$$

Cross and Fisher succeeded in calculating the transition temperature without the Hartree-Fock approximation of the four-fermion-terms. They obtained

$$\frac{T_{\mathrm{SP}}}{J} = 0.8\ \frac{4\tilde{g}^2}{\omega_0^2 \pi J} \quad \text{or} \quad T_{\mathrm{SP}} = 1.02\ \frac{\tilde{g}^2}{\omega_0^2} \tag{2.24}$$

and in addition, the energy gap Δ and the magnetic energy gain E_m at $T = 0$ K

$$\Delta \propto \delta^{2/3} \quad \text{and} \quad E_m \propto \delta^{4/3}. \tag{2.25}$$

From Eq. 2.24 it is evident that T_{SP} does not explicitly depend on the coupling constant J, but is merely given by the ratio of the spin-phonon coupling constant $\tilde{g}$ and the unrenormalized phonon frequency ω_0. According to this result the spin-Peierls transition is governed by the lattice properties. A soft lattice and/or a strong spin-phonon coupling favor the spin-Peierls transition.

The schematic representation of the energy spectrum of a one-dimensional antiferromagnetic Heisenberg chain is given in Fig. 2.5. The left panel represents the characteristic features of the uniform chain. For $T > T_{SP}$ one finds a so-called spinon continuum bound by the upper and lower curves. This continuum results from two S=1/2 excitations, referred to as spinons. Each spinon is described by the dispersion relation $E(k) = \pi/2J \sin(kc)$, $(0 \leq k \leq \pi/c)$.

Energy and momentum of the two-spinon continuum are given by $E(q) = E(k_1) + E(k_2)$ and $q = k_1 + k_2$, respectively. The lower boundary is found for $k_1 = 0$ and $k_2 = q$ (or vice versa) and the upper boundary for $k_1 = k_2 = q/2$. The peculiar spectrum is related to the degeneracy of the ground state at $k = 0, \pm\pi/c$ where quantum fluctuations lead to an occupation of the states at $\pm\pi/c$. Because of the gapless excitations the susceptibility remains finite.
The right panel of Fig. 2.5 shows the main features of the excitation spectrum of the Peierls-distorted one-dimensional spin chain. The non-degenerate singlet groundstate is separated by an energy gap from the triplet (magnon) states for $T < T_{SP}$, illustrated by the dashed line. The two solid lines enclose the 2-triplet continuum with minimum energy[4] of 2Δ. The dashed line corresponds to bound states of two spinons.

2.2.1 The Spin-Peierls Systems in Magnetic Fields

The influence of the magnetic field on spin-Peierls systems is taken into account by adding a Zeeman term to Eq. 2.20 which reads:

$$\mathcal{H}_m = -g\mu_B H \sum_i s_i^z \qquad (g \simeq 2) \ . \tag{2.26}$$

While the non-degenerate singlet groundstate in the D-phase remains unchanged, the first excited triplet state splits up resulting in a smaller energy gap Δ between the singlet groundstate and the first excited triplet state.
The singlet groundstate is energetically favorable until the applied magnetic field H exceeds a critical value H_{crit}. Interestingly, H_{crit} is smaller than $H = k_B\Delta/g\mu_B$ at $T = 0$, something one would actually expect. This can be understood by adopting the pseudo fermion picture. The magnetic field can be seen as a measure of the band filling; or in other words, the Fermi wave vector depends on the magnetic field [32]. In the U-phase the band is half-filled for a zero magnetic field ($2k_F(H = 0) = \pi/c$). A finite magnetic field corresponds to a more than half-filled band. Hence, in finite magnetic fields the realisation of a filled and empty band can only be achieved for an incommensurate (I) lattice distortion. This means that the ratio between the wavevector $2k_F(H)$ and π/c is an irrational number. However, for small fields the transition to the D-phase is stabilized by Umklapp scattering processes while in higher fields the I-phase is energetically favored.

In the language of the pseudo fermion picture, the deviation from half filling in the U-phase is given by $\frac{\Delta k}{2\pi/c}$ which can be calculated via

$$\frac{\Delta k(H)}{2\pi/c} = \frac{k_F(H)}{\pi/c} - \frac{1}{2} = \frac{M}{g\mu_B} = \frac{\chi H}{g\mu_B} \ , \tag{2.27}$$

where M is the magnetization of the spin chain given by

$$M = \frac{g\mu_B}{N} \sum_{l=1}^{N} s_l^z \ . \tag{2.28}$$

χ denotes the susceptibility, g and μ_B are the g-value and the Bohr magneton, respectively.

[4] Binding effects are neglected here.

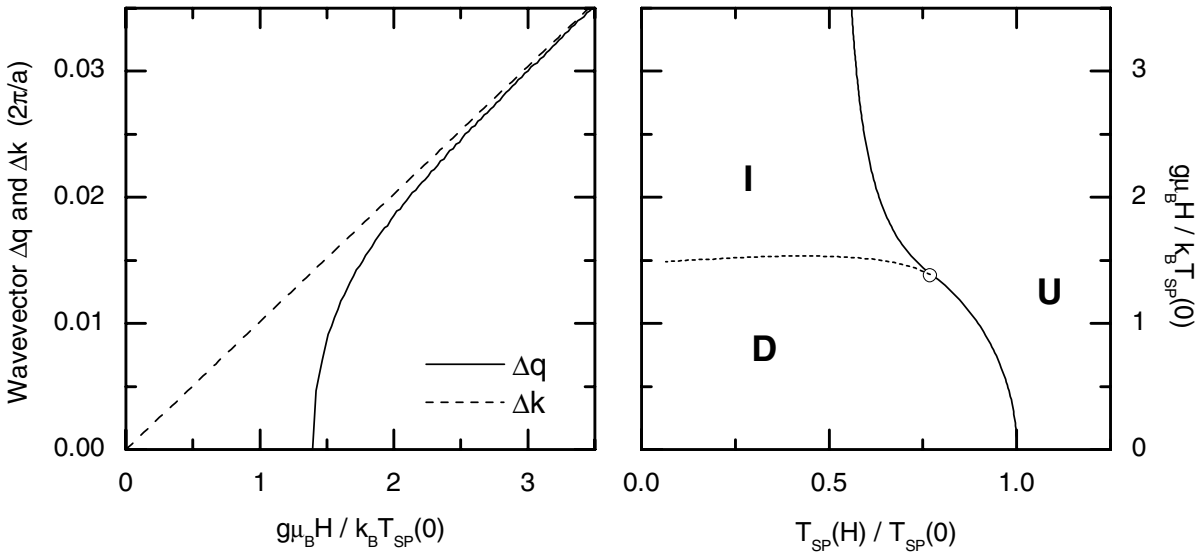

Figure 2.6: Left: Deviation $\Delta q = q(H) - \pi/c$ of the wavevector of the I-phase from that of the D-phase. The difference between the wavevector favored by the magnetic field from π/c is denoted by $\Delta k = 2k_F(H) - \pi/c$ [32]. Right: Universal phase diagram of a spin-Peierls system. The solid line denotes the calculated phase boundary [32]. The D-I phase boundary is indicated by the dashed line.

The competition between the wavevector $q = 2k_F(H)$ favored by the magnetic field and the wavevector $q = 2k_F(0) = \pi/c$ described by the dimerisation is visualized in Fig. 2.6. Here $\Delta k(H) = 2k_F(H) - \pi/c$ and $\Delta q(H) = q(H) - \pi/c$ are plotted. The former describes the deviation from half filling and the latter shows the difference between the wavevector of the distorted lattice of the I-phase and that of the D-phase. In the D-phase substantial differences between $2k_F(H)$ and $q = 2k_F(0) = \pi/c$ are present. Exceeding a critical magnetic field, the transition to the I-phase takes place and $2k_F(H)$ and $q(H)$ rapidly approach each other with further increasing the field.

The right panel of Fig. 2.6 visualizes the universal phase diagram of a spin-Peierls system. The I-U phase boundary was calculated by Cross [32]. The open circle denotes the so-called Lifschitz-point where the three phase boundaries meet. The numerical result for (T_L, H_L) reads:

$$T_\mathrm{L} \simeq 0.77\ T^0_\mathrm{SP} \quad \text{and} \quad g\mu_B H_\mathrm{L} \simeq 1.38\ k_B T^0_\mathrm{SP}\ . \tag{2.29}$$

Clearly, the transition temperature is reduced by a magnetic field. The reduction of T_SP for small magnetic fields is quadratic. The D/U-phase boundary is described approximately by

$$\frac{T_\mathrm{SP}(H) - T^0_\mathrm{SP}}{T^0_\mathrm{SP}} \simeq -0.09 \left(\frac{g\mu_B H}{k_B T^0_\mathrm{SP}}\right)^2 \quad \text{for } H \to 0\ . \tag{2.30}$$

For higher magnetic fields the I/U-phase-transition temperature is expected to saturate at $T_{I/U} = 0.5 T^0_{SP}$ because Umklapp scattering processes stabilizing the D-phase, but there is no contribution of Umklapp processes in the I-phase anymore. In the dimerized phase, Umklapp processes cause an effective doubling of the spin phonon coupling constant in Eq. 2.24 leading

to a doubling of the transition temperature compared to the saturation temperature in the I-phase.

As mentioned above, the lattice distortions in the I-phase are characterized by a wave vector $q = \Delta q(H) + \pi/c$ where $(2\pi/c)/q(H)$ denotes the periodicity of the distortion pattern in units of the lattice constant c. In the framework of the Ginzburg-Landau formalism the structural distortion is described by an order parameter Q. While in the dimerized phase the order parameter is given by an alternating structural distortion with a constant dimerization amplitude $(-1)^n Q$ the incommensurate phase is featured by a modulation of Q with the wave vector $\Delta q(H)$. In the simplest case a sinusoidal modulation of the order parameter is considered and reads:

$$Q_n = (-1)^n Q_0 \cdot \cos(\Delta q n c_0) \ , \tag{2.31}$$

where c_0 describes the original lattice constant along the spin chains [24].
One can also imagine the I-phase made of domains which are still dimerized. In this so-called soliton-lattice model the phase of the dimerization amplitude Q_n alters by π over a correlation length ξ. The modulation is then given by

$$Q_n = (-1)^n Q_0 k \cdot \mathrm{sn}(\frac{n c_0}{k\xi}, k) \ , \tag{2.32}$$

where $sn(x,k)$ stands for the elliptical Jacobi-function with modulus $k \in [0,1]$ given by the distance of the domain walls $L = \pi c_0/\Delta q$ [33, 34]. We see two interesting cases: for $k \to 1$ Eq. 2.32 transforms to $\tanh(x)$ describing a single soliton. For $k \to 0$, accounting for the decreasing soliton distance, $sn(x,k)$ goes over to a sinusoidal modulation. Similar to $\Delta k(H)$ (see Eq. 2.27) in the uniform phase, $\Delta q(H)$ is related to the magnetization M via

$$\frac{\Delta q}{2\pi/c} = \frac{M}{g\mu_B} \ , \tag{2.33}$$

where $2\pi/c$ describes the reciprocal lattice vector of the undistorted spin chain.

2.2.2 Magnetic Frustration

So far only an antiferromagnetic exchange between the nearest neighbors has been considered. Taking antiferromagnetic next nearest neighbor interaction into account, frustration comes into play. The one-dimensional spin chain governed by frustration and dimerisation can be described by the Hamilton operator

$$\mathcal{H} = \sum_l J \left(1 - (-1)^l \delta\right) \hat{s}_l \cdot \hat{s}_{l+1} + J' \hat{s}_l \cdot \hat{s}_{l+2} \tag{2.34}$$

where δ accounts for the dimerisation and $J_{1,2} = J(1 \pm \delta)$ stands for the alternating coupling between the nearest neighbors.
In Fig. 2.7 the general phase diagram of dimerized and frustrated spin chains is depicted as $T = 0$ [35]. Let us discuss the most important regions. For $\delta = 0$ and $J' = 0$ one has a uniform Heisenberg chain that exhibits no gap in the excitation spectrum. For $\delta = 0$ the groundstate remains gapless as long as the frustration ratio J'/J does not exceed the critical value $\alpha_c = 0.2411$, obtained by a numerical scaling analysis [36–38]. For $J'/J > \alpha_c$ and $\delta = 0$ the groundstate is also dimerized due to spontaneous symmetry breaking, i.e., through the

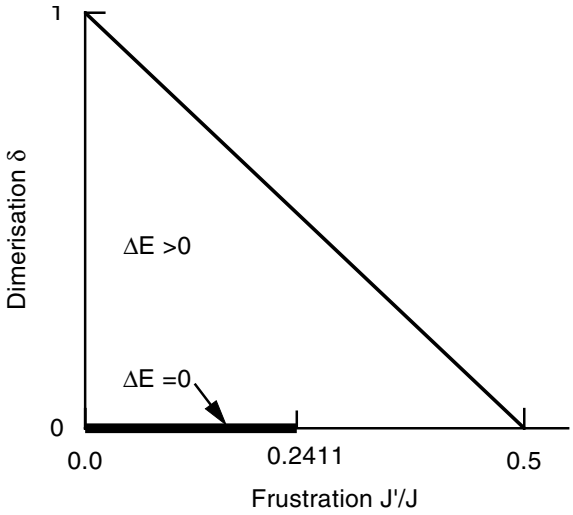

Figure 2.7:
Phase diagram of an AFM Heisenberg chain with $|\vec{S}| = 1/2$ as function of frustration J'/J and dimerisation $\delta = (J_1 - J_2)/2J$ at $T = 0$ [35].

formation of singlet pairs.
Exact results for the groundstate are obtained for the so-called Majumdar-Gosh-point ($J'/J = 0.5$ and $\delta = 0$) where the groundstate is made up of spin dimers with a finite energy gap and for the groundstate on the line $2J'/J + \delta = 1$, which is a product wavefunction of independent singlet dimers [39–41]. The system is always gapped as soon as the dimerisation ($\delta > 0$) is switched on. No analytical results for the groundstate can be obtained in this region.

Chapter 3

Thermal Transport in Solids

In this chapter a brief and fundamental introduction to the heat transport in solids will be given. This chapter is not intended to be a complete summary of all heat transport mechanisms known, but is rather concerned with a specific selection of the basic transport properties of phonons, electrons and magnetic excitations and the interplay between them in an experimentalist's point of view. Detailed calculations that blur the physics are omitted here. References will be given concerning the transport properties of "magnons" and the influence of phonon scattering on magnetic excitations giving an overview of previous experimental and theoretical treatments on magnetic materials.

3.1 Heat Transport by Phonons

A general expression for the thermal conductivity κ on the basis of a kinetic theory has been given by Debye [42]. In the simplest form κ reads

$$\kappa = \frac{1}{3} cvl \ , \tag{3.1}$$

where in the modern language c is the specific heat of the quasiparticle excitations, v the mean velocity of these particles, and $l = v\tau$ the mean free path (τ is the relaxation time). The theoretical problem of heat transport through an insulating solid has been treated by various research groups [43–47]. The heat transport of phonons is essentially governed by the scattering of phonons on the sample boundary, on lattice imperfections or on defects and phonon-phonon scattering processes. The latter process can be distinguished in normal or so-called N processes which conserve phonon quasi momentum and resistive or so called Umklapp processes. Although N processes do not give rise to thermal resistance they may have a strong impact on other resistive scattering processes as they may alter the occupation of possible phonon states [45, 48, 49].

For a quantitative description of our data, presented in chapters 5 to 8, we will use a Debye model for the phononic thermal conductivity [45–47, 50]. Therefore I want to introduce this central equation here:

$$\kappa^{ph} = \frac{k_B}{2\pi^2 v} \left(\frac{k_B}{\hbar}\right)^3 T^3 \int_0^{\Theta_D/T} \frac{x^4 e^x \tau\left(\omega, T\right)}{\left(e^x - 1\right)^2} dx \ , \tag{3.2}$$

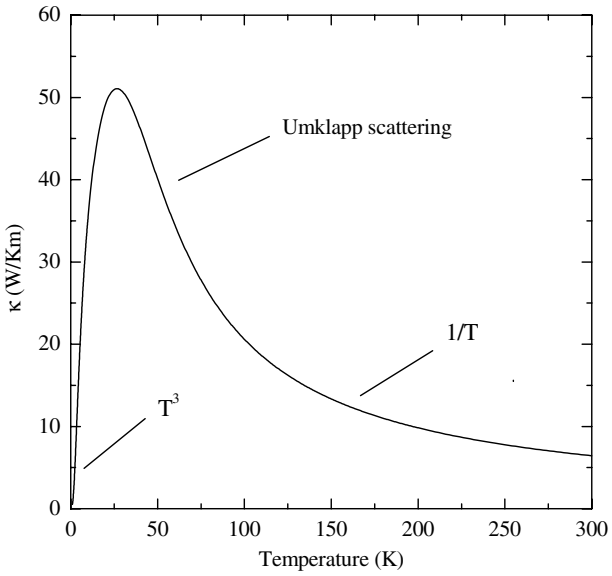

Figure 3.1: Generic thermal conductivity of an insulator. The curve was obtained by applying Eq. 3.2 and a set of reasonable parameters. The T^3-dependence of κ at low temperatures reflects the specific heat c. At high temperatures Umklapp processes dominate, resulting in a $1/T$ dependence of κ.

where v is the sound velocity, Θ_D the Debye temperature, ω the phonon frequency, $x = \hbar\omega/k_BT$ and $\tau(\omega, T)$ the mean lifetime of a phonon. The total scattering rate τ^{-1} is given by

$$\tau^{-1} = \tau_{bd}^{-1} + \tau_{pt}^{-1} + \tau_{um}^{-1} + \dots \ . \tag{3.3}$$

Here τ_{bd}^{-1}, τ_{pt}^{-1}, and τ_{um}^{-1} refer to the standard relaxation processes for conventional phonon heat transport, i.e., to boundary scattering, scattering by point defects, and Umklapp scattering, respectively [44]. The relaxation rate τ_{bd}^{-1} is obtained by $\tau_{bd}^{-1} = v/L$ with the characteristic sample length L. As at very low temperatures this scattering process dominates in high quality crystals and hence the mean free path l is essentially constant, the thermal conductivity reflects the T^3 behavior of the specific heat.
The point defect scattering rate is given by $\tau_{pt}^{-1} = P\omega^4$. The frequency dependency of this scattering mechanism can be qualitatively understood. Long wavelength phonons are less scattered on point defects than phonons with shorter wavelengths (for details see also chapter 5).
The phonon Umklapp scattering rate is approximated by $\tau_{um}^{-1} = UT\omega^3 \exp(-\Theta_D/uT)$ [44]. With increasing temperature this scattering scheme becomes important due to the rapidly increasing number of phonons. Roughly speaking, the relaxation rate τ^{-1} will be inversely proportional to the density of phonons n_{ph}, which are bosons. Thus, we get for the relaxation time

$$\tau^{-1} \propto l^{-1} \propto n_{ph} \propto \left[exp\left(\frac{\hbar\omega}{k_BT}\right) - 1 \right]^{-1} \ . \tag{3.4}$$

According to the Debye model Umklapp scattering sets in above a certain threshold value of the reciprocal lattice vectors of the phonons. Hence the frequency of the phonons involved is approximately given by

$$\hbar\omega \simeq k_B\Theta_D/b \tag{3.5}$$

where Θ_D is the Debye temperature and the constant $b > 1$ [7, 44].
For temperatures ($T \gg \Theta_D$) the specific heat c is nearly constant, thus $\kappa \propto \Theta_D/bT$. At lower

temperatures ($T \ll \Theta_D$) c also varies with temperature, but the exponential variation in l is so dominant that $\kappa \propto exp(\Theta_D/bT)$.
The thermal conductivity of an insulator is shown in Fig. 3.1. The curve was obtained by using Eq. 3.2 and reasonable values for the parameters[1]. One finds one maximum of moderate absolute value at low temperatures.

Of course, various other processes are conceivable. For example, a process which may become important in systems with sheet-like structures, is scattering on planar defects. The scattering rate is given by: $\tau_D^{-1} = D\omega^2$. For a detailed summary of scattering rates, I refer to [44].

3.2 Heat Transport by Electrons

In metals we have an additional electronic contribution to the thermal conductivity that may, for fairly pure simple metals, exceed the phonon contribution. The Wiedemann-Franz law (WFL) links the electrical conductivity with the electronic thermal conductivity via

$$\kappa_{el} = L \cdot \sigma \cdot T \tag{3.6}$$

where σ is the electrical conductivity and L the Lorenz number[2]. The WFL holds when the energy of each electron is conserved in each collision. At low temperatures the dominant source of collisions is elastic impurity scattering. Hence, the WFL is to a good approximation valid at low temperatures. At high temperatures, the scattering of electrons by thermally excited vibrations of the ions becomes important. If the change in energy of each electron in such a collision is small compared to $k_B T$ then it turns out that the WFL law is also valid. This requirement is fulfilled for $T \gg \Theta_D$. In the intermediate temperature range, failures of this law are expected [7, 51].
At very low temperatures the electrical conductivity of a metal becomes constant and according to the WFL $\kappa_{el} \propto T$. At higher temperatures, electron-phonon scattering becomes effective. Here, the electrical conductivity σ of a metal is to a good approximation proportional to T^{-1} [52]. Hence, the thermal conductivity is constant. At intermediate temperatures electron-phonon scattering lessens, thus κ_{el} increases rapidly with decreasing temperature.
There are some subtle differences between phononic and electronic heat transport which we refer to. At the lowest temperatures the phononic and electronic thermal conductivity reflect the specific heat of their excitations, respectively. This implicates that the thermal conductivity of a metal is proportional to T, while for an insulator it is proportional to T^3. One should be aware that for phonons the constant mean free path is determined by the sample boundary, while for electrons it is determined by lattice imperfections. This can be qualitatively understood if we consider the wavelengths involved. At the lowest temperatures only those low lying acoustical phonons are excited whose wavelengths are much longer than the interatomic spacing and thus almost unaffected by disorder on an atomic scale. However the wavelengths of conduction electrons in metals are about equal to the interatomic spacing, which in turn leads to a strong scattering of electrons on lattice imperfections on atomic dimensions.

[1] $\Theta_D = 453K$, $L = 0.75\ mm$, $v = 7600\ m/s$, $P = 7.7 \cdot 10^{-43} s^3$, $U = 2.6 \cdot 10^{-31} s^2/K$, $u = 5$.

[2] For the free electron gas the Lorenz number reads: $L = \frac{\pi^2}{3}\left(\frac{k_B}{e}\right)^2 = 2.45 \cdot 10^{-8} W\Omega K^{-2}$.

In conclusion, the absolute values of the purest metals (e.g., pure gold) can reach thousands of W/Km. Insulators are usually the much poorer conductors, however, exceptions to this rule can be found in diamond ($\kappa(100\text{K}) \approx 10000$ W/Km) or sapphire ($\kappa(30\text{K}) \approx 20000$ W/Km) [53][3].

3.3 Heat Transport by Magnetic Excitations

The transport of heat by phonons and electrons has been studied thoroughly. Already thirty years ago there was a growing interest in finding experimental and theoretical evidence for heat transport by excitations in magnetically ordered systems, and in particular in low-dimensional quantum spin systems (see [54–57] and references therein).
At first look one can say that magnons can influence the thermal conductivity either by scattering phonons diminishing the heat transport or by transporting heat. Unfortunately, it is more complex than this. Sanders et al. point out that a complicated interplay between magnons and phonons is to be expected as interactions between phonons and magnons must be present in order to obtain a heat flux into the magnon system [58]. As in an ordinary measurement of the thermal conductivity a heater attached to the sample creates at first phonons, a sizeable magnetic contribution can only be detected if a coupling to the phonon system allows a temperature gradient to build up for the magnon system. Moreover, the thermocouples which detect the temperature gradient are again coupled to the phonon system; hence without phonon-magnon coupling, only the phononic contribution to the heat current is experimentally detected even if the magnon heat flux is immense. Based on a phenomenological approach they obtained the relation

$$\kappa_{meas} = (\kappa_{ph} + \kappa_m) \cdot \left(1 + \frac{\kappa_m}{\kappa_{ph}} \frac{tanh(1/2A \cdot L)}{1/2A \cdot L}\right)^{-1} , \tag{3.7}$$

where κ_{meas} is the experimentally observed thermal conductivity, κ_{ph} and κ_m are the phonon and magnon contribution, respectively, and L is the sample length. The constant A is proportional to $\tau_{mp}^{-1/2}$ where τ_{mp} is the phonon-magnon relaxation time [58]. Thus, the measured thermal conductivity is the sum of $\kappa_{ph} + \kappa_m$ only if the phonon-magnon relaxation time becomes very small ($A \to \infty$) which just indicates a strong coupling between phonons and magnons. If the phonon-magnon relaxation time becomes very large then $\kappa_{meas} = \kappa_{ph}$, and only the phonon thermal conductivity can be measured, regardless of the magnitude of the intrinsic magnon conductivity. An application of their theory to the ferrimagnetic yttrium iron garnet (YIG) with short relaxation times and to the antiferromagnet MnF_2 compound with long relaxation times shows a possible magnetic contribution in YIG and little or no magnon component in MnF_2. This is well in accordance with experiment, suggesting that almost two thirds of the zero-field thermal conductivity is due to magnons in YIG, while a magnetic contribution in MnF_2 is absent [59].
To recapitulate, the observation of a magnetic contribution to the total thermal conductivity is closely related to the phonon-magnon interaction, which also may considerably affect the phonon thermal conductivity. In other words magnons can act as strong scattering centers for phonons. Experimental evidence for the scattering of phonons by magnetic excitations leading to a strong damping of the phonon thermal conductivity in a narrow temperature region is found in the two dimensional quantum spin system $SrCu_2(BO_3)_2$. For a detailed

[3] The absolute values depend considerably on the impurity concentrations.

discussion of this phenomenon, I refer to chapter 5 and the references therein.
Finally, it is worth noting that in antiferromagnets and ferrits containing paramagnetic and diamagnetic impurities[4] the thermal conductivity may be governed by mutual magnon and phonon drag at low temperatures [60]. It is claimed that the temperature dependence of the thermal conductivity in antiferromagnets depends considerably on the kind of impurities in the region, where due to unilateral or mutual drag, phonons and magnons have a common drift velocity. In the case of diamagnetic impurities, κ was found to decrease monotonically with increasing temperature, while for paramagnetic impurities a maximum exists in κ if the Neél temperature exceeds the Debye temperature.
From the above mentioned considerations, it is obvious that a separation into a phonon and magnon component is actually impossible in the case of coupled magnetoelastic modes, where the excitations are considered to be partially phononic and partially magnonic. In addition, even if there are distinct magnetic and phononic contributions of the thermal conductivity present, we are still faced with the problem of the experimental separation. A straightforward method to separate phonons from electrons can be achieved by the use of the Righi-Leduc effect, which is the thermal analogon to the Hall effect [61]. Here, the application of a magnetic field perpendicular to the heat current separates the electronic from the phononic contribution to κ. A tranversal temperature gradient builts up, that is correlated to the electronic part of κ. Unfortunately, no similar technique is applicable for the separation of phonons and magnons. What remains though, are measurements of the thermal conductivity in magnetic fields, as the phonon thermal conductivity does not directly depend on the magnetic field and/or the measurement of κ along different crystallographic directions, exploiting the anisotropy effects of κ. Another useful but also indirect technique is the doping of the sample affecting both the phonon and magnon heat transport. The combination of these techniques often offers conclusions about the possible presence of additional magnetic contributions.

During the last few years, new low-dimensional spin systems have been discovered and have renewed interest in measuring the thermal conductivity (κ) of compounds with unusual magnetic properties [1, 2, 62–65]. One reason for this is that in these materials a large magnetic contribution κ_m to the heat current may be present. This has been observed, e.g., for the spin ladder material $Sr_{14-x}Ca_xCu_{24}O_{41}$ [65, 66]. In Fig. 3.2 the thermal conductivity along different crystallographic directions of the spin gap materials $Sr_{14}Cu_{24}O_{41}$ and $Ca_9La_5Cu_{24}O_{41}$ is illustrated [66]. For both compounds a pronounced anisotropy in the heat transport is found. Enormous maxima at about 140 K for $Sr_{14}Cu_{24}O_{41}$ and at 175 K for $Ca_9La_5Cu_{24}O_{41}$ are observed for the thermal conductivity along the chain and ladder direction (κ_c). In $Sr_{14}Cu_{24}O_{41}$, low temperature maxima arise at about the same temperature for all three crystal directions but with rather different absolute values. Although some anomalous behavior for κ_a is apparent at higher temperatures, in $Sr_{14}Cu_{24}O_{41}$ (see inset of Fig. 3.2) the thermal conductivities perpendicular to the chains and ladders (κ_a, κ_b) can be interpreted in the framework of a usual phonon thermal conductivity for both compounds. An interpretation of the unusual thermal conductivity along the c-axis was already given by Sologubenko et al. for $Sr_{14}Cu_{24}O_{41}$ [65]. They ascribed the high temperature maximum to a magnetic contribution that adds to the phononic one, giving rise to the low temperature maximum. The additional findings in $Ca_9La_5Cu_{24}O_{41}$ strongly support their suggestions.
First, the strong suppression of κ_{ph} in comparison to the stoichometric compound combined

[4] To my knowledge no results for ferromagnetic materials have been published.

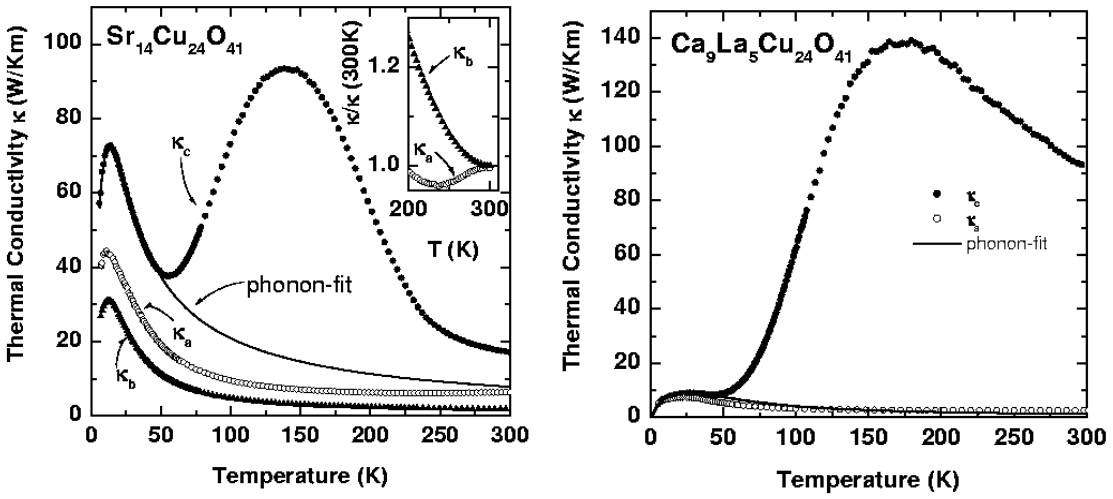

Figure 3.2: Left: Thermal conductivity of $Sr_{14}Cu_{24}O_{41}$ along the three crystallographic axis a,b and c, respectively. The solid line shows a phonon fit to κ_c. The inset shows the enlarged high temperature region for κ_a and κ_b normalized to the value at 300 K. Right: Thermal conductivities κ_a and κ_c of $Ca_9La_5Cu_{24}O_{41}$ along the a and c direction. The solid line represents a hypothetical phonon contribution to κ_c. According to C. Hess [66].

with the increase of κ_c at high temperatures, supports the idea that there are two independent contributions to the heat transport. Second, other possible additional contributions can be excluded due to the electronic properties of the two compounds concerning their different hole concentrations and the very different ordering phenomena [66].
Through a detailed theoretical analysis, Hess et al. determined from the thermal conductivity data the mean free path that is in both compounds very large (several thousand $\mathring{A}$). Reasonable spin gaps are obtained by fitting their experimental curves with a model for magnon thermal conductivity, which backs the interpretation that the high temperature peak is caused by an additional magnetic contribution for both materials. To summarize, the spin ladder compounds are by far one of the most reliable candidates for two more or less independent contributions to κ comprising a phonon contribution and a sizeable magnon contribution.
However, there are various other studies on the thermal conductivity in low dimensional spin systems where magnetic contributions are discussed, such as $KCuF_3$ [67], Yb_4As_3 [68] and the spin-Peierls compound $CuGeO_3$ (see Chapter 6 and the references therein). Recently, measurements of the thermal conductivity on the quasi-one-dimensional spin $S = 1/2$ chain compounds $SrCuO_2$ and Sr_2CuO_3 have been reported [69]. The thermal conductivity data resemble closely those of the spin ladders. Again, κ along the spin chains exceeds in both compounds the thermal conductivities perpendicular to the chains, and in addition, moderate maxima at about 60 K for $SrCuO_2$ and at 100 K for Sr_2CuO_3 are observed for the heat transport along the chains *only*. Yet, the discrimination of phonon and magnon contributions is very difficult here because an unambiguous separation of the phonon background is apparently not possible. Nevertheless, a substantial magnetic contribution to the heat current at high temperatures is very likely in these low dimensional compounds.

There are still, however, many unsolved problems concerning the transport of energy by magnetic excitations. Some of these problems are, the unusual size and temperature dependence

of the magnetic contributions in the spin ladders, the relation between the topology of the spin system and its transport properties, and the impact of scattering processes among the excitations or with other quasiparticles such as phonons on the heat transport. A straightforward phenomenological model for heat transport by magnetic excitations presented in chapter 6 for $CuGeO_3$ reveals that the knowledge concerning whether "magnon-magnon" scattering is important or not could considerably simplify the interpretation of the experimental findings. Unfortunately, a theory based on microscopic grounds for heat transport in spin systems has not yet been developed.

Chapter 4

Experimental

One objective of this thesis is to set up a device for measuring the thermal conductivity in the temperature range between 2.2 and 300 Kelvin and in high magnetic fields. First, I will describe the basic method for measuring the thermal conductivity on bulk material, then I will give a detailed discussion of the experimental setup. The measurement device for electrical resistivity measurements is explained elsewhere [70], therefore only a short description of the main aspects and the essential features performing these resistivity measurements on organic systems is given here.

4.1 Thermal Conductivity

There are various techniques available for measuring the thermal conductivity, e.g., the comparative method, the 3ω-technique and the standard steady state method [71–73]. Even though the 3ω-technique has the advantages of acquiring the temperature dependence of the thermal conductivity much more readily than other techniques and of minimizing radiation losses at temperatures above 100 Kelvin (discussed in this chapter), this method is for practical reasons difficult to apply on samples where the thermal transport properties depend strongly on the crystallographic directions [71, 74]. The method of choice is therefore the differential steady state method, which is very reliable and well established [75].

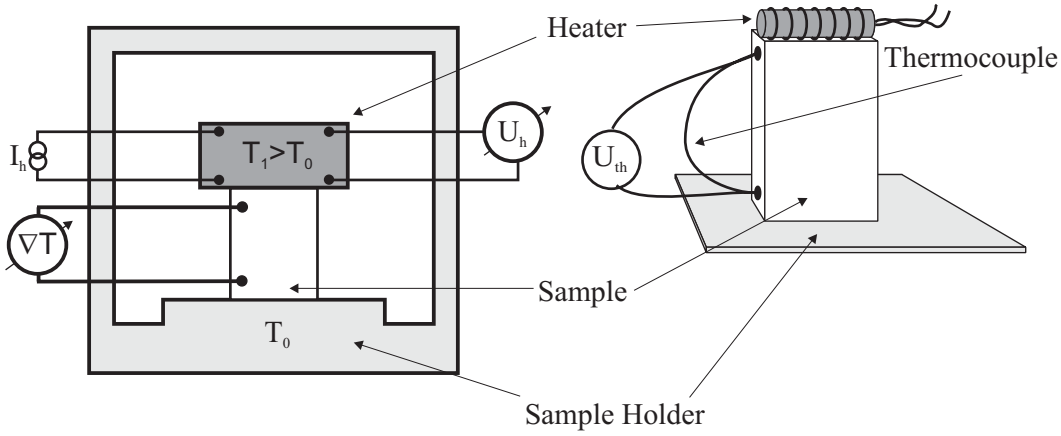

Figure 4.1: Differential Steady State Method.

A scheme of this method are shown in Fig. 4.1. A heater placed on top of the sample generates a heat current passing through the sample. The sample is anchored to the sample holder, which is on a stable base temperature T_0. A temperature gradient builds up which can be detected, for example, by a thermocouple.
The relation used to determine the thermal conductivity κ can be derived from its definition:

$$\vec{j}_q = -\kappa \cdot \vec{\nabla} T \ . \tag{4.1}$$

This holds for an isotropic and electrical insulated sample. According to Eq. 4.1 a heat current $\vec{j}_q$ through a sample is related to a temperature gradient along the sample, which has to be measured. The minus sign indicates that heat flows down a temperature gradient from the hotter to the colder region. It should be mentioned that for crystals that do not have cubic symmetry, Eq. 4.1 must be replaced by

$$j_i = -\kappa_{ij} \cdot \frac{\partial T}{\partial x_j} \ , \tag{4.2}$$

where κ_{ij} are the elements of a second rank tensor. To measure the thermal conductivity of anisotropic samples, one therefore has to refer to the principal axis.
The heat current through the sample can be written as

$$j_q = \frac{P_h}{A} \ , \tag{4.3}$$

where P_h is the heater power and A the cross section of the sample. The measurement of the temperature difference along the sample is carried out by using carefully calibrated thermocouples (Section 4.1.2).
For a small temperature gradient the following relation holds

$$\vec{\nabla} T = \frac{\Delta T}{l} \ , \tag{4.4}$$

with ΔT the temperature difference and l the distance between the endpoints of the thermocouple fingers. The relation between the temperature difference ΔT, the thermopower $S(T, B)$ of the thermocouple and the corresponding voltage drop ΔU_{th} is given by:

$$\Delta T = \frac{\Delta U_{th}}{S(B, T)} \ , \tag{4.5}$$

where S depends on the temperature and on the magnetic field. Combining the above equations yields κ:

$$\kappa = \frac{P_h \cdot S(B, T)}{\Delta U_{th}} \cdot \frac{l}{A} \ . \tag{4.6}$$

In order to measure the power P_h supplied by the heater, a four-wire method is applied where a Knick J152 Source supplies a constant current. The voltage across the heater is detected by a Keithley 2000 multimeter. The base temperature T_0 can be stabilized within 0.1 mK below 10 Kelvin and within a few mK above 10 Kelvin using a Neocera temperature controller in combination with a Cernox temperature sensor. Making use of the high resolution thermocouples (see Section 4.1.2) in combination with the high temperature resolution ΔU_{th} can be resolved within < 10 nV using a Keithley 2182 nanovoltmeter. The relative accuracy of κ is therefore within a few percent, the absolute accuracy is of the order of 10 to 15 % which has to be attributed to uncertainties in the sample geometries and possibly ill-defined distances between the thermocouple ends.

4.1.1 Sample Insert and Cryostat

The schematics of the sample insert are shown in Fig. 4.2. Essentially, the measurement device consists of two parts – a stainless steel tube and an inset designed to measure transport quantities, e.g., the thermal conductivity.

The steel tube together with the top section containing eight pin connectors form a single vacuum space that is evacuated via a NW40KF port. The vacuum space should be brought to pressure $\leq 10^{-5}$ mbar because the thermal conductivity is measured adiabatically. The cooling device comprises of a brass tube that is soldered to the steel tube and a cooling stage made of oxygen free copper.
In order to establish a good thermal contact, a thin film of Apiezon-N grease is put on the contact surfaces of the brass tube and the cooling stage. The cooling of the sample holder and the sample takes place via the measurement leads that are thermally anchored to the cooling stage. However, the thermal contact between the sample holder and the cooling stage mediated by the thin measurement leads is not sufficient to reach the lowest temperatures. Therefore a cooling switch allows control over the cooling rate and permits operation at temperatures down to ≈ 2 Kelvin.
The switch consists of two parts – a copper link and a stainless steel capillary tube which serves as the cooling link control. The copper link is thermally anchored to the cooling stage via a copper ribbon. The ribbon is glued with GE-varnish to the top of the link and to the stage, respectively. The lower part of the link is needle shaped and fits into the drill-hole of the sample holder. Highly ductile Indium is put into the drill-hole to guarantee good thermal contact. The cooling power can be controlled by the quality of the thermal contact between the copper link and the drill-hole.

The inset is suspended from the lower part of the top section on four capillary tubes that are also used as runnings for the measurement leads. To minimize offset voltages caused by temperature differences in the leads and to avoid heat conduction from the hot to the cold end of the insert, one couples them thermally to the cooling stage. This is achieved by winding the leads around small copper pins which are prior evaporated with a thin film of Delta Bond 152 (two-component adhesive) to ensure electrical insulation.

It is important to note that the material and the diameter of the leads have to be chosen carefully. By experience, 50 μm copper wires should be used for measuring the voltage of the thermocouple. To measure the resistivity of the temperature sensors, a four-wire technique is used, where all of the leads are made out of 100 μm manganin. Furthermore, the Hall-probe is connected to 50 μm current leads made of copper and to 100 μm manganin leads for measuring the voltage. Finally, two heaters have to be connected: the heater for the sample holder which establishes a constant base temperature between 2.3 and 300 Kelvin, and the heater on the top of the sample generating the temperature gradient. As the heater for the sample holder has to sustain relatively high currents, 100 μm copper supplies are used. All of the leads of the small sample heater are made of copper wires with diameters less than 50 μm.

A detachable socket made out of oxygen free copper and provided with various copper pins, is fixed with screws to the sample holder. All measurement leads are soldered to the pins in order to keep the ends of the leads at the same temperature. This is found to be neces-

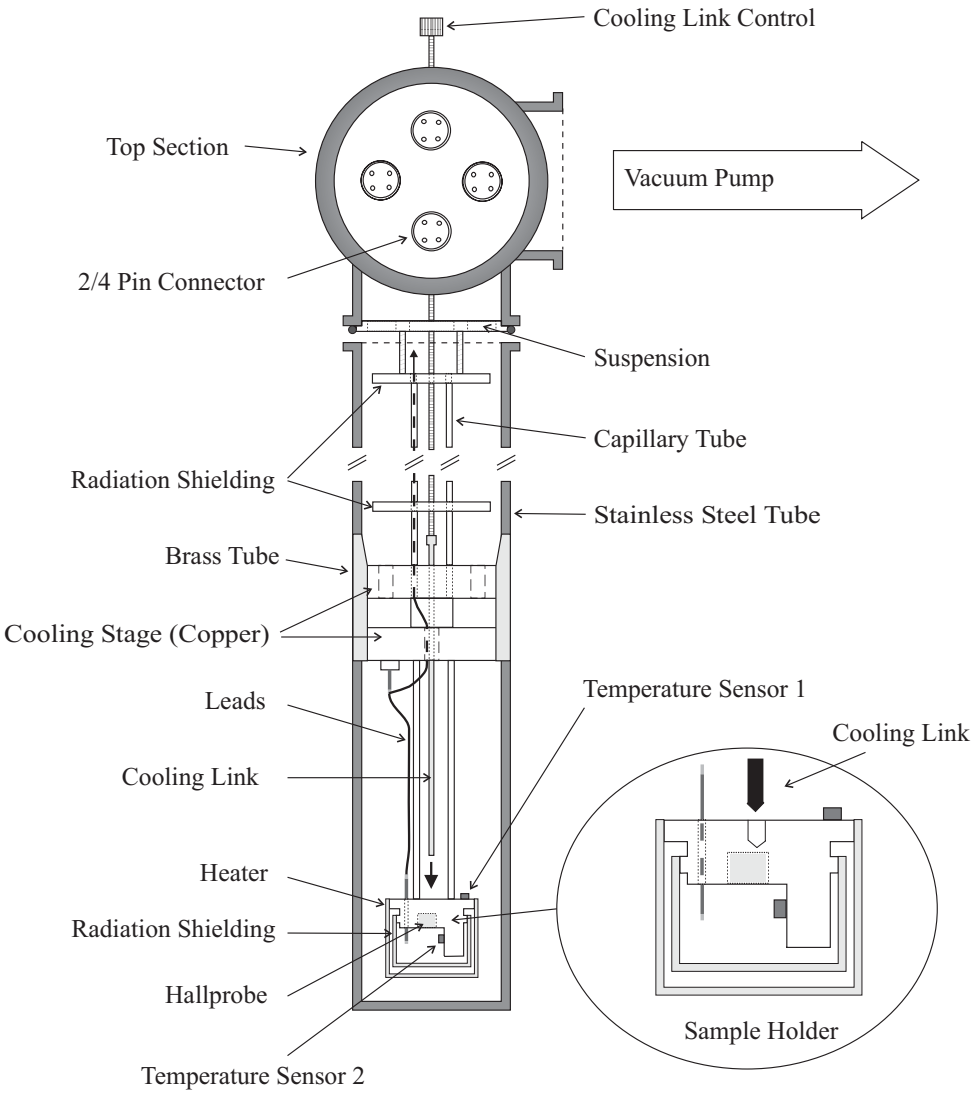

Figure 4.2: Schematics of the sample insert.

sary especially for the thermocouple leads (for further details see section 4.1.2). A radiation shielding and the heater surround the sample holder. Both are coated with a thin gold film to prevent oxidation radiation losses.
In conjunction with the measurement device described above, a cryomagnetic system was completed composed of cryostat[1] and vacuum pumps to operate the measurement device. The cryostat consists of a high field superconducting magnet designed to produce fields of 15.8 Tesla in normal operation and in excess of 17 Tesla when using the λ-plate refrigerator that maintains the liquid helium at 2.2 Kelvin. For details, please refer to [75, 76].

[1] Cryogenic Ltd, London, UK.

4.1.2 Calibration

The calibration of the thermocouples is completed in two steps. First, one calibrates two Lakeshore Cernox 1050-BC temperature sensors between 2.2 Kelvin and 300 Kelvin using a Lakeshore CX-1050-AA sensor as a reference[2]. The uncalibrated temperature sensors and the reference sensor are carefully mounted on the sample holder.
The absolute value of the temperature is detected using the reference sensor together with a Neocera Temperature Controller LTC-21[3]. A second LTC-21 is used monitoring the resistivities of the Cernox sensors, which are measured by a four-wire technique. The Cernox sensors can be operated with 1 μA, 3 μA and 10 μA. It is recommended to use 10 μA at temperatures above 10 Kelvin. Below 10 Kelvin, currents of 1 or 3 μA are appropriate to reach the lowest temperatures of $\sim$ 2.2 Kelvin because the heat power produced by the sensor is already of the order of 0.01 Watt. To record the reference temperature and the voltages of the uncalibrated sensors, a LabView program was implemented. The accuracy of the resistivity versus temperature curves of the Cernox sensors are crucial for the thermocouple calibration procedure. Below 10 Kelvin the absolute values of the temperatures of the two sensors differ less than 1 mK. With increasing temperature the sensitivity goes down and the difference can reach 20 mK at 300 Kelvin.
Second, the thermopower calibration is conducted. Two types of thermocouples are calibrated:

- AuFe-Chromel-P (gold with 0.07 % iron) thermocouples[4] with a diameter of 76 μm per wire. A remarkable feature of this thermocouple is the high thermopower at low temperatures, which makes them suitable for low temperature measurements. The thermopower below 30 Kelvin depends strongly on magnetic field, therefore a magnetic field calibration is absolutely necessary.

- Constantan-Chromel-P thermocouples which have much higher thermopowers compared to AuFe-Chromel-P thermocouples at temperatures above 50 K. Their magnetic field dependence is almost negligible at higher temperatures ($< 10\%$ for $T > 50$ K)[2]. This type of thermocouple is therefore most suitable for high temperature measurements because no magnetic field calibration is necessary and a high signal-to-noise ratio is achieved.

The calibration of the thermocouples in zero magnetic field is straightforward. One needs the two carefully calibrated temperature sensors, a heater generating a temperature gradient, quartz glass as a thermal insulator, and a little sapphire tile as a good thermal conductor (Fig. 4.3). The two calibrated temperature sensors are carefully mounted on the sample holder. One end of the thermocouple is placed close to temperature sensor 1 and the other close to temperature sensor 2. The temperature difference between the endpoints causes a voltage drop across the thermocouple, which is measured by a Keithley 2182 nanovoltmeter[5]. I want to emphasize that the other ends of the two Chromel-P wires have to be at the same temperature T_0, which can be achieved by proper thermal anchoring.

[2]Lake Shore Cryotronics, Inc. Ohio, USA.
[3]Neocera Inc., Beltsville, USA.
[4]Leico Ind., Inc., NY, USA
[5]Keithley Instruments, Inc. Cleveland, Ohio, USA.

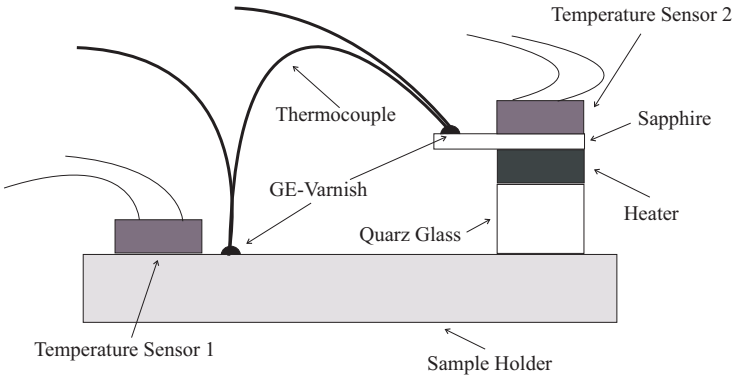

Figure 4.3: Setup for calibrating the thermocouples.

The determination of the thermopower of the thermocouples is sketched now. For small temperature differences the differential thermopower ΔS is given by

$$\Delta S = S_{Chromel} - S_{Au} = \frac{\Delta U - \Delta U_{offset}}{(T_2 - T_1) - \Delta T_{offset}} \ , \tag{4.7}$$

where $T_{1,2}$ denotes the temperatures measured by sensor 1 and 2 respectively.
Even if the heater is switched off, there is always a small offset voltage ΔU_{offset} caused by measurement supplies and soldering joints and a small offset temperature ΔT_{offset} between the Cernox temperature sensors due to, e.g., calibration errors. One minimizes these errors by conducting the following measurement sequences:

- Stabilize the base temperature via sensor 1 while the heater is switched off.
- Measure the offset voltage ΔU_{offset} and the temperature ΔT_{offset}.
- Switch on the heater, stabilize the base temperature again and measure the voltage drop ΔU and $T_2 - T_1$.
- Calculate ΔS via formula 4.7.

In order to check the validity and reproducibility of the procedure, several thermocouples of each type with different wire lengths are calibrated. The differences between the compared thermopowers are very small ($< 1\%$). Hence, the calibration procedure is reliable and of high accuracy.

To identify and qualify systematic errors in the measurement of κ, it is essential to measure standards, i.e, materials with known and established thermal conductivities. Among the materials available [74], I decided to carry out the test measurement on quartz glass (SiO_2) [6] because the thermal conductivity versus temperature curve which has been measured by various researchers [53] is "universal" and shows a striking feature, namely a temperature independent plateau around 5 Kelvin. Furthermore, the material can be tailored easily.

[6] Herasil 1, Heraeus Inc., Mainz, Germany.

As the thermal conductivity of glasses are in general very poor it is important to minimize errors due to radiation loss and to avoid the shunting of the sample by the thermocouple itself. Therefore the test measurement is conducted on a quartz glass sample in a rectangular bar shaped form with a large square cross section A of $5 \times 5\ mm^2$ and a length l of 10 mm. The quartz glass is glued onto the sample holder with GE-varnish, the thermoelement couple is fixed to the sample by Delta Bond 152, with a spacing Δx of the thermocouple ends of ≈ 2 mm.

In general, the heat does not flow entirely through the sample. There is always a minor fraction flowing through the thermocouple and through the leads of the sample heater. As the heater leads are made of very thin and long manganin or copper wires ($< 50\mu$m), heat losses through these wires are almost negligible.
However, the gold wire of the thermocouple is connected in parallel to the sample. It is therefore necessary to make sure that the sample is not thermally shunted by the gold wire[7] (see Fig. 4.1). The measurement error δ caused by the gold wire is roughly estimated by:

$$\delta = \frac{\kappa_{gold}}{\kappa_{sample}} \cdot \frac{A_{gold}}{A_{sample}} \cdot \frac{\Delta x_{sample}}{l_{gold}} \ . \tag{4.8}$$

The thermal conductivity of pure gold can reach values of the order of 1000 W/Km [77]. The value of κ of quartz glass at 10 Kelvin is of the order of 0.1 W/Km [53]. The error δ estimated from Eq. 4.8 is then approximately 10 %. It is reasonable to assume that the error is much smaller than calculated above because of two main reasons. First, the absolute value of κ for the gold-0.07%-iron wire is greatly reduced compared to pure gold due to point defect scattering caused by the iron impurities [78]. Second, Delta Bond 152 used to contact the thermocouple to the sample is a very poor thermal conductor.

At higher temperatures the effect of heat radiation losses might become important. The heat current caused by radiation reads:

$$\dot{Q}_{rad} = \epsilon \sigma_{SB} A_{sample} \left(T_s^4 - T_0^4 \right) \ . \tag{4.9}$$

where σ_{SB} is the Stefan-Boltzmann constant and ϵ ($0 < \epsilon < 1$) is the emissivity, which is close to 1 for glasses [79]. T_s and T_0 denote the sample and environment temperature, respectively. In order to estimate the heat from blackbody infrared radiation one can make the simplifying assumptions that the sample loses heat only from the side surfaces and not from the top or from the attached heater. Assuming that the average temperature of the sample sides is $T_0 + \Delta\mathrm{T}/2$ and taking only the leading term in ΔT one gets

$$\dot{Q}_{rad} \approx 2\epsilon \sigma_{SB} A_{sample} T_s^3 \Delta T \ . \tag{4.10}$$

Finally, the error due to radiation loss is approximately

$$\frac{\dot{Q}_{rad}}{j_q A} \approx \frac{8\epsilon \sigma_{SB} T_s^3}{\kappa} \frac{l^2}{\sqrt{A}} \tag{4.11}$$

where j_q is given by Eqs. 4.1 and 4.5. At 300 Kelvin the radiation error is roughly estimated to ≈ 10 % for a SiO_2 sample with the above dimensions.

[7] I neglect errors possibly caused by heat currents through the Chromel-P leads.

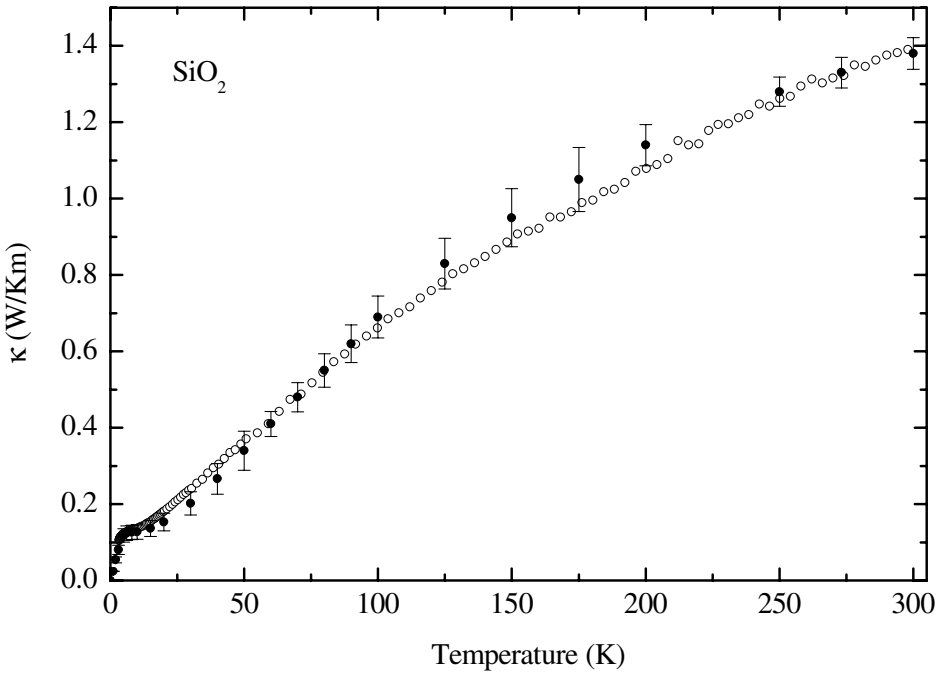

Figure 4.4: Test measurement on a SiO_2 sample (open circles) using AuFe-Chromel thermocouples. Data points with errorbars represent the recommended curve, based on a compilation of data by several researchers [53].

From Eq. 4.11 we infer that radiation loss can be minimized by measuring samples of a large cross section A and of a small length l. Subsequently, I show a comparison between the test measurements on our quartz glass sample and the recommended curve based on a compilation of thermal conductivity data of various samples.

In Fig. 4.4 the experimental results are illustrated. The data obtained agree with the recommended curve within a few percent. Around 5 K the plateau is clearly visible. Even more, at temperatures well above 100 K where errors due to blackbody infrared radiation may become important, the data is very close to the reference curve. I conclude, that the thermocouple calibration is reliable and precise. This is confirmed by the agreement between the zero magnetic field thermal conductivity measurements on quartz glass and previous results.

I will now depict the calibration of the thermocouples in external magnetic field. Quartz glass is a material with a magnetic field independent thermal conductivity. This permits the application of the steady state method to calibrate the thermocouples in magnetic fields.
One simply measures, according to Eq. 4.6, the known thermal conductivity of a quartz glass sample in various magnetic fields. The thermopower S(B,T) depends on the magnetic field causing a voltage change ΔU_{th} that is detected. Besides the thermopower S, all other quantities in Eq. 4.5 and 4.6 are field independent[8], κ included. Thus, the magnetic field dependent thermopower S(T,B) can be calculated back via Eq. 4.5 and 4.6.
I remark that the calibration of the thermocouples in magnetic fields from 1 to 17 Tesla in one Tesla steps is accomplished on the same quartz glass sample on which the zero field mea-

[8]The small field dependence of the Cernox temperature sensors can be neglected [80].

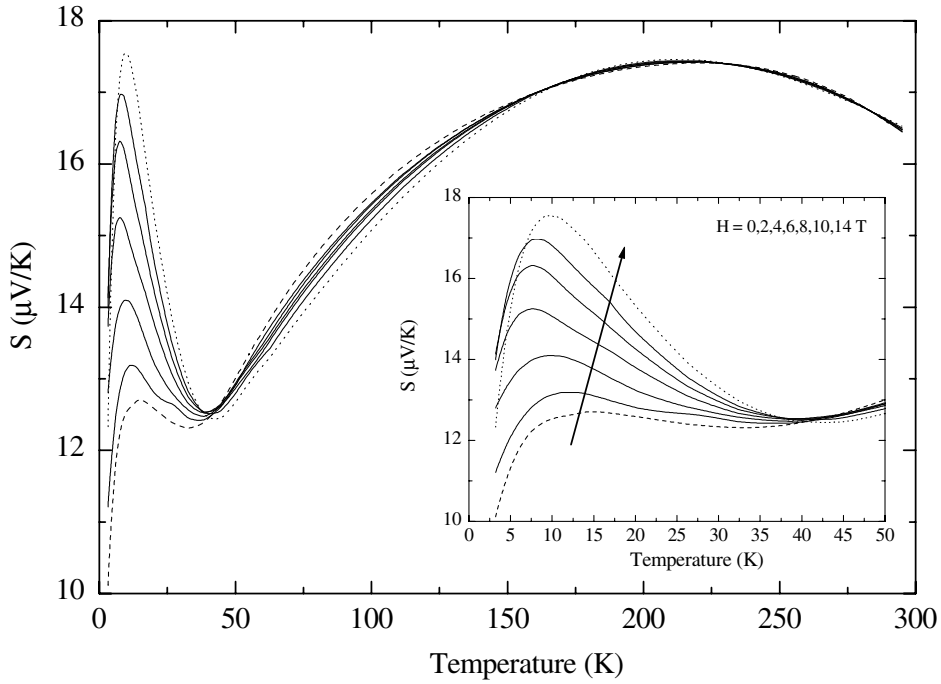

Figure 4.5: Thermopower S of a AuFe-Chromel-P thermocouple for various magnetic fields. With increasing magnetic field the thermopower is strongly enhanced at low temperatures (inset).

surements have been performed in order to avoid discrepancies due to different geometry.

In Fig. 4.5 a selection of curves are plotted demonstrating the strong dependence of the thermopower S on magnetic fields below ≈ 50 Kelvin. The field dependence is mainly attributed to the Au(0.07Fe%) wire [81]. The data qualitatively agree with earlier results found by various authors [82, 83]. However, there are huge differences at low temperatures in the sensitivity; the magnetic field dependence of S alters considerably even for thermocouple wires obtained by the same company. It is therefore advisable to check the validity of the calibration of different thermocouples from time to time.

The Constantan-Chromel-P thermocouple shows the highest sensitivity above 40 K among the standard thermocouples, typically used for low temperatures measurements [80]. As shown in Fig. 4.6, the magnetic field dependence can be neglected above 50 K. At lower temperatures the magnetic field dependence grows. However, compared to the AuFe-Chromel thermocouples the field dependence is almost negligible.
Comparing the two types of thermocouples it is better to use the AuFe-Chromel-P thermocouple at temperatures < 30 K, because the signal-to-noise ratio for Constantan-Chromel-P becomes very small. At higher temperatures one can take advantage of the larger thermopower of the Constantan-Chromel-P thermocouple.

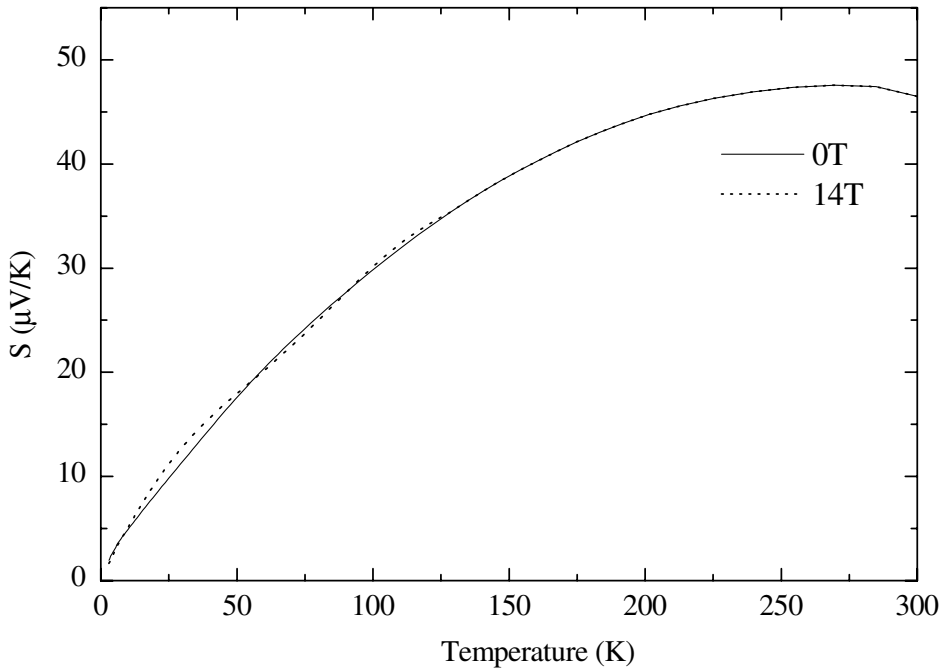

Figure 4.6: Thermopower S of Constantan-Chromel-P thermocouple for two different magnetic fields. Obviously, at higher temperatures the magnetic field dependence of the thermopower is negligible.

To perform thermal conductivity measurements of the spin-Peierls system $CuGeO_3$ in the I-phase, the thermocouples had to be calibrated at very high magnetic fields (up to 30 T) and low temperatures ($\sim$ 2 K) [9]. In Fig. 4.7 the thermopower as a function of the magnetic field is shown. The solid line denotes the result of the calibration procedure conducted for magnetic fields up to 17 T in a standard cryomagnetic system with a superconducting magnet (the "line" results from the interpolation scheme discussed below). The points are the results of the thermopower obtained in the High-Field Laboratory. The high field data confirm the previous data well. Obviously, at lower fields the data match perfectly.
The decreasing signal-to-noise ratio with increasing magnetic field is attributed to vibrations of the measurement setup caused by the water cooling of the hybrid magnet system.

To obtain the thermopower for measurements in magnetic fields different from those obtained by the calibration procedure, I implemented an interpolation routine [84]. In the following, I will mention the important points.
The calibration procedure gives the thermopower S of the thermocouples as a set of data points $S(T_i, H_j)$ forming a two dimensional mesh, whereas S is a function of temperature T and applied magnetic field H. As we do not have an analytic expression for S(T,H) that let us calculate its value at an arbitrary point, interpolation methods must be used. Two methods are applied: a simple bilinear and a so-called bicubic interpolation scheme. The first is used at the mesh boundary, because no second derivative can be obtained numerically, which means that the gradient of the interpolated function changes discontinously at the boundary of each

[9] The calibration of the thermocouples were completed at the High Field Laboratory in Nijmegen (Netherlands).

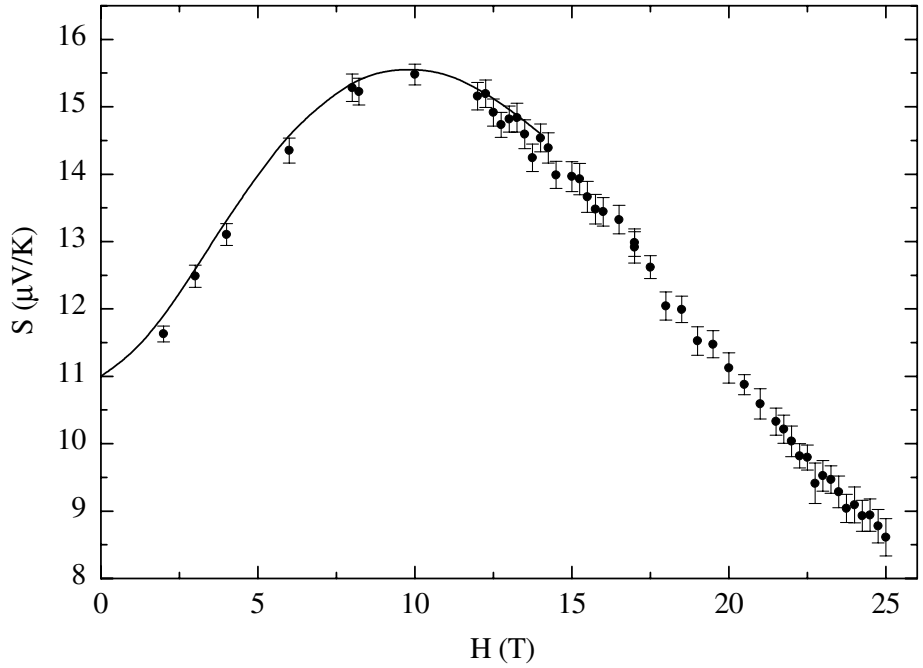

Figure 4.7: Thermopower of AuFe-Chromel thermocouple at 4 Kelvin in magnetic fields up to 25 Tesla. The solid lines denotes the calibration result obtained by conducting the measurement in a standard cryogenic system equipped with a superconducting magnet. The filled circles denote the measurement conducted in a High-Field Laboratory (see text).

grid square. For our purposes the bilinear interpolation scheme is sufficient. The second interpolation scheme increases the accuracy and smoothness inside the mesh. For further information about the algorithms used, please refer to [85].

4.1.3 Contacting the Samples

A large amount of experience in experimentation is necessary to contact the samples accurately. Different samples require different techniques in contacting the thermocouples to the sample and mounting the crystals onto the sample holder. In this section I will describe the methods used to measure the thermal conductivity of low-dimensional spin systems with high accuracy.

$CuGeO_3$

The sheet-like structure of the $CuGeO_3$ crystals makes it difficult to obtain reliable results from the thermal conductivity along all three crystallographic axes. The way chosen to perform the measurements along the b and c axis within high accuracy is to cut thin slices from a bulk sample. This is easy because $CuGeO_3$ cleaves within the b-c-plane. Attention has to be given so that the surface within the b-c-plane is flat and glossy. The sample is then glued (using GE-varnish) with the small a-c- or a-b surface, depending on the measurement direction, onto the sample holder. In order to balance different thermal expansion coefficients between the sample and the holder, one puts a small piece of paper ($\sim$ 25 μm thick), soaked with GE-varnish inbetween. Establishing an excellent thermal contact between the sample

and the sample holder is an essential factor in deriving reliable measurement results. Therefore it is advantageous to use additional copper foils as supporting planes between the sample and the sample holder. A small SMD-Chip-resistor, which serves as the heater, is glued with GE-varnish onto the top of the sample in order to generate a heat current (shown in Fig. 4.1). As the sample is an electrical insulator, no insulating layer must be deposited prior to placing the heater on top of the sample.
The SMD-resistors are available in different sizes, permitting small thermal conduction losses between the sample and the heater. The resistance ranges from $\sim$ 100 Ω to $\sim$10 kΩ. To be sure that almost all the heat, produced by the resistor, enters the sample, copper wires of diameter $\leq$ 50 μm and of length $\sim$ 5 to 10 cm are soldered to the heater. For $CuGeO_3$ accurate results can be obtained only if one glues the thermocouples onto the b-c-planes because the material cleaves easily.
For the same reason it takes a lot of effort to measure the thermal conductivity of $CuGeO_3$ along the a-axis. The heat transport in this direction is dominated by the sheet-like structure. This causes difficulties in reproducing the thermal conductivity curves. Therefore I had to conduct a vast number of thermal conductivity measurements to verify the results. This is very time consuming and thus I measured the thermal conductivity along the a-direction only on pure $CuGeO_3$.

$SrCu_2(BO_3)_2$ and $Sr_2CuO_2Cl_2$

Despite their anisotropic properties $SrCu_2(BO_3)_2$ and $Sr_2CuO_2Cl_2$ are easier to handle than $CuGeO_3$ and can be contacted and mounted in a common way. A detailed treatise of this is given by Uhlenbruck [75].

The Bechgaard Salts

Heat transport measurements on the organic compounds $(TMTCF)_2X$ are difficult to conduct. There are several reasons for this. First, these materials are very brittle and difficult to

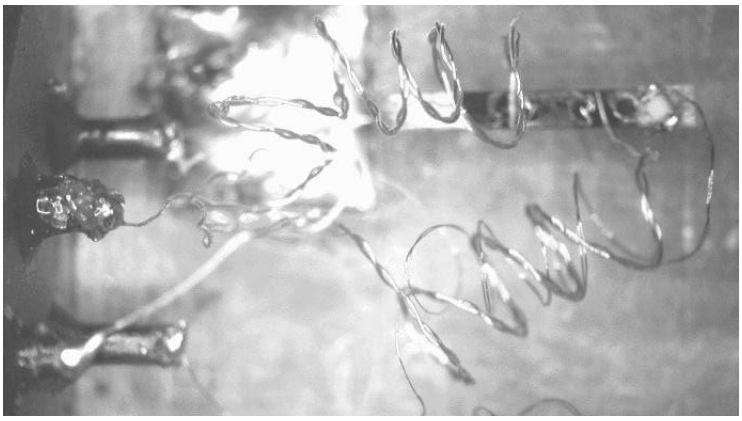

Figure 4.8: Thermal conductivity measurement setup for the organic $(TMTCF)_2X$ compounds. The organic sample (black) is flexibly mounted to the holder by a gold wire (left end of the sample). The SMD-chip resistor is seen on the right end of the sample. The spiral wires belong to the thermocouple.

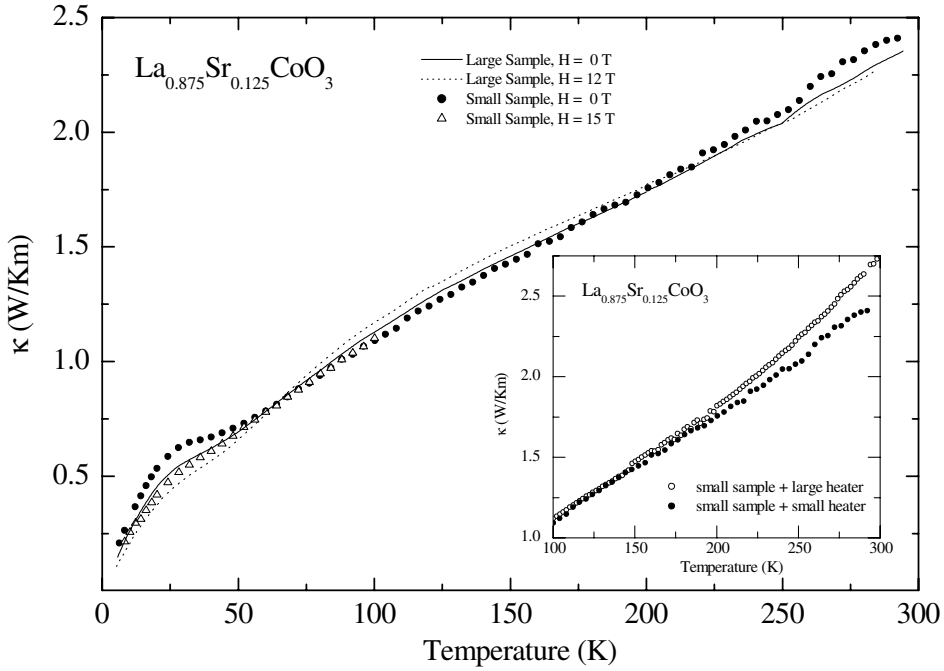

Figure 4.9: Thermal conductivity of $La_{0.875}Sr_{0.125}CoO_3$ as a function of temperature of two samples. The solid and dashed lines denote the measurements on the large $La_{0.875}Sr_{0.125}CoO_3$ sample in zero magnetic field and in 15 T. The thermal conductivity of the small $La_{0.875}Sr_{0.125}CoO_3$ sample in zero magnetic field (○) and in 12 T (△) agree with κ of the large sample perfectly. Inset: κ of the small sample with a "suitable" heater (●) and of the same sample with an oversized heater (○) . For discussion see text.

handle. Second, they are sensitive to solvents, e.g., to acetone. Hence, one has to replace the common solvents with others in order to clean the samples. Finally, while cooling down the samples mechanical stress can cause microcracks or in the worst case the crystal can break. A solution to this dilemma is flexible thermal coupling between the sample and the holder to balance the stress caused by thermal expansion.

The experimental setup is shown in Fig. 4.8. A thin gold wire or copper ribbon is soldered to a small copper foil that is glued to the sample holder. On one end the sample is fixed with standard silver paint to the gold wire. The thermocouples are attached with GE-varnish to the sample and a minute SMD-Chip resistor is glued onto the other end of the organic sample. As the thermal conductivities of the organic conductors are low [86, 87] and the cross section is very small, the surface-to-volume ratio is increased and losses due to blackbody radiation may become important (see Eq. 4.11). In addition, heat may flow through the thermocouple or heater leads. We can eliminate the second of these problems by using very long thermocouples (≈15 cm). The copper leads of the heater are ≈ 10 cm long and ≈ 30 μm thick. Radiation losses are minimized by shortening the samples according to Eq. 4.11 to an overall length of ≈ 2 mm.

A straightforward test of our setup was carried out by measuring a large "reference" sample, where errors due to radiation are negligible, with a cross section of 4 × 3 mm^2 and a length of 8 mm in the normal way and another sample of the same type with dimensions comparable

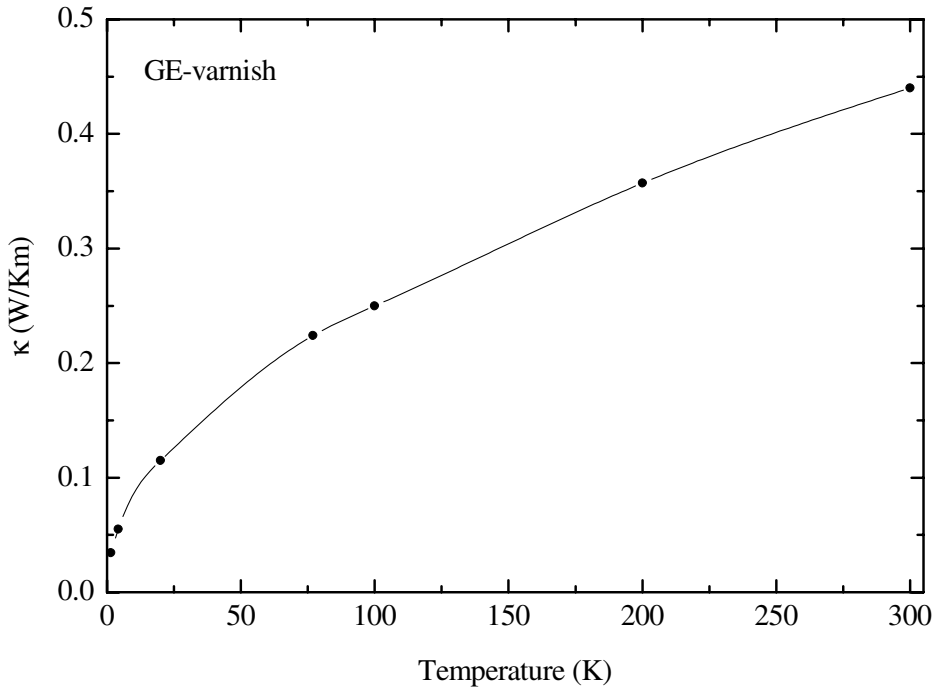

Figure 4.10: Thermal conductivity of GE-varnish. The line is a guide to the eye.

to the organic systems (cross section: 0.5×0.4 mm^2) with the modified setup.
The sample of our choice was $La_{0.875}Sr_{0.125}CoO_3$ because the absolute values of κ are known and the thermal conductivities of the $(TMTCF)_2X$ salts and $La_{0.875}Sr_{0.125}CoO_3$ are comparable to each other over the entire temperature range. Furthermore, $La_{0.875}Sr_{0.125}CoO_3$ has a black surface and therefore a similar emissivity ϵ (see Eq. 4.11) can be expected. From an experimental point of view, the advantage is that the material can be cut easily in a rectangular form. The test measurements confirm the validity of the setup (Fig. 4.9). Small differences between the thermal conductivity results may be due to black body infrared radiation at high temperatures. The discrepancies at low temperatures can be attributed to differences in the point defect scattering rates of the samples [78]. A note of caution: Measuring small samples with small absolute values of κ may render the wrong results at high temperatures if an oversized heater is attached to the sample, as illustrated in Fig. 4.9 (inset). The error at high temperatures is most likely due to radiation loss. Thus, it is necessary to use suitable heaters with cross sections equal to the cross section of the sample.

Finally, a general remark has to be made about the thermal conductivity of GE-varnish. The heat conduction is actually, even at room temperature, very poor and drops with decreasing temperature (Fig. 4.10). One should therefore minimize as much as possible the spacing between sample, heater and heat sink.

4.2 Electrical Resistivity

The electrical resistivity measurements are carried out on the organic systems $(TMTCF)_2X$ along the crystallographic a axis using the standard four-wire technique. While cooling down the sample from room temperature, one measures the voltages and currents quasi-continuously. Offset voltages (currents) in the dc-measurement are compensated by changing the polarity.
The major problems arising in conjunction with these organic compounds are manifold. First, the electrical resistivity varies over seven orders of magnitude for $(TMTTF)_2PF_6$ between 4 and 300 Kelvin, which becomes insulating at low temperatures. One has to take care that the input impedance of the voltmeter does not become comparable to that of the sample to be measured. Therefore, a Keithley 2400 sourcemeter (input impedance $> 10^{10}$ Ohm) with sourced voltage and limited current is used in order to get the resistivity versus temperature curve in one turn without changing the measurement setup. To avoid heating effects at low temperatures, the compliance limit is set to 100 μA and the voltage is fixed at 10 Volts.

The resitivities of the organic conductors $(TMTSF)_2PF_6$ and $(TMTSF)_2ClO_4$ are determined by a conventional lock-in technique using an Ithaco 3961B two-phase lock-in amplifier, where the output frequency is set to 87 Hz. A current of some microamperes is passed through the sample so that the corresponding voltage can be easily detected by the lock-in amplifier. In case of $(TMTSF)_2ClO_4$ the voltage across the sample becomes so small at low temperatures that a Stanford preamplifier SR560 has to be used, maintaining the same current. A detailed description of the measurement setup is given in [70].
Second, the samples are very fragile so that microcracks cause kinks in the resistivity versus temperature curves if the samples are cooled down too fast. It is remarkable that these cracks have a much stronger impact on the electrical resistivity than on thermal conductivity measurements. It has turned out that cooling rates below 0.2 K/min between temperatures of 300 and 100 Kelvin and rates of 0.5 K/min between 100 and 4.2 Kelvin are necessary to prevent damage of the sample and to allow decent measurement times. Because cracks appear often at high temperatures, it is advisable to operate in this temperature region at even lower cooling rates.
Last but not least contacting these fragile samples turns out to be difficult in the sense that elastic tension from the measurement leads may damage the crystals. These tensions can be avoided by pasting thin gold wires with diameters of $\approx 30\mu$m, instead of copper leads of the same diameter, to the sample. Before the four gold wires are glued with silver paint onto the sample, four gold pads are evaporated onto the sample to minimize contact resistances. Experience shows that the thickness of the gold pads should be between 50 and 100 nm, sufficient for low contact resistances and for circumventing the loosening of the gold pads from the sample during the cooling process.
Let us continue with the discussion of the accuracy of the measurement. In order to get the absolute value of the resistivity, the geometrical factor l/A, where l denotes the distance between the voltage leads and A denotes the cross section, must be determined.

There are two main reasons why fairly large errors from the geometrical factor l/A arise:

- The crystals are long thin needles which cannot be tailored and are often odd-shaped. This makes the determination of A very difficult.
- It is a problem to deposit the silver paste exactly onto the gold pads so that the distance between two blots of silver paint turns out ill-defined.

In addition, more and more cracks are created when cycling the temperature, which prevents the reproducibility of the resistivity curves. Surprisingly, the thermal conductivity is not very sensitive to such microcracks and therefore well reproducible. Due to these reasons comparing different samples in view of the crystal quality on the basis of electrical resistivity measurements is more or less impossible. As a rule of thumb one can say that the absolute values of ρ can be estimated only within a factor of two or three.

Chapter 5

$SrCu_2(BO_3)_2$

$SrCu_2(BO_3)_2$ can be viewed as the experimental realisation of the well-known Shastry- Sutherland model, studied by theoreticians already in the early eighties [88]. A unique spin arrangement is present in this compound that has led to a pronounced interest in studying this low-dimensional quantum spin system, where the ground state is non-magnetic and a finite energy gap in the magnetic energy spectrum exists.
Among the many compounds realizing low-dimensional spin systems, $SrCu_2(BO_3)_2$ facilitates a detailed theoretical understanding of low-dimensional magnetic systems due to its simple structure and the lack of additional complicated structural phase transitions. Even more, the ground state can be solved exactly, allowing a detailed investigation of the magnetic properties.

In this chapter I will first discuss the structural and magnetic features of $SrCu_2(BO_3)_2$. We will see that the gap does depend on the topology of the spin arrangement and the relevant exchange constants. Our experimental results for the thermal conductivity will be shown as a function of temperature and of a magnetic field along two crystallographic directions. Then, I will focus on some theories dealing with resonant scattering of phonons by magnetic excitations. It is shown that spin-phonon coupling in conjunction with spin conservation has to be taken into account to describe our experimental results. I will show that because of the uncomplex circumstances in $SrCu_2(BO_3)_2$, mentioned above, the thermal conductivity, which as a transport quantity is a challenge for theoreticians, can be well modeled and understood.

5.1 Structure and Magnetism

The crystal structure of $SrCu_2(BO_3)_2$ is depicted in Fig. 5.1. At room temperature the compound has a tetragonal unit cell[1] with the cell constants of $a = 8.995\mathring{A}$ and $c = 6.649\mathring{A}$. It consists of $CuBO_3$ layers in the a-b plane made up of $(BO_3)^{3-}$ groups and Cu^{2+} ions, separated by nonmagnetic Sr^{2+} ions. A closer inspection of the lattice reveals that the $CuBO_3$ layers do not form planes but show a distinct buckling, meaning the distance between Cu^{2+} ions sitting on two adjacent planes is $3.5930\mathring{A}$ or $4.2325\mathring{A}$, respectively.
The projection along the c axis reveals the interesting magnetic structure formed by the Cu^{2+} spins, carrying spin s=1/2 (Fig. 5.2 a). The nearest copper moments couple via superexchange over two symmetrically equivalent oxygens, belonging to adjacent (BO_3) groups.

[1] The system undergoes a 2^{nd} order structural phase transition at 395 Kelvin, discussed in detail in Ref. [89].

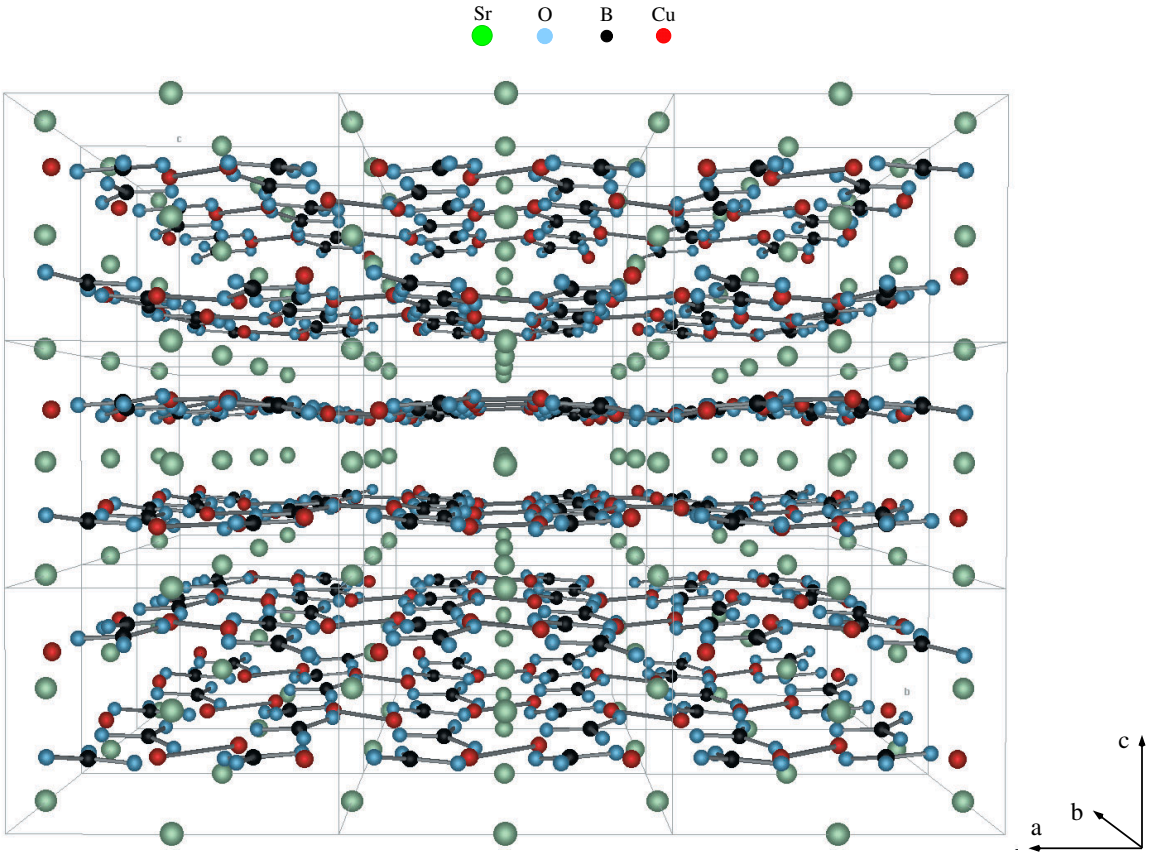

Figure 5.1: The low temperature crystal structure of $SrCu_2(BO_3)_2$.

Considering the dimer bridging angle (Cu-O-Cu) of 102.42°, one expects an antiferromagnetic intradimer exchange according the Goodenough-Kanamori rules. An additional pathway for next-nearest-neighbor interactions is provided by the $(BO_3)^{3-}$ groups. Assuming antiferromagnetic interdimer coupling, one gets a strongly frustrated magnetic system where each spin is coupled to pairs of spins on dimers.
If one neglects to a first approximation the interlayer exchange constant $J_\perp/J_1$ ranging from 0.094 to 0.21, $SrCu_2(BO_3)_2$ can be considered as the experimental realisation of a two-dimensional spin system with orthogonally connected dimers. The model system has already been studied by Shastry and Sutherland [88]. In Fig. 5.2 b), c) the mapping from the real lattice to the corresponding model lattice is shown. The solid lines indicate intradimer coupling (J_1) and the dashed lines symbolize the interdimer interaction (J_2). In order to understand the basic features of the system, let us first focus on the original Hamiltonian describing well the thermodynamic properties. The Hamiltonian reads:

$$\mathcal{H} = J_1 \sum_{\langle i,j \rangle} \hat{s}_i \cdot \hat{s}_j + J_2 \sum_{\langle\langle i,k \rangle\rangle} \hat{s}_i \cdot \hat{s}_k \ , \tag{5.1}$$

where $\langle i,j \rangle$ denotes the summation over nearest- and $\langle\langle i,k \rangle\rangle$ over next-nearest-neighbors [90]. If we take a look at Fig. 5.2 d) it is clear that for the vanishing J_2 the model is equivalent to a dimer system, while for $J_1 = 0$ we recognize the square lattice Heisenberg model (see Fig. 5.2 b),c)).

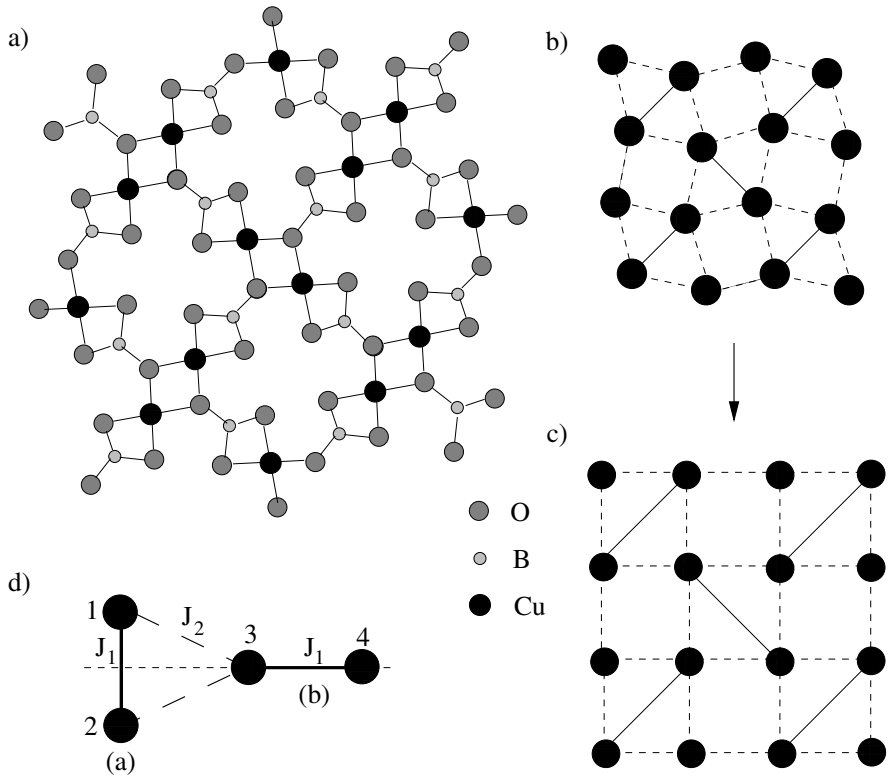

Figure 5.2: Part of copper-borat plane a), corresponding Shastry-Sutherland model b) and c) and elementary unit d).

Let us consider the product of the singlets on dimers by

$$|\Psi\rangle = \prod_a |s\rangle_a \text{ with } |s\rangle = \frac{1}{\sqrt{2}}(|\uparrow\downarrow\rangle - |\downarrow\uparrow\rangle) \,, \tag{5.2}$$

where the second term denotes the dimer singlet basis [91]. By elementary calculation one sees that $|\Psi\rangle$ is an exact eigenstate of the Hamiltonian 5.1, and in addition the groundstate if $J_2 = 0$. It remains the groundstate for $J_2 > 0$ if the ratio J_2/J_1 is smaller than 0.603(3) [92].

The unique spin arrangement imposes a stringent constraint on the motion of the elementary triplet excitations. Coupling between states on adjacent dimers is restricted by the symmetry of the elementary unit, depicted in Fig. 5.2 d). As the above considerations are important interpretating the thermal conductivity results, a theoretical explanation will be sketched out here. Using the standard basis for triplets

$$\begin{aligned} |t_1\rangle &= |\uparrow\uparrow\rangle \\ |t_0\rangle &= \frac{1}{\sqrt{2}}(|\uparrow\downarrow\rangle + |\downarrow\uparrow\rangle) \\ |t_{-1}\rangle &= |\downarrow\downarrow\rangle \end{aligned} \tag{5.3}$$

and starting from a singlet on dimer (a) and a singlet on dimer (b) it is easy to show that

$$\mathcal{H}^{\star}_{ab}|s\rangle_a|s\rangle_b = 0 \text{ with } \mathcal{H}^{\star} = J_2(\vec{S}_1 + \vec{S}_2)\vec{S}_3. \tag{5.4}$$

Eq. 5.4 simply implies that the wave function (Eq. 5.2) is an exact eigenstate of the Hamiltonian. Next, one can consider the situation, where only one triplet is excited on the elementary unit. Starting from a singlet on (a) and a triplet on (b), and vice versa one obtains:

$$\mathcal{H}^{\star}_{ab}|s\rangle_a|t_m\rangle_b = 0 \text{ with } m = 0, \pm 1 \tag{5.5}$$

$$\mathcal{H}^{\star}_{ab}|t_{\pm 1}\rangle_a|s\rangle_b = \pm\frac{J_2}{2}|t_{\pm 1}\rangle_a|t_0\rangle_b \mp \frac{J_2}{2}|t_0\rangle_a|t_{\pm 1}\rangle_b \tag{5.6}$$

$$\mathcal{H}^{\star}_{ab}|t_0\rangle_a|s\rangle_b = \frac{J_2}{2}|t_1\rangle_a|t_{-1}\rangle_b - \frac{J_2}{2}|t_{-1}\rangle_a|t_1\rangle_b \ . \tag{5.7}$$

Eqs. 5.5 - 5.7 state that one can only create a triplet on a horizontal dimer if another triplet already exists on the adjacent vertical dimer. All other nine virtual processes having a triplet on (a) and a triplet on (b) can be calculated in the same manner. Note that the operator $\mathcal{H}^{\star}$ does not conserve the number of triplets.

It has been shown that due to these restrictive processes hopping becomes possible only through a closed path leading to a strong localisation of the one triplet excitations and therefore leading to a flat dispersion of the one triplet branch [91, 92]. Without going into too much detail, this can be seen in Fig. 5.3. Let us take a look at a four dimer cluster, where one triplet (t_1) is already excited, i.e. one starts from the configuration $|t_1sss\rangle$. Applying $\mathcal{H}^{\star}$ gives

$$\mathcal{H}^{\star}|t_1sss\rangle = \frac{J_2}{2}|t_1t_0ss\rangle - \frac{J_2}{2}|t_0t_1ss\rangle \ , \tag{5.8}$$

which corresponds to (1) in Fig. 5.3. Now, in order to follow one possible hopping process, one retains only the second term in Eq. 5.8 and apply again $\mathcal{H}^{\star}$ and so forth [91]. We end up with one possible hopping process which is of the sixth order (6). A detailed theoretical examination of the two triplet branch shows that the two magnon dispersion is much stronger [92]. This can be explained by a higher probability of correlated hopping processes, where one triplet assists the hopping of the other one [91, 92]. The experimental findings agree with these theoretical predictions rather well, and I will come back to this point when discussing the thermal conductivity results.

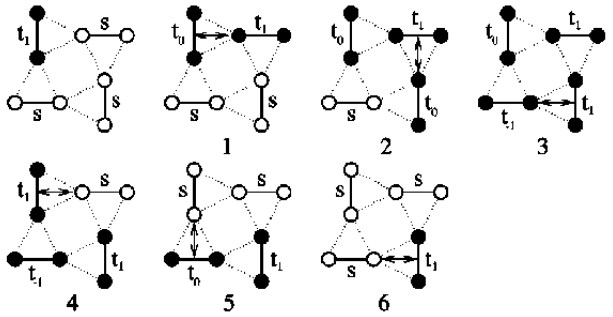

Figure 5.3: Example of the lowest order hopping process of a triplet in $SrCu_2(BO_3)_2$. Open circles denote singlet states, filled circles are the triplet states. According to S. Miyahara [91].

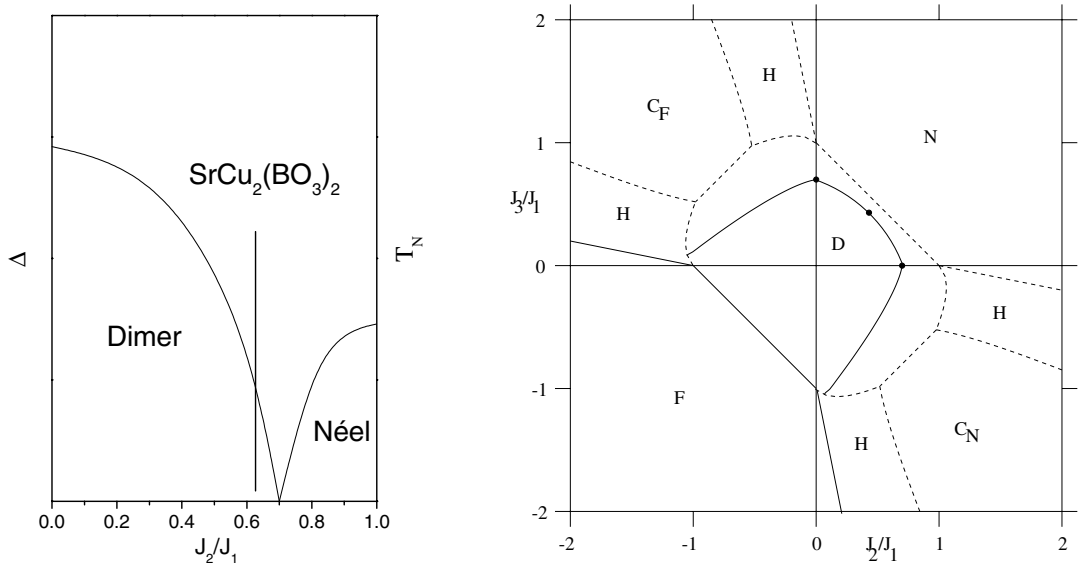

Figure 5.4: Left: Schematic phase diagram of the Shastry-Sutherland model, Δ and T_N denote the gap and the Néel temperature, respectively [90]. Right: Extended phase diagram of the Shastry-Sutherland model. (F) stands for ferromagnetic, (N) for Néel, C_F and C_N for columnar and (H) for helical, respectively. The dashed lines indicate the classical phase boundaries with an oval-like dimer phase in the middle [93].

The spin gap calculated up to the fourth order by perturbation theory is given by

$$\frac{\Delta}{J_1} = 1 - (\frac{J_2}{J_1})^2 - \frac{1}{2}(\frac{J_2}{J_1})^3 - \frac{1}{8}(\frac{J_2}{J_1})^4 \ . \tag{5.9}$$

From Eq. 5.9 it is obvious that for $J_2 = 0$ the spin gap Δ equals J_1, which is just the energy needed to break up a singlet dimer bond. Note that no first order correction appears in Eq. 5.9.

The schematic phase diagram for the original Shastry-Sutherland model and the calculated phase diagram for the extended Shastry-Sutherland model is illustrated in the left and right panel of Fig. 5.4, respectively. With an increasing J_2/J_1 ratio, the spin gap becomes smaller and at $J_2/J_1 = 0.603(3)$ a quantum phase transition occurs resulting in a gapless Néel ordered state [92]. According to Knetter et al., the parameters are known within high accuracy with $J_1 = 6.16(10)$ meV (71.4(68) Kelvin), $J_2 = 3.71(50)$ meV (43.0(95) Kelvin) and $J_\perp = 1.3(2)$ meV (15.3(1) Kelvin) [92]. The closeness of the ratio J_2/J_1 to 0.69 should allow to drive the system from one phase to the other, e.g., by applying external or chemical pressure to the system. To my knowledge this has not been achieved so far.

A refinement of the original model is achieved if one takes the second next nearest-neighbor coupling (denoted by J_3 in the right panel of Fig. 5.4) into account, leading to the so-called modified or generalized Shastry-Sutherland model, where the dimer state (Eq. 5.2) is still an exact eigenstate [93]. I want to make some remarks on the phase diagram concerning the phases and the phase boundaries. As the ferromagnetic and the dimer states are exact ground states no quantum fluctuations are present here and the phase boundary between them is exact as well. So are the ferromagnetic to helical boundaries, shown by the solid lines. The dimer to Néel transition at $J_2 = J_3$ is of first order type, whereas a controversial discussion

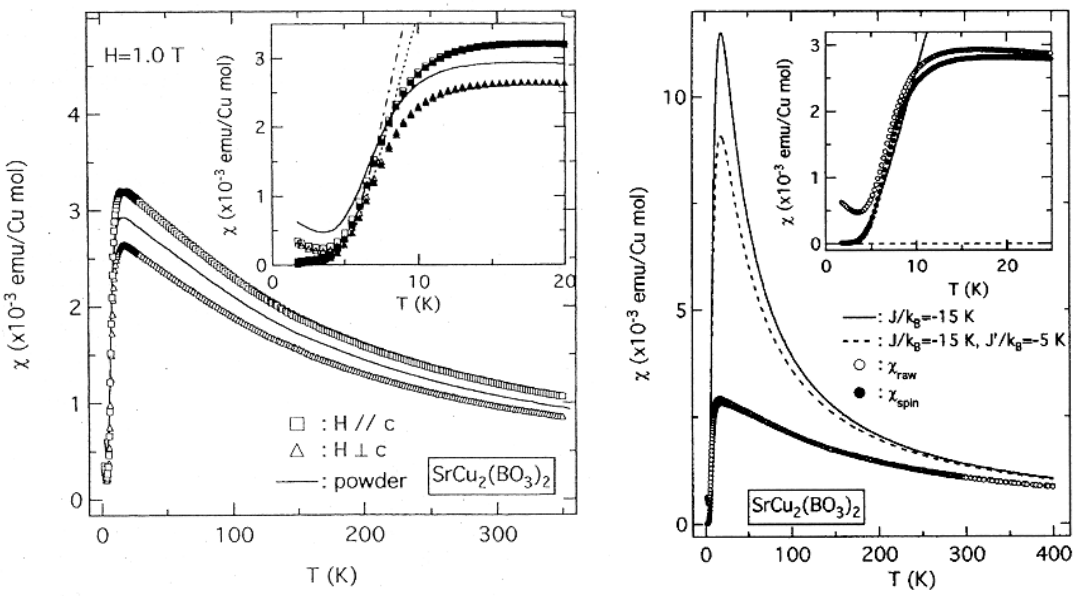

Figure 5.5: Magnetic susceptibility χ of $SrCu_2(BO_3)_2$. Left: Temperature dependence of χ of a powder sample (solid line) and a single crystal along (square) and perpendicular (triangle) to the c axis. The magnetic field strength is denoted by H. Right: Lines show the theoretical curves based on a dimer model with (dotted) and without (solid) second next-nearest-neighbour interaction (according to Kageyama [95, 96]).

exists about the order of the transition for $J_3 = 0$ [93]. At the moment it is believed that the transition at that point is of first order, because there is an abrupt change in energy going from the Néel phase to the dimer state [94].
Finally, I want to mention the other magnetically ordered phases. The three phases to be discussed briefly are the two columnar C_N and C_F and the helical (H) phases. In the C_N phase the spins are antiferromagnetically ordered along one axis and have a period of four in the perpendicular direction. In the C_F phase, the spins show ferromagnetic order along one of the axes and have period of four along the other direction. A typical helical configuration (H) is given by successively rotating the spins by an angle Θ along one of the axis, while perpendicular to this axis the spins alternate between this angle nonuniquily.

There is support in experiments that $SrCu_2(BO_3)_2$ achieves the exact dimer ground state. In Fig. 5.5 magnetic susceptibility (χ) measurements are illustrated. Decreasing the temperature the susceptibility drops below 15 Kelvin to zero and the system reaches the singlet ground state, as shown in the insets of Fig. 5.5. The temperature dependences of χ are essentially the same, while the anisotropy of χ for the different magnetic field orientations is just a consequence of the slightly different g-factors. Kageyama et al. find, choosing a simple isolated dimer model for fitting χ below 6 Kelvin, for the singlet triplet gap $\Delta \simeq 34$ Kelvin that is in agreement with nuclear magnetic resonance (NMR) [95], Raman scattering [97], electron spin resonance (ESR) [98], and inelastic neutron scattering measurements [99]. Qualitatively, the theoretical and experimental curves coincide, but nevertheless the attempt to describe the experimental curve quantitatively by a simple dimer model for χ obviously fails. This is actually expected because spin frustration, which is not considered in the dimer model, is

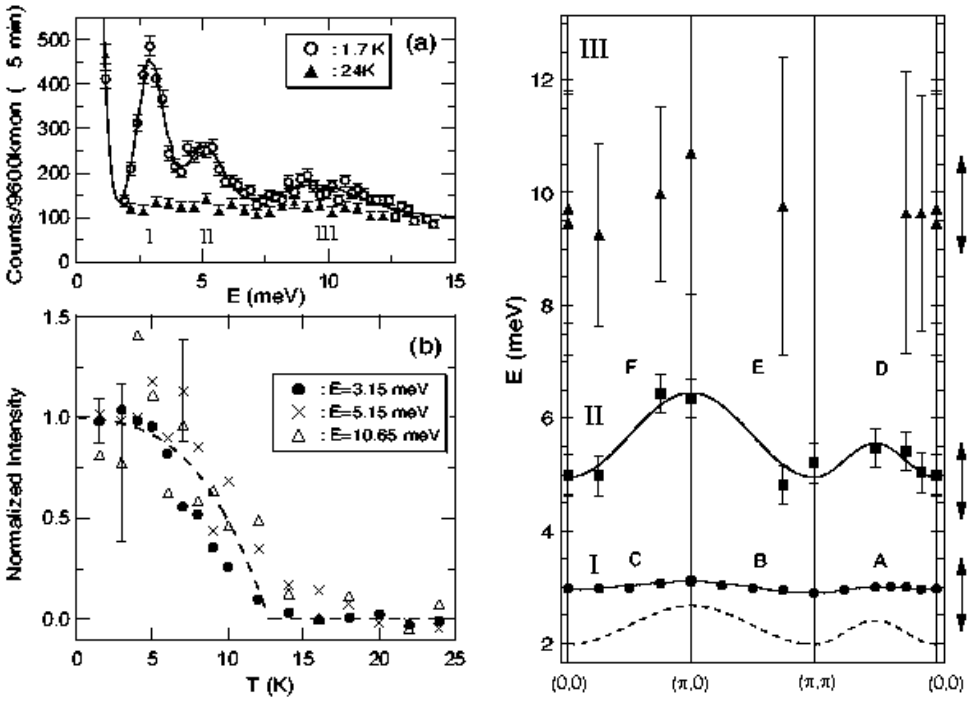

Figure 5.6: Left: Energy scans obtained at 1.7 Kelvin with peaks centered at 3.15 meV (I), 5.15 meV (II) and 10.65 meV (III) and 24 Kelvin curve showing essentially no peaks supporting the magnetic origin of the transitions. The peaks are centered at 3.15 meV, 5.15 meV and 10.65 meV. Right: Dispersion relations of the excitation energies of band I, II and III (According to Kageyama [99]).

essential in $SrCu_2(BO_3)_2$ [92, 95, 96]. Only at temperatures well below the gap data and fit agree satisfactorily (Fig. 5.5). Even a mean field approximation only slightly improves the fit [100]. I will come back to this point when discussing the thermal conductivity results in the forthcoming chapter.

The experimental proof of the flat dispersion of the single triplet excitations is given by inelastic neutron scattering, shown in Fig. 5.6, left panel, curve (I). At first sight, the bandwith of ~ 0.2 meV seems to be extremely small compared to other strongly interacting quantum spin systems. In the one-dimensional spin-Peierls system $CuGeO_3$ for example, one observes a width of ~ 14 meV for the single triplet branch along the spin chains [101]. In the two-dimensional plaquette system CaV_4O_9, the width parallel to the plane is yet ~ 7 meV [102]. Refering to systems where magnetic correlations are mainly suppressed by spatial separation of the spins, one would expect flat dispersions, experimentally observed in the isolated dimer systems $Cs_3Cr_2Br_9$ (width 1.8 meV) and $BaCuSiO_6$ (width 0.7 meV) [103, 104]. In $SrCu_2(BO_3)_2$ however, one has a highly correlated system where not the spatial spin separation, but the orthogonality of the dimers is the keyfactor to the flat single triplet dispersion (curve I). The second prominent feature in Fig. 5.6 is the occurrence of two-triplet excitations above ~ 5 meV (curve II), which is less than twice the energy of single-triplet excitations (I). It is essentially the formation of bound states resulting in this reduction of the two-triplet excitation energy.

5.2 Experimental Results of the Thermal Conductivity

For our study two samples of rectangular form of $\sim 0.6 \times 1.9 \times 3$ mm^3 with the long direction along the a and c axis, respectively, were cut from larger single crystals of $SrCu_2(BO_3)_2$ grown by the traveling solvent floating zone method [105]. The thermal conductivity was measured by the conventional steady state method described in Chapter 4.

In Fig. 5.7 (left) the thermal conductivity $\kappa_a(T)$ ($= \kappa_b$ in tetragonal $SrCu_2(BO_3)_2$) and $\kappa_c(T)$ in zero magnetic field is shown. For both, parallel and perpendicular to the magnetic planes, pronounced double-peak structures are observed with the low T maxima occurring at ≈ 4.5 K. For κ_a the high T maximum lies at ≈ 60 K and for κ_c at ≈ 30K.
The right upper panel of Fig. 5.7 illustrates the high temperature region of the thermal conductivity as a function of 1/T. In the lower panel the enlarged low temperature region is plotted.
The magnetic field dependence of the thermal conductivity is shown in Fig. 5.8. The low T maximum is suppressed strongly by a magnetic field for both κ_a and κ_c. The magnetic field dependence at higher temperatures is only weak ($\leq 2\%$) and close to the relative measurement accuracy.

The occurrence of such a pronounced double peak structure of the thermal conductivity is very unusual. I want to remind the reader that for a conventional insulator[2] only *one* low temperature maximum caused by phonons is expected. Moreover, no magnetic field dependence of a heat current generated by phonons only, should be present (see also chapter 3). However, as $SrCu_2(BO_3)_2$ is a low-dimensional quantum spin system, one can ask for the role of magnetic excitations for the heat transport.

The behavior of κ observed here is reminiscent of that found in other low-dimensional spin systems [1, 63, 65]. In particular, in $CuGeO_3$ κ also shows an almost field-independent maximum at ~ 20 K and a second one around 5 K, that is strongly suppressed by a magnetic field. This has been interpreted in terms of a magnetic and a phononic contribution to the heat current with maxima at different temperatures [63]. However, the interpretation of the thermal conductivity data in the case of $CuGeO_3$ remains controversial because an unambiguous separation of different contributions to the thermal conductivity is, from the experimental point of view, difficult. A closer inspection of the heat transport reveals a complicated behavior with respect to temperature, magnetic field and doping (see chapter 6).

For several reasons, a clear interpretation of the behavior of the thermal conductivity in $SrCu_2(BO_3)_2$ can be given here. First, due to their flat dispersion, the single-triplet excitations are not expected to contribute significantly to the heat current. This has already been discussed in section 5.1. Therefore no magnetic contribution from single-triplet excitations to the heat transport can be expected for both the heat current parallel and perpendicular to the planes. Second, a magnetic contribution (κ_m) in a 2-d magnetic system should be strongly anisotropic, as is observed, e.g., in $Sr_{14-x}Ca_xCu_{24}O_{41}$ [65], but not according to our measurements. The lack of a strong anisotropy also excludes an explanation in terms of multi-triplet

[2] $SrCu_2(BO_3)_2$ is a highly insulating compound. To my knowledge, no doping has been successful so far to make the system electrically conducting.

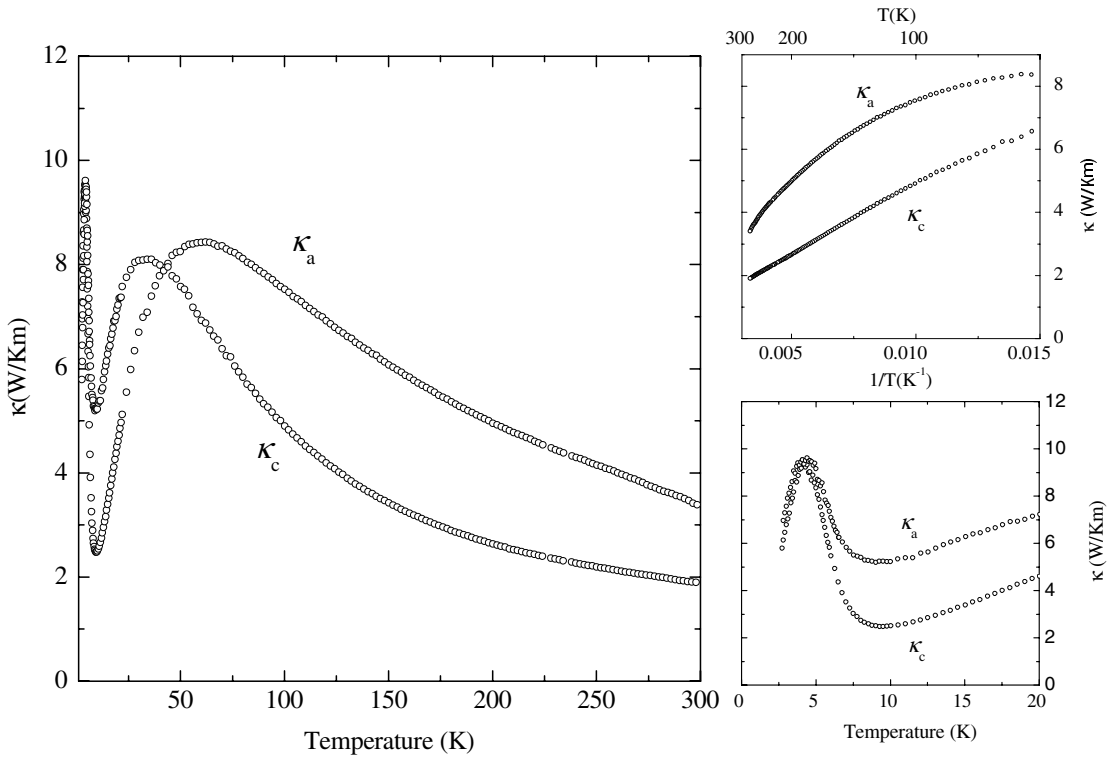

Figure 5.7: Left: Thermal conductivity of $SrCu_2(BO_3)_2$ along (κ_a) and perpendicular (κ_c) to the magnetic planes. Right: In the upper panel the high temperature region of the thermal conductivity is plotted as function of 1/T. In the lower panel the enlarged low temperature region is shown.

excitations (depicted in Fig 5.6 left panel by curves II and III). These excitations move much more easily than the single-triplet excitations, but again only within the magnetic planes [92].

Finally, the relation $\kappa \propto cvl$ (c is the specific heat, v the group velocity and l the mean free path) predicts similar temperature dependencies of κ_m and the magnetic specific heat c_m. But measurements of c in fields up to 12 T show that c_m gives rise to a *maximum* of c/T at temperatures close to the *minima* of κ_a and κ_c for the respective magnetic fields (see Fig. 5.8) [106].

From these arguments, one can exclude a sizeable magnetic contribution to the heat current in $SrCu_2(BO_3)_2$, so that $\kappa \approx \kappa_{ph}$ [3].
How can we explain the double peak structure and its magnetic field dependence? As the cause of the double peak structure and its magnetic field dependence we propose that an additional scattering channel for phonons opens due to magnetic excitations.

[3] A small magnetic contribution to κ_a can of course not be excluded. Such a contribution might explain in part the different temperature dependences of κ_a and κ_c, but it is unimportant in the context of the double peak structure.

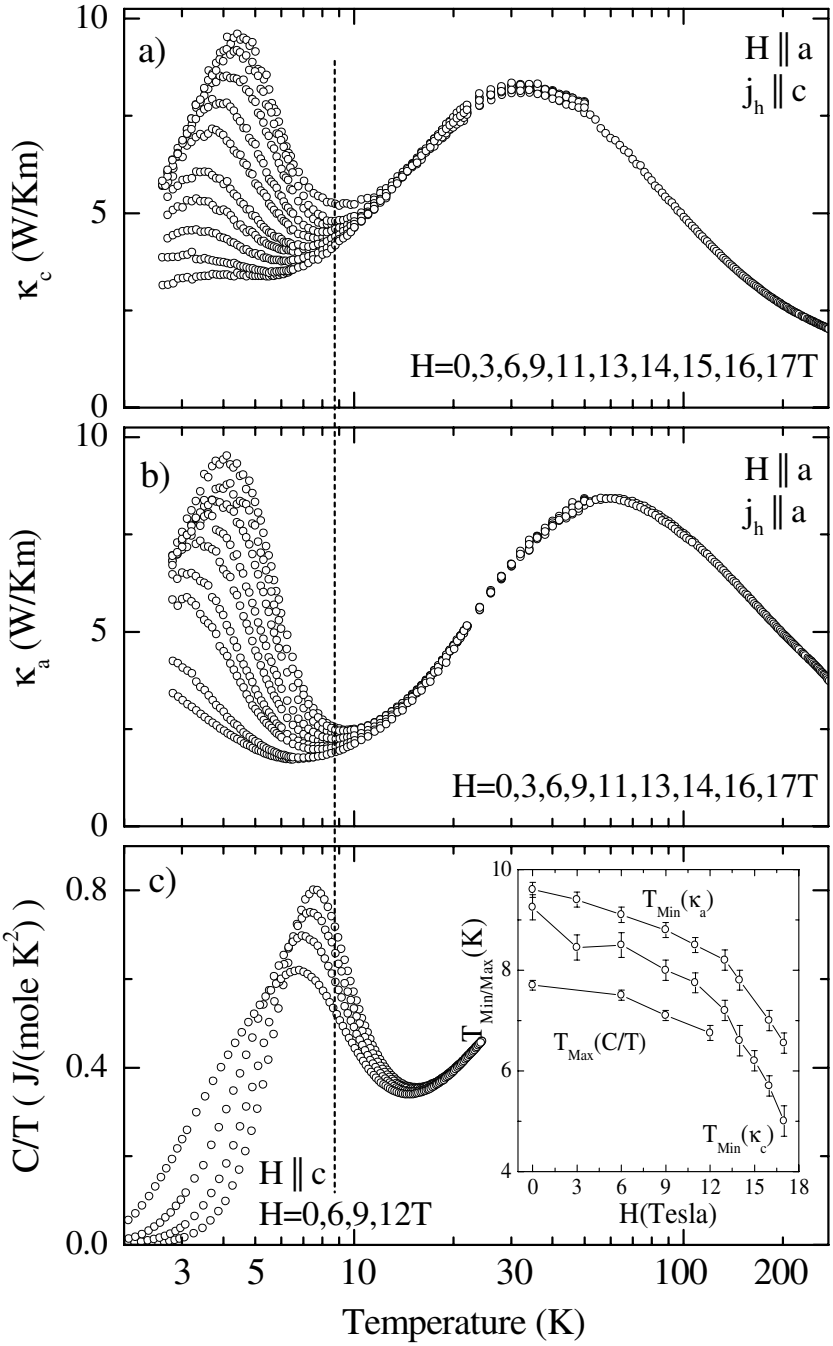

Figure 5.8: Thermal conductivity κ_c (a) and κ_a (b) on a logarithmic temperature scale for various magnetic fields. Increasing the magnetic field, the low-T maximum is suppressed. (c) Specific heat at various fields $H||c$ (the peak height decreases with increasing field). Data points are from [106]. The inset shows the variation of the minima of κ_a and κ_c and the maxima of c with magnetic field.

The absence of a strong anisotropy of κ_a and κ_c is then easily understood, since both the anisotropy of the spin-phonon coupling and/or of the phonon system itself are expected to be much weaker than that of the 2-d magnetic system. In addition, this scenario yields a straightforward explanation for why the minima of κ_a and κ_c occur close to the maxima of c/T. The latter is the temperature derivative of the magnetic entropy and thus directly related to the number of magnetic excitations that serve as scatterers for the phonons. One has to admit that the minima of κ_a and κ_c do not exactly occur at the maxima of c/T shown in the inset of Fig. 5.8. However, the relative change with increasing field is almost the same. The fact that even the minima for κ_a and κ_c do not appear exactly at the same temperature can be understood in terms of the anisotropy of the genuine phononic heat current or presumably to small additional magnetic contributions in κ_a. Furthermore, the mean free path of the phonons can strongly depend on temperature, thus having a crucial impact on the temperature dependence of κ which could explain the small shift between the minima in thermal conductivities and the maximum in the specific heat.
I want to come back to the high temperature behavior of the thermal conductivity. As I assume a pure phononic contribution to the heat transport in both directions, I expect in the high temperature limit ($T >> \Theta_D$) a T^{-1} dependence of κ. The findings are shown in the inset of Fig. 5.7 with $\kappa_c \propto T^{-1}$ as expected for phonon heat transport restricted by phonon-phonon Umklapp scattering [107], whereas κ_a follows a $T^{-0.6}$ dependence. I want to stress that the finding of a 1/T dependence of the phonon heat transport caused by phonon-phonon scattering processes is not at all a matter of course. First, due to the derivation of the formula [107] one should observe such a temperature dependence above the Debye temperature that is of the order of 450 K in $SrCu_2(BO_3)_2$. Second, it has been argued that the change in the volume of the sample, due to the temperature variation or the participation of more complicated scattering processes, e.g., four-phonon processes, can produce severe deviations from the 1/T dependence of the thermal conductivity. All the scenarios discussed above predict a temperature dependence of the phonon heat current of T^m with $-2 \leq m \leq -1$. In this context one can speculate that the $T^{-0.6}$ dependence of κ_a, i.e., the heat current parallel to the magnetic planes is presumably not only due to phononic, but also due to a small magnetic contribution.

In this section a qualitative interpretation of our data has been given. In the following sections I want to work out a model to describe our experimental findings quantitatively. It is later revealed that spin-phonon coupling and spin conservation have to be considered and are essential ingredients towards understanding our experimental results.

5.3 Scattering Mechanisms and Modeling of the Data

This section is primarily devoted to various scattering scenarios besides the well-known point-defect, boundary and phonon-phonon Umklapp scattering mechanisms, already discussed in chapter 3. In order to explain our thermal conductivity results quanitatively one needs an additional scattering channel for phonons. I will account here for the most important ideas to describe our data. A detailed discussion will reveal, that a model based on resonant scattering of phonons by magnetic excitations describes the double peak structure and the observed magnetic field dependence of the thermal conductivity of $SrCu_2(BO_3)_2$.

5.3.1 Scattering on Elastic Deformations

Scattering on Lattice Distortions

It is straigthforward to consider scattering of phonons on elastic deformations created by the excited triplets. These local distortions of the lattice give rise to phonon-phonon interaction leading to a scattering rate τ_{def}^{-1}, which adds to the conventional scattering rates already discussed in chapter 3. In a phenomenological approach it is straightforward to write down the formula for τ_{def}^{-1}:

$$\tau_{def}^{-1} = C\omega^4 F(T) \ . \tag{5.10}$$

The formula is comprehensible. C is a coupling constant describing the scattering strength of the phonons on the deformations and ω^4 results from the assumption that the distortions can at first approximation be considered as point-like defects (see Chapter 3). It is reasonable to assume that the scattering rate depends on the population F(T) of thermally excited triplets, given by

$$F(T) = (1 + 2cosh(h\beta))\frac{e^{-\Delta_0\beta}}{1 + (1 + 2cosh(h\beta))e^{-\Delta_0\beta}} \tag{5.11}$$

$$\text{with } h = g\mu_B H \text{ and } \beta = 1/k_B T,$$

where Zeeman splitting is already included. Only Δ_0 denoting the spin gap appears in formula 5.11, as for simplicity, only single triplet excitations are considered and any binding effects between adjacent excited triplets are neglected [99]. Note that Eq. 5.11 cannot be valid for the entire temperature range. To see this, let us take a look at the temperature dependence of F(T). The distribution F(T) increases monotonically and saturates for temperatures well above the gap ($k_B T >> \Delta_0$) at 0.75. We can imagine that with an increased number of triplets the effect of scattering on local distortions should lessen. This is because with increasing temperature more and more adjacent triplets appear, resulting in large areas where the translation invariance of the lattice is restored.

Scattering on Fluctuating Lattice Distortions

To overcome the above problem one must consider the scattering of phonons on the fluctuations of distortions, rather than on the distortions themselves. In this case the distribution function F(T) must be replaced by another one which takes these fluctuations into account. Again, considering only singlet triplet excitations one ends up with the following formula:

$$F(T) = (1 + 2cosh(h\beta))\frac{e^{-\Delta_0\beta}}{(1 + (1 + 2cosh(h\beta))e^{-\Delta_0\beta})^2} \tag{5.12}$$

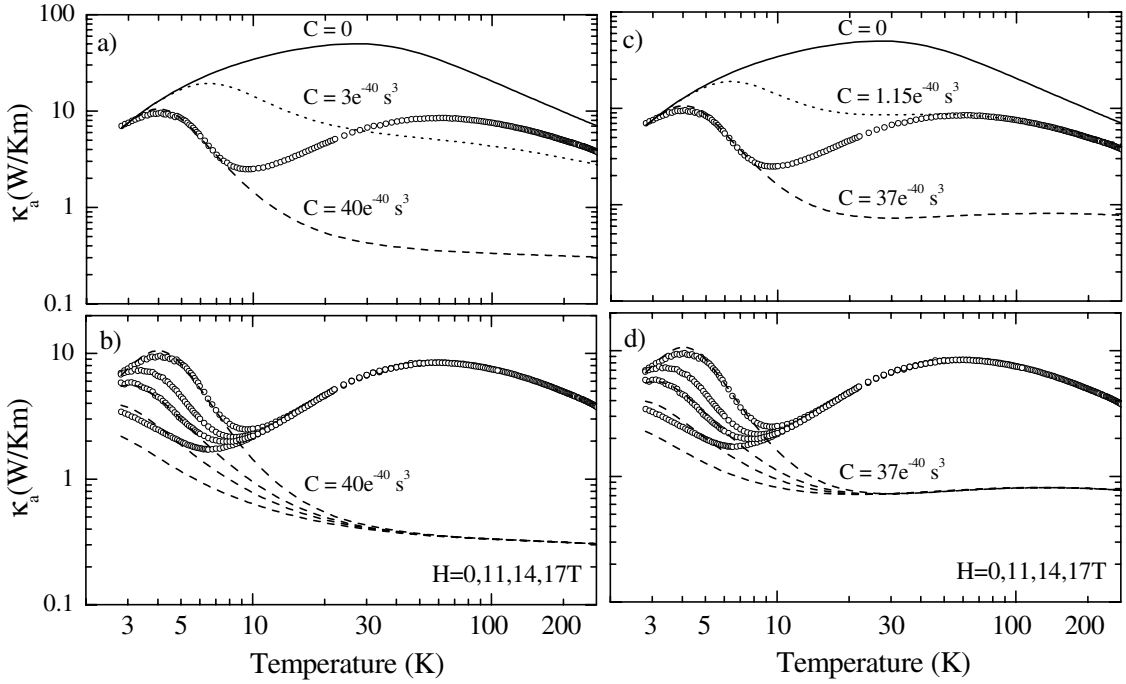

Figure 5.9: In panel a)-d) the experimental thermal conductivity data κ_a ($\circ$) in zero magnetic field and in various magnetic fields (H denotes the magnetic field strength) on a logarithmic scale are given. The lines in panel a) and b) denote the theoretical curves obtained by assuming scattering on elastic deformations. In panel c) and d) the calculated curves for scattering on fluctuations of elastic deformations are illustrated. Switching off the scattering of phonons on local deformations, one obtains hypothetical pure phononic contributions (solid lines in a) and c)). For further discussion see text.

which is simply the product of Eq. 5.11 with the singlet population. For a quantitative description I fit the data by the Debye model for the phonon thermal conductivity (see chapter 3). As previously discussed, the total scattering rate reads:

$$\tau^{-1} = \tau_{bd}^{-1} + \tau_{pt}^{-1} + \tau_{um}^{-1} + \tau_{def}^{-1} \tag{5.13}$$

where τ_{bd}^{-1}, τ_{pt}^{-1}, and τ_{um}^{-1} refer to the standard relaxation processes for conventional phonon heat transport, i.e., to boundary scattering, scattering by point defects, and Umklapp scattering. Subsequently, for τ_{def}^{-1} Eq. 5.11 or Eq. 5.12 is used.

One might argue that there are so many parameters to adjust that it should be possible to fit any of the peaks or even the minimum. This is, however, not the case here, because

	P $[10^{-43}s^3]$	U $[10^{-31}s^2/K]$	u	C $[10^{-40}s^3]$
a), b)	7.7	2.6	5.0	0,3,40
c), d)	7.7	2.6	5.0	0,1.15,37

Table 5.1: Parameters for the fitting of the thermal conductivity data.

the gap ($\Delta_0 \approx 34K$), the sound velocity ($v \approx 6700m/s$), the characteristic sample length (L $\approx 0.7 \cdot 10^{-3}m$) and the Debye temperature ($\Theta_D \approx 453K$) are fixed. The sound velocity and Θ_D are calculated from the measured elastic constant c_{11} [108]. Hence only four adjustable parameters, namely (P, U, u and C), are left and the curves are definite.

The results of the theoretical calculations for the heat transport along the a-axis are given in Fig. 5.9. Let us first discuss scattering on elastic distortions, as illustrated in panel a) and b) of Fig. 5.9. Increasing the scattering rate τ_{def}^{-1} via C lowers the hypothetical phononic contribution (solid line) as depicted in panel a). For an appropriate scattering strength $C = 40 \cdot 10^{-40}s^3$ and reasonable fitting parameters (see table 5.1), one ends up with a curve fitting the low, but not the high temperature peak (dashed line). It is interesting that the experimental observation of the magnetic field dependence of the low temperature peak can be modeled roughly without adjusting any parameter (see Fig. 5.9 b)). Using g ≈ 2.07 [96], the model reproduces the influence of the magnetic field to some extent. However, huge discrepancies between theory and experimental findings above ~ 20 Kelvin do not support this model.

Improvement is hardly achieved by implementing the second mechanism – scattering on the fluctuations of elastic deformations (Fig. 5.9 c) and d)). Using the same parameters (beside the coupling constant C) as above, the influence of the scattering rate (Eq. 5.10) is still too strong at higher temperatures. Obviously, one may reproduce either the high or the low temperature maximum, but not both.
Concerning the magnetic field dependence it is according to Eqs. 5.11 and 5.12 easy to understand that the field dependence must be almost equal in both cases.

In summary, I conclude that the scattering of phonons on local distortions due to triplet excitations has to be ruled out as the dominant scattering process. In view of the two peaks to be explained, we are in need of a scattering process lowering the phononic transport in a fairly narrow temperature interval between the peaks. From this argument we are led to consider a completely different scattering mechanism, namely resonant scattering.

5.3.2 Resonant Scattering

To describe our data, alternative models have to be considered. The idea presented subsequently is based on a scattering regime that was already discussed thirty years ago, namely the idea of resonant scattering [50, 109, 110]. We will see that the resonant character of this process provides the hampering of the thermal transport by phonons in a small temperature region. In $SrCu_2(BO_3)_2$ the elementary triplet excitations are almost dispersionless and form local two-level systems with a unique singlet ground state and a three-fold excited state with a spin gap of $\Delta_0 \approx 35$K.

The basic idea of resonant scattering is depicted on the left hand side in Fig. 5.10. Let us first focus on the process where the spin system is initially in the ground state (Fig. 5.10 a)). The excitation begins with the absorption of a phonon of energy ω, thereby exciting the magnetic system under the constraint of spin conservation. Then another phonon of the same energy is emitted and the magnetic system is de-excited (I). This may also happen in reverse order, with emission preceeding absorption so that there are two possible intermediate states (II). In both cases an incoming phonon (k, ω) is elastically scattered into an outgoing phonon

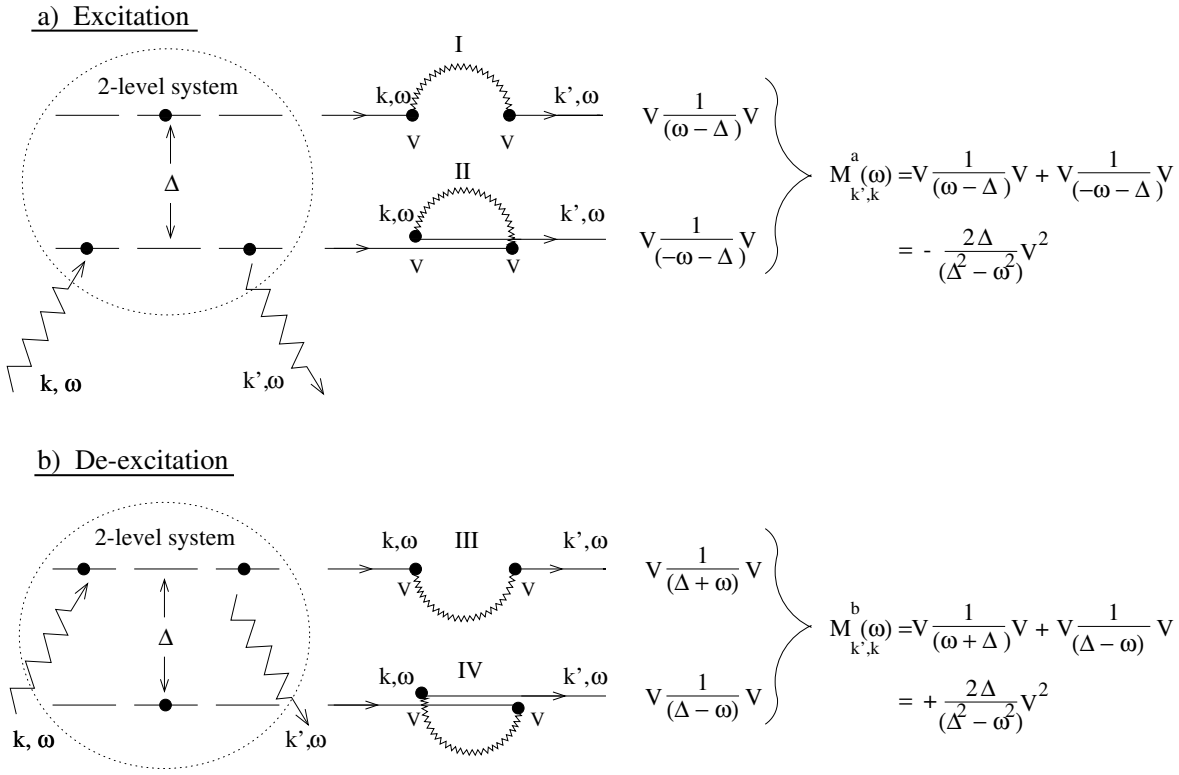

Figure 5.10: Excitation- a) and de-excitation b) scheme for the resonant scattering process. Here, Δ is the energy splitting of the two levels involved. The frequency and momentum of the incoming and outgoing phonon are given by (ω,k) and (ω,$k^{'}$), respectively. The spin lattice coupling parameter is denoted by V.

(k', ω). Since the initial and final spin states are the same, overall energy conservation is required (elastic scattering). The corresponding propagators for processes I and II calculated by G. Uhrig indicate two interesting features [111]. First, the coupling strength V between the lattice and the spin system appears twice because the incoming phonon is absorbed *and* reemitted. Second, when the outgoing phonon is emitted before the incoming is absorbed, the sign of ω has to be reversed. Summing over these states gives the first relevant matrix element $M^a_{k',k}$. In addition the spin system may be initially in the upper state. In this case the corresponding matrix element is given by $M^b_{k',k}$. If excitation (or de-excitation) starts from a localized state like the dispersionless triplet excitations of $SrCu_2(BO_3)_2$, there is no directional correlation between the absorbed and the emitted phonon. The net effect is therefore the same as that of point-like defects except for the frequency dependence.
Based on Fermi's Golden Rule the transition rate is

$$\tau_{res}^{-1} \propto \mid M_{k',k}(\omega) M^*_{k,k'}(\omega) \mid \rho(\omega) \ , \tag{5.14}$$

where $\rho(\omega)$ is the density of states (DOS) in which the system is scattered. One considers here only acoustic phonons in three dimensions, where the DOS $\propto \omega^2$. Inserting $M^a_{k',k}$ and $M^b_{k',k}$ into Eq. 5.3.2 gives

$$\tau_{res}^{-1} \propto V^4 \cdot ((\frac{1}{\omega-\Delta} + \frac{1}{-\omega-\Delta})^2 \cdot N_0 + (\frac{1}{\omega+\Delta} + \frac{1}{\Delta-\omega})^2 \cdot N_1) \cdot \omega^2 \tag{5.15}$$

with N_0 and N_1 the density of singlets and triplets, respectively.

In order to proceed, one needs to know V. In first order the coupling must be proportional to $\partial_{\mathbf{r}} u(\mathbf{r})$, where $u(\mathbf{r})$ is the lattice displacement. Taking the Fourier transform leads to $V \propto k \cdot u(k)$. Remembering from elementary quantum mechanics that the displacements are expressed in terms of $u(k) \propto 1/\sqrt{\omega(k)}(b_k + b_k^\dagger)$ and combining the above relations gives $V \propto \sqrt{\omega}$, assuming acoustic phonons. With the above considerations, one ends up with the following expression for the relaxation rate:

$$\tau_{res}^{-1} = C\omega^2 |M_{k',k}(\omega) M_{k,k'}^*(\omega)| F(T) = C \frac{4\omega^4 \Delta^2}{(\Delta^2 - \omega^2)^2} \cdot (N_0 + N_1) \ , \tag{5.16}$$

where C is the overall coupling strength between phonons and the two-level system. $F(T)$ contains information on the state of the two-level system, e.g., the thermal population of the states.
Note that for frequencies $\omega \ll \Delta$ the frequency dependence of τ_{res} becomes proportional to ω^4, which is typical for Rayleigh scattering. In comparison to previous results, the frequency dependence is of the same form, but the factor for the temperature dependent population of the magnetic states is different [50, 110]. For example, Neelmani et al. have not found a sum for the density of states but a difference in the population of the spin states. Unfortunately, they do not give a precise calculation and therefore it is not clear why they have this difference in the population of the spin states.
In the following I will use Eq. 5.16 as a starting point. It will be seen that different functions $F(T)$ will be used. This is due to the fact that $F(T)$ depends on the details of the explicit model.

In this subject I want to mention that resonant scattering is successfully applied to various other processes, namely the scattering of phonons on nonmagnetic defects or on paramagnetic ions. Pohl et al. could model the thermal conductivity data of KCl containing nitrite ions by using a resonant form of the scattering rate [112]. It was argued that the rotation frequencies of the free NO_2 ions are coupled to phonons of similar frequency and therefore diminish the thermal conductivity in a certain temperature range. Besides resonant scattering by molecular impurities, it was found that atomic impurities can also change the thermal conductivity in the same way. Experimental support was given by Walker et al. who measured the thermal conductivity of KCl containing Na^+, I^- and Ca^{2+} impurities [113]. Although the expression for the scattering rate is different from that of Pohl et al., the dips in the thermal conductivity curves are modeled nicely.
The influence of spin phonon coupling on the lattice thermal conductivity has been investigated intensively in the 1960s. Various spin-lattice relaxation processes have been discussed by Orbach et al. [114]. For rare earth salts, elastic and inelastic processes can be considered, e.g., a process is called a direct one if the outgoing phonon equals the energy difference of the two spin states. This is exactly the case considered above. If there is no overall energy conservation, i.e., incoming and outgoing phonon have different energies, one calls it an indirect Orbach process. For further reading, see the following references [110, 114].

5.3.3 Resonant Scattering Rates

In this subsection various possible scenarios of resonant scattering are discussed. It turns out that one of the discussed spin phonon scattering scenarios successfully accounts for our experimental findings. I will illustrate different ideas that can be interesting for other systems and shine some light on important selection rules to be noticed. Furthermore, the following discussion reveals that spin conservation plays an essential role and influences the resonant scattering rate considerably. Now, I turn to our low-dimensional spin system $SrCu_2(BO_3)_2$, starting with the simplest case and refining the model step by step.

Before I proceed, some clarifying remarks about the spin gap have to be made. In $SrCu_2(BO_3)_2$ triplets on adjacent dimers can form composite objects, so-called bound states. For example, a triplet on dimer (a) and on dimer (b) on the elementary unit in Fig. 5.11 can form a bound state with the total spin $S_{tot} = 0, 1$ and 2, respectively. The coupling $B\vec{S}_a\vec{S}_b$ between two triplets on adjacent dimers leads to the total energies $2\Delta_0 - 2B$, $2\Delta_0 - B$ and $2\Delta_0 + B$ for total spin $S_{tot} = 0, 1$ and 2, respectively. Here Δ_0 is the energy of a single triplet and B is the binding energy. The corresponding level scheme is illustrated in Fig. 5.16 d).

To elucidate the various possible resonant scattering rates, I start from the general equation 5.16. I will present three realistic scattering schemes, followed by a direct comparison of the numerical results to the experimental data.

A: Excitation and De-excitation on One Dimer

I consider now the following scattering process. A triplet on dimer (a) is thermally excited; a second triplet is both excited and de-excited on dimer (b) (see Fig. 5.11). According to Eq. 5.16 we must calculate N_0 and N_1.
Before doing this, it is worthwhile to note that resonant scattering starting from the magnetic ground state is not effective. The reason is that the ground state is a coherent, translational invariant state with zero momentum so that the emitted and absorbed phonons must have the same momentum and energy. In addition, a phonon cannot create only one triplet due to spin conservation. There must already be one thermally excited triplet, on dimer (a) in Fig. 5.11 which combines with a second triplet on (b), so that the total spin is conserved. The probability c_1 that we find a thermally excited triplet on dimer (a) is given by

$$c_1 = \frac{3 \cdot e^{-\Delta_0 \beta}}{1 + 3e^{-\Delta_0 \beta}} \ , \tag{5.17}$$

with $\beta = 1/k_B T$. The elementary gap Δ_0 for the single thermally excited triplet is used here.

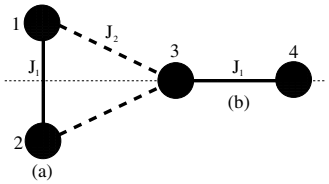

Figure 5.11: Elementary unit made of two orthogonal dimers.

Subsequently, we have to compute the population factors of the singlet (N_0) and triplet (N_1) states. We find

$$N_0 = \frac{1}{1 + 3e^{-\Delta_0 \beta}} \tag{5.18}$$

$$N_1 = \frac{1 \cdot e^{-\Delta_s \beta}}{1 + 3e^{-\Delta_0 \beta}}. \tag{5.19}$$

Spin conservation restricts the possible transitions, i.e., the number of the possible states of the second triplet, created by the scattering process, is reduced. This is reflected by the "1" in the nominator of Eq. 5.19 instead of a "3". It is important to remark that we already have to incorporate binding effects here. As the thermally excited triplet and the triplet on the adjacent dimer (b) created by the scattering process combine to a bound triplet we have to use $\Delta_s = 2(\Delta_0 - B) - \Delta_0 = \Delta_0 - B$ in the nominator of Eq. 5.19. In principle, one would also have to take the binding effects in the partition sum into account, i.e., in the denominators of Eqs. 5.17, 5.18, and in Eq. 5.19. According to the level scheme in Fig. 5.16 d) the partition sum Z would be complicated here and for the following models more complicated or even not analytically solvable. In order to avoid this, the singlet triplet gap Δ_0 is used for Z, i.e, in the denominators. This does almost not change the calculated curves. This is due to the fact that, roughly speaking, an average partitition sum is considered, when Δ_0 is used.

For finite magnetic field strengths, we have to take the Zeeman splitting of the energy levels into account. Due to the conservation of the total s^z component, Δ_s does not depend on the magnetic field. But the elementary gap Δ_0 has to be replaced by $\Delta_0 + s^z h$ with $h = g\mu_B H$. Hence, the probability of finding a thermally excited triplet given by Eq. 5.17 is modified to

$$c_1 = \frac{(1 + 2cosh(\beta h)) \cdot e^{-\Delta_0 \beta}}{(1 + (1 + 2cosh(\beta h)) \cdot e^{-\Delta_0 \beta})} \ . \tag{5.20}$$

We see that $F(T)$ in Eq. 5.16 is to be replaced because of spin conservation by $F(T) = c_1(N_0 + N_1)$. Thus we obtain finally for the resonant scattering rate:

$$\tau_{res}^{-1} = C \cdot \frac{4\omega^4 \Delta_s^2}{(\Delta_s^2 - \omega^2)^2} \cdot \frac{(1 + 2cosh(\beta h)) \cdot e^{-\Delta_0 \beta} \cdot (1 + e^{-\Delta_s \beta})}{(1 + (1 + 2cosh(\beta h)) \cdot e^{-\Delta_0 \beta})^2} \ . \tag{5.21}$$

So far the scattering process has been treated as a very local one, under the assumption that the excitation and de-excitation processes take place on one dimer only. It will be seen, that it is reasonable to assume that because of the symmetry of the Shastry-Sutherland model, one can and one has to go beyond this local picture.

B: Excitation and De-excitation on Two Dimers

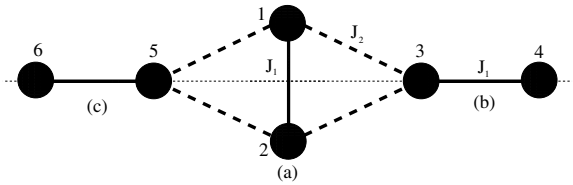

Figure 5.12: Elementary unit made of three orthogonal dimers.

Let us consider the case where two dimers are involved in the process, i.e., there is a thermally excited triplet on dimer (a) and a second triplet created by a scattering process can be excited or de-excited on dimer (b) or on dimer (c) (see Fig. 5.12). Again, we have to find $F(T)$. I give the result and subsequently explain its meaning; F(T) reads:

$$F(T) = 2 \cdot c_1 \cdot (N_0 \cdot 1 + N_1 \cdot 1 + N_0 \cdot N_0 + N_1 \cdot N_1 - N_0 \cdot N_1 - N_1 \cdot N_0) \ . \tag{5.22}$$

As there has to be a thermally excited triplet on dimer (a) (see Fig. 5.12) for the scattering process to take place, the prefactor c_1 from Eq.5.20 appears in Eq. 5.22. The factor 2 arises because one can start with the excitations and de-excitations either on dimer (b) or on dimer (c). The terms in the brackets correspond to the possible scattering channels. The first term $N_0 \cdot 1$ describes the scenario where both excitation processes (the corresponding matrix elements are $M^a_{k',k}(\omega)$ and $M^a_{k,k'}(\omega)$, see also Fig. 5.10 a)) run on one of the horizontal dimers, e.g., on dimer (b). $N_0 \cdot 1$ means that we start with an excitation process on (b). The probability of finding the spin system in the ground state is N_0. At this point one has completed the $M_{k,k'}$ process. According to Fermi's Golden Rule this process has to be considered twice. As we consider the case where the total process occurs on the same dimer, we know already that the system is definitely in the groundstate. Hence one gets $N_0 \cdot 1$. The second term $N_1 \cdot 1$ arises from the corresponding scattering via de-excitation. If the process $M^a_{k',k}(\omega)$ takes place on dimer (b) and $M^a_{k,k'}(\omega)$ on dimer (c) one gets the third term $N_1 \cdot N_1$. Now, it should be clear how to get the remaining terms[4]. Again, taking binding effects and the influence of the magnetic field onto the states into account, we find for the rate:

$$\tau^{-1}_{res} = K \cdot \frac{2 + (1 + 2cosh(\beta h)) \cdot e^{-\Delta_0 \beta} - e^{-\Delta_s \beta} + e^{-2\Delta_s \beta} + (1 + 2cosh(\beta h)) \cdot e^{-\beta(\Delta_s + \Delta_0)}}{2(1 + (1 + 2cosh(\beta h)) \cdot e^{-\Delta_0 \beta})^3}$$

$$K = C \cdot \frac{8\omega^4 \Delta_s^2}{(\Delta_s^2 - \omega^2)^2} \cdot (1 + 2cosh(\beta h)) \cdot e^{-\beta \Delta_0} \ . \tag{5.23}$$

The two scattering schemes discussed so far are restricted to one or two dimers, i.e., we consider a very local picture. Now, I want to discuss a scattering scheme where excitation and de-excitation can take place on many different dimers not necessarily close to each other.

[4]The neighbors above and below dimer (a) are not considered as a triplet on (a) can create further triplets only on dimer (b) and (c).

C: Excitation and De-excitation on Many Dimers

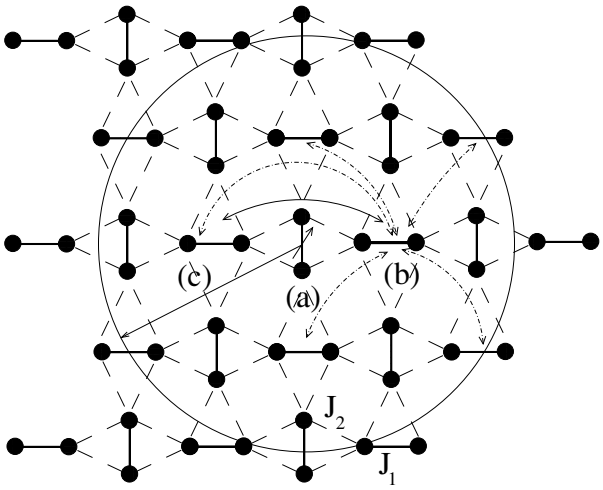

Figure 5.13: Thermally excited triplet on dimer (a) (denoted by straight arrow, solid line). Dimers (b) and (c) comprise the elementary unit where excitation and de-excitation occur and vice versa(solid arrow). Dashed arrows correspond to the case where "long range correlation" lead to various additional scattering schemes. The "cloud of dimers" where excitation and de-excitation can occur is marked by the circle.

Imagine that we have for some reason correlation effects between the triplet states over a certain length (indicated by the circle in Fig. 5.13). We recall F(T) in Eq. 5.22 in a slightly different form:

$$F(T) = 2 \cdot c_1 \cdot (N_0 \cdot (1 + n \cdot N_0 - n \cdot N_1) + N_1 \cdot (1 + n \cdot N_1 - n \cdot N_0)) \ , \tag{5.24}$$

where n counts the number of dimers on which the processes are likely to occur. For $n = 1$, Eq. 5.24 is equal to Eq. 5.22. With the condition $n >> 1$, which is the requirement for the radius of the circle in Fig. 5.13 to be large, we can neglect the "1" in the brackets of Eq. 5.24 and find:

$$F(T) = 2 \cdot c_1 \cdot n \cdot (N_0 - N_1)^2 \ . \tag{5.25}$$

To derive the final equation for $F(T)$ we proceed as above by including binding and magnetic field effects and find

$$\tau_{res}^{-1} = C \cdot \frac{8\omega^4 \Delta_s^2}{(\Delta_s^2 - \omega^2)^2} \cdot \frac{(1 + 2cosh(\beta h)) \cdot e^{-\Delta_0 \beta} \cdot (1 - e^{-\Delta_s \beta})^2}{(1 + (1 + 2cosh(\beta h)) \cdot e^{-\Delta_0 \beta})^3} \ , \tag{5.26}$$

where n is included in the overall scattering constant C.

Comparison between Theory and Experiment

For the quantitative description we again make use of the Debye model (Eq. 3.2). The total scattering rate is obtained here by replacing τ_{def}^{-1} in Eq. 5.13 with τ_{res}^{-1}. Let us first compare the calculated and measured thermal conductivity data for the zero magnetic field . In Fig. 5.14 and 5.15 the experimentally observed data (points) and the calculated curves (solid lines) are plotted for both directions of the heat current. All three models $\mathbf{A} - \mathbf{C}$ for the resonant scattering rate discussed above reproduce κ_c in zero magnetic field almost perfectly (Fig. 5.15). Obviously, for κ_a the fit functions are also well in accordance with the experimental data for temperatures above $\approx 10K$, whereas below $\approx 10K$ a slight shift between fit and experimental data occurs in all three models. A closer inspection of Fig. 5.14 c) and Fig. 5.15 c) (model **C**) reveals that the high temperature maximum (at $\approx 30K$) in κ_c and the minimum in the thermal conductivity curve of κ_a are less well reproduced than for the other two models.
One could argue that the parameters for the different phonon scattering mechanisms do not fix the calculated curves unambiguously, and therefore a clear decision for which model gives the best fit might actually be impossible. Since the Debye model for the phonon thermal conductivity is a good approximation only for temperatures well below the Debye temperature Θ_D, I have tried to describe the low temperature maxima and minima as well as possible for both directions of the heat current and have taken this as the criteria for "best fit". We finally end up with the the parameters summarized in Table 5.2. Reasonable values are obtained for the parameters P, U, u and C for all three models. Moreover, the gap Δ_0 chosen in order to optimize the fit (Table 5.2), agrees well with former results. The small value for Δ_s gives a clear indication that strong binding effects occur. This is confirmed through theory [92] and experiment where in the $s = 1$ channel the lowest composite excitation (made from 2 elementary triplets) is found at about 4.7 meV ($\approx 55\ K$) which is just 1.7 meV ($\approx 20\ K$) above the elementary gap at 3 meV ($\approx 35\ K$) (see Fig. 5.6). Therefore the fits support the observation of strong binding effects [98, 99].
Having determined the parameter set (see Table 5.2), one calculates the field dependence without adjusting any of the parameters. A strong magnetic field dependence is found in all theoretical models. But the magnetic field dependence $\partial\kappa(B)/\partial B$ of the calculated thermal conductivities is much stronger than that found in the experiment. Especially in high magnetic fields, the deviations between theoretical description and experiment are severe. In the following section it will be shown that this discrepancy arises from binding effects.

		P $[10^{-43}s^3]$	U $[10^{-31}s^2/K]$	u	C $[10^9 s^{-3}]$	Δ_0[K]	Δ_s[K]
A	κ_a	8	2.4	5.2	22	29	15
	κ_c	12	6.9	6.7	5.7	29	15
B	κ_a	8	2.7	4.9	43	34	17
	κ_c	10	6.0	8.4	1.2	34	17
C	κ_a	30	3.5	6.9	60	34	17
	κ_c	14	8	12.5	39	34	17

Table 5.2: Parameters for the fitting of the thermal conductivity data. The fixed quantities Debye temperature Θ_D and the velocity v are given in Chapter 5.3.1. The characteristic sample lengths L are $\approx 0.7 \cdot 10^{-3}m$ for κ_a and are $\approx 0.5 \cdot 10^{-3}m$ for κ_c, respectively.

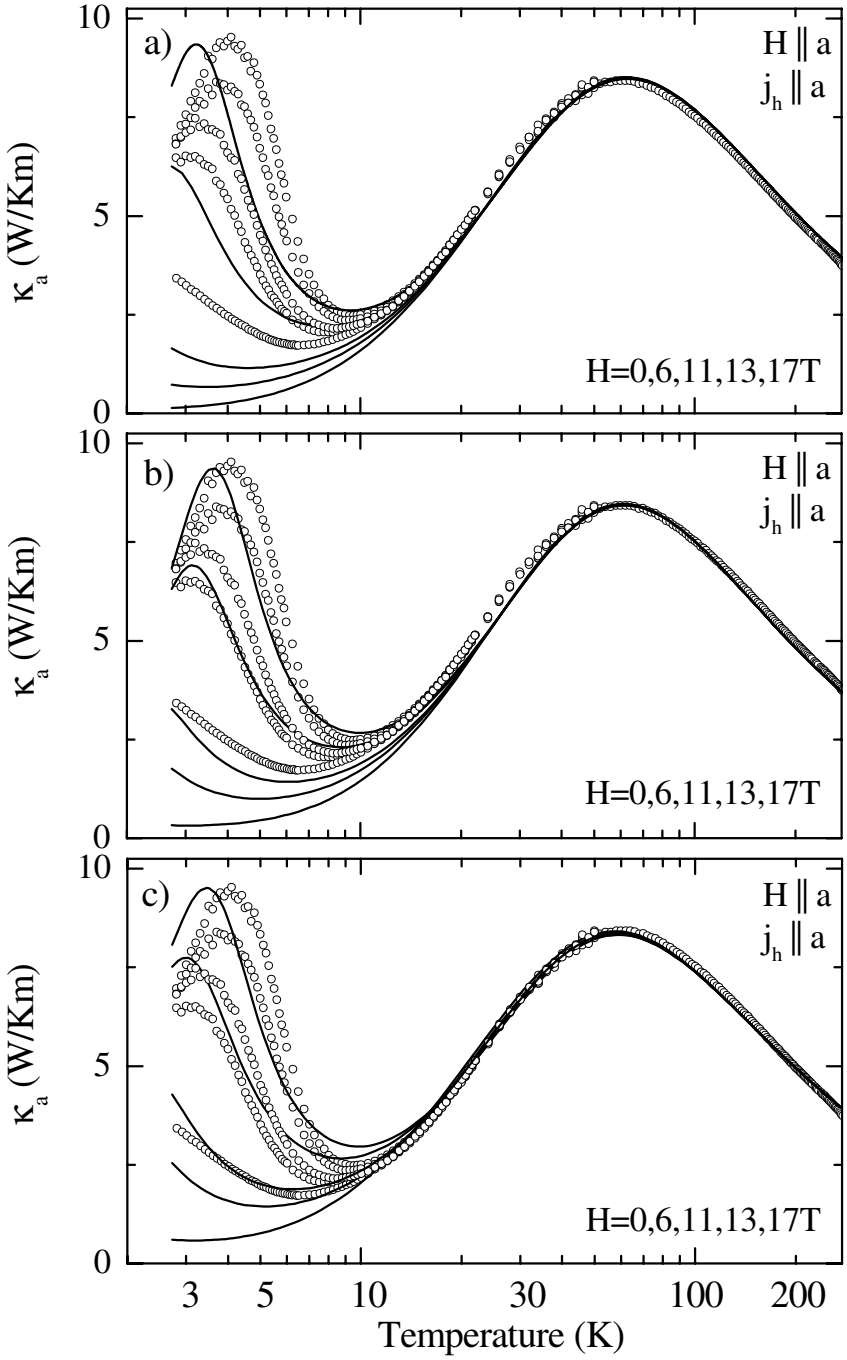

Figure 5.14: Thermal conductivity (κ_a) of $SrCu_2(BO_3)_2$ along the magnetic planes for selected magnetic fields. The lines in panels a), b) and c) correspond to the theoretical curves obtained by using the Debye model for phonon thermal conductivity, in conjunction with the resonant scattering rate τ_{res} of the theoretical models **A, B** and **C**, respectively.

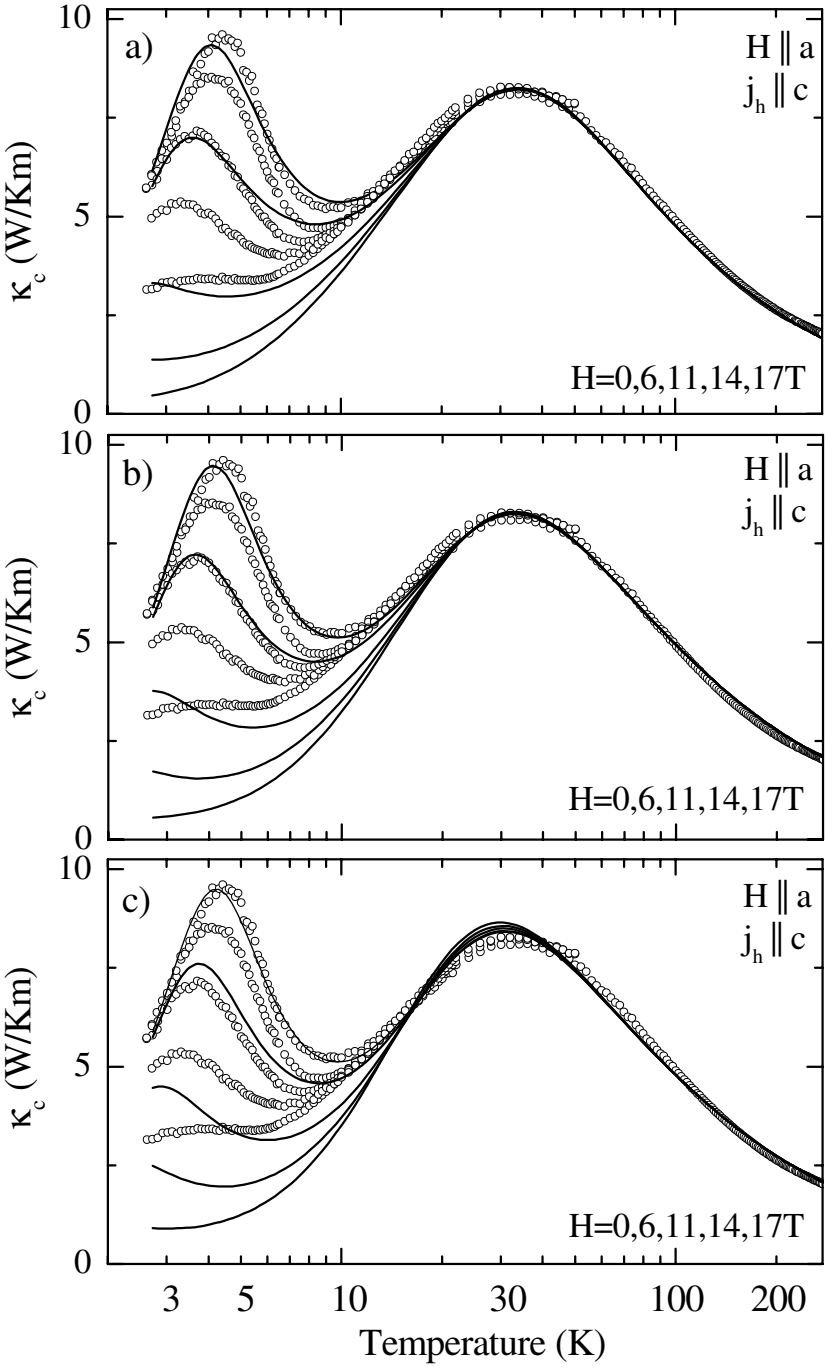

Figure 5.15: Thermal conductivity of $SrCu_2(BO_3)_2$ perpendicular (κ_c) to the magnetic planes for selected magnetic fields. The lines in panels a), b) and c) correspond to the theoretical curves obtained by using the Debye model for phonon thermal conductivity, in conjunction with the resonant scattering rate τ_{res} of the theoretical models **A, B** and **C**, respectively.

Bound Singlets

From the fits, I obtained for $\Delta_0 \approx 34$ K, for $\Delta_s \approx 17$ K and for the binding energy $B \approx 15 - 17$ K. Triplet states ($s = 1$) are found at $2\Delta_0 - B \approx 50$ K. Bound states with the total spin $s = 0$, so-called bound singlets are at $2\Delta_0 - 2B \approx 36$ K, i.e., the energy of a composite *singlet* is almost equal to the elementary gap [92] as depicted in Fig. 5.16. Therefore bound singlets have to be treated as scattering centers for resonance scattering, too. In this case a dimer adjacent to a bound singlet is excited and the corresponding three triplets combine to $s_{tot} = 0$. Since $s_{tot} = 0$, this contribution to the resonance scattering does not depend on a magnetic field and lowers the sensitivity of the total resonance scattering rate to a magnetic field.

The contribution of the bound singlets to the scattering rate is treated similarly to that of the single triplets. To get a deeper understanding of the microscopic mechanisms, I will derive the scattering rate and the specific heat calculated within the same model [111]. Essentially, we adopt a local picture in the style of model **B**, discussed for the case where only triplets were taken into account (see preceding discussion).
For this, it is useful to introduce the quantity m_s:

$$m_s := sinh((2s+1)\beta h/2)/sinh(\beta h/2) \tag{5.27}$$

where $s = 0, 1, 2$ denote the total spin of the composite state. A tedious but straightforward calculation gives the probability c_2 that a pair of adjacent dimers is in a state made of two triplets:

$$c_2 = \frac{1}{Z} \cdot [m_0 \cdot e^{-(2\Delta_0 - 2B)\beta} + m_1 \cdot e^{-(2\Delta_0 - B)\beta} + m_2 \cdot e^{-(2\Delta_0 + B)\beta}] \tag{5.28}$$

with m_s from Eq. 5.27. The complete partition sum Z of the system of two dimers with the energies stated above for two triplets reads:

$$Z = 1 + 2m_1 \cdot e^{-(\Delta_0)\beta} + m_0 \cdot e^{-(2\Delta_0 - 2B)\beta} + m_1 \cdot e^{-(2\Delta_0 - B))\beta} + m_2 \cdot e^{-(2\Delta_0 + B))\beta} \ . \tag{5.29}$$

In the present case we are faced with exclusion effects, i.e., single and 2-triplet objects block each other. Each dimer is connected to four other dimers. Thus, taking care of double counting, we have $2L$ bonds in a system of L dimers. The probabilities c_1 and c_2 are not the densities $n_i = N_i/L$ since exclusion effects are not yet considered. Regarding Fig. 5.13, we derive the following exclusion criteria. Suppose we have a single triplet on dimer (a). No additional single triplet can be on the four next nearest neighbour dimers because we had 2-triplet states instead. Therefore every single triplet blocks four sites for other single triplets. For the same reason, these four sites are also blocked for 2-triplet states by the single triplet on dimer (a). Now, we assume a composite object exists between dimer (a) and (b). Consequently, two sites for single triplet states are blocked and for 2-triplet states six sites are blocked. Hence, we get for the densities (per dimer) of possible single triplet states n_1 and 2-triplet states n_2 the self-consistent equations:

$$n_1 = \frac{N_1}{L} = c_1 \frac{1}{L}(L - 4N_1 - 2N_2) \tag{5.30}$$

$$n_2 = \frac{N_2}{L} = 2c_2 \frac{1}{L}(L - 4N_1 - 6N_2) \ .$$

Finally, a straightforward calculation yields:

$$n_1 = \frac{c_1(1+2c_2)}{1+4c_1+6c_2+16c_1c_2} \tag{5.31}$$

$$n_2 = \frac{2c_2(1+2c_1)}{1+4c_1+6c_2+16c_1c_2} \ .$$

A further complication arises from a repulsive interaction v between neighboring triplets. Composite objects and triplets repel each other if they are neighbors. This can be understood in the following way. If we had an isolated dimer system, the size of the gap would be equal to the intradimer coupling J_1. However, the actual gap is about $J_1/2$. The reduction of the gap is due to virtual processes comprising excitations on dimers in the vicinity [115]. For single triplet states, the two active neighbors of each triplet matter (see Fig. 5.13, in leading order only the two dimers (b) and (c) are important for triplet (a)). Hence, we introduce the repulsion

$$R = \frac{J_1 - \Delta_s}{2}$$

and compute the repulsive field on a mean field level:

$$v = R(n_1 + 3n_2/2) \ .$$

Note that $n_2/2$ is the density of composite objects per bond. The factor 3 arises since a free neighboring dimer is part of three different bonds. The repulsive field v which is computed self-consistently acts twice on single triplets and three times on composite objects, as there are three relevant dimers in the vicinity to the composite object. This leads to a modification of Eq. 5.28 and 5.29, namely

$$c_2 = \frac{1}{Z} \cdot [m_0 \cdot e^{-(2\Delta_0 - 2B + 3v)\beta} + m_1 \cdot e^{-(2\Delta_0 - B + 3v)\beta} + m_2 \cdot e^{-(2\Delta_0 + B + 3v)\beta}] \tag{5.32}$$

and

$$Z = 1 + 2m_1 \cdot e^{-(\Delta_0 + 2v)\beta} + m_0 \cdot e^{-(2\Delta_0 - 2B + 3v)\beta} + m_1 \cdot e^{-(2\Delta_0 - B + 3v))\beta} + m_2 \cdot e^{-(2\Delta_0 + B + 3v))\beta} \ .$$

The probability c_1 of Eq. 5.20 must also be changed. Here one has to replace Δ_0 by $\Delta_0 + 2v$.

Apparently, there are various free parameters to adjust in order to fit the data. It is possible to fix the parameter R, B and Δ_0 by computing the specific heat c and thus check our model. It is important to note that the chosen values of B and Δ_0 are well in accordance with those obtained by inelastic neutron scattering and electron spin resonance experiments [95, 99]. In order to compute the specific heat one has to find the total energy of the system. From the densities and the energies of the single triplets ($E_1(T)$) and the composite objects ($E_2(T)$), it is straightforward to calculate the total energy $E(T) = E_1(T) + E_2(T)$ at each temperature. We obtain:

$$E_1(T) = n_1 \left(\Delta_0 + \frac{-he^{h\beta} + he^{-h\beta}}{m_1} \right)$$

$$E_2(T) = n_2(2\Delta_0 - 2B) +$$

$$n_2 \left(\frac{Bm_1e^{-B\beta} - 2hsinh(h\beta)e^{-B\beta} + 3Bm_2e^{-3B\beta} - 2hsinh(h\beta)e^{-3B\beta} - 4hsinh(h\beta)e^{-3B\beta}}{m_0 + m_1e^{-B\beta} + m_2e^{-3B\beta}} \right) \ .$$

From $E(T)$ the specific heat is obtained by $c = \partial E/\partial T$.

To illustrate the validity of our model we compute the specific heat for various magnetic fields. For the realistic parameters $\Delta_0 = 36$ K, $R = 18$ K (from $J_1 = 72$ K [115]) and $B = 17$ K, we obtain the results depicted in Fig. 5.16 c). At low temperatures the agreement with experiment is very good; position and height of the peak are considerably improved relative to an isolated dimer model [106]. At higher temperatures we presume that the local model developed above is too simplistic since the dispersion of the bound states and/or unusual phononic effects are neglected [99, 115].

Let us turn to the thermal conductivity again. The resonant scattering, decisive for the thermal conductivity, is calculated in the *same* model with the *same* parameters. The rate is easily obtained by reflecting the possible excitation and de-excitation processes. This was covered already, thus I will skip the calculations here and give the results: $\tau_{res}^{-1} = C\omega^4(A_1 + A_2)$ with

$$A_1 = \frac{2n_1(N_0 + N_1 + (N_0 - N_1)^2)(\Delta_0 - B)^2}{((\Delta_0 - B)^2 - \omega^2)^2} \tag{5.33}$$

$$A_2 = \frac{3n_2(N_0 + N_1 + 2(N_0 - N_1)^2)\Delta_0^2}{(\Delta_0^2 - \omega^2)^2} \ , \tag{5.34}$$

where $N_1 = (n_1 + 3n_2/2)/3$ and $N_0 = 1 - 3N_1$. Using this τ_{res}^{-1} together with the usual scattering rates we fit the experimental κ_a and κ_c by Eq. (3.2). As shown in Fig. 5.16 our model yields an almost perfect fit of the measured κ_c (for $H = 0$) over the entire temperature range. Above 10 K the fit of κ_a is also nearly perfect, whereas below 10 K a slight temperature shift (≤ 1 K) between fit and experimental data occurs. Since the gap Δ_0, the binding energy B, and the interaction R are determined from the specific heat, there remains only four adjustable parameters P, U, u, and C (see Table 5.3).
These values are reasonable for an insulator and are comparable in magnitude to those found, e.g., in the spin ladders [65]. Different values for κ_a and κ_c are expected in an anisotropic crystal. Our model reproduces the overall influence of the magnetic field very well. The high temperature maxima remain unchanged, whereas the low temperature maxima are continuously suppressed. Again the agreement between calculated and experimental values is better for κ_c than for κ_a. Although the field influence on κ_a is slightly overestimated by our model, the experimental values of κ_c are still quantitatively reproduced up to the highest field.

	P $[10^{-43}s^3]$	U $[10^{-31}s^2/K]$	u	C $[10^6 s^3]$
κ_a	7.7	2.6	5.0	3.35
κ_c	7.9	5.7	10.0	1.15

Table 5.3: Parameters for the fitting of the thermal conductivity data.

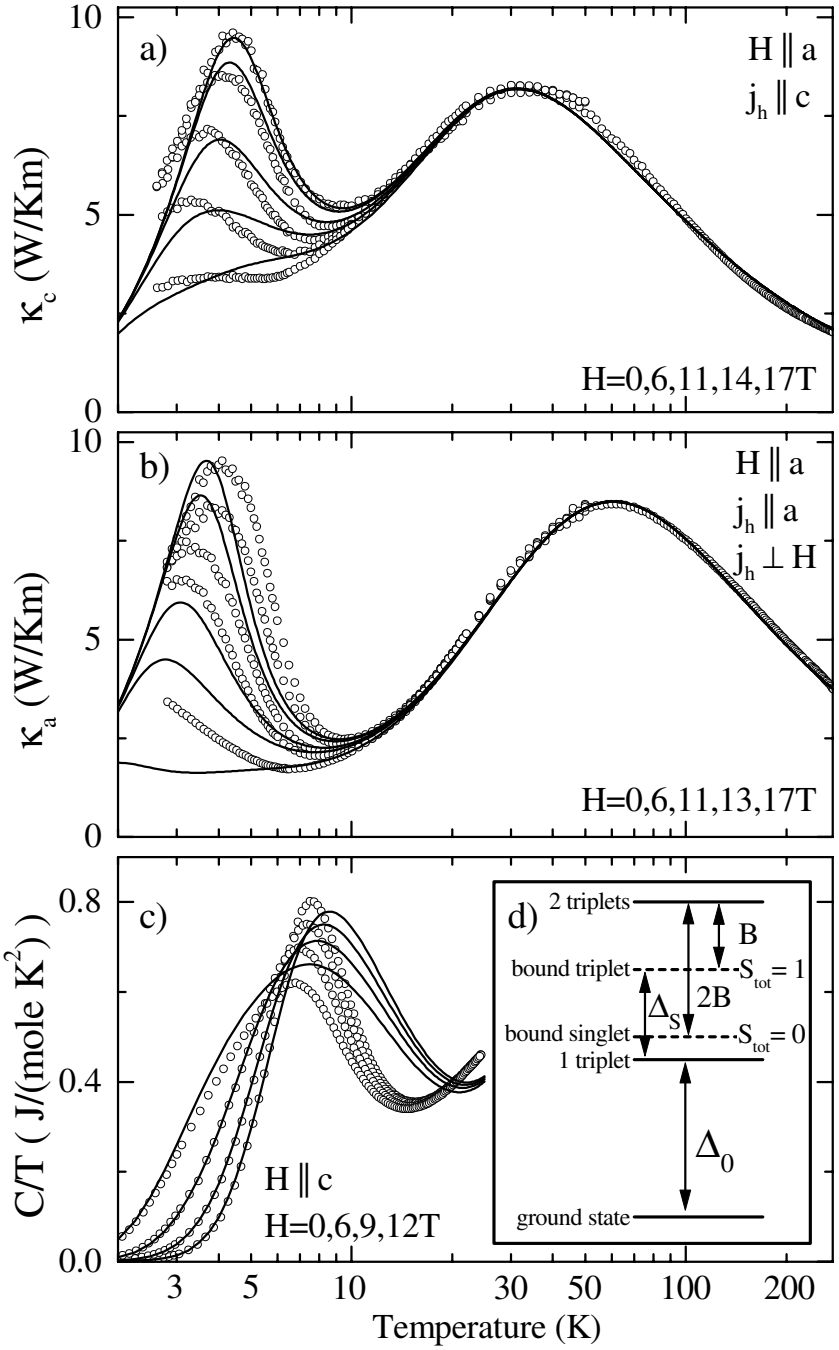

Figure 5.16: Thermal conductivity κ_c (a) and κ_a (b) on a logarithmic temperature scale for various magnetic fields (see figure). On increasing field the low-T maximum is suppressed. The lines are theoretical curves calculated with the "resonant scattering model". (c) Specific heat at various fields $H||c$ (the peak height decreases with increasing field). Data points are from Ref. [106]; the lines result from the same theoretical model. (d) Level scheme used in our model: the solid lines denote the energies of the ground state, 1 triplet and 2 elementary triplets, respectively. The dashed lines indicate bound states with $s_{tot} = 0$ or 1, which are built from two elementary triplets. B is the binding energy and Δ_0 is the elementary gap. Δ_s is the energy difference relevant for the resonance scattering.

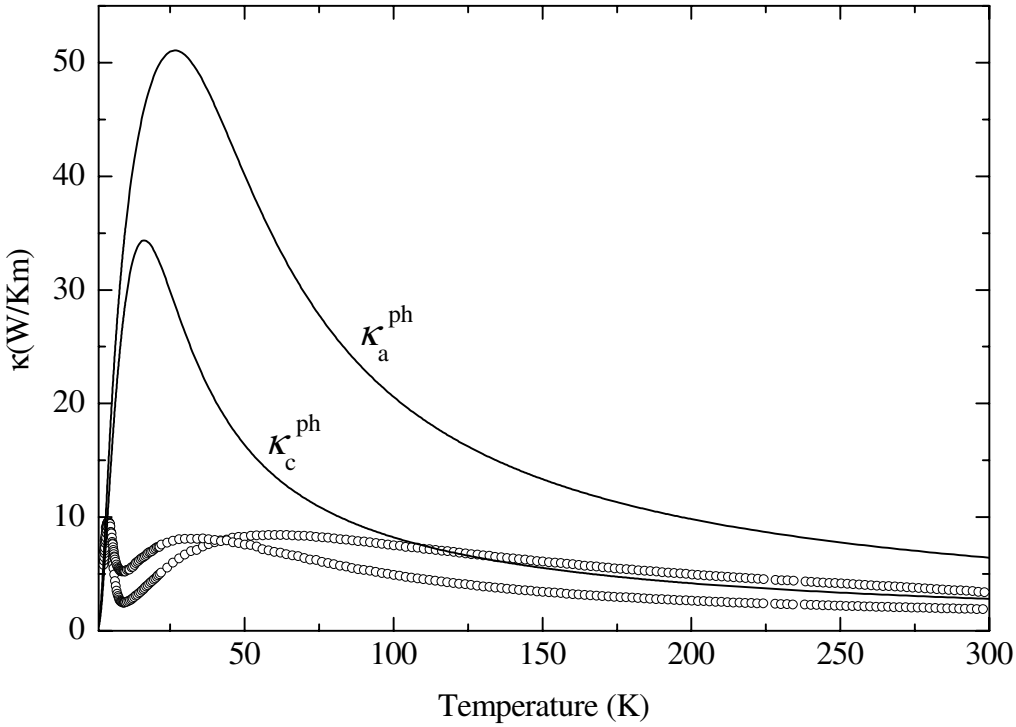

Figure 5.17: Shown are the experimental data (∘) together with conventional phononic contributions κ_a^{ph} and κ_c^{ph} (–) obtained by switching off the scattering of phonons by magnetic excitations (see text).

In the calculations, one can switch off the resonant scattering by magnetic excitations. Therfore one has to set $C = 0$. $\kappa_{ph}(C = 0)$ obtained in this way is much larger than the measured thermal conductivity, as shown in Fig. 5.17. As expected for resonant scattering, the damping of the phonon heat transport is most pronounced for $T \approx \Delta_s$. Note, however, that even at room temperature the suppression is sizeable. This strong damping gives further evidence for a large spin phonon coupling in $SrCu_2(BO_3)_2$, as has been inferred before from sound wave anomalies [108].

Bringing this chapter to a close, I want to sketch out briefly an attempt that was supposed to further improve the accordance between theory and experiment.
The interesting fact that the magnetic susceptibility can be described rather well by an RPA-molecular field approach, initiated the idea that probably a renormalisation of the magnetic field reproduces the field dependence of the thermal conductivity even better [108]. Therefore we measured the magnetic susceptibility of one of our samples, as illustrated in Fig. 5.18. The data were fitted according to the following model:

$$\chi = \frac{\chi_0}{(1 - (j_{eff}/C) \cdot \chi_0)} \ , \tag{5.35}$$

where j_{eff} is an effective exchange coupling constant.

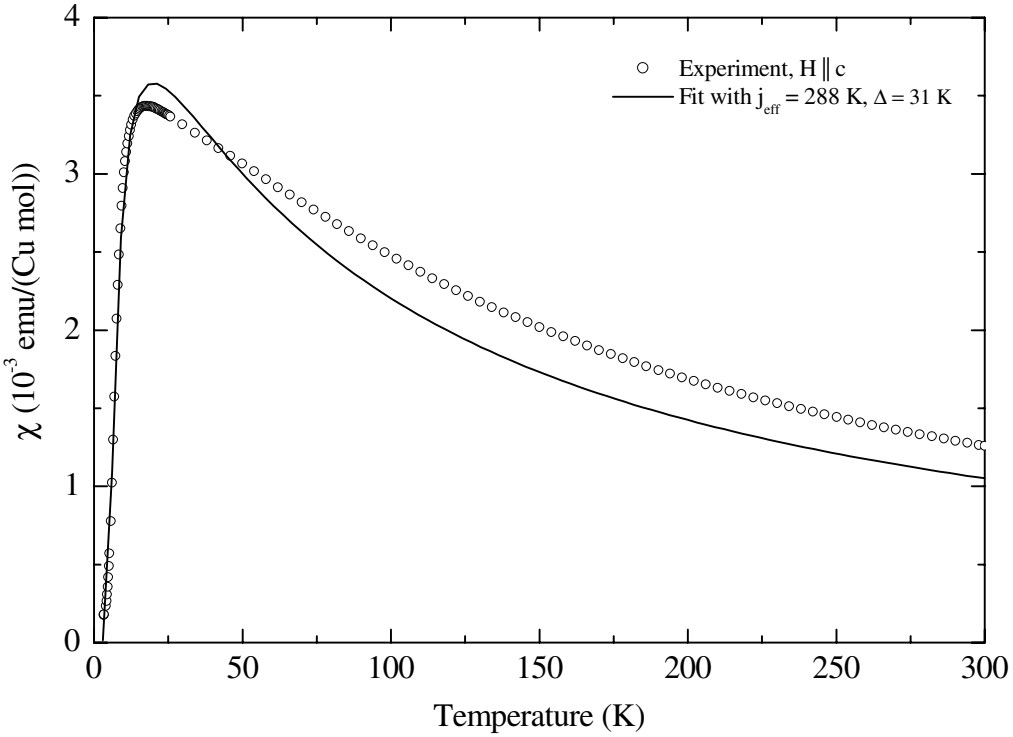

Figure 5.18: Magnetic susceptibility χ as function of temperature in a magnetic field of 1 Tesla applied parallel to the c-axis. The full line denotes the fit.

χ_0 is the susceptibility per mole Cu of an isolated dimer model, given by

$$\chi_0 = C \cdot \frac{e^{(-\Delta_0/k_B T)}}{1 + 3e^{(-\Delta_0/k_B T)}} \ , \tag{5.36}$$

with $C = \frac{N_A g^2 \mu_B^2}{k_B}$. For a gap of $\sim$ 31 K and $j_{eff} \sim$ 288 K, the experimental data are reasonably well reproduced. The value of the gap obtained here is close to the accepted value of $\sim$ 35 K.
The effective exchange coupling constant j_{eff} reflects the coupling of one Cu spin to its nearest neighbors. In the a-b-plane, one spin of a dimer couples to the four nearest neighbors. In addition, there is also an out-of-plane coupling to two spins on the plane above and to two spins on the plane below (see Fig. 5.1). The in-plane coupling constant J_2 is $\approx$ 42 K and the out-of-plane coupling constant $J_\perp$ is about 15 K [92]. Thus we get $4(J_2 + J_\perp) \approx 224$ K, which is close to j_{eff}, obtained from the fit.

In order to compute the effective field in the vicinity of the spin a standard molecular field approach is used. Each spin 'feels' the sum of the external field and of an internal exchange "field", namely

$$h_{eff} = h_{ext} - j_{eff} \cdot < s^z > \ ,$$

where $< s^z >$ is the expectation value of the s^z-component of the total spin. For a two level system, $< s^z >$ is easily computed and one yields

$$h_{eff} = h_{ext} - j_{eff} \cdot \frac{sinh(h_{tot})\beta e^{-\Delta_0 \beta}}{1 + e^{-\Delta_0 \beta}(1 + 2cosh(h_{tot}\beta))} \ . \tag{5.37}$$

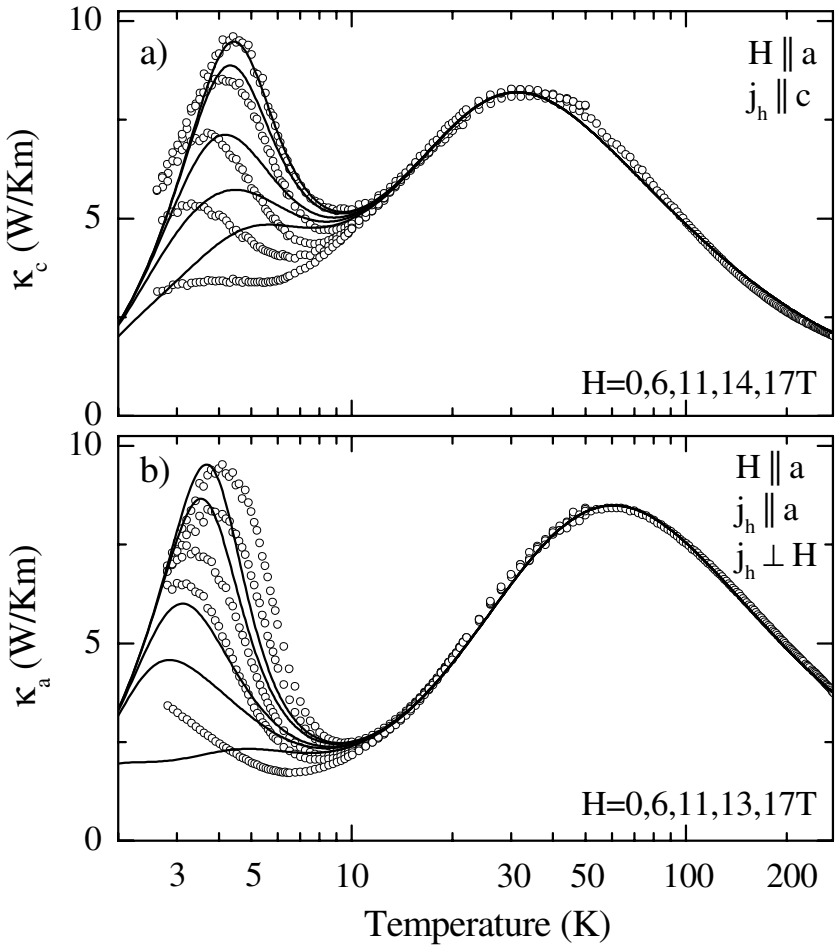

Figure 5.19: Thermal conductivity κ_c (a) and κ_a (b) on a logarithmic temperature scale for various magnetic fields (see figure). On increasing the magnetic field, the low-T maximum is suppressed. The lines are theoretical curves calculated for the same magnetic fields for an RPA approach.

The magnetic field dependence of the thermal conductivity is modeled by replacing h by h_{eff} in Eqs. 5.33 and 5.34 and by using the effective exchange coupling $j_{eff} = 288$ K. All other parameters are the same as those used in order to obtain the theoretical curves plotted in Fig. 5.16. The values of these parameters are summarized in Table 5.3.

The results are shown in Fig. 5.19. The fitting procedure in order to obtain the thermal conductivity was carried out as done before. Of course, the zero field curves are equal to those in Fig. 5.16 because $h_{eff} = 0 + j_{eff} \cdot 0 = 0$. The RPA approach does not considerably improve the field dependence of the thermal conductivity. One is rather tempted to say that the discrepancies between theory and experiment even increase, especially in the narrow temperature range between 5 and 10 K.

5.3.4 Summary

In summary, the thermal conductivity parallel (κ_a) and perpendicular (κ_c) to the magnetic planes of the low-dimensional quantum spin system $SrCu_2(BO_3)_2$ has a characteristic double-peak structure with two maxima. For both directions the low temperature maxima have a pronounced magnetic field dependence. A significant magnetic contribution to the heat current can be excluded, since the double peak structure is not anisotropic and because the magnetic excitations are (almost) localized.
A quantitative analysis in terms of resonant scattering of phonons by magnetic excitations explains the double peak structures and their magnetic field dependence very well and gives evidence for strong spin-phonon coupling. I want to emphasize that spin-phonon coupling in conjunction with spin conservation had to be taken into account in order to describe our results. Moreover, the inclusion of bound triplets and bound singlets is necessary for a correct description of the magnetic field dependence. Our model describes the specific heat almost perfectly with the same parameter set used for the thermal conductivity.

Chapter 6

$CuGeO_3$

It was already in the 1970s when convincing experimental evidence was given for the spin-Peierls transition occuring in a few organic compounds, e.g, in TTF-AuBDT [116]. The first inorganic compound showing a spin-Peierls is $CuGeO_3$ discovered by Hase et al. in 1993 [117]. This has strongly renewed the interest of both theoreticians and experimentalists in the study of the spin-Peierls phenomenon.
For theoreticians, on the one hand, the simpler lattice structure of $CuGeO_3$ compared to the organic compounds [116] helps to understand of the phase transition and related phenomena. On the other hand, large single crystals of high quality can be synthesized, to allow a detailed experimental investigation of the system. Thus $CuGeO_3$ can be regarded as a unique substance for gaining a deeper understanding of magnetism, structural phase transitions and the interplay of both with respect to a quasi-one-dimensional spin system.
Due to an enormous amount of experimental and theoretical results, the physical properties of $CuGeO_3$ are well known and to a large extent understood.

However, a precise and systematic investigation of the thermal transport properties has not been given so far. From theory it is known that magnetic excitations in an ideal $s = 1/2$ Heisenberg chain move without dissipation, which may lead to an additional contribution κ^{mag} to the heat current [118]. Therefore, quasi-one-dimensional spin chains in $CuGeO_3$ may give rise to a magnetic heat current. Thus the system is interesting for studying possible magnetic contributions to κ. Up to now, Ando et al. and Vasil'ev et al. have performed thermal conductivity measurements on pure and doped specimen [63, 64, 119–121]. However, different results of the thermal conductivity are obtained. We will clarify this and we will show with a systematic investigation of the heat transport along all three crystallographic axes that the proposed explanation of Ando et al. for the heat transport in $CuGeO_3$ can be doubted. Moreover various scenarios to explain the thermal conductivity are apparently possible.

6.1 Structure and Magnetic Exchange

At room temperature an orthorhombic crystal structure with the space group $D_{2h}^5 - Pbmm$ was proposed by Völlenkle et al. [122] (see Fig. 6.1) and after the discovery of the spin-Peierls transition further measurements confirmed this result [123–126].

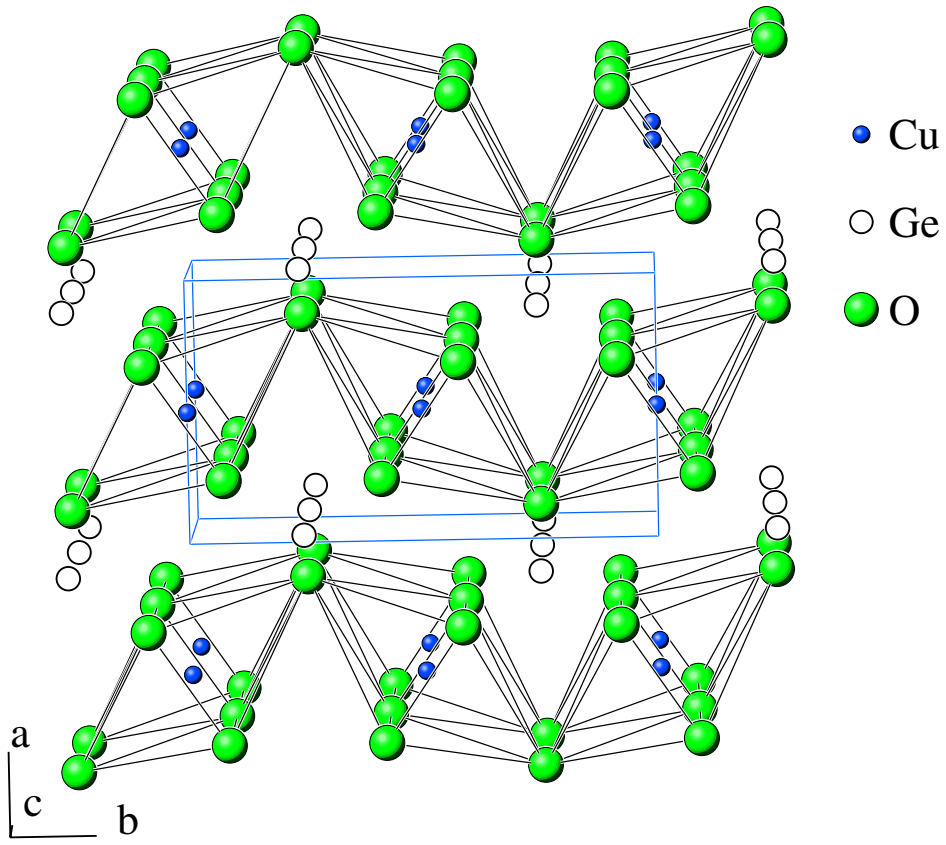

Figure 6.1: Crystal structure of $CuGeO_3$ in the uniform high temperature phase.

There are essentially two elementary building blocks – the CuO_6 octahedra, as in the high-temperature superconductors, and the GeO_4 tetrahedra. The octahedra can be decomposed into plaquettes made up of a Cu atom surrounded by four oxygen atoms usually referred to as O(2) and two apex O(1). It is remarkable that the Cu-O(2) distance ($\simeq 1.93\mathring{A}$) is much shorter than Cu-O(1) distance ($\simeq 2.75\mathring{A}$). One Ge and two O(1) and O(2), respectively, build up the GeO_4 tetrahedra. The stacking of the edge sharing CuO_6 octahedra and the corner sharing GeO_4 tetrahedra results in Cu^{2+} and Ge^{4+} chains parallel to the c axis. These chains are linked together via O atoms, and form layers parallel to the b-c plane which are only weakly coupled along the a axis. The unit cell contains two formula units of $CuGeO_3$ because of the alternating tilting of the octahedra along the b axis. Along the c axis the nearest neighbor (nn) coupling between the Cu^{2+} moments arises from superexchange via the O ligands located inbetween. The Cu-O-Cu bond angle of $\simeq 99^0$ leads to some peculiarities with respect to the magnetic exchange. According to the Goodenough-Kanamori-Anderson rules one would expect ferromagnetic exchange between (nn) Cu^{2+} moments [127]. However, one should be aware that these rules are based on the assumption that the σ covalent bonding between the partially filled d-shells of Cu^{2+} ions and the p orbital of the O ligand is most important. Therefore, these rules do not hold anymore if π bonding and/or d-d hybridisation become important. In fact, calculations and experiments show that an antiferromagnetic coupling is present along the c axis that is very weak [128, 129]. According to Khomskii and

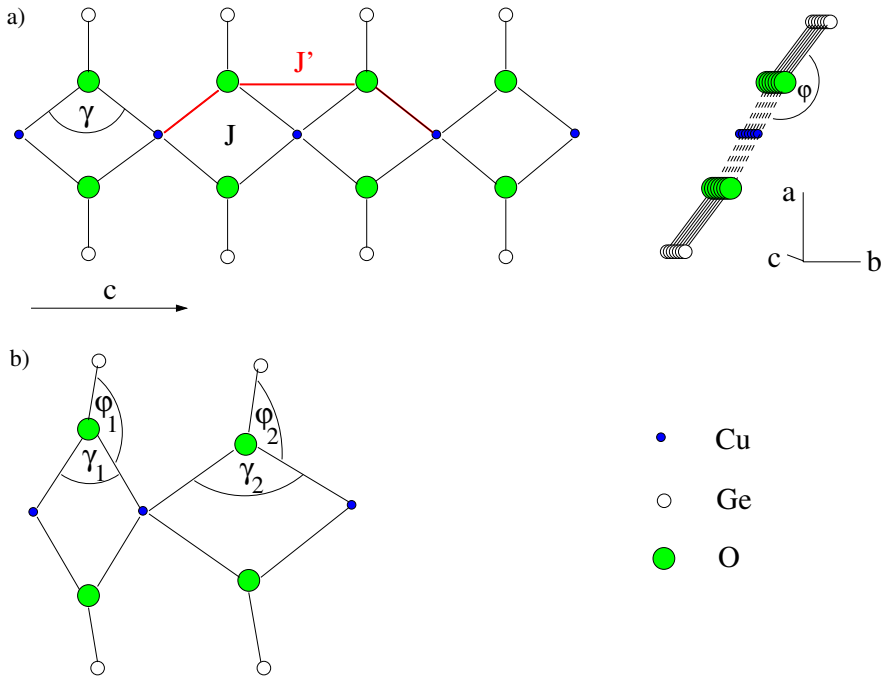

Figure 6.2: a) Undistorted chain segment. The coupling constant J denotes nearest and J' next nearest interaction. The Ge side group does not lie inside the Cu-O-Cu plane. At room temperature $\gamma \simeq 99^0$ and $\varphi \simeq 159^0$. b) Low temperature structure. For clarity the distortions have been strongly enlarged. In fact, the alternations of the *Cu-O-Cu*- and the Cu-O-Ge bond angles are very small: $\gamma_1 - \gamma_2 \simeq 0.8^0$; $\varphi_1 - \varphi_2 \simeq 1.8^0$.

Geertsma, the *Cu-O-Cu* bond angle of $\simeq 99^0$ is not sufficient to establish antiferromagnetic (nn) exchange interaction [128, 129]. They argued that the influence of the Ge-O is responsible for antiferromagnetic coupling. If one takes Hund's rule and the Pauli exclusion into account one understands qualitatively why the exchange interaction strongly depends on the geometry and the type of orbitals occupied.
Let us recall that for a Cu-O-Cu bond angle of $\simeq 180^0$ a strong antiferromagnetic coupling is observed, as for example in La_2CuO_4. Here, the single occupied $d_{x^2-y^2}$-orbitals of (nn) Cu^{2+} ions can only hybridize with one doubly occupied p-orbital of the O^{2-} ion. For a 90^0 Cu-O-Cu bond angle the $2p$ lobes of an oxygen ion cannot point towards two neighboring Cu^{2+} ions simultaneously. In this case a weak ferromagnetic exchange is favoured by gaining Hund's energy.
In the same manner, the influence of the Ge-O side group can be understood. Let us therefore assume two extreme cases where the side group lies exactly in or perpendicular to the Cu-O-Cu plane. The first case leads to a hybridisation of the p orbitals and thus to an antiferromagnetic exchange for all γ. If the Ge-O bond is orthogonal to the Cu-O-Cu plane, then the sign of the (nn) coupling remains unchanged. With respect to the above consideration, it is obvious that the antiferromagnetic coupling depends strongly on the angles φ and γ. Both, a larger φ and a larger γ increase the antiferromagnetic (nn) coupling. Interestingly, the γ dependence means that a larger distance between the Cu^{2+} moments results in a stronger coupling (see Fig. 6.2). For the (nn) coupling constant Geertsma and Khomskii specify $J_c \simeq 130$ K. In $CuGeO_3$, next nearest neighbor (nnn) coupling plays an important

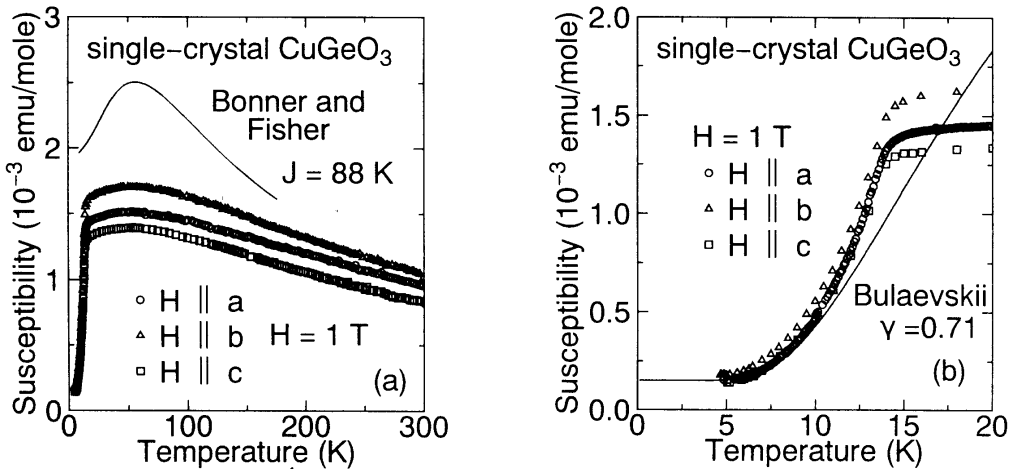

Figure 6.3: Magnetic susceptibility of $CuGeO_3$ [117].

role as there is a considerable overlap between the p orbitals of adjacent O atoms along the chain direction. Following Geertsma and Khomskii the ratio $J_c^{'}/J_c$ lies between 0.23 and 0.3. Lorenz et al. find experimentally a value of 0.35 for the ratio [130].
Finally a few words about (nn) superexchange interaction along a and b direction. As for the (nnn) interactions along the c axis there are two transfer paths with two oxygens along the b axis. However, along the b direction one finds a small exchange coupling constant $J_b \simeq 8$ K $\simeq 0.06 J_c$ [129]. There are two main reasons why the coupling constants $J_c^{'}$ and J_b differ so much. First, the angles and the bonding lengths are different for the b and c direction, respectively. Second, strong frustration of J_b occurs, because from one Cu^{2+} ion two exchange paths exist to two Cu^{2+} ions on the adjacent chains that are shifted by one lattice parameter along the c direction. In comparison with the b direction, the bonding lengths along the a direction are considerably larger. Therefore one expects an even weaker antiferromagnetism or a weak ferromagnetic coupling [126, 131]. Nishi et al. find in accordance with Regnault et al. for $J_a \simeq -0.01 J_c$, i.e., a weak ferromagnetic coupling.

6.2 The Spin-Peierls Transition in $CuGeO_3$

In Fig. 6.3 the magnetic susceptibility χ of $CuGeO_3$ is shown for all three crystallographic axes. The inorganic compound $CuGeO_3$ exhibits an isotropic drop of the magnetic susceptibility which typically signatures the spin-Peierls transition. For all directions χ drops below $\simeq 14$ K exponentially towards zero. The sharp drop is a result of the opening of a spin gap due to the formation of dimers. From the low temperature dependence of χ Hase et al. derived for the gap $\Delta \simeq 24$ K. The value is well in accordance with ESR [132–134], specific heat [135–144] and neutron scattering measurements [101, 145–151]. A closer inspection of the righthand panel in Fig. 6.3 reveals that for different directions of the magnetic field the transition occurs at slightly different temperatures. This can be attributed to different g-factors for different directions of the magnetic field. In the left panel the experimental data are shown together with a theoretical curve based on the theory by Bonner and Fisher for a one dimensional spin-1/2 chain with antiferromagnetic exchange interaction J between nearest neighbors. With the single parameter $J \simeq 88$ K the broad maximum of the experimental

data and theory coincide. Obviously, the model is too simplistic to describe the experimental findings qualitatively. Fabricius et al. have shown that a much better fit is obtained by taking significant frustration ($J^{'}/J = 0.35$) into account [36, 152, 153].
The second salient accompanying feature of the spin-Peierls transition is a lattice dimerisation that does not have to occur necessarily along the chain direction alone. It has been reported that in TTF-CuBDT there is also a lattice distortion perpendicular to the chains at the same time as the dimerization along the chains takes place [154]. In $CuGeO_3$, X-ray measurements and neutron scattering measurements observe the superlattice reflections below T_{SP}, supporting the dimerisation of the lattice [123, 124, 155]. The low temperature ($T < 14$ K) phase is characterized by an orthorhombic unit cell with lattice parameters $a^{'} = 2 \times a$, $b^{'} = b$ and $c^{'} = 2 \times c$. The distortion along the c direction leads to a splitting of the former O(2) sites in O(2a) and O(2b) sites with shorter O(2a)−O(2a)- and larger O(2b)-O(2b) distances. The doubling along the a axis is a consequence of the rotation of the GeO_4 tetrahedra around the c axis in opposite sense for neighboring tetrahedra. In Fig. 6.2 b) the distortion along the chain direction is shown. The relatively small changes of the angles are correlated with relatively small losses of elastic energy.

6.3 Magnetic Excitation Spectrum and Spin-Phonon Coupling

In view of the thermal conductivity measurements on $CuGeO_3$, the interesting question arises whether a sizeable magnetic contribution to the heat current may be present. In principle, any dispersive excitation can transport energy and add to the always existing phonon thermal conductivity of crystals.
The magnetic excitation spectra along the different crystallographic axes were determined by inelastic neutron scattering experiments [101, 148, 149]. The dispersion curves at 1.8 K and zero magnetic field are displayed in Fig. 6.4 for the b and c axis, respectively. As the curves were determined in the dimerized phase, the data represent the one triplet excitations that are separated by a gap Δ from the ground state and by $\Delta - 2B$ from the two triplet continuum [151]. From Raman scattering it is known that two triplets can combine due to mutual attraction to bound states leading to an energy reduction $2\Delta - 2B$, where Δ is the elementary gap for exciting one triplet and ($B \simeq 1$ K) the binding energy [156–163]. In comparision to the two-dimensional spin-gap system $SrCu_2(BO_3)_2$, the binding energy is almost negligible (see Chapter 5). Clearly, the dispersion along the c axis is about three times as large as the dispersion found along the b axis. Furthermore, even along the a axis a small but measurable dispersion is observed. This does not support the assumption that we deal with a purely one-dimensional, but rather with an almost two-dimensional spin system.
The energy minimum in the excitation spectrum can be identified with the formation of a singlet-triplet gap. Regnault et al. find for the gap $\Delta \simeq 2$ meV $\simeq 23$ K. The ratio $2\Delta/k_BT \approx 3.32$ coincides remarkably well with the BCS type mean field result ($2\Delta \approx 3.53 k_BT$). This is surprising since the temperature dependence of the gap does not at all follow an ordinary BCS-like gap, but is rather constant up to temperatures of $\simeq 12$ K and goes rapidly to zero when approaching the transition temperature [150]. A quantitative analysis is given by Nishi et al. with the result that even when the critical exponent in the gap equation is chosen to be very small, no agreement between experiment and BCS theory is obtained [101].
Let us turn to the determination of the exchange constants. The solid lines in Fig. 6.4 are theoretical curves based on calculations by Bonner and Blöthe for an ideal spin 1/2 alternat-

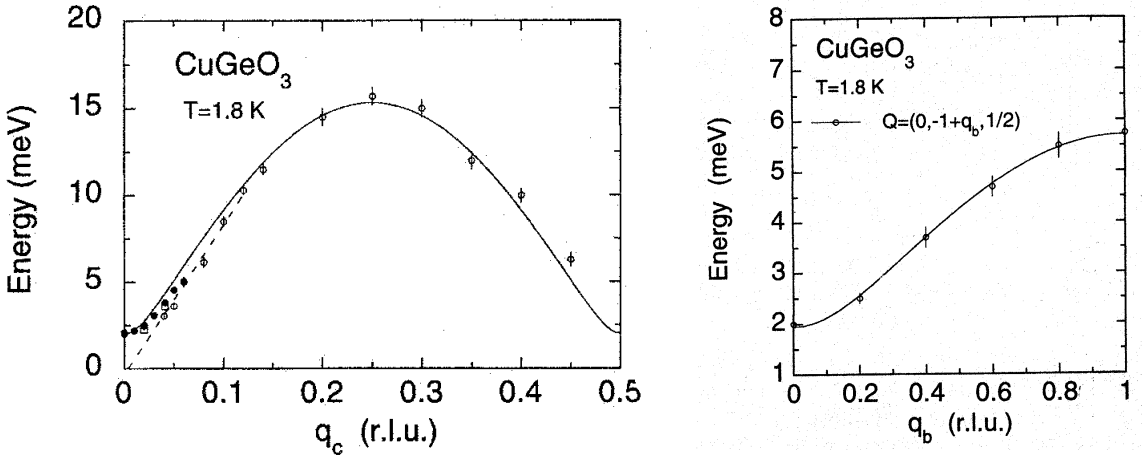

Figure 6.4: Magnetic excitation spectrum of $CuGeO_3$ along and perpendicular to the spin chains [149].

ing Heisenberg chain [164]. From the theoretical dispersion curve for the wavevector along the c axis, obtained under the assumption of (nn) coupling and no coupling perpendicular to the spin chains, Regnault et al. find for $J_c \simeq 120$ K, and $\delta \simeq 0.042$ for the distortion parameter. Using classical spin wave theory, the magnitude of $0.011J_c$ for the interchain coupling J_a and $J_b \simeq 0.11J_c$ is obtained. The dispersion curves for the wave vector along the b and c direction are shown in Fig. 6.4, respectively. The obtained coupling constants agree nicely with those found by Nishi et al. [101]. In spite of this, calculations based on different models reveal that the coupling constants cannot be determined unambiguously by fitting the dispersion curves [36, 165]. A closer inspection of the experimental curve in the left panel of Fig. 6.4 shows that the former is slightly tilted with respect to the theoretical curve. This was explained by G. Uhrig and W. Brenig taking the influence of the interchain coupling J_b into account [166, 167].

In $CuGeO_3$ the coupling between phononic and magnetic degrees of freedom play an important role leading to, e.g., anomalies in the elastic constants [168]. To simplify the calculations, most theories adopt an approximation where lattice dynamical effects are excluded.
In chapter 2 an introduction of the spin-Peierls theory, based on the results of Cross and Fisher, is given where the phononic system is treated adiabatically. Although a lot of experimental observations can be understood in this framework, e.g, the magnetic excitation spectrum and the susceptibility, the energy scales of the phononic and magnetic systems in $CuGeO_3$ are not clearly separated from each other and therefore the adiabatic treatment is not a priori justified. Moreover, in contrast to the conventional Cross-Fisher theory where the relevant optical phonon mode weakens and freezes out when approaching T_{SP} no phonon softening associated with the transition for the two spin-Peierls active T_2^+ phonon modes was observed [23]. Thus it was argued that the Cross Fisher theory does not cover the physics relevant in $CuGeO_3$ completely [169]. Gros and Werner showed that with an RPA approach a soft phonon does not necessarily have to exist [170]. Following their analysis, a softening of the active phonon and a displacive phase transition takes place if the bare frequency $\omega_0 < 2.2T_{SP}$. For higher frequencies an order-to-disorder transition occurs without phonon softening [171]. According to Braden et al., the frequencies of the two modes are $\omega_{0,1} \simeq J_c$ and $\omega_{0,2} \simeq 2J_c$

and no phonon softening is to be expected [23]. Finally, I want to point out that Uhrig et al. have treated the problem of spin-phonon coupling "the other way around", where the renormalisation of the coupling constant J by the phonons is considered [169]. Mainly two results are derived – first, no phonon softening occurs and second, the renormalisation leads to a sizeable magnetic frustration along the spin chains even if there is no frustration present in the absence of phonons.

6.4 Thermodynamic Properties of $CuGeO_3$

In this section a short review of the important thermodynamic properties of $CuGeO_3$ is given. First I will consider measurements of the specific heat, thermal expansion and magnetostriction. The analysis of the thermodynamic properties reveals the importance of frustration along the quasi-one-dimensional spin chains in $CuGeO_3$. Second, the H-T phase diagram will be discussed. Finally, important experimental results are compared with the prominent Cross-Fisher theory [130].

6.4.1 Specific Heat and Thermal Expansion

The specific heat of $CuGeO_3$shown in Fig. 6.5, was studied by R. Ziemes [143]. At the spin-Peierls transition a pronounced anomaly is observed at $T_{SP} = 14.35$ K for zero magnetic field. Below T_{SP} the system is in the dimerized phase and a spin gap in the magnetic excitation spectrum is present. Hence, one expects for the magnetic specific heat an activated behavior. Together with the common phononic contribution, the total specific heat in the low temperature region reads: $c_p = \beta T^3 + \Gamma exp(-\Delta E/k_B T)$. Fitting the data with the above formula yields $\beta = 0.3 mJ/molK^4$ and $\Gamma = 3.6 mJ/molK$. The obtained value for the spin gap $\Delta = 23$ K is in good accordance with the results from inelastic neutron scattering [101, 149]. Focusing on the specific heat curve at 16 Tesla, two striking features are detected. First, the transition temperature is drastically lowered ($T_{SP} \simeq 10\ K$) and the anomaly is not that pronounced anymore. Second, in the inset the low temperature region reveals an interesting difference between the specific heat for $H = 0$ Tesla and 16 Tesla. The 16 Tesla curve can be described rather well by a T^3-law whereas in zero magnetic field the exponential onset at the lowest temperatures dominates (as already discussed above). Phononic contributions do not depend on magnetic field. But in the incommensurate (I) phase so-called phasons are present that are excitations of the phase of the ordering parameter. According to Bhattacherjee et al. these quasiparticles can be regarded as three-dimensional continuous excitations with linear dispersion [172]. Similar to phonons (in three dimensions) a T^3-law for the specific heat is expected.
The thermal expansion $\alpha_i = \frac{1}{L_i}\frac{\partial L_i}{\partial T}$ for $H = 0$ and 16 Tesla is plotted in Fig. 6.6 [130]. As in the specific heat, huge and sharp anomalies at $T_{SP} \simeq 14.35$ K along the three crystallographic directions are visible. Along the a axis the anomaly is negative whereas, along the b and c direction the anomalies are positive. We might be tempted to think that the largest anomaly should arise along the spin chains, i.e., along the c axis. Obviously, this is not the case. The largest anomaly is along the b and the smallest along the c direction. This implies that the lattice distortions along the one-dimensional spin chains are in fact smaller than perpendicular to the chains. The influence of the magnetic field is very similar for all directions. The shift of the anomalies is accompanied by a lowering of about a factor of one-half compared to the zero field curves. To show rigorously that the structural anisotroy in zero magnetic

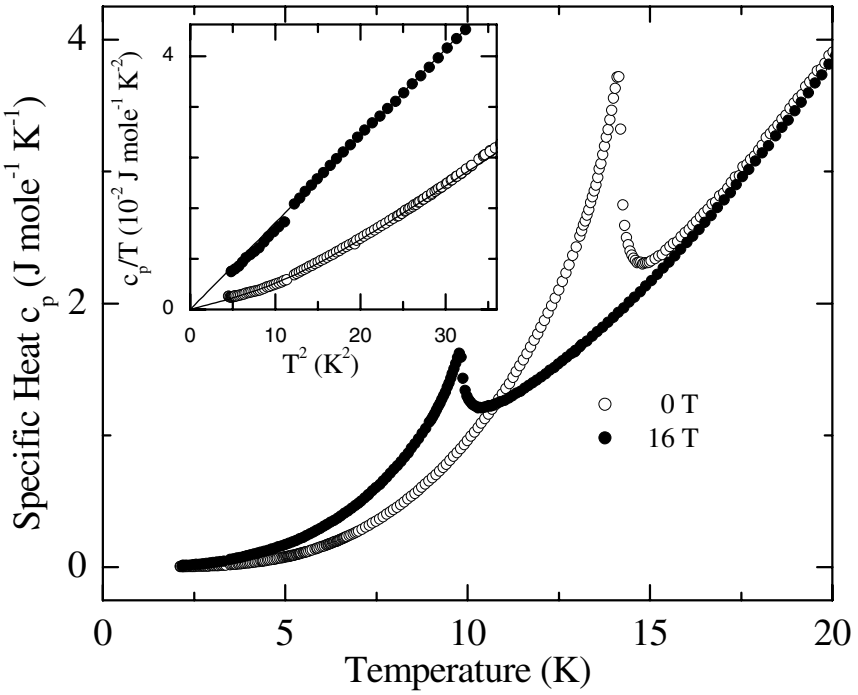

Figure 6.5: Specific heat of $CuGeO_3$ for $H = 0$ and 16 Tesla [143]. The inset shows c_P/T versus T^2. The solid lines are theoretical curves [130].

field and at 16 Tesla is the same, a reduced representation for the thermal expansion is given in the right panel of Fig. 6.6 [130]. Here, the assumption was made that the thermal expansion is a sum of the usual anharmonic phonon contribution and anomalies due to the spin phonon coupling [173, 174]. In order to obtain the anomalous contribution ($\delta\alpha_i$), Lorenz claimed that a substraction of the extrapolated curve (dotted line), representing the usual phonon contribution, from the experimental data can be done reliably. Obviously, the scaling is almost perfect for both the thermal expansion in the dimerized (H=0 Tesla) and in the incommensurate phase (H=16 Tesla). In conclusion, a magnetic field independent structural anisotropy is present in $CuGeO_3$.

6.4.2 Pressure Dependencies and Magnetic Frustration

Very interesting results have been obtained by analyzing the thermal expansion, the specific heat and the magnetostriction data within a phenomenological approach [175]. In order to obtain the uniaxial pressure dependencies of the transition temperature T_{SP}, the anomalies in the thermal expansion ($\Delta\alpha_i$) and the specific heat (Δc_p) data have been analysed making use of the Ehrenfest relation $\frac{\partial T_{SP}}{\partial p_i}|_{p_i\to 0} = T_{SP}\frac{\Delta\alpha_i}{\Delta c_p}$. The uniaxial pressure dependencies of $H_{D/I}$ are extracted using the Clausius-Clapeyron equation appropriate for analyzing the first order D/I-phase transition: $\frac{\partial H_{D/I}}{\partial p_i}|_{p_i\to 0} = \frac{\Delta L_i/L_i}{\Delta M}$, where $\Delta L_i/L_i$ is the jump along the i-axis and ΔM the change in the magnetization. The values are given in Table 6.1. To begin with, I want to emphasize that the uniaxial pressure dependencies are very large and reflect the structural anisotropy of the thermal expansion. Of all calculated values, the uniaxial pressure dependencies along the b direction are the largest followed by the a and c direction, respec-

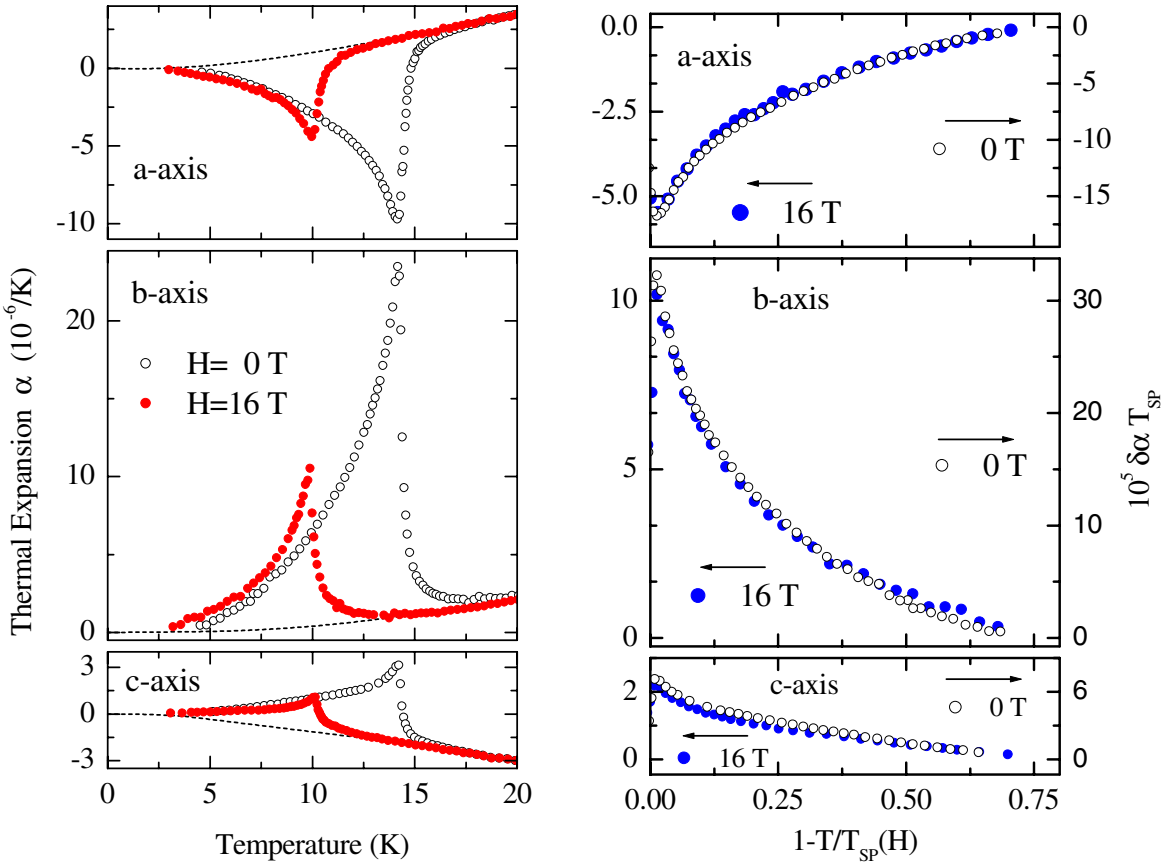

Figure 6.6: Left: Thermal expansion α of $CuGeO_3$ for $H = 0$ and 16 Tesla. Right: Scaling of α for the zero and 16 Tesla curve. Note: Zero Tesla corresponds to the right y-axis and 16 Tesla to the left y-axis, respectively [130].

tively. From the identical relative changes of the transition temperatures at $H = 0$ T and $H = 16$ T, Lorenz et al. claimed that only the absolute values of the U/D and U/I-phase boundaries change and furthermore the position of the phase boundaries is determined by T_{SP} alone [130]. Hence $CuGeO_3$ under pressure seems to reflect the universal phase diagram proposed by theory for a spin-Peierls system.
Let us now compare results of the magnetostriction $\Delta L_i/L_i$ of Fig. 6.7 [130] . The jumps

	U/D $H = 0$	U/I $H = 16$ Tesla	D/I $T = 4.5$ K
	$T_{SP} \simeq 14.35$ K	$T_{SP} \simeq 10.1$ K	$H_{D/I} \simeq 12.4$ Tesla
	$\partial T_{SP}/\partial p_i$	$\partial T_{SP}/\partial p_i$	$\partial H_{D/I}/\partial p_i$
p_a	-3.7 K/GPa	-2.8 K/GPa	-4 Tesla/GPa
p_b	7.2 K/GPa	5.3 K/GPa	7 Tesla/GPa
p_c	1.6 K/GPa	1.1 K/GPa	2 Tesla/GPa

Table 6.1: Uniaxial- and hydrostatic pressure dependencies of T_{SP} and of $H_{D/I}$ for the U/D–, U/I– und D/I–transition in $CuGeO_3$ [130].

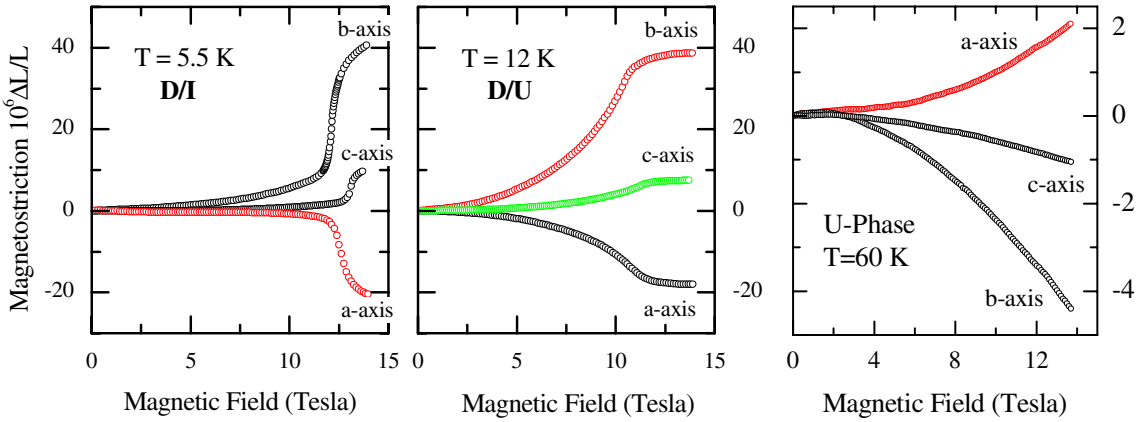

Figure 6.7: Left: Magnetostriction of $CuGeO_3$ at 4.5 K (D/I transition) and at 12 K (D/U transition). Right: Magnetostriction of the U-phase of $CuGeO_3$ [130].

crossing the D/I boundary clearly indicate a first order phase transition whereas a continuous D/U transition occurs. In the U-phase no anomalies are observed; the absolute values are about one order of magnitude smaller and sign changes take place. Based on the thermodynamic relation $\frac{1}{H}\frac{\partial \Delta L_i/L_i}{\partial H}|_{T,p_i} = \frac{\partial \chi_i}{\partial p_i}|_{T,H}$ one can extract the uniaxial pressure dependence of the magnetic susceptibility for different directions from the measured magnetostriction and compare these to the pressure dependence of the transition temperatures. A crucial result is the one to one correspondence between the pressure dependence of T_{SP} and χ in the U-phase. Within the conventional spin-Peierls theory, T_{SP} depends only on the spin phonon coupling and on ω_0 (see Chapter 2), but not explicitly on the exchange constant J. Lorenz et al. showed that an extended model that takes frustration along the spin chains into account, can explain the T_{SP} - χ correlation [130].
I want to sketch the basic results. The nnn coupling $J^{'}$ depends essentially on the O-O binding length. The compressibility along this axis is very small, leading to the assumption that the frustration ratio $J^{'}/J$ is essentially given by $-\partial \ln J/\partial p_i \simeq \partial \ln \chi^{max}/\partial p_i$. It becomes evident that the spin gap depends on both dimerisation and frustration [176]. A perfect modeling of the magnetic susceptibility succeeds for coupling constants $J = 160$ K and $J^{'}/J = 0.35$ up to 1000 Kelvin. For the same set of parameters the maxima of the susceptibility, thermal expansion and specific heat are reproduced. To conclude, frustration along the spin chains plays a crucial role in $CuGeO_3$ understanding its thermodynamic properties.

6.4.3 H-T Phase Diagram

From thermal expansion and magnetostriction, the phase diagram for $CuGeO_3$ is derived (see Fig. 6.7) [130]. From first sight the phase boundaries do not match exactly for the different magnetic field directions. This can be attributed to the different g-factors. The hysteresis found at the D/I-phase boundary shows the first order character of this phase transition. With increasing temperature, the hysteresis becomes significantly smaller and almost vanishes at the Lifshitz-Point (T_L, H_L) where the D/U-, I/U- and D/I- boundaries meet. According to Cross (T_L, H_L) is given by $gH_L/2T^0_{SP}$= 1.03 Tesla/K and T_L/T^0_{SP}= 0.77 [32]. From experiment, extracted values for $CuGeO_3$ are $g_i H_L/2T^0_{SP} \simeq 0.92$ Tesla/K and $T_L/T^0_{SP} \simeq 0.77$, respectively. To compare the experimentally obtained D/U- and I/U-phase boundary found for $CuGeO_3$

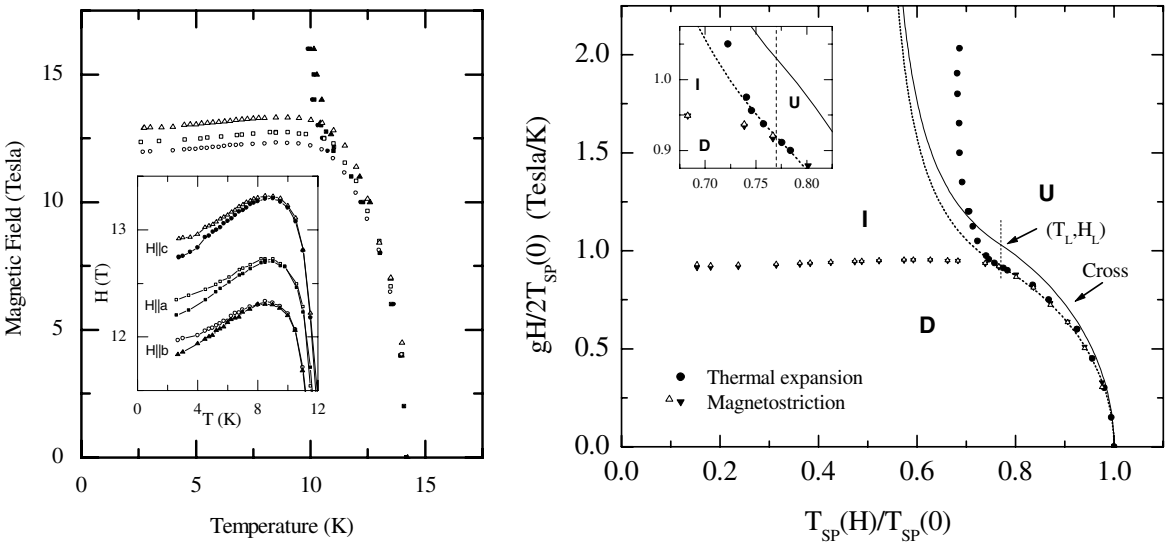

Figure 6.8: Left: H-T phase diagram for H parallel to the a, b, c axis, respectively. The phase boundaries are derived from thermal expansion and magnetostriction (with increasing magnetic field). The inset shows the hysteresis found by cycling the magnetic field (solid symbols: decreasing field, open symbols: increasing field. Right: Comparison of the experimentally found H-T phase diagram and the theoretical one (Cross [32]). The dotted line is obtained by dividing the solid line by 1.12. [130].

with the theoretical curve, a presentation in reduced units $g_i H/2T^0_{\rm SP}$ versus $T_{\rm SP}(H)/T^0_{\rm SP}$ is more convenient. Let us first consider the D/U-phase boundary. The calculated curve (solid line) and the experimental curve of $CuGeO_3$ are very similar to each other but do not match. Concerning the Lifshitz-Point (T_L, H_L) perfect agreement is achieved for H_L, while the theoretical value for T_L is about 12 % higher than the one found experimentally. An astonishing good theoretical modeling of the experimental D/U-phase boundary is achieved when dividing the solid line by 1.12. The dotted line meets exactly the experimental data. A plausible explanation is given by Lorenz et al. [130]. To calculate the phase boundary, Cross and Fisher used in their approach the susceptibility of an undimerized Heisenberg chain at $T = 0$ which is given by $\chi(T=0) = N_A g^2 \mu_B^2/\pi^2 k_B J_{eff} \simeq 1.5{\cdot}10^{-3}$emu/mol. Following Cross' suggestions one should rather use the measured susceptibility at the spin-Peierls transition ($\simeq 1.68 \cdot 10^{-3}$ emu/mol) in order to calculate the phase boundary. The comparison of the above two values for χ indeed gives the difference of about 12%. What about the I/U-phase boundary? Here, the mismatch between the Cross-Fisher theory and the results for $CuGeO_3$ is larger. Above $\simeq$ 23 Tesla ($gH/2T^0_{\rm SP} \simeq 1.7$ Tesla/K) the $T_{\rm SP}$ is for $CuGeO_3$ almost field independent and saturates at $\simeq 0.69{\cdot}T^0_{\rm SP}$. The Cross and Fisher theory gives us a much higher saturation field $gH/2T^0_{\rm SP} > 5$ Tesla/K and $T_{\rm SP}(H) = 0.5{\cdot}T^0_{\rm SP}$which can be essentially understood in the loss of one half of the Umklapp-energy for very large fields and hence to a reduction of $T_{\rm SP}$ of one half [24, 32]. Hence, it was noted by Lorenz et al. that frustration might become important explaining these discrepancies.

6.5 Thermal Conductivity of $CuGeO_3$

The following sections are devoted to measurements of the thermal conductivity on pure and doped $CuGeO_3$ single crystals. First, a review of measurements already performed on pure $CuGeO_3$ is given. Then my own results are presented, followed by a discussion. Second, the influence of Zn and Mg doping on the heat transport is presented.

6.5.1 Previous Thermal Conductivity Measurements on $CuGeO_3$

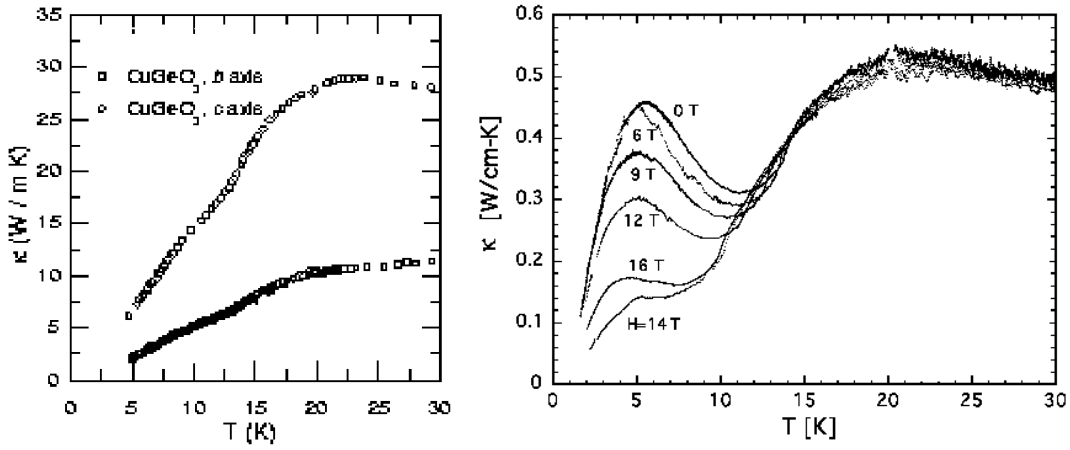

Figure 6.9: Left: Thermal conductivity of $CuGeO_3$ along the c and b axis in zero magnetic field, according to Vasil'ev et al. [64]. Only one maximum at $\simeq 23.3$ K can be observed. Right: According to Y. Ando et al. [63] an additional unusual peak in the thermal conductivity (κ) along the c direction can be seen at $\simeq 5.5$ K for zero magnetic field. Increasing the magnetic field the low temperature maximum is continuously suppressed. Note that for $T < T_{SP}$ the 16 Tesla curve lies above the 14 Tesla curve.

To my knowledge two research groups have published thermal conductivity measurements on single crystals of $CuGeO_3$.
The experimental results obtained by Vasil'ev et al. are shown on the left of Fig. 6.9. A broad maximum is observed at $T \simeq 23.3$ K and was assigned to a pure phonon contribution [64]. At the spin-Peierls temperature a small kink is visible that is attributed to the change of the properties of the lattice in conjunction with the opening of a spin gap. Along the b axis the absolute value of the thermal conductivity κ is about three times smaller with a less pronounced and even broader maximum at more or less the same temperature [64].
In the contrary, a very unusual behaviour for κ is obtained by Ando et al. (see right Fig. 6.9). Coming from high temperatures, κ increases and peaks at $\simeq 22$ K. Close to the spin-Peierls temperature κ drops rapidly. Lowering the temperature further, a second maximum arises at $\simeq 5.5$ K, finally dropping to zero. Switching on the magnetic field, the low temperature maximum is continuously suppressed by increasing the magnetic field. At 14 Tesla the peak has almost vanished. A new low temperature upturn emerges at higher fields (see right Fig. 6.9). Although the behavior near and above the spin-Peierls transition is similar to the thermal conductivity found by both groups, the salient low temperature peak is only observed by Ando and coworkers. They assumed that this discrepancy is related to the sample quality. In the following chapter, we will clarify the picture and show that the low

temperature maximum is evident. Furthermore, our systematic measurements of κ along the three crystallographic directions will reveal that the picture is much more complicated than proposed by Ando et al. [63].

6.5.2 Our Experimental Thermal Conductivity Results

In the upper panel of Fig. 6.10, the thermal conductivity κ_c as a function of temperature along the c axis in zero magnetic field is shown. Obviously, the measurements confirm the double peak structure found by Ando et al. [63]. The low temperature maximum is located at approximately the same temperature ($\simeq 5.5$) and peaks at an even higher absolute value. From this I conclude that the crystal is of high quality with only a moderate amount of defects and impurities. The high temperature maximum peaks at $\simeq 16$ K, i.e., close to T_{SP}. With further increasing the temperature κ_c drops down to about 20 W/Km at 50 Kelvin and decrease then almost linearly.
The striking feature of the strong suppression of the low temperature maximum with magnetic field is depicted in the inset of Fig. 6.10. Notably, the low temperature peak does not shift as a function of temperature, at least not for magnetic fields below 12 Telsa (in contradiction to $SrCu_2(BO_3)_2$(see Chapter 5)). We also observe that up to 14 Tesla , κ_c changes by about a factor of 3. Going to even higher fields κ_c increases again below T_{SP}. Above T_{SP} the absolute value of the thermal conductivity does alter only marginally with magnetic field. The position of the high temperature maximum with respect to temperature is not affected by the magnetic field. The results of the thermal conductivity along the c direction (κ_c) strongly resemble those found by Ando and coworkers [63].

The heat transport along the b direction is presented in the lower panel of Fig. 6.10. The double peak structure is observed as well, with the maxima occuring at around the same temperatures. But there are various differences to κ_c. Considering the zero magnetic field thermal conductivity, the absolute value of κ_b is about one third of the absolute value of κ_c over the entire temperature range. Above 50 Kelvin κ_b decreases approximately by 1/T with increasing temperature, whereas κ_c decreases almost linearily towards higher temperatures. Furthermore, almost no field dependence of κ_b for temperatures in excess of around 16 Kelvin is found (see inset of lower panel). And finally, a pronounced shift of the high temperature maxima with increasing magnetic field is observed. As for κ_c, the minimum shifts obviously to lower temperature with the field.

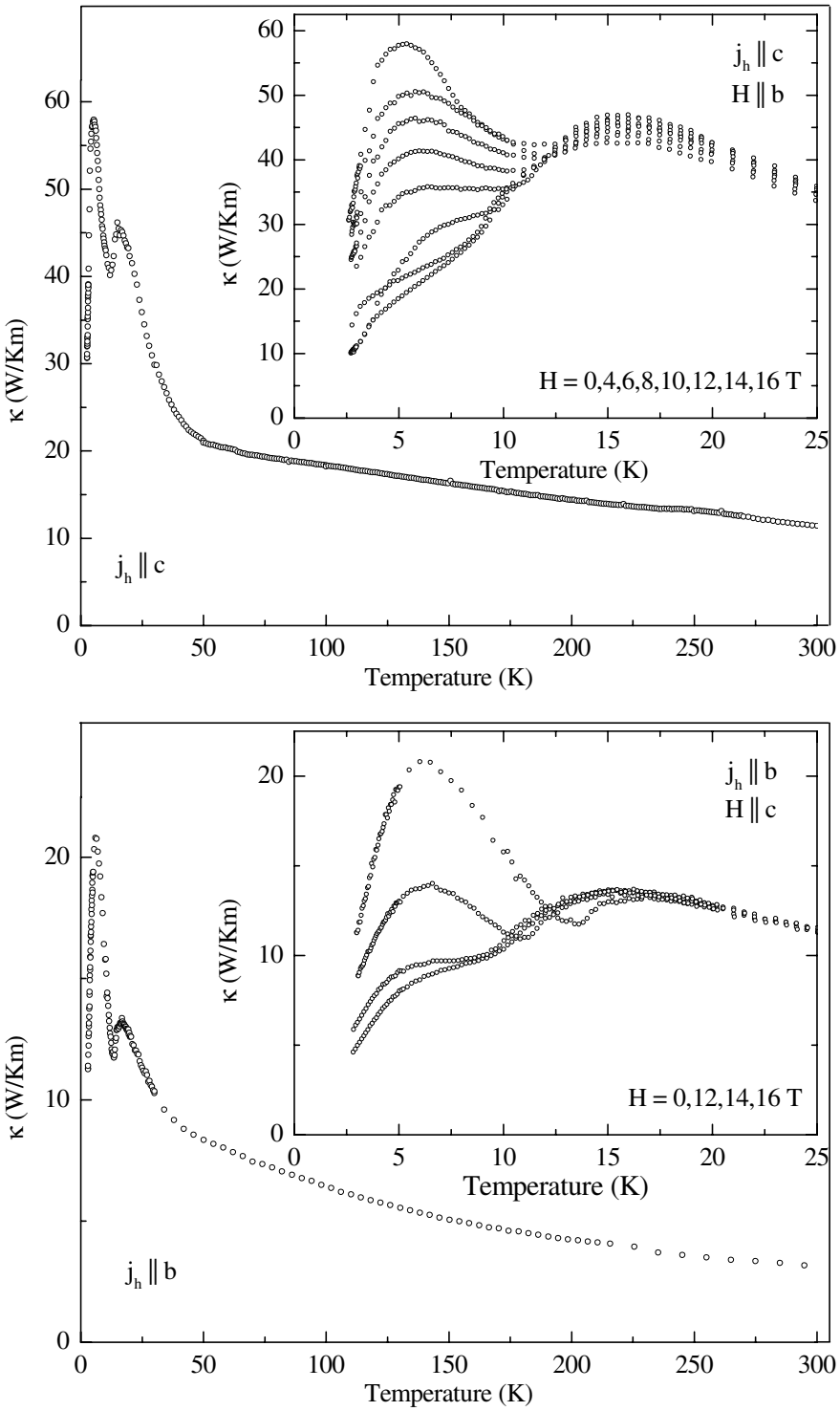

Figure 6.10: Upper panel: Thermal conductivity κ_c of $CuGeO_3$ along the c axis as a function of temperature in zero magnetic field. The inset shows the enlarged temperature region of κ_c for various magnetic fields. Lower panel: Thermal conductivity κ_b of $CuGeO_3$ along the b axis as a function of temperature in zero magnetic field. The inset shows the enlarged temperature region of κ_b for various magnetic fields. With increasing field the low temperature maxima are suppressed.

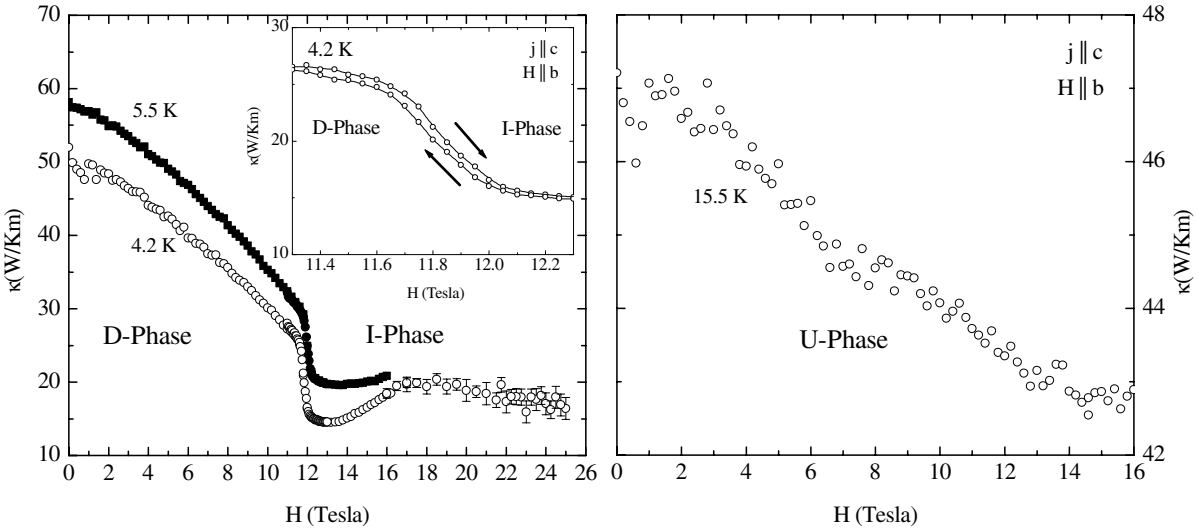

Figure 6.11: Left: Thermal conductivity κ_c of $CuGeO_3$ as a function of magnetic field at 4.2 (○) and 5.5 Kelvin (●). The high field measurements are marked by errorbars. The inset shows the enlarged region where the transition from the dimerized (D) to the incommensurate (I) phase occurs. By cycling the magnetic field forth and back a small hysteresis is observed. Right: Magnetic field dependence of κ_c at 15.5 Kelvin, i.e., in the uniform (U) phase.

The thermal conductivity versus magnetic field measurements are depicted in Fig. 6.11. In the right panel, κ_c is shown as a function of the magnetic field at a temperature of 15.5 K. This means, the system is in the uniform phase. Apparently, the magnetic field dependence of κ_c is marginally small. With increasing field the thermal conductivity decreases linearily. Going to lower temperatures, i.e., moving to the D/U-phase, the magnetic field dependence of κ changes drastically as illustrated in the left panel of Fig. 6.11. The transition from the D- to the I-phase can be clearly identified in the left panel of Fig. 6.11. For both temperatures, i.e., 4.2 K and the 5.5 K, κ_c decreases monotonically for fields up to 12 Tesla. A jump at about 12 Tesla is observed in the thermal conductivity, that can be related to the occurrence of the so-called incommensurate phase [177]. Above $\sim$ 12.5 K κ increases again. High field measurements were performed in a hybrid magnet system[1] to find out more about the heat transport in the I-phase. It seems that the thermal conductivity saturates at about 18 Tesla, whereas a small reduction for even larger magnetic fields is indicated. The errorbars result from vibrations of the watercooled electromagnet, causing induction voltages. Although the cryostat was mechanically decoupled from the water cooling system and the electromagnet, the small signal-to-noise ratio puts a severe constraint on high resolution measurements.
The inset of Fig. 6.11 shows the thermal conductivity in the vicinity of 12 T, i.e., close to the D/I-phase transition. Upon cycling the magnetic field, a small hysteresis, also found in the magnetostriction, opens up manifesting a first order phase transition.

In the following I want to check whether the anomalies in the thermal conductivity ver-

[1]This is a combination of a superconducting magnet and a electromagnet, generating fields in excess of 25 Tesla. For more details, see homepage of University of Nijmegen and The Nijmegen High Field Magnet Laboratory (HFML), The Netherlands.

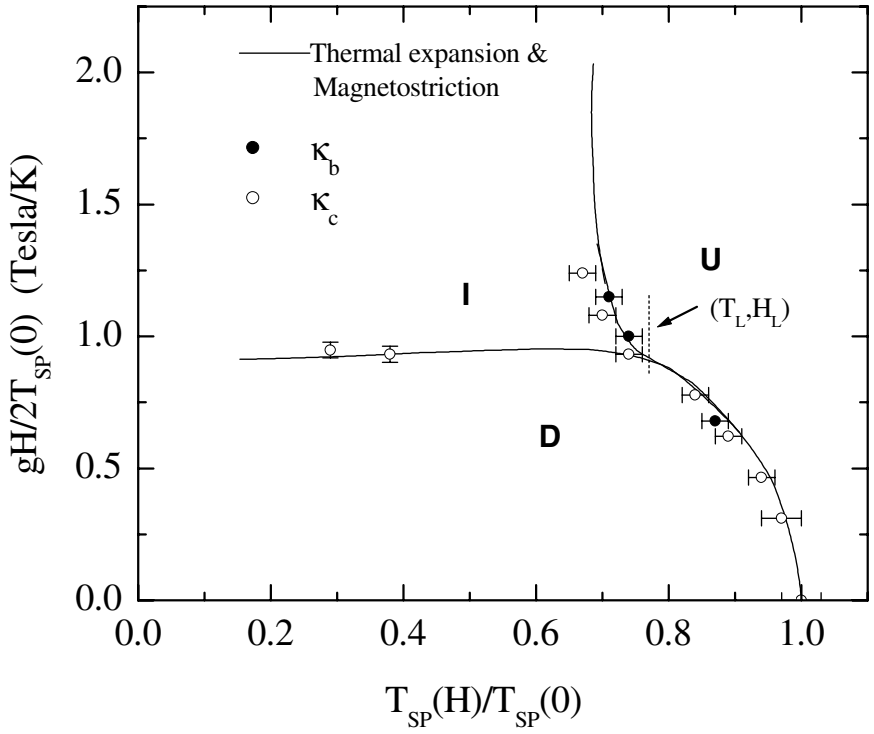

Figure 6.12: H-T phase diagram for $CuGeO_3$ in reduced units obtained by thermal expansion and magnetostriction [130]. The data points result from the analysis of κ_c and κ_b, respectively. The used g-values were 2.23 for the field along the b (κ_c) and 2.06 for the field along the c direction (κ_c).

sus temperature ($\kappa(T)$) and versus magnetic field ($\kappa(B)$) curves reflect the universal phase diagram for spin-Peierls systems. Therefore I consider the point of maximum slope of the thermal conductivity versus magnetic field curves at the D/I-phase transition (see Fig. 6.11 left), and the point of maximum slope of thermal conductivity versus temperature curves close to $T_{\rm SP}$.
A strong indication that this is indeed the case is given in Fig. 6.12. The phase boundaries obtained by measurements of thermal expansion and magnetostriction are plotted together with data extracted from the thermal conductivity, according to the procedure explained before. The agreement is stunning. The discrepancies reveal the experimental uncertainties of the quantitative analysis of the thermal conductivity data. However, the thermal conductivity measurements confirm the H-T phase diagram.

Before going into a detailed discussion of the findings, we complete the experimental data with the measurement of the thermal conductivity along the a axis (see Fig. 6.13). A completely different result is obtained. In contrast to the thermal conductivity along the b and c axis, only one broad maximum at $\simeq 32$ Kelvin is found in κ_a. Other remarkable points are the absence of any magnetic field dependence and the often cited $1/T$ dependence of κ at elevated temperatures prominent for phonons.
Let us finally note the anisotropy of the absolute values: $\kappa_b < \kappa_a < \kappa_c$, for temperatues above $T_{\rm SP}$, depicted in Fig. 6.13 (right). The inset of Fig. 6.13 clearly shows that we cannot address

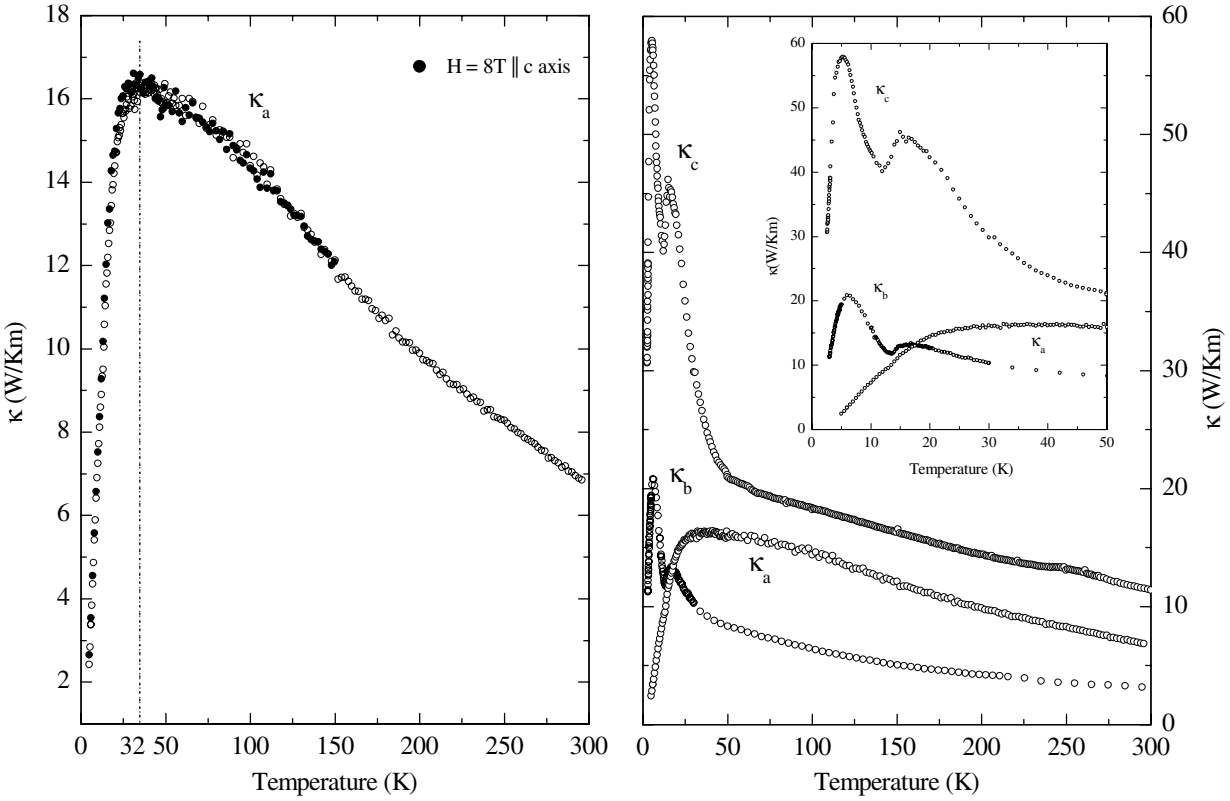

Figure 6.13: Left: Thermal conductivity of $CuGeO_3$ along the a axis for zero (○) and 8 Tesla (●). Right: Comparison of the thermal comductivities along the a, b and c direction. The inset shows the enlarged temperature region.

the maximum of κ_a to any of the maxima observed in κ_b or κ_c.
On the one hand, the thermal conductivity of $CuGeO_3$ shows pronounced double peak structures along the b and c directions which strongly depend on the magnetic field. On the other hand, only one maximum and no magnetic field dependence is observed for κ_a. The subsequent discussion will reveal a puzzling and complicated picture of the heat transport in $CuGeO_3$.

6.5.3 Discussion

The coming section will deal with possible scenarios explaining our experimental results and model calculations for magnetic heat transport and anisotropy considerations.

In principle we are faced with at least three different possible interpretations of the double peak structure of the thermal conductivity of $CuGeO_3$. As $CuGeO_3$ is an electrical insulator, we expect only two possible sources to the heat transport, namely a phononic and a magnetic contribution. Further on, we assume that the total thermal conductivity can be regarded as a sum of a magnetic and a phononic contribution, i.e., $\kappa = \kappa_{Ph} + \kappa_m$. This leads to the three scenarios depicted in Fig. 6.14.

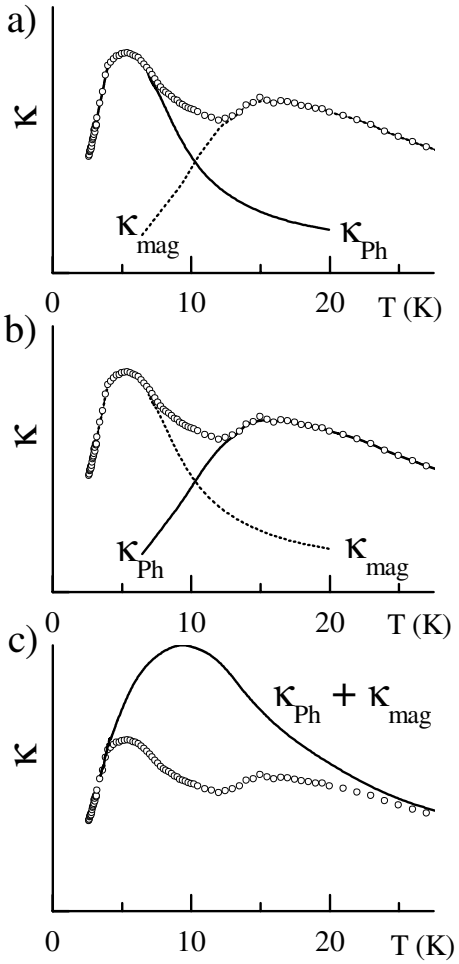

Figure 6.14: Different possible explanations for the double peak structure in $CuGeO_3$. a): Model proposed by Ando et al. [63]. Low temperature peak is essentially phononic, high temperature peak is mainly caused by magnetic excitations. b): Low temperature maximum is due to magnetic excitations, high temperature peak is attributed to phonons. c): There is one maximum due to phonons and/or "magnons" (solid line), suppressed by lattice fluctuations around T_{SP}.

Scenario a)

This model was already proposed by Ando et al. [63]. Based on measurements of the specific heat and the magnetic susceptibility, an interpretation of the double peak structure is given in terms of scattering of phonons on magnetic excitations for the low temperature peak, and a magnetic contribution is supposed to cause the high temperature maximum. Following their arguments this maximum is related to the peak in the magnetic specific heat at $\simeq J/2 \simeq 80$ K. They claim that the shift of the maximum in κ to lower temperatures with respect to the maximum in c comes from the fact that the mean free path of the magnetic excitations increases very rapidly when the temperature is lowered and overcompensates the decrease in the number density.
As no microscopic theories for the thermal conductivity in $CuGeO_3$ are available so far, Ando et al. base their assumptions on the kinetic approach where $\kappa \sim c \cdot v \cdot l$, with c the specific heat, v the velocity and l the mean free path of the magnetic excitations, respectively.
According to the kinetic approach, the magnetic field dependence of the low temperature maximum is explained as follows: as the spin gap opens below T_{SP} the number density of the magnetic excitations becomes so small that no magnetic contribution can cause the low temperature peak at $\simeq 5.5$ K. Hence, this peak is only caused by a phononic contribution.

The strong suppression of this peak with magnetic field is then understood by closing the spin gap due to Zeeman splitting, hence increasing the number of magnetic excitations results in a strengthening of "phonon-magnon" scattering.
But there are other plausible scenarios. Two scenarios which are likely to occur are discussed below.

Scenario b)

In this scenario the low temperature maximum is attributed to a magnetic contribution and the high temperature peak can be assigned to the conventional phonon heat transport. At first sight this is amazing, because below T_{SP} a gap opens and the magnetic excitations die out rapidly, i.e., the number density and hence the magnetic specific heat vanish. From this, one would expect no or at least only a very weak magnetic contribution to the heat current below T_{SP}. However, when we consider scattering among the magnetic excitations as the most important scattering mechanism, the relaxation rate und hence the mean free path l may become larger. Thus it appears that if the increase of the mean free path overcompensates the decrease of the number of excitations, then κ_m increases according to the semiclassical transport equation. The suppression of κ_m with increasing magnetic field follows then from the enhancement of the "magnon-magnon" scattering by closing the gap due to Zeeman splitting.

The occurrence of such a scenario is exhibited by two examples. B. Zeini and coworkers showed that in the $High\text{-}T_c$ superconductor $YBa_2Cu_3O_7$ where the heat transport is essentially carried by phonons (κ_{ph}) and electrons (κ_{el}), the maximum below T_c of the thermal conductivity along the superconducting planes must be substantially attributed to ${\kappa_{el}}^2$ [178]. In the superconducting phase the electrons combine to Cooper-pairs carrying no entropy. Thus the electronic heat transport is caused by the dynamics of quasiparticle (QP) excitations. An enhancement of the electronic thermal conductivity in the superconducting phase is possible if the increase of the mean free path overcompensates the decrease of the number of QP. To check this experimentally, a separation of the QP and phononic contributions to the thermal conductivity below T_c based on measurements of the longitudinal and transverse thermal conductivity (Righi-Leduc-effect) in high magnetic fields was performed. The data analysis shows explicitly that the QP contribution to the thermal conductivity is strongly enhanced below T_c and that the magnetic field dependence of κ can be attributed mainly to the magnetic field dependence of the QP contribution [61].

The second example is another fundamental system, namely ^3He which has been extensively studied both by theoreticians and experimentalists [180]. The prominent feature of superfluidity in ^3He was discovered by Osheroff et al. in 1972[3] [181]. Unusual new superfluid phases have been discovered involving spin triplet p-wave pairing, in contrast to the spin singlet s-wave pairing characteristic of metallic superconductors [182,183]. The present discussion of the thermal conductivity deals with the so-called B phase having an isotropic BCS-like energy

[2]Note that in conventional superconductors the thermal conductivity can increase or decrease depending on the excitations dominating the heat transport. If the electronic contribution dominates κ, a decrease in the thermal conductivity is observed. If the phononic contribution dominates the electronic contribution, an enhancement of κ is present, because of the extinction of the electrons below T_c. For a review see [178,179].

[3]I want to make the point that since ^3He atoms are fermions, the nature of the superfluid state of liquid ^3He is fundamentally different from that of liqiud ^4He. The transition in ^3He for example occurs at a temperature which is a thousand times lower than that for ^4He [180].

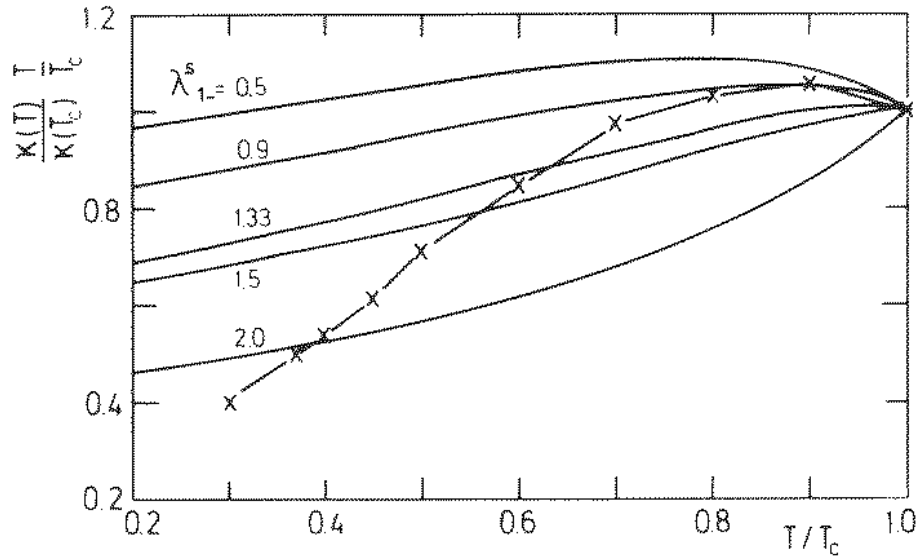

Figure 6.15: The calculated thermal conductivity of ^3He in the B phase in reduced units versus temperature at $P = 20$ bar (according to Einzel) ([180]) for different average scattering amplitudes λ^s_{1-}. Experimental data points ($\times$) obtained at 20 bar, according to Wellard et al. [180].

gap [182]. As the transport properties are thoroughly discussed in the textbook of Vollhardt and Wölfle [180] I will focus instead on the thermal transport property of the system. The thermal conductivity is seen to be

$$\kappa = \frac{1}{3} \cdot c \cdot < v^2 >_{th} \cdot \tau \ , \tag{6.1}$$

where c is the specific heat of the single-particle excitations, given by

$$c = \frac{\Delta^2}{k_B T^2} n_{ex} \ , \tag{6.2}$$

with n_{ex} the number density of excitations, Δ the energy gap, and k_B the Boltzmann constant. I want to remark that this is essentially the same expression found for the specific heat of s-wave pairing superconductors. The mean-square velocity $< v^2 >_{th}$ reads:

$$< v^2 >_{th} = \frac{k_B T}{\Delta} v_F^2 \ . \tag{6.3}$$

Finally, for the relaxation rate one has

$$\frac{1}{\tau} = A \cdot \frac{\pi^2}{6} \frac{\Delta}{\hbar} \cdot n_{ex} \ , \tag{6.4}$$

where the parameter A contains information about angular dependencies of the scattering amplitude [180]. Inserting Eqs. 6.2-6.4 into Eq. 6.1 we note that n_{ex} cancels out and κ can be written in the following form:

$$\kappa = \frac{v_F^2}{T} \cdot A^{-1} \cdot \frac{2\hbar}{\pi^2} \ , \tag{6.5}$$

yielding the remarkable result that $T \cdot \kappa(T)$ is approximately constant as found for normal Fermi liquids [184, 185]. Both experimental and theoretical curves (for certain λ^s_{1-}) show immediately below the transition temperature an enhancement of κ (see Fig. 6.15). At very low temperatures, however, the experimental curve falls below the theoretical results. This is explained by additional scattering effects not considered in the model calculations [180].

Scenario c)

Taking the speculations a step further, let us now turn our attention to scenario c) in Fig. 6.14. There is possibly only one maximum due to phonons and/or "magnons" that is suppressed in a narrow temperature scale caused by lattice fluctuations close to T_{SP}. As T_{SP} shifts to lower temperatures with increasing magnetic field, the low temperature peak is further suppressed. A similar model is successfully applied to the two-dimensional spin dimer system $SrCu_2(BO_3)_2$. For a detailed discussion, please refer to chapter 5.

Anisotropy Considerations

Unfortunately, it is very difficult to favour one of the proposed models based only on the experimental results. Therefore numerical calculations are discussed; a one-dimensional model for a magnetic contribution to the thermal conductivity, and anisotropy considerations, will be examined.

First, I will discuss the anisotropy considerations. Assuming a magnetic contribution to the heat current, we can then ask the question whether the anisotropy of the constantly present phononic contribution, differs from that of a possible magnetic contribution and hence allows us to discriminate these contributions.

Roughly, the thermal conductivity along the i-th ($i = 1, 2, 3$) direction can be simply estimated by $\kappa_i \approx c \cdot v_i \cdot l_i$. If one considers the case where we attribute the anisotropy of κ merely to the anisotropy of the velocities for different directions and assume an isotropic mean free path l, we obtain $\kappa_2/\kappa_1 = v_2/v_1$. This is actually only valid for the case of exactly one-dimensional dispersion relations. I will show that if we allow the energy spectrum to be two- or three-dimensional the theoretical results are rather different [111]. We use in analogy to former considerations the kinetic approach. The thermal conductivity along the i-th direction is given by the explicit expression:

$$\kappa_i \propto l_m \int_{BZ} \left(\frac{\partial \omega}{\partial k_i} \right)^2 \frac{1}{|\nabla_k \omega|} f(T, \omega) d^d k \ , \tag{6.6}$$

where $f(T, \omega)$ is the temperature and frequency dependent part of the integrand. Using the linearized dispersion relation Eq. 6.17[4] and retaining the angular dependent contribution only, we can rewrite Eq. 6.6 in the following form:

$$\kappa_i \propto \int_\Omega \frac{v_i^2 \left(k_i^2/k\right)}{\sqrt{\sum_{i=1}^d v_i^2 \left(k_i/k\right)^2}} \, d\Omega \quad with \quad k = \sqrt{\sum_i k_i^2} \ . \tag{6.7}$$

[4] We assume for simplicity that $\sin(k_i) \approx k_i$.

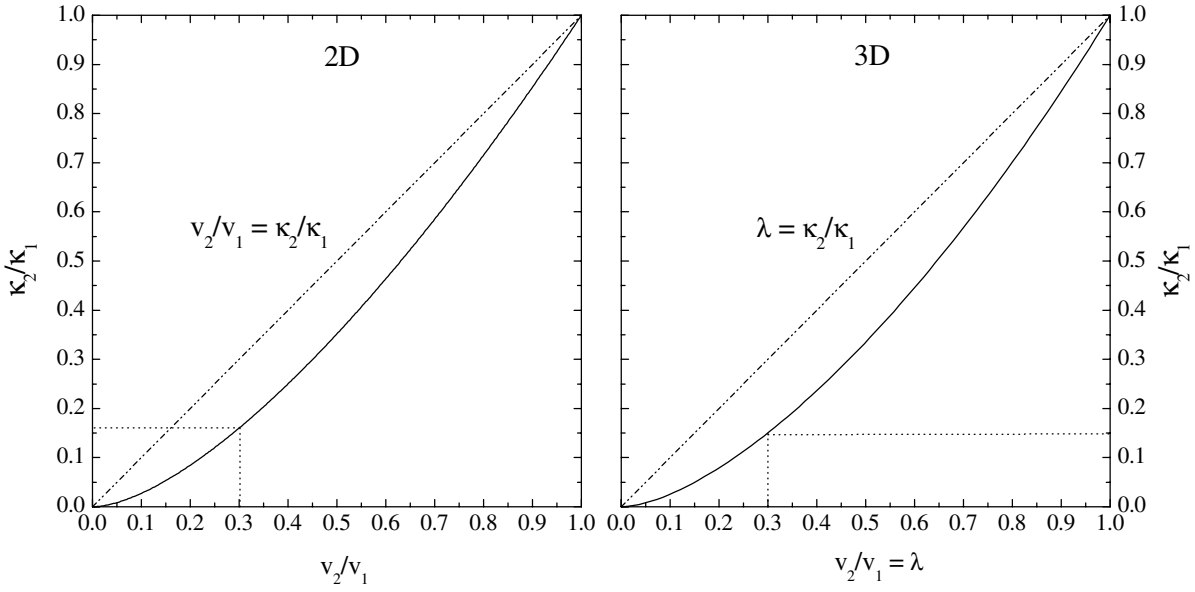

Figure 6.16: Thermal conductivity ratio (κ_2/κ_1) as a function of the velocity ratio (v_2/v_1) for the 2- (left) and 3-dimensional (right) case. For both, a ratio of $v_2/v_1 \simeq 0.3$ corresponds to $\simeq 0.15$ in the thermal conductivity ratio.

Here, k_i is the wave number for the i-th direction. In two dimensions ($d = 2$) it is straightforward to calculate κ_i and hence the ratio [111]:

$$\frac{\kappa_2}{\kappa_1}^{(2-d)} = \left(\frac{v_2}{v_1}\right)^2 \cdot \frac{\int_0^{2\pi} \frac{sin^2 d\phi}{\sqrt{v_1^2 cos^2\phi + v_2^2 sin^2\phi}}}{\int_0^{2\pi} \frac{cos^2 d\phi}{\sqrt{v_1^2 cos^2\phi + v_2^2 sin^2\phi}}} \; . \tag{6.8}$$

Before discussing this result I digress to the three-dimensional case. Commencing with Eq. 6.7 one gets with the constraint $v_1 = 1$ and $v_2 = v_3 = \lambda \leq 1$ the results for the ratio in three dimensions in a close analytic form [111]:

$$\frac{\kappa_2}{\kappa_1}^{(3-d)} = \frac{\lambda^2}{2} \frac{(2-\lambda^2) \cdot \ln(\frac{1}{\lambda}(\sqrt{1-\lambda^2}+1))/\sqrt{1-\lambda^2} - 1}{1 - \lambda^2 \ln(\frac{1}{\lambda}(\sqrt{1-\lambda^2}+1))/\sqrt{1-\lambda^2}} \; . \tag{6.9}$$

The results for both the 2- and 3-dimensional case are presented in Fig. 6.16. The thermal conductivity ratio κ_2/κ_1 as a function of the velocity ratio v_2/v_1 is plotted for the simple case (dotted straight line) where one-dimensional dispersions are assumed and for the cases where two- and three-dimensional energy spectra are allowed. Apparently, the 2-d and 3-d results differ only slightly. Only for $v_2/v_1 = 0$ and $v_2/v_1 = 1$ the velocity ratio and thermal conductivity ratio are equal for the 2-d and 3-d cases. Evidently, the thermal conductivity ratio is in general not proportional to the ratio of the velocities.
As a consequence one should be very cautious with anisotropy considerations. As long as the thermal conductivities along two different directions exhibit the same temperature dependence and differ only by their absolute values it is questionable if an unambiguous discrimination of phonon- and magnon-contributions succeeds.
It is worthwhile to point out another remarkable feature. According to Eq. 6.7, only the

derivative of the dispersion function $\omega(k_i)$ with respect to k_i is relevant for κ_i. Hence, one obtains the same results, irrespective of whether a constant gap Δ appears in the dispersion function. In other words, the same thermal conductivity ratio is obtained if one performs the calculation, e.g., for acoustic phonons (gapless dispersion) or for a system with a gap but the same k-dependence.

Concerning the measured thermal conductivities κ_b and κ_c of $CuGeO_3$, we find very similar temperature dependencies of κ_b and κ_c, whereas the absolute values differ by a factor ≈ 0.3. Let us consider the anisotropy of the phonon velocities. From ultrasonic measurements the sound velocities along the b and c axis are measured to $v_b \simeq 2400m/s$ and $v_c \simeq 7600m/s$, whence the ration for the phonon velocities $v_b/v_c \simeq 0.3$ is obtained [168, 186] .
From inelastic neutron scattering measurements the velocity ratio for the magnetic excitations can be deduced from the ratio of the bandwidths of the magnetic excitation spectra. Unfortunately, this ratio is also 0.3.
This means the ratio of the phonon thermal conductivities along the b and c direction is equal to the ratio of the possible 'magnon' thermal conductivities along the corresponding directions. This result is obtained irrespective of whether a one, two or three-dimensional dispersion relation is assumed. Thus, it seems to be unpromising that an experimental proof of the existence of a magnetic contribution in $CuGeO_3$ can be given via the anisotropy of κ_b and κ_c.

Let us now discuss the thermal conductivity along the a direction (see Fig. 6.13), plotted in Fig. 6.17. As the magnetic exchange coupling constant along the a direction is considerably smaller than along the b or c direction ($J_a \sim 0.01 J_c$) we do not expect any or only a very weak magnetic contribution to the heat transport. Hence, measuring the thermal conductivity along the a direction should give us more information and the possibility to decide whether a magnetic contribution to the heat current is present or not. In contrast to κ_b and κ_c, only *one* maximum is observed for κ_a.
Unfortunately, we cannot assign the single maximum of κ_a at $\simeq 32$ K to either of the maxima found in κ_c (κ_b) that are located at about 5 K and 15 K. This prevents a clear identification of an additional magnetic contribution and we are still left with the puzzling anisotropic transport properties of $CuGeO_3$[5].
However, the experimental findings are peculiar because no pronounced phonon maximum is detected, which is expected for clean crystalline insulators. As, however, no magnetic contribution is present, we attempted to model the experimental data by means of a Debye model for phonon thermal conductivity (see Chapter 3). The theoretical results are depicted in Fig. 6.17 (solid line). The parameter set used is shown in table 6.2. As the velocity

	L $[10^{-5}m]$	P $[10^{-42}s^3]$	U $[10^{-31}s^2/K]$	u
κ_a	1.2	2.49	1.8	12

Table 6.2: Fitting parameters for κ_a.

[5]Experimentally, The Righi-Leduc (Thermal Hall) effect allows the unambiguous separation of the phononic from the electronic contribution [61]. A similar method is, to my knowledge, not applicable in order to separate the phononic from a magnetic contribtution.

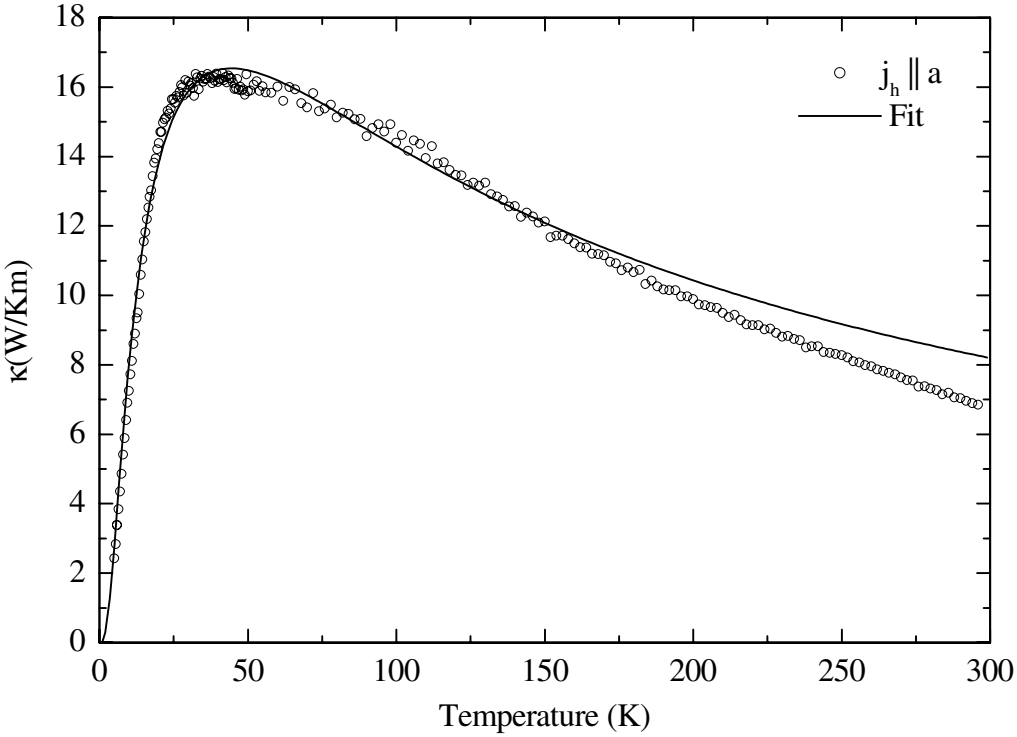

Figure 6.17: Thermal conductivity along the a direction. The theoretical curve is obtained using a Debye model for phonons.

($v \simeq 3600 m/s$) and the Debye temperature Θ_D ($\simeq$ 300 K) are fixed only four adjustable parameters remain. Up to $\sim$ 175 K experiment and theory agree nicely, at higher temperatures small deviations are found. The remarkable fact is that the characteristic length L, which is actually fixed by the sample geometry and should be of the order of 1 mm, has to be chosen two orders of magnitude smaller. This strongly supports the idea that scattering of phonons on additional defects suppress the prominent low temperature maximum found in the phonon thermal conductivity of single crystals. As $CuGeO_3$ cleaves very easily perpendicular to the a direction, sheet-like defects along this direction are likely to occur. Moreover, it is a well known fact that the phonon maximum in insulators decreases rapidly and shifts to higher temperatures with increasing defect concentration [78]. This is the most probable explanation of the uncommon thermal conductivity along the a direction in $CuGeO_3$.

The anisotropy considerations do not clarify the picture of the heat transport in $CuGeO_3$. Therefore, I want to study theoretically if either of the low temperature maxima could be of magnetic origin. First, a rough estimation of the mean free path necessary in order to produce a magnetic contribution to the heat current of the order 10 W/Km is made.

We estimate l from the kinetic expression $\kappa \simeq cvl$. The numerical value of v is extracted from the magnetic excitation spectrum [149]. One obtains the numerical value for the magnetic specific heat c based on the assumption that for c an activated behavior is to be expected in the D-phase with $c = \Gamma exp(-\Delta/k_B T)$ and $\Gamma = 3.6 J/molK$ [130]. One finds a large but reasonable value of $l \sim 7000$ $\AA$ in the dimerized phase (T $\simeq$ 6 K). Above T_{SP}, one can use

the theoretical values for c, calculated by Klümper et al. for a magnetic exchange constant of $J = 160$ K [153,187]. With the same value for v and κ used above, we find a meaningful mean free path of about 500 $\mathring{A}$ at 20 K. From these estimations it is evident that either maximum might be caused by a magnetic contribution.

Numerical Calculations

A straightforward model for the one-dimensional magnetic heat transport based on a kinetic theory will now be presented in order to get a more quantiative picture. We start with the kinetic expression for the heat transport which can be found in several textbooks [7, 51]:

$$\kappa_m = \frac{d}{dT} \sum_k v_k \epsilon_k l_k n_k \ , \tag{6.10}$$

where v_k denotes the velocity, ϵ_k the energy, n_k the distribution function, and l_k the mean free path. For simplicity we assume a momentum independent mean free path l_k. If we had no triplet dispersion the distribution function would read:

$$n_k = \frac{3 \cdot e^{-\frac{\hbar\omega}{k_B T}}}{1 + 3e^{-\frac{\hbar\omega}{k_B T}}} \ , \tag{6.11}$$

which is just the probability distribution of a two level system. The "3" of n_k accounts for the threefold degenerate triplet states. Accounting for the moderate dispersion of the triplets in $CuGeO_3$, the distribution function is slightly modified and reads:

$$n_k = \frac{3 \cdot e^{-\frac{\hbar\omega}{k_B T}}}{1 + 3z} \tag{6.12}$$

with

$$z = \left(\frac{1}{2\pi}\right)^d \int_{BZ} e^{-\frac{\hbar\omega}{k_B T}} d^d k \ , \tag{6.13}$$

where d denotes the dimension and BZ the Brillouin zone [188, 189]. The denominator is the partitition sum, where z takes the dispersion of the magnetic excitations into account. After inserting Eqs. 6.12 and 6.13 into 6.10 and some calculations one gets an expression for the magnon thermal conductivity:

$$\kappa_m = \frac{3 N l_m k_B^2}{\pi\hbar} T \int_{x_{min}}^{x_{max}} e^x \cdot \frac{x^2(1+3z) - 3xz'}{(1+3z)^2} dx \tag{6.14}$$

with

$$z' = \left(\frac{1}{2\pi}\right)^d \int_{BZ} \frac{\hbar\omega}{k_B T} e^{-\frac{\hbar\omega}{k_B T}} d^d k \ , \tag{6.15}$$

where $x = \hbar\omega / k_B T$, $x_{min} = \Delta / k_B T$ and $x_{max} = E_{max} / k_B T$. The number of spin chains per unit area is signified by N. The lower (Δ) and upper boundary (E_{max}) of the dispersion appear in the integral of Eq. 6.14, but for the one dimensional case, κ_m does not explicitly depend on the particular form of the magnon dispersion.

We assume two scattering channels, namely scattering of "magnons" by defects, or by sample

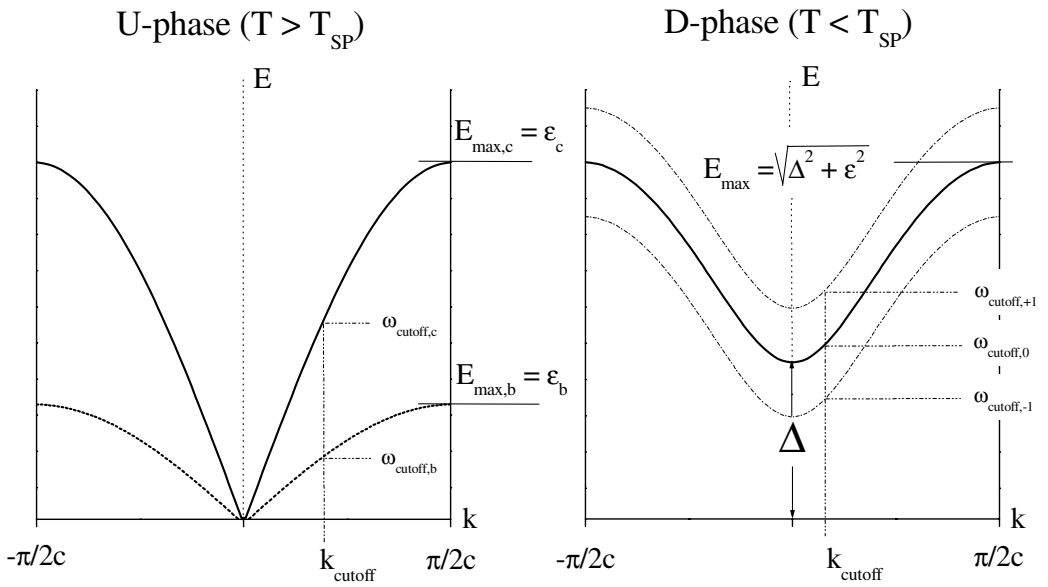

Figure 6.18: Left: One-dimensional dispersion relations in the U-phase for two different band widths $E_{max,b}$ and $E_{max,c}$. Note that the two curves correspond to the lower boundary of the spinon continuum, respectively (for comparision, see Fig. 2.5). Right: Dispersion relations in the gapped D-phase. The dotted lines (right) show the splitting of the triplet dispersion into three branches for finite magnetic fields $< 12\ T$.

boundaries, and "magnon-magnon" scattering. Due to the lack of theoretical models of the microscopic scattering processes in spin systems, we describe the former by a ω-independent scattering length l_0 and the latter by a density dependent length $l_{m-m} \simeq 1/n_{tot}$, where the total magnon density evident for scattering centers is given by

$$n_{tot} = \frac{1}{2\pi} \int_{BZ} n_k \cdot \Theta\left(\omega - \omega_{cutoff}\right) d^d k \ . \tag{6.16}$$

In contrast to κ_m (Eq. 6.14), n_{tot} depends explicitly on the form of the "magnon" dispersion $\omega(k)$. In the dimerized phase the dispersion is approximated by

$$\omega^2 \propto \Delta^2 + \sum_{i=1}^{d} (\epsilon_i \sin(k_i))^2 \ , \tag{6.17}$$

where ϵ_i and k_i denote the bandwidth and the wavenumbers, respectively[6]. In the uniform phase, Δ is set to zero. In analogy to the lattice thermal conductivity where the Debye temperature can be seen as a measure for the onset of Umklapp processes influencing the heat flow drastically, we introduce a cutoff frequency for "magnons" which corresponds to a definite wavevector k_{cutoff} in reciprocal space. Consequently, only those magnetic excitations with lengths of the wavevectors of about half the size of the magnetic Brillouin zone should participate in scattering processes hampering the heat transport. Evidently, the total scattering length l_m is: $l_m = (l_0^{-1} + l_{m-m}^{-1})^{-1}$.
To gain more physical insight let us consider the low temperature region ($k_B T \ll \hbar\omega$) where

[6] In our particular case: $d = 1$.

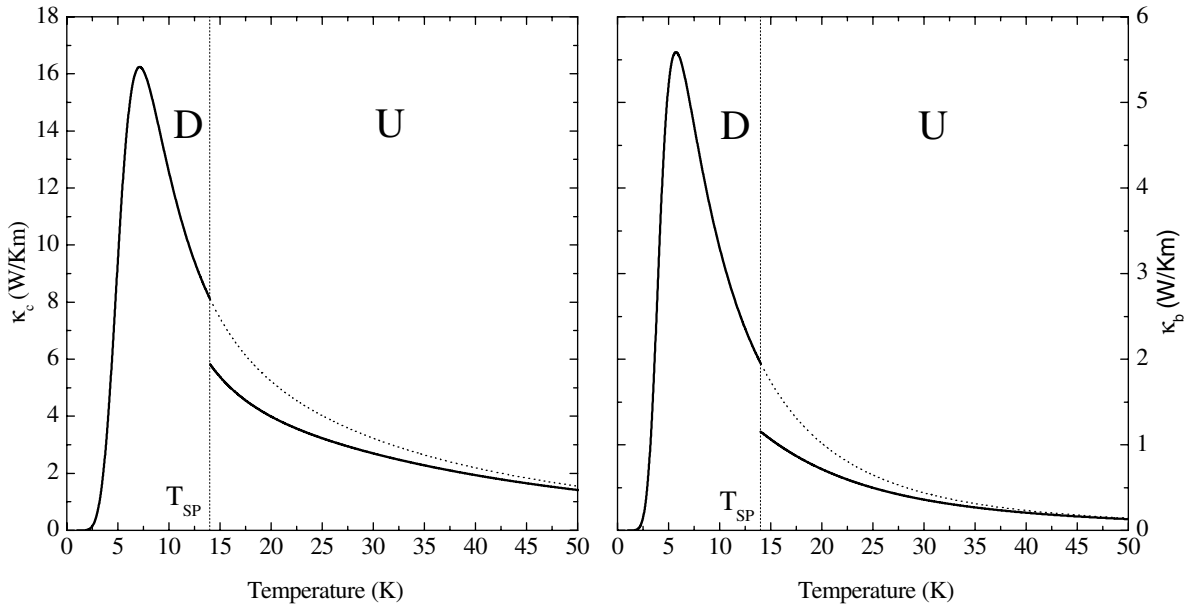

Figure 6.19: Hypothetical magnetic contribution to the heat transport for the D- and U-phase in zero magnetic field along b and c direction. For more details see text.

the above equations for κ_m and l_m simplify considerably [7]. A direct analytical form of the low temperature thermal conductivity is then achieved:

$$\kappa_m \simeq \frac{3Nk_B^2}{2\pi\hbar}\frac{\Delta^2}{T}e^{-\Delta/T}\cdot l_m, \text{ with } T \to 0 \ . \tag{6.18}$$

For the "magnon-magnon" mean free path we find

$$l_{m-m} \simeq \frac{\pi}{3}\sqrt{\frac{2}{\pi}}\frac{\hbar}{k_B}\sqrt{\frac{v^2}{T\Delta}}e^{\Delta/T}, \text{ with } T \to 0 \ . \tag{6.19}$$

Inspecting Eqs. 6.18–6.19, we get an idea what happens and we discover that two competing effects determine the heat transport. From Eq. 6.18 we learn that for $l_m = l_0$ the thermal conductivity κ_m drops exponentially to zero with $T \to 0$. The physical reason is the exponential extinction of the "magnons". Inserting Eq. 6.19 into Eq. 6.18, i.e., $l_m = l_{m-m}$, the thermal conductivity κ_m diverges with $1/\sqrt{T^3}$. This can be ascribed to the steep increase of the mean free path of the magnetic excitations with $T \to 0$.

We will now consider the predictions of the one-dimensional model with respect to heat transport along the crystallographic b and c directions, where a sizeable magnetic contribution may be expected for $CuGeO_3$. The exact numerical calculations were carried out by using Eqs. 6.12-6.16.
Before discussing the results it is necessary that the technical aspects of the calculation are unfolded. There are only two parameters to adjust, namely the mean free path l_0 and ω_{cutoff} (k_{cutoff}). The upper boundaries ($\sim$ 180 K and $\sim$ 70 K for the b and c direction, respectively) of the excitation spectra are extracted from neutron scattering results [149]. Thus

[7] For the sake of simplicity we neglect the cutoff frequency here.

ϵ_i of Eq. 6.17 is also unambiguously determined. We have to be cautious with the lattice parameters. In the dimerized phase we have to use $\tilde{b} = b/2$ and $\tilde{c} = 2c$, where b and c are the lattice parameters at room temperature[8]. The same lattice parameters must be used in the uniform phase, i.e., we calculate the magnetic thermal conductivity in the uniform and the dimerized phase for both directions with the dispersion relations illustrated in Fig. 6.18. For a moment one might be confused that the same value has to be used in the U-phase. The reason for this is the smallest size of the Brillouin zone has to be chosen for each phase. As no dimerization occurs along the b direction, the lattice parameter is fixed to $b = 8.468\mathring{A}$.
The calculations are now clear. Choosing the large but reasonable value $l_0 \approx 9000\mathring{A}$ and a rather small cutoff $k_{cutoff} \approx 0.1/c$, the thermal conductivity along the c direction in the D-phase is obtained for a spin gap Δ (= 24 K) with the appropriate parameters given before. The result is depicted to the left of Fig. 6.19. A large maximum close to 5 K is observed in the D-phase falling off rapidly towards higher temperatures (solid line). If we ignore the spin-Peierls transition, the dotted line would give us the correct thermal conductivity curve above T_{SP}. However, as the spin gap vanishes above T_{SP}, one has to set $\Delta = 0$ while keeping the other parameters fixed and has to repeat the calculation to obtain the correct κ_c in the U-phase (solid line). Evidently, a jump at T_{SP} occurs. Towards higher temperatures the curves show the expected behavior – they merge as the spin gap becomes comparably small with respect to the considered temperatures.
The same calculations are performed for the heat transport along the b direction, as illustrated on the left of Fig. 6.19. It is important to note that beside the upper boundary of the excitation spectrum and the lattice constant, no further parameters are adjusted. The results are comparable to those found for the c direction. In addition to the maxima at $\simeq 5$ K the thermal conductivity ratio is $\kappa_b/\kappa_c \approx 0.3$ which is well in accordance with experiment. It should be noted, however, that the anisotropy ratio κ_b/κ_c depends considerably on the cutoff frequency ω_{cutoff}. For slightly different cutoff frequencies, the model produces thermal conductivity ratios quite different from 0.3.

Next I attempt to model the magnetic field dependence of κ in the dimerized phase without introducing any further parameter. As depicted on the right of Fig. 6.18 the dispersion is split into three branches when applying a magnetic field. We can account for this by splitting the thermal conductivity into three components according to

$$\kappa_m = \frac{1}{3}\left(\kappa_{-1} + \kappa_0 + \kappa_{+1}\right) \ , \tag{6.20}$$

where κ_{-1}, κ_0 and κ_{+1} are calculated via Eq. 6.14 replacing $3z$ by $z_{-1} + z_0 + z_{+1}$, $3z^{'}$ by $z^{'}_{-1} + z^{'}_0 + z^{'}_{+1}$ (z_i, $z^{'}_i$ $(i = -1, 0, 1)$) arise from the lifting of the degeneracy by the magnetic field) and shifting the upper and lower integration limits by $-g_i\mu_B H$, 0 and $+g_i\mu_B H$, respectively. In the experiment, the magnetic field was aligned along the b direction while the heat current along the c direction was measured and vice versa. Hence, we use $g_b = 2.23$ and $g_c = 2.06$ [133, 190, 191]. As the magnetic excitations are expected to scatter on each other regardless of their s^z component the total mean free path in each component κ_i is replaced by

$$l_m = \left(l_0^{-1} + l_{m-m,-1}^{-1} + l_{m-m,0}^{-1} + l_{m-m,+1}^{-1}\right)^{-1} \ . \tag{6.21}$$

[8]The magnetic unit cell and the structural unit cell are different. According to the magnetic dispersions along the b and c direction (Fig. 2.5) we use $\tilde{b} = b/2$ and $\tilde{c} = 2c$, respectively. However, the results are not very sensitive to the lattice parameters chosen.

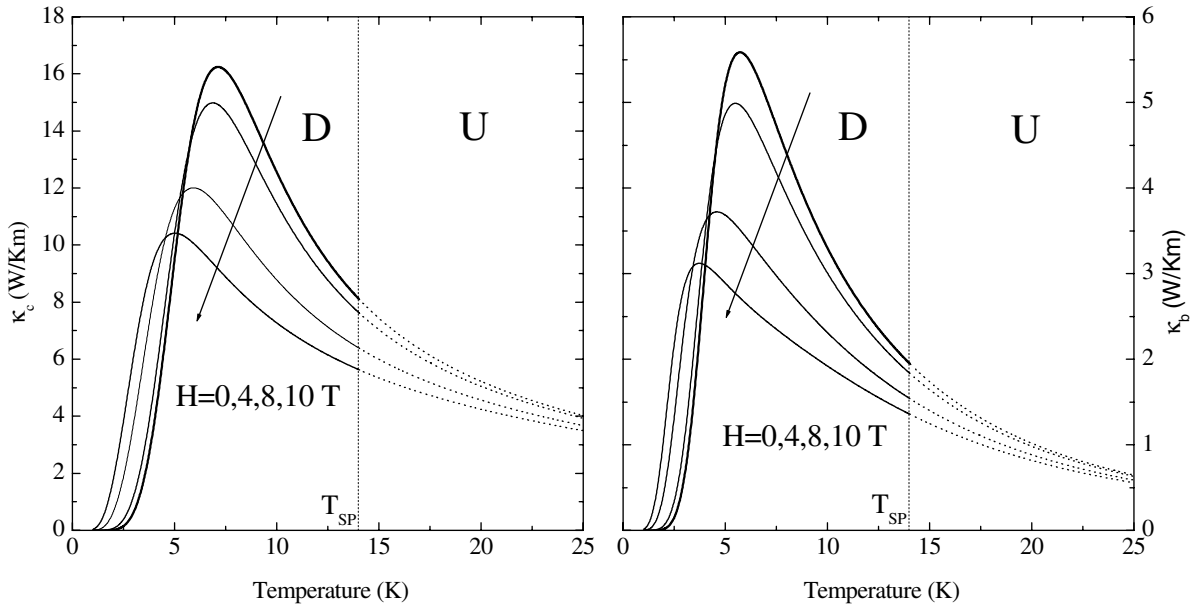

Figure 6.20: Calculated magnetic field dependence of the thermal conductivity in the D-phase along the b and c direction. For more details see text.

Eq. 6.21 implies an adhoc assumption concerning the cutoff frequency. As our model follows the standard theory for phonon heat transport where Umklapp scattering impinges considerably the heat current, we use a common cutoff momentum $k_{cutoff} \approx 0.1/c$ for the three branches (and not a common cutoff frequency) which corresponds to different cutoff frequencies, illustrated in Fig. 6.18 (right). Note, that the value of k_{cutoff} is the same used previously to generate the zero field data.

The thermal conductivity calculated for different magnetic fields is illustrated in Fig. 6.20. Evidently, with increasing magnetic field the maximum in the D-phase is strongly suppressed and shifted to lower temperatures for both κ_b and κ_c. This is caused by the subtle balance between the number of magnetic excitations contributing to the heat current and the "magnon-magnon" mean free path. With increasing magnetic field the spin gap becomes smaller leading to a drastic increase of the $s^z = -1$ "magnon" number density. This enhancement causes on the one hand a larger κ_{-1} contribution compared to κ_0 and κ_{+1}, which originates the shift of the total thermal conductivity towards lower temperatures and reduces on the other hand the total mean free path l_m and thus κ, which is more and more governed by $l_{m-m,-1}$.
Obviously, the calculated field dependence and the experimental observations do not agree very well. The model produces with reasonable parameters l_0 and ω_{cutoff} a sizeable low temperature maximum at around 5 K for both directions (κ_c) and (κ_b) with the correct anisotropy ratio. But the theoretically obtained field dependence of is too weak and the experiment clearly shows no shift of the low temperature peak of κ with increasing magnetic field.

Now the attempt is made to model the high temperature maximum for both κ_b and κ_c. The

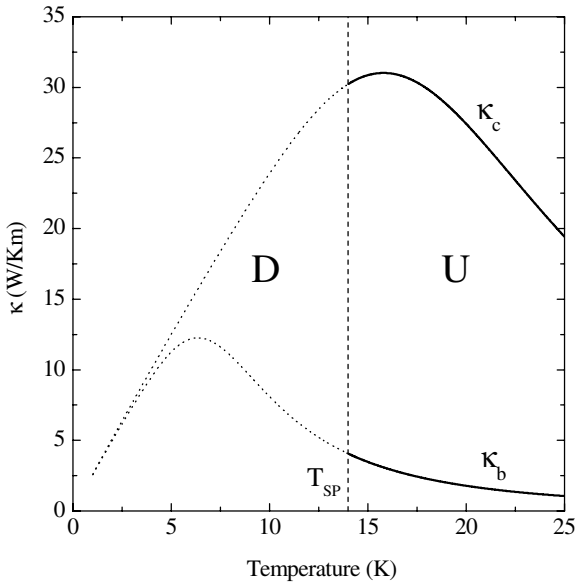

Figure 6.21: Calculated magnetic thermal conductivity in the U-phase for the heat transport along (κ_c) and perpendicular (κ_b) to the spin chains. The solid lines represent the scope of the 1-d calculations.

cutoff momentum k_{cutoff} can be varied between 0 and $\pi/2c$, as mentioned before. Setting $k_{cutoff} = 0.45/c$, $l_0 = 1700\mathring{A}$ and $\Delta = 0$ and keeping all other parameters for the heat transport along the c direction unaltered, a maximum in the undimerized phase at around 16 K can be produced with an absolute value comparable to that found in experiment (Fig. 6.21). Again, changing only the upper boundary of the excitation spectrum (E_{max} = 70 K) and the lattice parameter, we obtain the theoretical thermal conductivity along the b direction. Clearly, the model already fails here in reproducing the experimentally observed anisotropy κ_b/κ_c and the temperature dependence. Where does this come from? A closer look at the dispersion curve in Fig. 6.18 (left) gives us the answer. All excitations with momenta above the threshold k_{cutoff} are allowed to scatter thus hampering the heat transport. I want to remind the reader, that k_{cutoff} enters only into the mean free path. For very small cutoff k_{cutoff} momentum, the corresponding cutoff frequencies for the b and c direction are almost the same. For very large k_{cutoff} (here $k_{cutoff} = 0.45/c$ which is about one third of the half Brillouin zone) the corresponding cutoff frequencies and hence the corresponding temperatures are very different from each other. This and the exponential dependence of n_{tot} leads to the strong damping of κ_b in this case.

Summing up, the model considering "magnon-magnon" scattering only accounts for sizeable magnetic contributions of κ and produces for certain parameter sets (l_0, k_{cutoff}) the low temperature peak and the anisotropy in accordance with experiment. The value for k_{cutoff} of 0.1/c indicating the onset of Umklapp scattering is very small. One would rather expect much larger k-values for Umklapp processes to occur. The magnetic field dependence in the D-phase can to some extent be modeled without introducing any further parameter.
However, the model breaks down completely if one attempts to generate a maximum of the magnetic heat current along both the b and c direction in the U-phase, as observed in experiment. Finally, I want to remark that no improvement is achieved concerning the magnetic field dependence of κ by incorporating scattering of "magnons" on acoustic phonons.[9]

[9] I assumed that the phonon-magnon scattering length is inversely proportional to the phonon density n_{ph}. Using a three dimensional isotropic dispersion relation for the phonons n_{ph} can be calculated.

I want to come back again to the magnetic field dependence of κ_c in the D- and I-phase, that has already been raised in section 6.5.2. Recalling scenario (a) we attributed the low temperature maximum mainly to a phononic contribution. If this was so we could understand the field dependence, depicted in Fig. 6.11 in the following terms. In the D-phase, clear from previous discussions, κ decreases with increasing field monotonically due to scattering on magnetic excitations. The drop of κ close to the critical magnetic field H_{crit} could be due to a new scattering channel – namely scattering of phonons on the fluctuating soliton lattice [192]. Theoretical calculations show that at higher fields the structural modulation in the I-phase changes gradually from soliton-like to sinusoidal, which could explain the moderate enhancement of κ for $H \geq 13$ Tesla. Yet another possible mechanism in order for explaining the magnetic field dependence above $H \geq 13$ Tesla could be a resonant soliton-phonon scattering model. Such a model has been reported by Buijs and coworkers [193] for $(CH_3)_4NMnCl_3$ and $(CH_3)_2NH_2MnCl_3$. They showed that the substantial reduction of the thermal conductivity in these quasi-one-dimensional antiferromagnetic Heisenberg systems can be well understood by assuming solitons as the dominant magnetic excitations on which the phonons scatter. However, we also find a suitable description in terms of magnetic excitations (scenario (b)) as well. As the number of "magnons" increase with increasing magnetic field, the thermal conductivity goes down due to enhanced "magnon-magnon" scattering. Again, at H_{crit} the sharp decrease of κ might then be attributed to additional scattering on the fluctuating soliton lattice. The slight increase within higher fields can be explained using the same argument as above or might be possibly due to an additional contribution caused by excitations of the domain walls in the I-phase called phasons [63]. We conclude this section with the statement that the thermal conductivity of $CuGeO_3$ is very complex, its explanation remains controversial and no conclusion can be given so far.

6.6 Thermal Conductivity of Doped $CuGeO_3$

Within the scope of this section we study systematically the influence of Mg and Zn doping on the heat transport of $CuGeO_3$ along the crystallographic b and c directions.
In the first subsection an introduction about the doping effects on the spin-Peierls transition is given. Then thermal conductivity measurements on Mg and Zn doped samples as a function of temperature and magnetic field are presented. In the last subsection I discuss the results and a summary will be given.

6.6.1 Introduction

In $CuGeO_3$ there are two possible ways of doping. One can replace the Cu atoms by, e.g., Zn, Ni or Mg, i.e., it is doped directly into the spin chains or one replaces Ge, located between the spin chains, by Si. Both, in- and off-chain doping drastically influences the spin-Peierls transition.
A universal (x,T) phase diagram for various dopants obtained by magnetic susceptibility measurements is found (see Fig. 6.22) [194].
First, I will discuss the difference between in- and off-chain doping. At first sight it is astonishing that substituting Ge, not part of the spin chains, by Si is about 3 times more effective with respect to the suppression of T_{SP} than a substitution of Cu by Zn, Mg and Ni, which are part of the chains. An explanation why Si doping is more effective can be given on geometrical

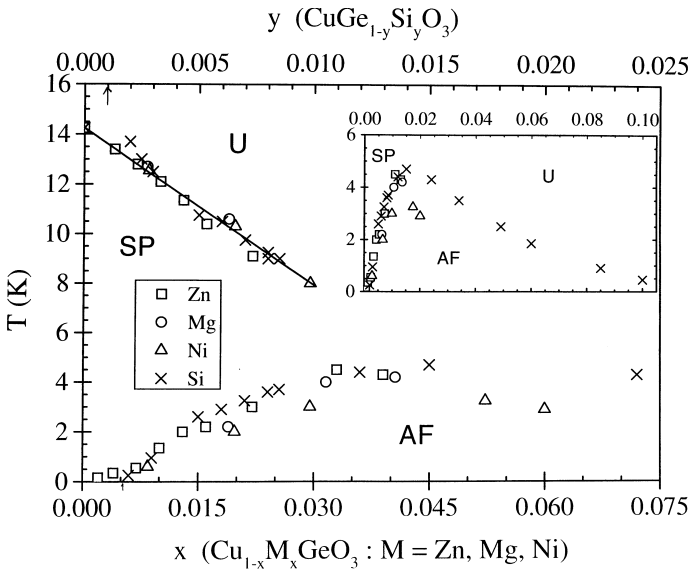

Figure 6.22: Doping dependence of T_{SP} and the Néel temperature T_N obtained by magnetic susceptibility measurements [194]. Note the different scale on the concentration axis for *Si* doping.

grounds.
It is known that the Cu-O-Cu superexchange path depends strongly on the hybridisation between the oxygen orbitals involved and the Ge orbitals [128]. Substituting Ge with the somewhat smaller Si leads to a considerable weakening of the magnetic next nearest neighbor exchange on two adjacent spin chains and therefore the replacement of Ge with Si should be a factor of 2 more effective than substituting the Cu atoms [128]. This can be understood qualitatively. The smaller Si pulls up the bridging oxygen and thus the Cu-O-Cu angle and the hybridisation of the O p-orbitals with the Si orbitals will be reduced leading to the weakening of the magnetic exchange. Therefore Si doping effectively interrupts the chains just as the substitution of the Cu atoms on the chains does. For a detailed review of antiferromagnetism in the dimerized and incommensurate phase in doped $CuGeO_3$, I refer to [195].

One of the most surprising feature is the occurrence of long range antiferromagnetic order for both doping directly into the spin chains (Zn, Mg, Ni on the Cu sites) and replacing Ge by Si. Moreover, the competing spin-Peierls and the Néel ordered state coexist in some interval of doping concentration [196–201]. Antiferromagnetic order and spin-Peierls transition mutually exclude each other as shown by several theoretical treatises of homogeneous systems [202, 203]. In disordered spin-Peierls systems, however, the theoretical studies show a possible coexistence of both states in agreement with experimental results [129, 204, 205]. Clearly, with increasing concentration, T_{SP} is drastically suppressed even for small amounts of dopants, while above a certain doping concentration no transition is observed anymore. Even for very small concentrations, the system can be driven into the Néel ordered state.
Manabe et al. reported susceptibility measurements on single crystals of $Cu_xZn_{1-x}GeO_3$ where even for extremely small Zn ($x = 0.99(8)$) concentration, antiferromagnetic long range order was found [206]. From the concentration dependence of the Néel temperature they inferred that any arbitrary small amount of Zn concentration favors the occurrence of the antiferromagnetic long range order. In the inset of Fig. 6.22 the concentration dependence of T_N is plotted. The highest T_N is still about 4 K lower than the lowest T_{SP}, hence coming from high temperatures first a spin-Peierls transition and then a Néel transition takes place.

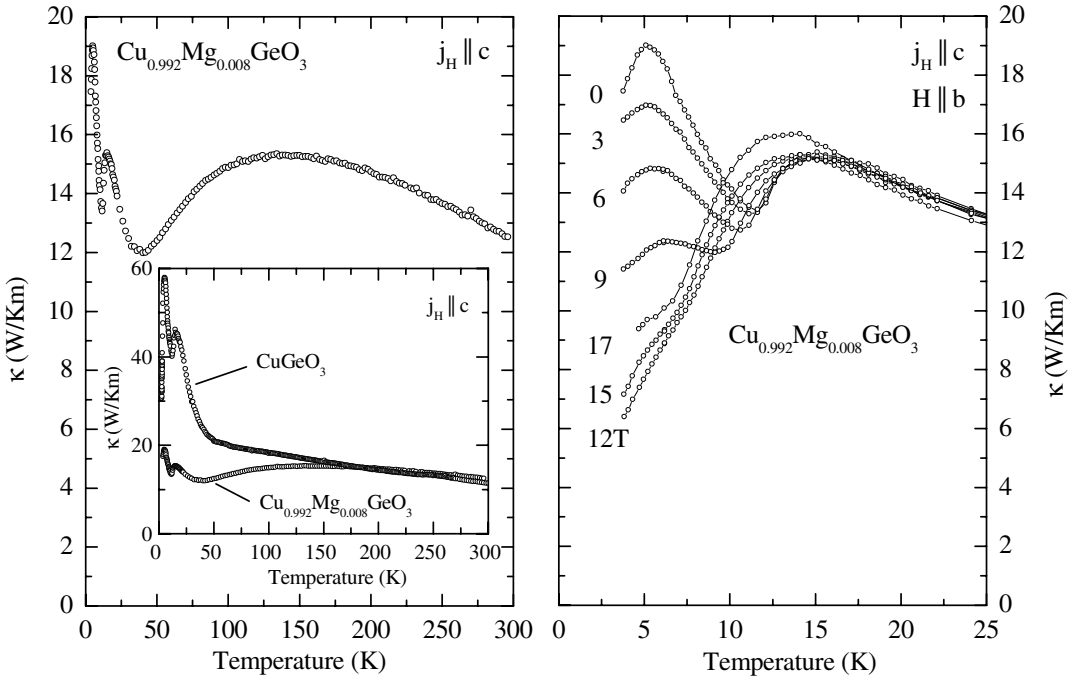

Figure 6.23: Left: Thermal conductivity κ_c of $Cu_{0.992}Mg_{0.008}GeO_3$ as a function of temperature along the spin chains in zero magnetic field. The inset shows the comparison to κ_c of undoped $CuGeO_3$. Right: Thermal conductivity κ_c of $Cu_{0.992}Mg_{0.008}GeO_3$ for various magnetic fields. The numbers denote the magnetic field strengths.

The Mg and Zn atoms substitute the Cu-atoms, i.e., one dopes directly into the spin chains, as already discussed before. Hence, both the phonon system and the magnetic system are influenced. On the one hand is is well known that the phonon thermal conductivity is very sensitive to impurities so that drastic changes in the phonon heat transport are expected [78]. On the other hand the spin chains are interrupted since the spin carrying Cu atoms are replaced by the nonmagnetic Mg or Zn atoms. Therefore an appropriate influence on the magnetic system concerning a possible contribution by magnetic excitations to the heat current is plausible.
Hence, I subsequently deal with the doping influence on the thermal conductivity in the hope of separating the phononic from a possible magnetic contribution to the heat current.

6.6.2 Experimental Results

Fig. 6.23 shows the temperature dependence of the thermal conductivity of $Cu_{0.992}Mg_{0.008}GeO_3$ along the spin chains. There are three distinct features attracting our attention. The first is the occurrence of an additional broad maximum at about 150 K besides the double peak structure at lower temperatures that is already known from undoped $CuGeO_3$. The second is the evidently smaller absolute value of κ at lower temperatures in comparison to undoped $CuGeO_3$ (see inset Fig. 6.23). Finally, the third speciality is the pronounced magnetic field dependence depicted on the right of Fig. 6.23. With increasing magnetic field the low temperature maximum is continuously suppressed while the maximum at around 15 K is slightly enhanced and shifted to lower temperatures. This is different from undoped $CuGeO_3$ where little field dependence of the 15 K peak is observed. In accordance with undoped $CuGeO_3$ the

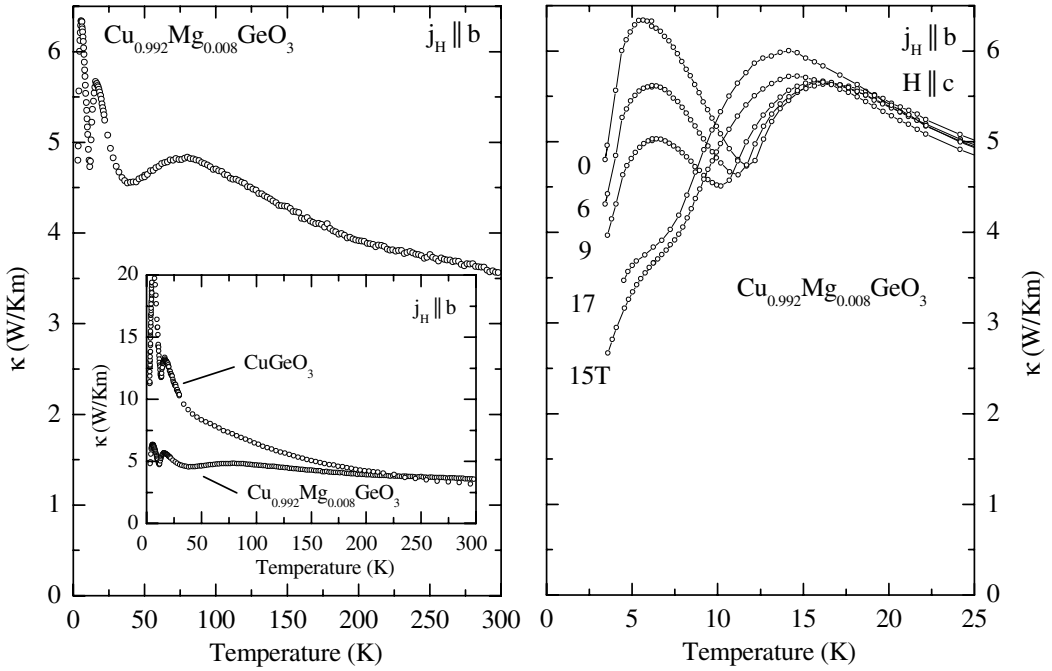

Figure 6.24: Left: Thermal conductivity κ_b of $Cu_{0.992}Mg_{0.008}GeO_3$ as a function of temperature along the spin chains in zero magnetic field. The inset shows the comparison to κ_b of undoped $CuGeO_3$. Right: Thermal conductivity κ_b of $Cu_{0.992}Mg_{0.008}GeO_3$ for various magnetic fields. The numbers denote the magnetic field strengths.

peak at ~ 5.5 K is not shifted to lower temperatures with increasing magnetic field. Note that the absolute values of the thermal conductivity curves obtained for magnetic fields of 15 and 17 T are higher than those found for a magnetic field of 12 T below ~ 15 K. Unfortunately, we cannot identify the Néel transition because it takes place below 2 K, i.e., below the lower temperature limit of our measurement device of ~ 2.2 K.

Takeya and coworkers reported measurements of the thermal conductivity on $Cu_{1-x}Mg_xGeO_3$ with x ranging from 0.016 to 0.040 along the c axis [119]. For the lowest doping concentration ($x = 0.016$) they observe the maintenance of the double peak structure of κ at lower temperatures as well. With increasing concentration of Mg the low temperature peak and its field dependence vanish rapidly while the maximum above T_{SP} is maintained up to the highest doping concentration ($x = 0.040$). At higher doping concentrations they are able to detect the Néel transition that is manifested in a slight change in curvature of the thermal conductivity versus temperature curve. Unfortunately, they show their data merely up to 30 K. Thus a comparision of the high temperature data with our observed broad maximum at about 150 K is not feasible.

For the thermal conductivity along the b direction a similar behavior is obtained for both, the temperature and the magnetic field dependence (see Fig. 6.24). Again, a low temperature double peak structure arises. But what is most interesting is the striking hump at about 85 K, seen on the left in Fig. 6.24.

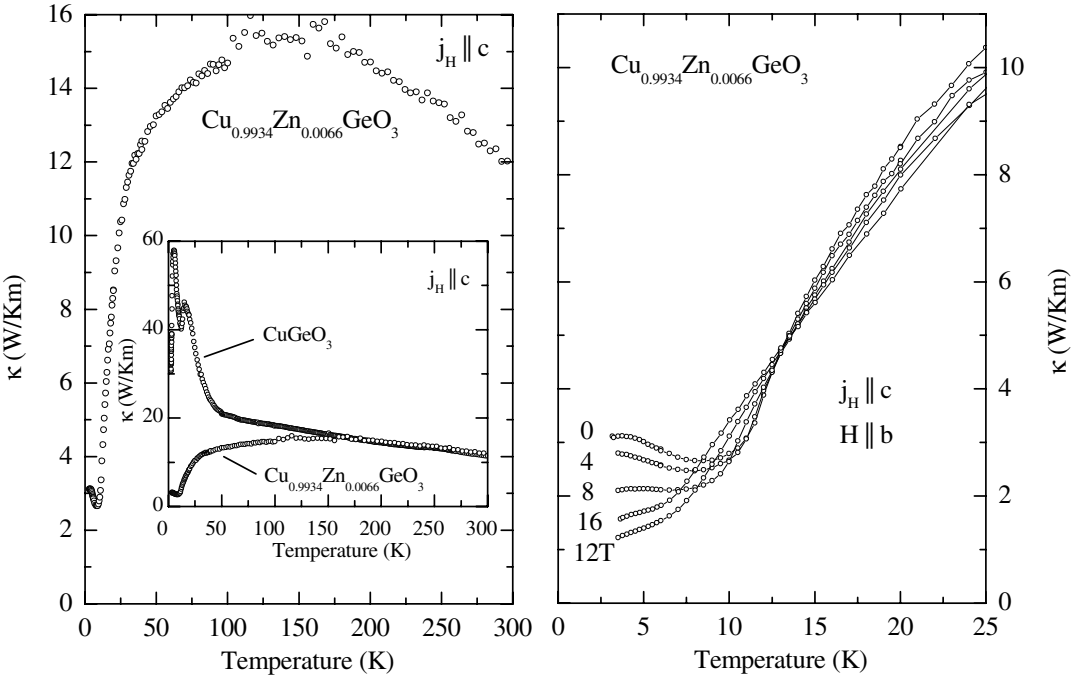

Figure 6.25: Left: Thermal conductivity κ_c of $Cu_{0.9934}Zn_{0.0066}GeO_3$ as a function of temperature perpendicular to the spin chains in zero magnetic field. The inset shows the comparison to κ_c of undoped $CuGeO_3$. Right: Thermal conductivity κ_c of $Cu_{0.9934}Zn_{0.0066}GeO_3$ for various magnetic fields. The numbers denote the magnetic field strengths.

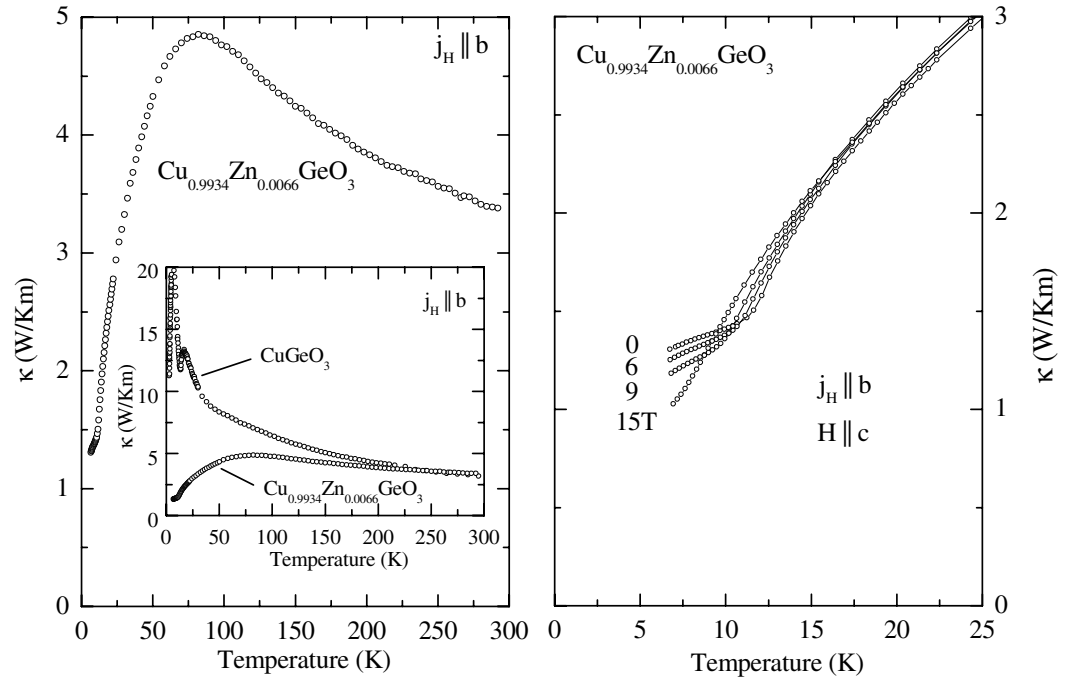

Figure 6.26: Left: Thermal conductivity κ_b of $Cu_{0.9934}Zn_{0.0066}GeO_3$ as a function of temperature perpendicular to the spin chains in zero magnetic field. The inset shows the comparison to κ_b of undoped $CuGeO_3$. Right: Thermal conductivity κ_b of $Cu_{0.9934}Zn_{0.0066}GeO_3$ for various magnetic fields. The numbers denote the magnetic field strengths.

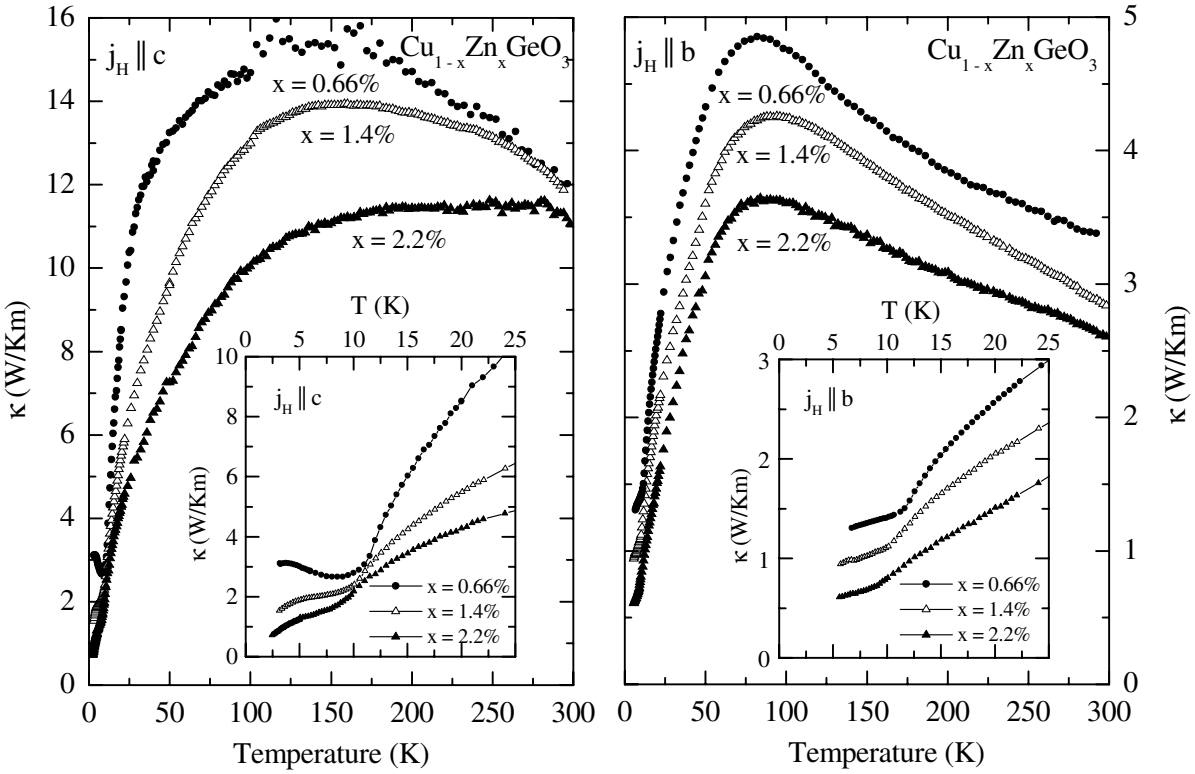

Figure 6.27: Thermal conductivity for three different Zn concentrations along the b and c-direction. The insets show the enlarged low temperature region.

Consistent with the measurements along the c direction, the damping from the substitution of Cu by Mg becomes transparent at low temperatures only (see inset Fig. 6.24). Remarkably, one finds the roughly the same thermal conductivity anisotropy ratio κ_b/κ_c (≈ 0.3) in $Cu_{0.992}Mg_{0.008}GeO_3$ as that observed in undoped $CuGeO_3$. For reasons already mentioned in section 6.5.2 and chapter 4, I did not attempt to measure the heat transport along the a direction.

The drastic effect of merely 0.66 percent Zn is shown in Figs. 6.25 and 6.26 for the heat transport along the b and c directions, respectively. Coming from high temperatures the thermal conductivity along the c direction increases and culminates in a broad maximum at ~ 150 K (shown in the left Fig. 6.25) as observed for κ_c of $Cu_{0.992}Mg_{0.008}GeO_3$. With further lowering the temperature κ_c falls at first smoothly and then drops down rapidly below 50 K.

The enlarged low temperature region, depicted in the right Fig. 6.25, reveals a broad minimum just below the spin-Peierls transition (~ 12.5 K) with a subsequent light increase and a plateau around 5 K for κ_c in zero magnetic field. The inset shows the comparison to the results obtained for the undoped sample. For temperatures above 150 K, the curves match almost perfectly, while at low temperatures the effect of Zn doping becomes obvious. The very small amount of Zn circumvents the formation of the double peak structure present in the undoped and the Mg doped sample.

The magnetic field dependence is similar to that found in $CuGeO_3$ and $Cu_{0.992}Mg_{0.008}GeO_3$. While still a significant magnetic field dependence of the order of 200 percent at ~ 5 K is

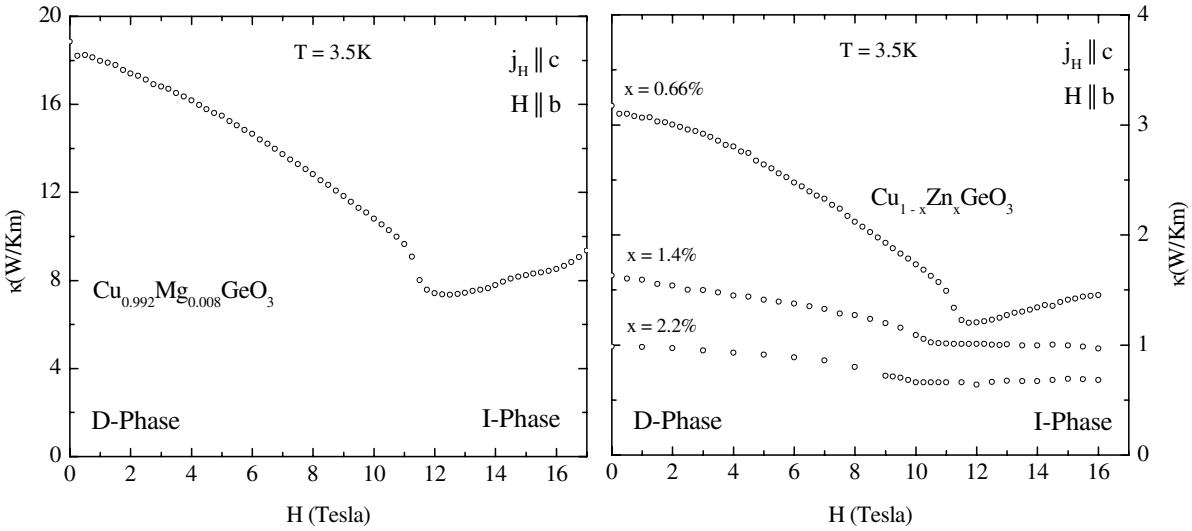

Figure 6.28: Left: Thermal conductivity κ_c of Mg and Zn doped samples as a function of magnetic field up to 17 Tesla at 3.5 Kelvin.

observed, the difference of the zero and 12 T curve above T_{SP} is merely about 10 percent and vanishes at higher temperatures.

The thermal conductivity along the b direction, i.e., perpendicular to the spin chains is signatured by a single maximum at about 85 K (see Fig. 6.26). Remember that we also observed such a maximum of κ_b for the Mg doped sample at about the same temperature. The low temperature behavior of κ_b does not distinguish very much from that of κ_c. Once again one finds a sharp reduction of κ with decreasing temperature. Moreover, the ratio κ_b/κ_c is about one-third over the entire temperature range, a result already obtained for undoped and Mg doped $CuGeO_3$.

I turn now to the influence of higher Zn doping, plotted in Fig. 6.27. We studied the concentration dependence of the thermal conductivity along the b and c direction by measuring in addition two samples with a Zn content of 1.4 and 2.2 %, respectively. With increasing Zn content the high temperature maximum of the thermal conductivity along the c direction becomes very broad and has almost vanished for x=2.2 %. Moreover, with increasing doping concentration the thermal conductivity resembles more and more the thermal conductivity of glasses, where κ is found to diminish monotonically with decreasing temperature [107]. The strong suppression of the heat transport in the vicinity of the spin-Peierls transition with relatively weak doping is shown in the inset of Fig. 6.27 (left). The weak upturn in κ of the $Cu_{0.9934}Zn_{0.0066}GeO_3$ sample alters drastically upon further doping. What remains is merely a slight change in the curvature of the thermal conductivity curve by increasing the Zn content to 2.2 %.

Next, I discuss the heat transport along the b direction, as illustrated in the right panel of Fig. 6.27. The continuous suppression of the thermal conductivity with increasing Zn doping is obviously present over the entire temperature range. In contradiction to the heat transport along the c direction, no crossing to a glassy-like behavior can be observed since all curves still show a pronounced maximum at about 80 K. The inset shows the conductivities of the three specimen in the vicinity of the spin-Peierls transition. Similar to κ_c, the sample with

lowest Zn content has the highest conductivity and an abrupt change of slope signatures the spin-Peierls transition. By increasing the Zn content the conductivity around the transition is strongly effected. It becomes more and more difficult to identify the transition as observed for the thermal conductivity along the c direction. As in the Mg doped sample no indications for a transition to long range antiferromagnetic order can be detected, not even for $Cu_{0.978}Zn_{0.022}GeO_3$, where measurements along the c direction were performed down to 2.5 K and where the Néel transition takes place at $\sim$ 3.5 K [194]. Obviously, one has to cover a larger temperature range to detect possible changes in the slope of the thermal conductivity curve, which seems to be very weak.
In order to study the magnetic field dependence below the spin-Peierls transition in more detail, the thermal conductivity is plotted as a function of the magnetic field for both the Mg and Zn doped samples in Fig. 6.28. The field dependence of the Mg doped sample as well as of $Cu_{0.9934}Zn_{0.0066}GeO_3$ resemble very much that of undoped $CuGeO_3$ depicted in Fig. 6.11. For these specimen we observe a continuous suppression with increasing magnetic field. At the D/I transition a sudden drop and a subsequent smooth increase with field are seen. But upon further Zn doping, the transition smears out and a plateau in the thermal conductivity, rather than an upturn of κ, is observed in the I-phase.

6.6.3 Discussion

The discussion in subsection 6.5.3 has already left us with a complex picture of the heat transport in undoped $CuGeO_3$. The experiments on Mg and Zn doped samples pose even new and more interesting questions:

1. Why are the experimental results of Zn and Mg doped samples so different in the low temperature region?

2. What causes the unusual temperature dependence of κ at higher temperatures ($T \geq 40$ K) which is manifested by an apparently linear decrease in undoped $CuGeO_3$ and by a minimum at $\sim$ 40 K followed by a broad maximum at around 150 K (85 K) for κ_c (κ_b) in $Cu_{0.992}Mg_{0.008}GeO_3$ which is also visible in the Zn doped samples?

3. Finally, do we really observe maxima due to additional contributions to the heat transport or do we actually have minima due to the scattering of phonons by magnetic excitations, or by structural instabilities, or vice versa, as sketched for $Cu_{0.992}Mg_{0.008}GeO_3$ in Fig. 6.29?

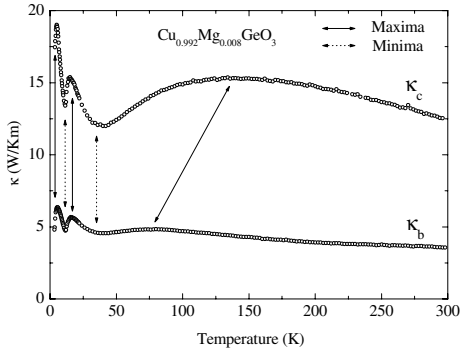

Figure 6.29:
Thermal conductivity of $Cu_{0.992}Mg_{0.008}GeO_3$ as a function of temperature along the b and c direction. The solid arrows indicate the maxima due to conceivable magnetic and/or phononic contributions. But the temperature dependence of the thermal conductivity could be also caused by minima, indicated by the dotted arrows.

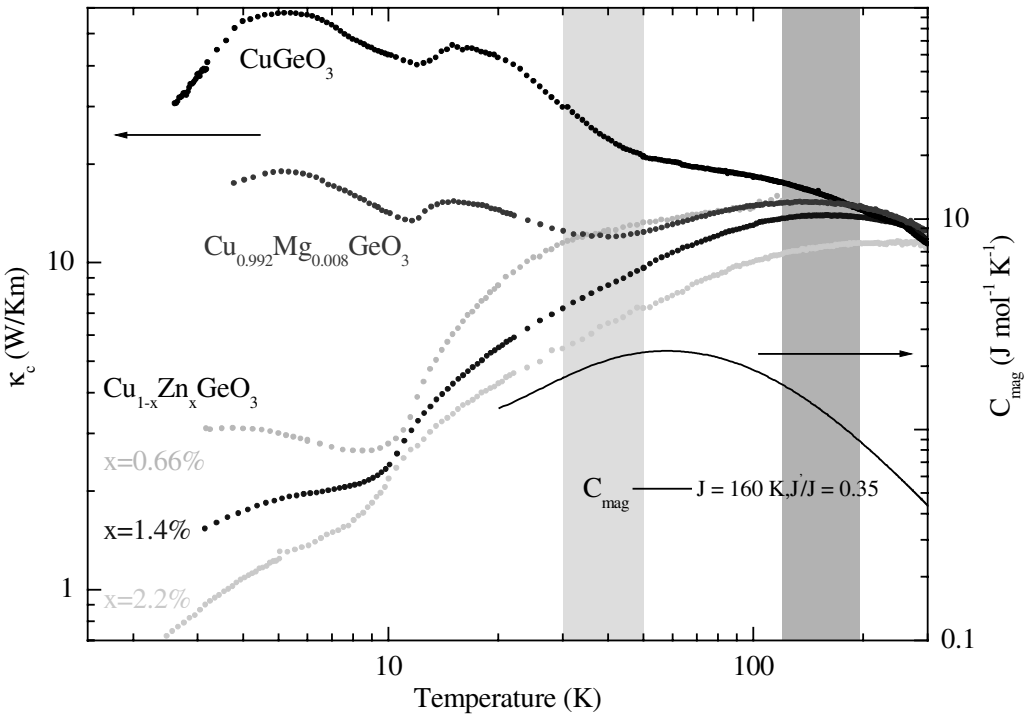

Figure 6.30: Compilation of the thermal conductivity measurements on undoped $CuGeO_3$ and on samples with different concentrations of Zn and Mg dopants along the c direction (κ_c) on double logarithmic scales. The solid line denotes the calculated magnetic specific heat c_m for a one-dimensional spin chain with nearest neighbor coupling constant $J = 160$ K and a frustration ratio of 0.35 [144, 153]. The area shaded in bright grey roughly marks the dips in the thermal conductivities. The temperature region where $CuGeO_3$ shows a shoulder and the doped samples are featured by a maximum is shaded in dark grey.

Let us turn to the first question. Remarkably, the thermal conductivity of the Zn doped, Mg doped and undoped samples are very similar at higher temperatures, concerning the temperature dependence and the absolute values, for both the b-and c direction, respectively. At temperatures below $\sim$ 150 K, the heat transport in $Cu_{0.992}Mg_{0.008}GeO_3$ is moderately lowered whereas the thermal conductivity in the 0.7% Zn doped sample is strongly damped showing no pronounced maxima anymore. Note that in both crystals the amount of impurity concentrations is almost equal and very small.
A conceivable scenario is disorder caused by impurities. The disorder leads to the damping of the thermal conductivity at lower temperatures. At higher temperatures the heat transport is mostly governed by thermal disorder. At first sight the stronger impact on the heat transport by Zn impurities is hardly to understand as the Zn^{2+} and Mg^{2+} ionic radii are of comparable size, and both, Zn^{2+} and Mg^{2+} are nonmagnetic and are expected to substitute Cu only.

A possible explanation could be a deteriorated homogeneity of the Zn impurity concentration compared to the Mg distribution. Experimental evidence for this to occur was given by Masuda and coworkers [207]. They reported the Zn content to be difficult to control, especially at low impurity concentrations. Measuring the fluctuations of the concentration of a few

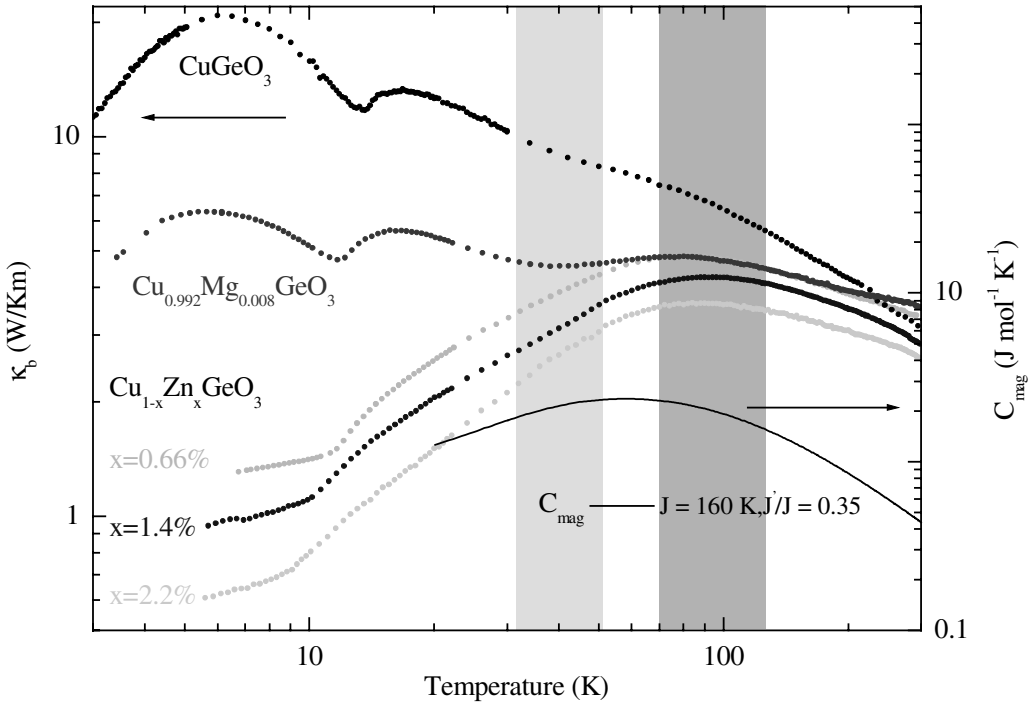

Figure 6.31: Compilation of the thermal conductivity measurements on undoped $CuGeO_3$ and on samples with different concentrations of Zn and Mg dopants along the b direction (κ_b) on double logarithmic scales. The solid line denotes the calculated magnetic specific heat c_m for a one-dimensional spin chain with nearest neighbor coupling constant $J = 160$ K and a frustration ratio of 0.35 [144, 153]. The area shaded in bright grey roughly marks the dips in the thermal conductivities. The temperature region where κ of $CuGeO_3$ shows a shoulder and κ of the doped samples are featured by a maximum is shaded in dark grey.

crystals they obtained a three times larger error for the Zn than for the Mg concentration. It might be possible that Zn atoms form clusters which have dimensions that are not small compared to all phonon wavelengths. These larger defects may thus serve as additional scattering centers hampering the heat transport at lower temperatures. It has been reported that those aggregates of atoms can change the thermal conductivity drastically [208]. Schwarz et al. conducted measurements on undoped and doped KCl crystals containing Ba^{2+} or Sr^{2+} clusters with expected diameters of $\sim 10nm$, where the absolute values of the doped samples were about one order of magnitude smaller than those of the undoped sample at lower temperatures.
Irrespective of the problematic of Zn concentration inhomogeneities, the thermal conductivity is systematically suppressed towards lower temperatures with increasing Zn content.

Let us move our attention onto question 2. The representation of the thermal conductivity along the c direction as a function of temperature on double logarithmic scales in Fig. 6.30 clearly reveals a dip around 40 K in undoped $CuGeO_3$ and in $Cu_{0.992}Mg_{0.008}GeO_3$, indicated by the bright grey shade. Even for $Cu_{0.9934}Zn_{0.0066}GeO_3$ a flattening around 40 K seems to be present. For higher Zn concentration, however, no distinct change of the thermal con-

ductivity can be detected in the temperature region around 40 K. At higher temperatures all measurements show a more or less pronounced maximum, unusual for phonon heat transport, marked by the dark grey shaded area. With increasing Zn concentration, the maximum shifts to higher temperatures.
Along the b direction the findings are quite similar, as illustrated in Fig. 6.31. The dips in the thermal conductivities of $CuGeO_3$ and $Cu_{0.992}Mg_{0.008}GeO_3$ are again located around 40 K while the Zn doped samples show no anomalies here. The maxima visible in all doped samples appear at much lower temperatures (around 100 K), instead. But even for the undoped specimen a shoulder at ≈ 100 K is clearly observable.

We definitely cannot exclude the idea that the maxima at high temperatures are contributions to κ caused by optical phonons, although their dispersions are small compared to the acoustic branches [209]. Strong additional damping of phonons may also arise from phonon-phonon scattering near a structural instability. Such a scenario can be excluded here, because the spin-Peierls transition, which is the only known instability present in $CuGeO_3$, takes place at much lower temperatures ($\simeq 14$ K).
Next, let us discuss whether a magnetic contribution to the thermal conductivity is possible in the temperature range of 40 K $\leq T \leq$ 300 K.
Theoretical calculations of the magnetic specific heat c_m for a one-dimensional spin chain show that c_m gives rise to a *maximum* at temperatures around 60 K. In addition, the theoretically obtained maximum of c_m is supported by the experimentally found maxima at $\sim$ 60 K of the magnetic contribution of the thermal expansions α_i along the a and c direction,respectively [130][10]. The relation $\kappa \propto cvl$ predicts similar temperatures dependencies of the thermal conductivity κ and the specific heat c. However, the maximum of the specific heat is close to the observed *minima* in κ_b and κ_c (see Figs. 6.30 and 6.31). According to this observation scattering of phonons on magnetic excitations is more plausible than an additional contribution by "magnons".
Furthermore, it is reasonable to believe that the magnetic correlation length ξ, which is approximately an upper boundary of the mean free path l, is very small at temperatures $T \geq J$, making a sizeable magnetic contribution unlikely.
From these arguments we tend to say that the high temperature structure is due to additional scattering of phonons on magnetic excitations in the narrow temperature range close to $T \approx 40$ K – a scenario discussed in the context of resonant scattering of phonons on magnetic excitations in $SrCu_2(BO_3)_2$ (see chapter 5).
Believing this scenario, it is comprehensible that for higher Zn doping, the dips are not visible anymore as the scattering of phonons on the Zn impurities excels the phonon scattering by the magnetic excitations.

We now return to the low temperature double peak structure already discussed in detail in chapter 6.5.3 where we found that a clear and unambiguous identification of a magnetic contribution is not possible in undoped $CuGeO_3$, and that all discussed scenarios are thinkable. Unfortunately, we cannot extract further information from the low temperature measurements of κ on $Cu_{0.992}Mg_{0.008}GeO_3$ as no drastic changes of the heat transport can be detected, i.e., the double peak structure still exists and the ratio $\kappa_b/\kappa_c \simeq 0.3$ is roughly the same as for

[10] For a Heisenberg spin chain with only nearest neighbor interaction the magnetic contribution to the thermal expansion and the specific heat, respectively, are proportional [210].

pure $CuGeO_3$.
Even in the Zn doped samples where the thermal conductivity is already drastically suppressed for small impurity concentrations, the thermal conductivity ratio κ_b/κ_c is also $\simeq 0.3$. We must therefore admit that the low temperature structure remains an unsolved puzzle.

Summing up, $CuGeO_3$ reveals a complex and anomalous thermal conductivity behavior. Both the temperature and magnetic field dependence of κ show many surprising features that are to a large extent not understood. Possible explanations for questions 1 and 2 have been given. Concerning the high temperature behavior, our considerations suggest the unusual temperature dependence of κ to be caused by mutual scattering of phonons on magnetic excitations in a relatively narrow temperature range. At low temperatures various ideas have been given for the occurrence of the double peak structure of the thermal conductivity. Unfortunately, non of the thinkable scenarios can be favored.
Nevertheless, the numerical calculations conducted gives hope that one succeeds in forming a deeper understanding of the heat transport in $CuGeO_3$ by theoretically studying the microscopic "magnon-magnon" and "phonon-magnon" scattering mechanisms. In this field many interesting questions are still to be answered, i.e., the frequency dependencies of the various scattering scenarios, namely of "magnon-magnon" Umklapp-scattering, of the "magnon"-scattering on point defects and other scattering processes.

Chapter 7

The Bechgaard Salts

The Bechgaard salts are remarkable quasi-one-dimensional electronic materials discovered in 1979 by Bechgaard [211]. During the last few years the properties of these materials have received considerable attention, since a strictly one-dimensional interacting electron system cannot be described by the usual Fermi liquid picture involving well defined quasiparticle excitations, common to the description of conventional metals and semiconductors. Instead, more exotic scenarios like the Tomonaga-Luttinger liquid are believed to be appropriate with interesting properties, for example, spin/charge separation, where independent spin and charge excitations with different velocities are expected. Such novel non-Fermi liquid type states are also relevant in other interacting electron systems like the high temperature superconductors and the heavy fermion materials near a quantum critical point.
In this chapter I will report the observation of anomalous thermal conductivities in the spin-Peierls system $(TMTTF)_2PF_6$ in the spin density wave compound $(TMTSF)_2PF_6$ and in the superconductor $(TMTSF)_2ClO_4$.

These data indicate a magnetic contribution to the heat current in all of these systems, present in a wide temperature range and dominating the room thermal conductivity. Remarkably, the temperature dependence of the thermal conductivity found here strongly resembles that of La_2CuO_4 (see chapter 8), the parent compound of the high temperature superconductors, indicating a pronounced and unusual magnetic contribution to the heat current in this material as well.

7.1 Structure and Basic Electronic Properties

The Bechgaard salts $(TMTCF)_2X$ are isostructural compounds, based on linear chains of, e.g., the organic molecules tetramethyltetrathiafulvalen (TMTTF) and tetramethyltetraselenfulvalen (TMTSF), with different inorganic interchain anions, e.g., PF_6, SbF_6 and ClO_4. The donors are planar molecules, as depicted in Fig. 7.1. At room temperature the triclinic $P\bar{1}$

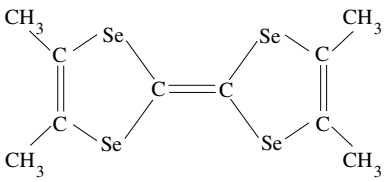

Figure 7.1: Molecule structure of tetramethyltetraselenfulvalen (TMTSF).

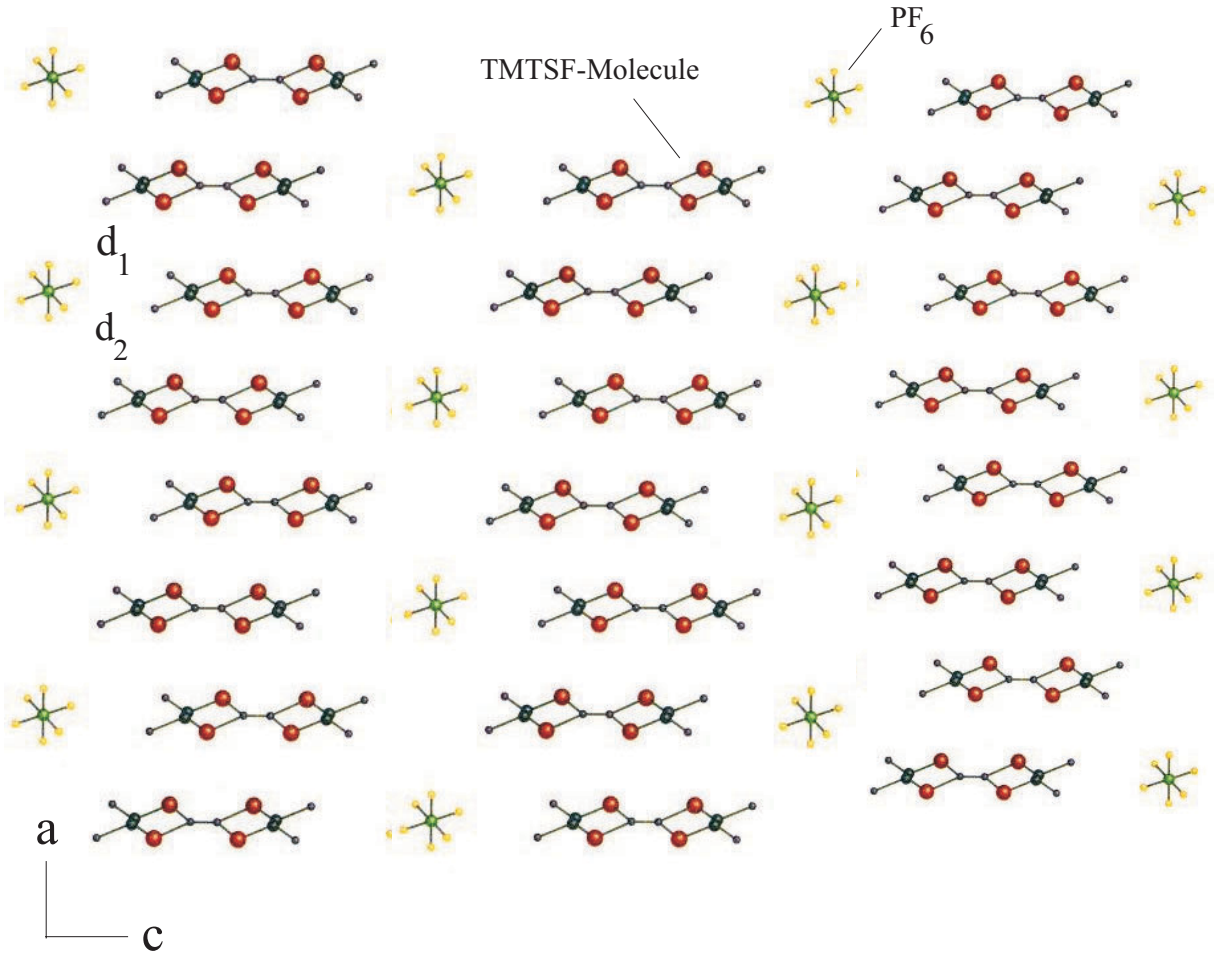

Figure 7.2: Projection of the crystal structure of $(TMTSF)_2PF_6$ in the a-c plane. The alternating distances between adjacent molecule planes, indicated by d_1 and d_2, reflect the dimerization that occurs along the a direction [212].

space group is specified [213]. The planar molecules form honeycomb-like planes, like graphite, i.e., an elementary unit cell contains two planar molecules. These planes are stacked along the a axis, as illustrated in Fig. 7.2. The highly one-dimensional electronic character results from the strong directional dependence of the orbitals involved and is established theoretically and experimentally [214–217]. Because of the charge transfer from the molecule orbitals to the counterions, the electronic bands are only partially filled. Here a full charge transfer of one electron from the two (TMTCF)-molecules causes the band involving the chains to be a quarter-filled hole band. A weak dimerisation occurs along the chain direction (indicated by d_1 and d_2 in Fig. 7.2) splitting the band into two subbands, on empty and one half-filled[1]. Without electron-electron interaction a half-filled bands results in a metallic state. But a on-site Coulomb interaction ($\simeq 1.16eV$ [218]) splits the half-filled band into a full lower and an empty upper Hubbard band, so that the systems should be insulators with a correlation gap Δ_ρ.

[1]The issue whether a half- or a quarter-filled band is a more appropriate description for the Bechgaard salts is still under debate.

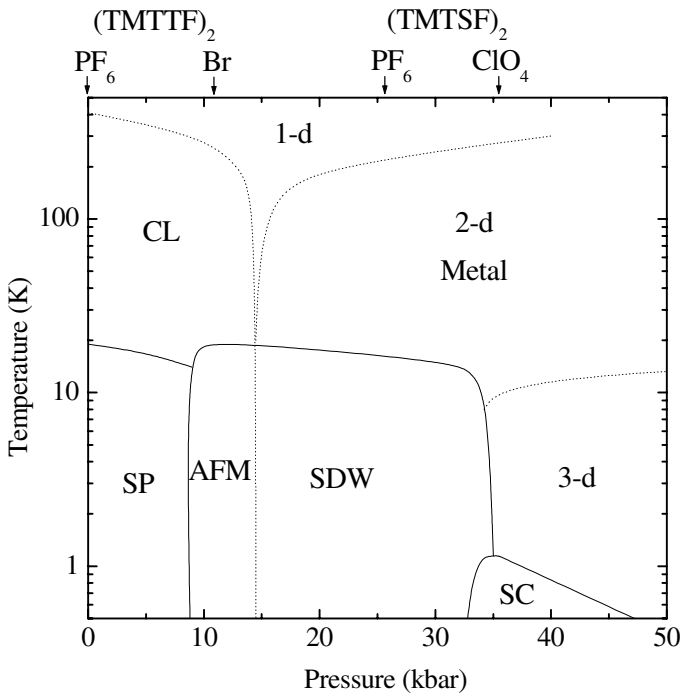

Figure 7.3: Schematic phase diagram of the $(TMTCF)_2X$ salts [215]. With increasing chemical or ambient pressure, the compounds become higher dimensional, and can be driven with the temperature as the second parameter to a variety of states. The abbreviations in the diagram have the following meaning: Mott-insulator/charge localisation (CL), spin-Peierls (SP), antiferromagnet (AFM), spin density wave (SDW), and superconductor (SC).

The phase diagram of the TMTSF and TMTTF salts is extremely rich, shown schematically in Fig. 7.3. For $(TMTTF)_2PF_6$ located on the lefthand side of the phase diagram with a correlation gap Δ_ρ estimated to $\simeq 500$ K [218], one observes a spin-Peierls transition at low temperatures, consistent with the above picture of a one-dimensional Mott-Hubbard insulator with one electron per chain and site. Here electronic correlations are assumed to be so strong that the charge carriers remain confined along the organic stacks.
With increasing pressure or – equivalently – anion substitution the system displays other ground states and even metallic behavior.
At first sight one would also expect an insulating state for $(TMTSF)_2PF_6$. But measurements of the electrical conductivity show a metallic behavior down to low temperatures. It is suggested that the weaker dimerisation resulting in a drastic lowering of the correlation gap ($\Delta_\rho \simeq 40$ K), determined, e.g., by optical conductivity measurements, is responsible for the metallic behavior [218, 219]. Moving from the left to the right in the phase diagram, optical conductivity measurements give evidence that a crossover from insulating to conducting states occur with increasing interchain charge transfer. It is suggested that electron-hole pairs are created with the electron and hole residing on neighboring chains [220].
However, the transport mechanisms are not yet understood. On the one hand there are conjectures stemming from one-dimensional theories of the Hubbard model that the ground state may be a Luttinger liquid, leading to charge/spin separation [221–223]. Experimental support of this theoretical prediction comes, e.g., from transport measurements indicating

strong correlation effects to be important [218, 224]. On the other hand it has been pointed out that the electrical transport can be understood in terms of a weakly interacting Fermi liquid [225]. Obviously, the controversy over Fermi-liquid or non-Fermi-liquid is still an open question.

7.2 Experimental Results

To the best of my knowledge measurements of the thermal conductivity have been restricted so far to $(TMTSF)_2ClO_4$, that becomes superconducting at $T \simeq 1$ K and at ambient pressure [226]. The results are vastly different. Durek and coworkers have observed a monotonic *decrease* in the heat transport below 50 K [87]. Choi et al. have found an essentially temperature independent thermal conductivity from 100 to 50 K and an *increase* below 50 K as the temperature is further lowered [86]. In both cases the measurements were conducted along the a direction only.
Moreover, the observed magnetic field dependencies are completely different. While a significant increase of κ with increasing magnetic field was detected below 40 K by Djurek et al., the measurements conducted by Choi et al. showed a slight reduction of the thermal conductivity with application of a magnetic field.
Finally, I want to mention that recently first measurements of the thermal conductivity in the superconducting state of $(TMTSF)_2ClO_4$ have been reported by Belin and coworkers [226]. These results strongly support the occurrence of a nodeless superconducting gap function for this system. Unfortunately, we cannot compare our results to those of Belin et al. since their thermal conductivity data are only published for temperatures below 2 K.

There are several reasons why thermal conductivity measurements of the Bechgaard salts are very sparse. First, the samples are very fragile, leading to cracks when cooling the sample down. Second, their needle-like shape can cause large radiation errors of the thermal conductivity at higher temperatures. A well grounded experimental setup and large crystals are therefore indispensable for high accuracy measurements. For a detailed discussion about the setup for the thermal conductivity and the resistivity measurements, please refer to chapter 4.

7.2.1 $(TMTTF)_2PF_6$

The experimental results of electrical resistivity measurements are shown in Fig. 7.4 (right panel, inset). Our measurements are well in accordance with previous results [227]. Below $\sim$ 100 K we clearly see an activated behavior leading to an insulating state for $T \to 0$. Note that ρ changes by about seven orders of magnitude.
The thermal conductivity of $(TMTTF)_2PF_6$ is depicted in Fig. 7.4[2]. There are two remarkable features: a low temperature maximum at around 20 K with a significant suppression of κ by applying a magnetic field, and a steep increase of κ above about 100 K. Note that this increase becomes smaller at higher temperatures indicating a tendency towards saturation or to a maximum at temperatures above room temperature Fig. 7.4 (left panel). Evidently, no anomaly at the spin-Peierls transition appears, illustrated in the inset.

[2] Thermal conductivity and electrical resistivity were measured on two different samples.

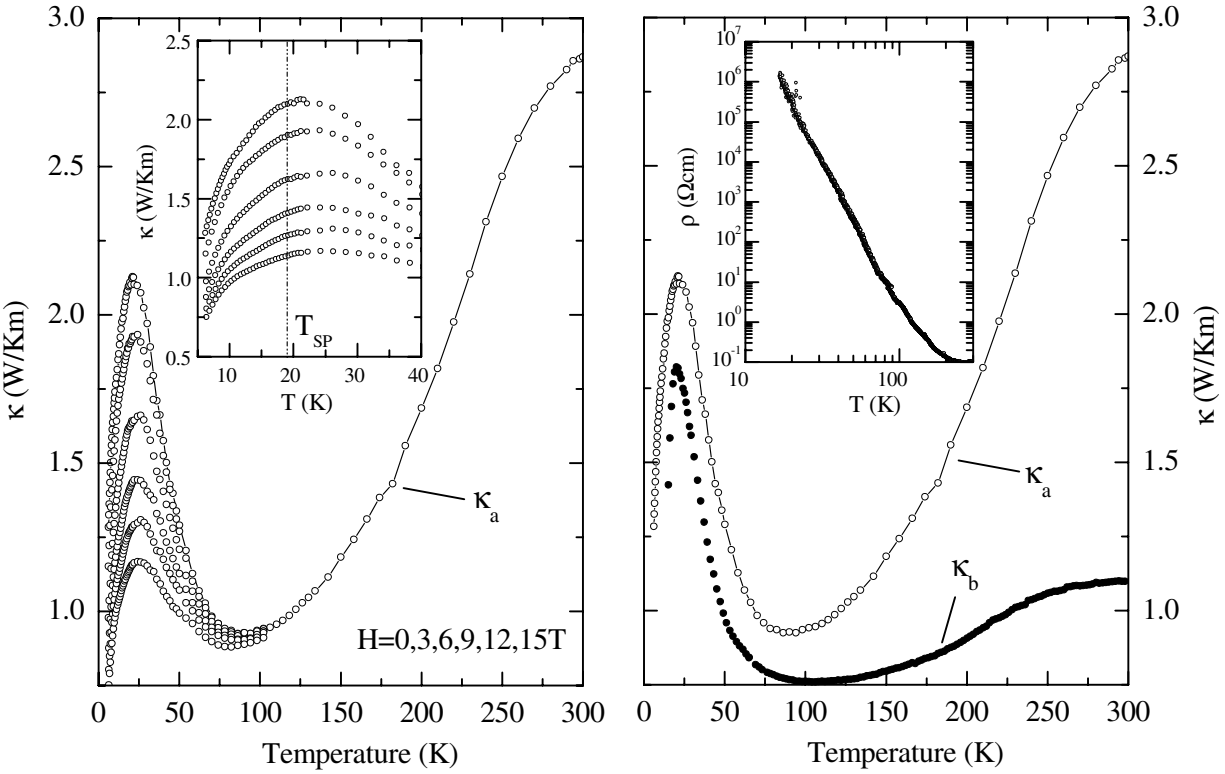

Figure 7.4: Left: Thermal conductivity (κ_a) of $(TMTTF)_2PF_6$ along the spin chains for various magnetic fields aligned parallel to the **a axis**. With increasing field the maximum at low temperatures is suppressed. The inset shows an enlarged view of the low temperature region. No anomaly can be observed at the spin-Peierls transition, marked by the vertical line. Right: Comparison of the thermal conductivities **parallel** (κ_a) and **perpendicular** (κ_b) to the spin chains. The electrical resistivity along the a direction is plotted in the inset.

The right panel of Fig. 7.4 shows the comparison of the thermal conductivity *parallel* (κ_a) and *perpendicular* (κ_b) to the stacking axis. To the best of my knowledge, this is the first time that (κ_b) has been measured on a Bechgaard salt. I want to emphasize that both (κ_a) and (κ_b) are obtained by measuring the same sample. While at temperatures below ~ 100 K the thermal conductivities along the two directions resemble each other very much, the thermal conductivity perpendicular to the stacking axis (κ_b) shows a much weaker increase towards higher temperatures saturating at ≈ 300 K[3].

7.2.2 $(TMTSF)_2PF_6$

$(TMTSF)_2PF_6$ is a metal from room temperature down to $T_{SDW} \approx 12$ K. The transition to a spin density wave state at T_{SDW} leads to a metal-to-insulator transition, consistent with the steep increase of ρ at the transition temperature, depicted in the right inset of Fig. 7.5. The thermal conductivity shows a small but distinct anomaly at the spin density wave transition, illustrated in the inset of the left panel of Fig. 7.5. The striking magnetic field dependence

[3]It should be remarked that because of the triclinic crystal structure the b direction of the sample does not exactly coincide with the crystallographic b direction.

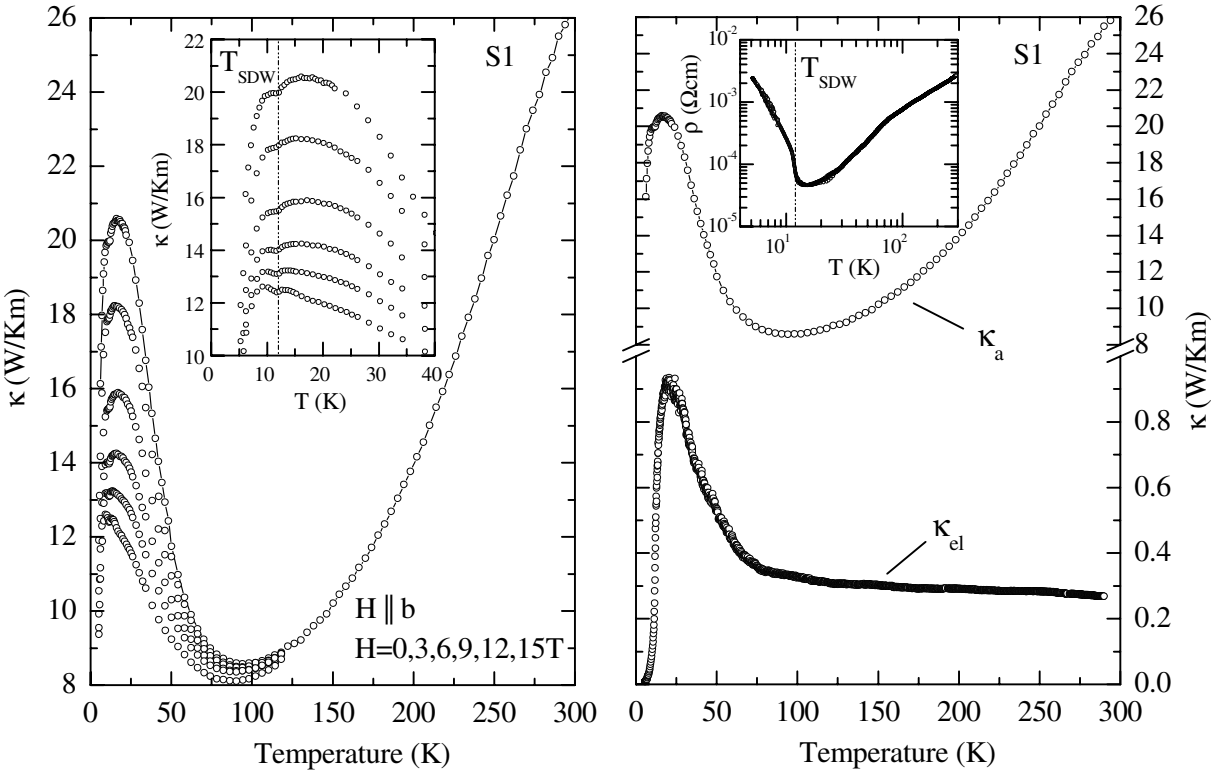

Figure 7.5: Left: Thermal conductivity (κ_a) of $(TMTSF)_2PF_6$ along the spin chains for various magnetic fields aligned parallel to the **b axis**. With increasing magnetic field, the maximum at low temperatures is suppressed. The inset shows an enlarged view of the low temperature region. Clearly, an anomaly can be observed at T_{SDW}, marked by the vertical line. Right: Comparison of the total thermal conductivity (κ_a) and the electronic thermal conductivity (κ_{el}) obtained by the Wiedemann-Franz-Law (WFL). Pay attention to the broken ordinate and the different scales for κ_a and κ_{el}. The electrical resistivity along the a direction is plotted in the inset. Measurements of κ on $(TMTSF)_2PF_6$ were conducted on two samples. Here, **S1** denotes sample one.

of the maximum at ~ 20 K and the steep increase above about 100 K is very similar to the results found for $(TMTTF)_2PF_6$. But no tendency towards a saturation of κ with increasing temperature is observed.

From the Wiedemann-Franz law (WFL) one can estimate the electronic thermal conductivity (κ_{el}) plotted together with total thermal conductivity (κ_a) for zero magnetic field in the right panel of Fig. 7.5. Evidently, the electronic contribution is rather small, especially at higher temperatures, and shows a *very different* temperature dependence compared to the total thermal conductivity towards higher temperatures. The jump at the spin density wave transition evident in the total thermal conductivity at ≈ 12 K can almost be completely attributed to the electronic thermal conductivity.

This can be seen by comparing the total thermal conductivity κ and the electronic contribution κ_{el} close to the transition, as illustrated in Fig. 7.6. The height of the jump is for both κ and κ_{el} almost equal ($\delta\kappa \approx 0.6\ W/Km$ for κ and $\delta\kappa_{el} \approx 0.7\ W/Km$ for κ_{el}). I want to point out that our electrical conductivity results agree well for both the temperature dependence and the absolute values with previous results [215]. It is important to note, however, that

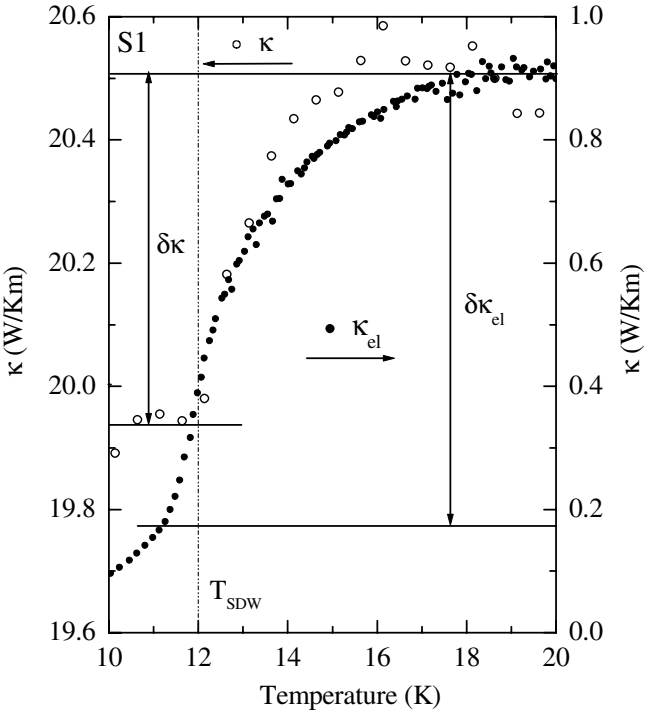

Figure 7.6:
Total thermal conductivity κ and electronic thermal conductivity conductivity κ_{el}, obtained by the Wiedemann-Franz-Law (WFL), of $(TMTSF)_2PF_6$ in the vicinity of the spin density wave transition T_{SDW}. The height of the jumps are denoted by $\delta\kappa$ and $\delta\kappa_{el}$, respectively.

the thermal conductivity and electrical resistivity measurements had to be performed on two different crystals, but of the same batch, due to experimental reasons (see chapter 4). Furthermore it is known that cracks having less dramatic effects on the heat transport than on the electronic transport may cause an effective difference in the geometric factors for thermal and electrical transport. Finally, according to theoretical results, a violation of the WFL can arise in a one-dimensional electron gas where spin and charge degrees of freedom are separated [228]. From this we conclude that we are well advised to consider the calculated electronic thermal conductivity merely as a crude estimation.

The absolute value of κ is one order of magnitude higher than that of $(TMTTF)_2PF_6$. In order to clarify the reason for that a second sample (S2) was measured. The results are shown in Fig. 7.7. The absolute value is much smaller but the temperature dependence is almost similar as shown in the right panel, where the zero field mesurement on the first sample S1 differs from the second measurement by a multiplicative factor of 0.3 (see Fig. 7.5). We conclude that there must be a difficulty in determing the cross sections of the samples entering the formula which gives us the thermal conductivity (see chapter 4). A possible reason could be the fragility of the samples leading to planar cracks along the needle axis and thus to effectively smaller cross sections where heat can flow.

I will turn now to the important observation that the magnetic field-dependence of the thermal conductivity does not depend on the direction of the magnetic field with respect to the crystallographic axis. While for sample S1 the field was aligned parallel to the a direction, i.e., along the stacking axis, for sample S2 the field pointed along the b direction, i.e perpendicular to the stacking axis. Evidently, the relative change under the influence of a magnetic

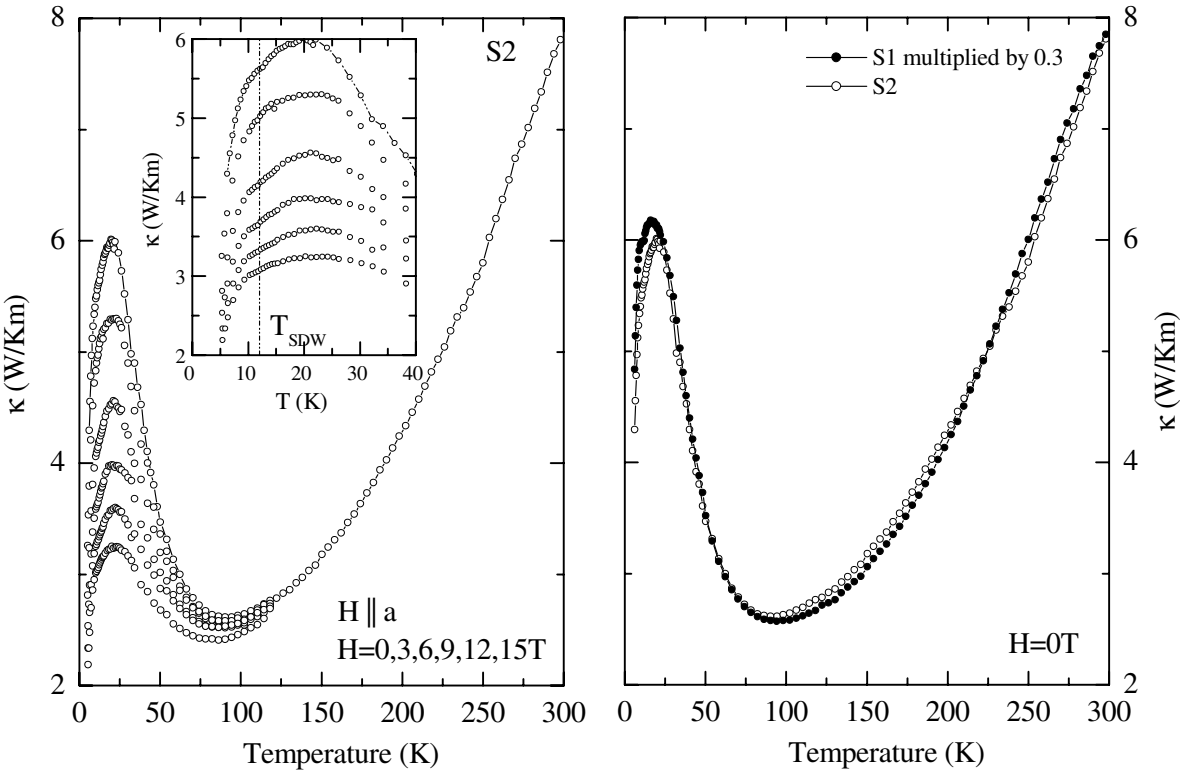

Figure 7.7: Left: Measurement of the thermal conductivity on a second $(TMTSF)_2PF_6$ sample (S2) along the spin chains for various magnetic fields aligned parallel to the **a axis**. Evidently the temperature and magnetic field dependence coincide with the first measurement S1 (see Fig. 7.5). The inset shows an enlarged view of the low temperature region. A small anomaly can be observed at T_{SDW}, marked by the vertical line. Right: The excellent agreement between the first (S1) and second zero field thermal conductivity measurement (S2) can be seen by multiplying the data of S1 with 0.3.

field is in both cases the same. For a moment this is surprising since magic angle effects and angular dependences of the resistivity have been reported to be prominent features of $(TMTSF)_2PF_6$ [229, 230]. We will come back to this point in the discussion below.

7.2.3 $(TMTSF)_2ClO_4$

$(TMTSF)_2ClO_4$ is peculiar among the $(TMTCF)_2X$ family since it becomes superconducting at ambient pressure. The resistivity along the a direction is plotted in the inset of the right panel of Fig. 7.8. For cooling rates < 0.1 K/min, a structura l transition with an ordering of the tetraedral anions occurs at $T_{AO} \simeq 24$ K. No sign of anomaly is observed in the resistivity curve. This could be due to our cooling rates of about 0.5 K which are perhaps somewhat too fast. However, the transition is even for very slow cooling rates not very pronounced [231]. The thermal conductivity along the a direction is very similar to those found in $(TMTTF)_2PF_6$ and $(TMTSF)_2PF_6$. A pronounced maximum around 20 K with an appreciable magnetic field dependence and a distinct increase of κ to higher temperatures is evident, as shown in the left panel of Fig. 7.8. The inset shows the enlarged low temperature region where a small dip in the thermal conductivity around the anion-ordering transition temperature can be seen.

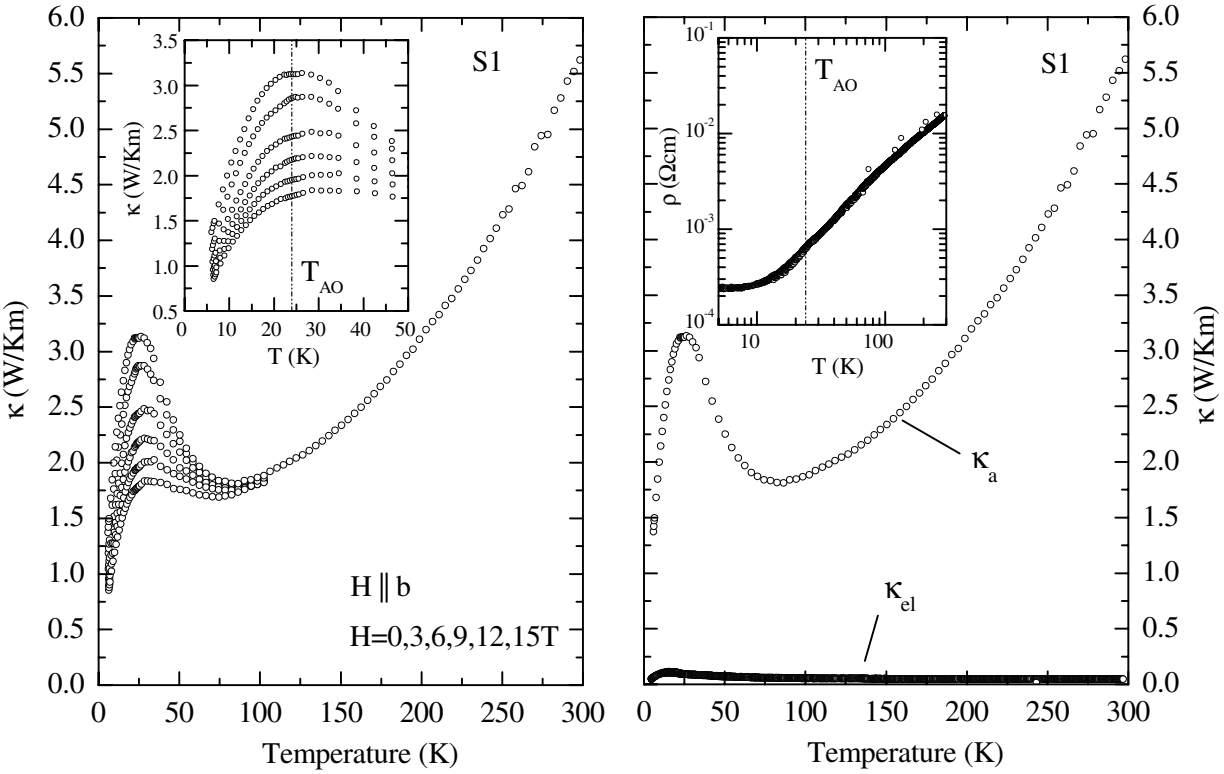

Figure 7.8: Left: Thermal conductivity (κ_a) of $(TMTSF)_2ClO_4$ along the spin chains for various magnetic fields aligned parallel to the **b axis**. With increasing field, the maximum at low temperatures is suppressed. The inset shows an enlarged view of the low temperature region. A small anomaly can be observed at T_{AO}, marked by the vertical line. Right: Comparison of the total thermal conductivity (κ_a) and the electronic thermal conductivity (κ_{el}) obtained by the Wiedemann-Franz-Law (WFL). The resistivity along the a direction is plotted in the inset. S1 denotes the measurement on sample one.

The electronic thermal conductivity obtained via the WFL is plotted together with the total thermal conductivity in zero magnetic field in the right panel of Fig. 7.8[4]. It is immediately clear that the electronic contribution to κ can be neglected.
A thermal conductivity measurement on a second sample (S2) was completed in order to verify the first zero magnetic field results (S1) and to study the dependence of κ on the magnetic field direction. The result, depicted in the right panel of Fig. 7.9, confirms the first measurement (S1), which is scaled by a multiplicative factor of ≈ 0.5.
As for $(TMTTF)_2PF_6$ no directional magnetic field influence on κ can be found. This is remarkable since angular magneto resistance effects have been found in $(TMTSF)_2ClO_4$ [232, 233].

I want to come back to one of the striking features of $(TMTSF)_2ClO_4$ – the anion-ordering phenomena. There are two possible orientations for the ClO_4 tedrahedron, as shown in Fig. 7.10. If one cools the compound down very slowly ($< 0.1\ K/min$), the anions may relax and order alternatingly along the [010] crystal axis for temperatures $T < T_{AO}$. Upon further

[4] ρ and κ were measured on two different samples.

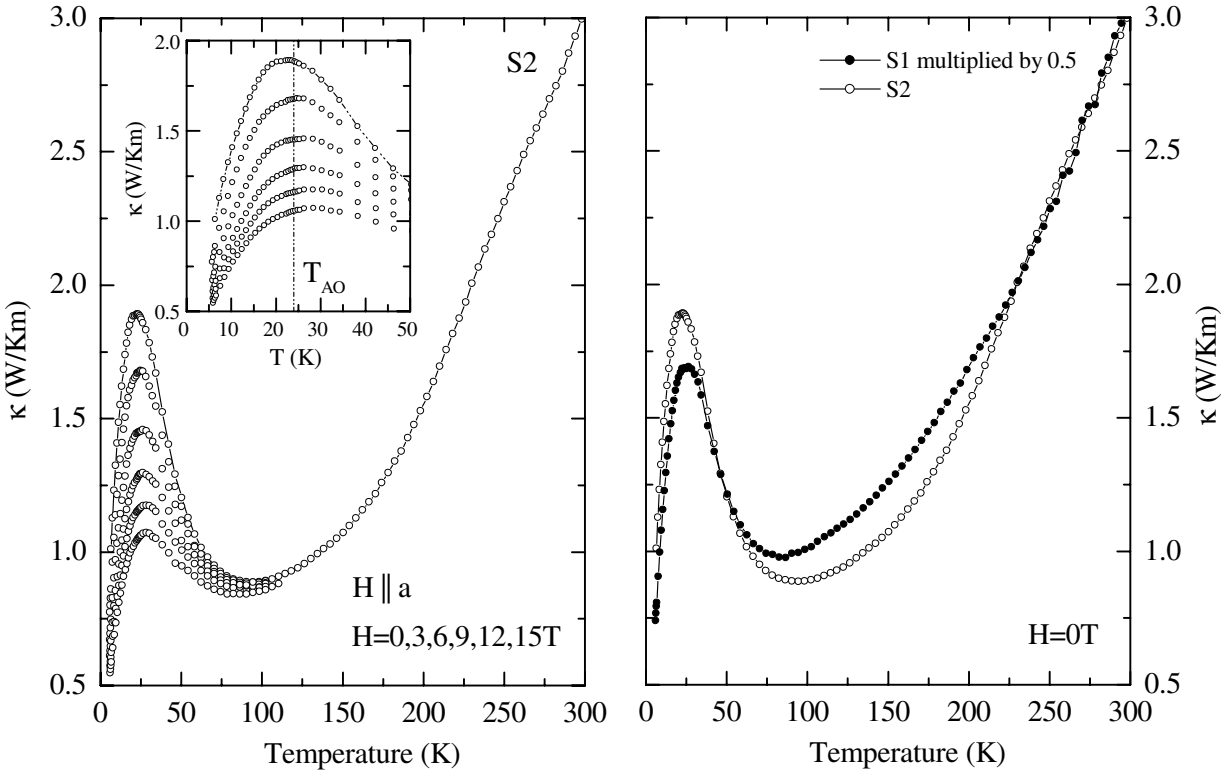

Figure 7.9: Left: Measurement of the thermal conductivity on a second $(TMTSF)_2ClO_4$ sample (S2) along the spin chains for various magnetic fields aligned parallel to the **a axis**. Evidently, the temperature and magnetic field dependence coincide with the measurement on sample S1 (see Fig. 7.8). The inset shows the enlarged low temperature region. A very small anomaly is indicated at T_{AO}, marked by the vertical line. Right: The satisfactory agreement between the thermal conductivity measurements on the first (S1) and second sample (S2) can be seen by multiplying the data of S1 with ≈ 0.5.

cooling a phase transition into the superconducting state occurs at ~ 1.2 K [226]. For very fast cooling rates ($> 50\ K/min$), no anion-ordering takes place and one observes a spin density wave transition at $T_{SDW} \approx 6$ K [234].
Lattice imperfections should create additional scattering centers hampering the heat transport regardless of the kind of excitations carrying the heat, hence we should be able to observe this order-disorder phenomena.
The results are plotted in Fig. 7.10. I conducted three runs – one after a slow cooling down, a second after a rapid cooling procedure and a third one after, again, slow cooling down. In the first run I measured the thermal conductivity upwardly (upper curve). At about 100 K the measurement was stopped and the sample was rapidly cooled ($> 50\ K/min$) down to around 5 K. Subsequently, an upward thermal conductivity measurement was conducted, leading to the lower curve. I did a third thermal conductivity run downwardly from about 100 K in order to check that no cracks were created during the rapid cooling down process.[5]. Obviously, the first measurement is excellently confirmed by the last one.

[5]The thermal conductivity measurements themselves are slow measurements; the rate is of the order of $0.1 K/min$.

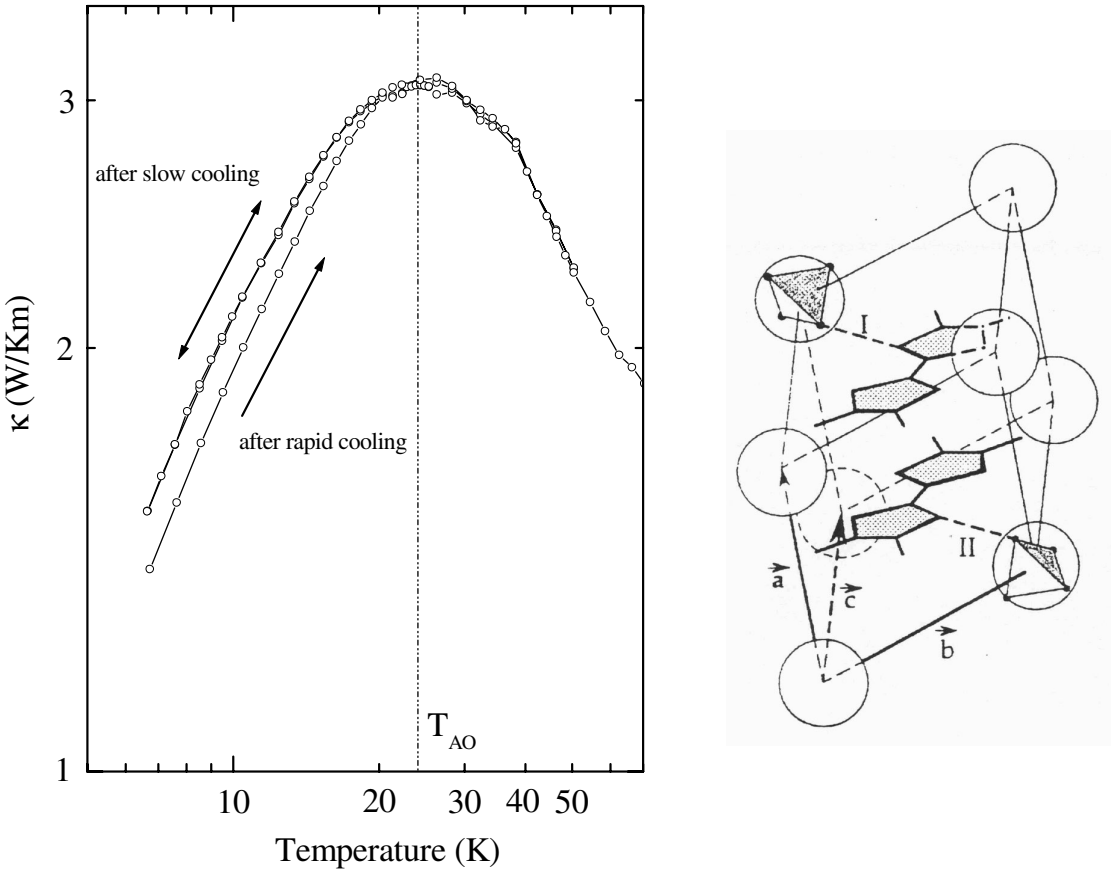

Figure 7.10: Left: Thermal conductivity of $(TMTSF)_2ClO_4$ along the a direction for two different cooling rates. The lower curve shows the thermal conductivity after rapid cooling from ≈ 100 K down to about 5 K with a rate $> 50\ K/min$ and subsequent slow upward measurement of κ . Both upper curves are obtained for slow cooling rates ($\leq 0.1 K/min$), one before and one after the "rapid cooling result" was detected. Right: Triclinic unit cell with two (I and II) possible orientations of the tetrahedral anion.

The data shown in Fig. 7.10 clearly reveal that below T_{AO} the thermal conductivity of the ordered state is somewhat larger than the thermal conductivity of the state where no anion-ordering takes place. Due to the measurement setup we were not able to go to lower temperatures, where the transitions into the superconducting (slow cooling) or SDW ground state (fast cooling) takes place.

7.3 Discussion

The most surprising result of the thermal conductivity is that irrespective of whether the materials are metallic or insulating, one identifies a common behavior of κ with two main features: First, a low temperature maximum around 20 K which strongly depends on the magnetic field. A concomitant phenomenon is that the suppression of the low temperature maximum occurs irrespectively the material and the orientation of the sample with respect to the field direction. Second, a steep increase of κ above about 100 K. The increase becomes evidently smaller in the spin-Peierls system $(TMTTF)_2PF_6$ saturating at about 300 K, while

for the spin density wave system $(TMTSF)_2PF_6$ and the superconductor $(TMTSF)_2ClO_4$ no saturation at room temperature is apparent.

The behavior of κ here is highly unusual and distinctly different from that expected for conventional insulators and metals. In conventional solids, the thermal conductivity has a phononic (κ_{ph}) and electronic (κ_{el}) contribution which add to the total thermal conductivity $\kappa = \kappa_{ph} + \kappa_{el}$. The electronic thermal conductivity is unimportant in the materials discussed here. This is obvious for the spin-Peierls system since it is an insulator. However, also in the metallic systems κ_{el} obtained by the Wiedemann-Franz law is only a minor fraction of the total thermal conductivity. In particular, neither its magnitude nor its temperature dependence can account for the two maxima of the total thermal conductivity.
The behavior of κ can also not be explained in terms of a pure phonon thermal conductivity. For clean crystals one maximum is usually found at intermediate temperatures, typically of the order 20-50 K (see chapter 3). Apparently, the low temperature maximum of κ found in our experiments can be attributed to the phononic thermal conductivity. Taking only acoustic phonon modes into account it is not possible to explain the high temperature maximum in this scenario. We note that an additional damping of phonons could in principle give rise to two maxima of κ_{ph}, if the associated scattering mechanism is active mostly in a narrow temperature intervall (see chapter 5). However, such an explanation is very unlikely for the materials considered here, since it would require a maximum of the conventional phononic thermal conductivity at too high temperatures. We should mention here that in the Bechgaard salts the heat carrying acoustic phonons are at comparatively low energies, as signaled by the low Debye-temperatures of the order of 60 K [227].
One should, however, take optical phonon modes into consideration. According to the vast number of atoms per unit cell optical phonon modes could be a thinkable origin of the large additional contribution to the heat current at higher temperatures. Certainly, we cannot rule out possible contributions from these modes. However, it is very unlikely that these modes transport heat themselves because in general their group velocities are small. Nevertheless, it was claimed that low lying optical modes excited at elevated temperatures may transfer energy to the acoustic modes, leading to an enhanced thermal conductivity [43].

Regarding the magnetic excitation spectrum, a quite natural explanation for the high temperature maximum of κ can be given for the spin-Peierls system, if an additional magnetic contribution to κ is assumed. Due to the strong electronic correlations the material corresponds to a one-dimensional Mott-Hubbard chain, i.e., a one-dimensional antiferromagnetic insulator. The magnetic coupling constant J as inferred from the spin susceptibility is of the order of 500 K [235, 236]. In such a material there are low energy magnetic excitations, called spinons, which may contribute to the heat current. Note that J is even larger than the Debye temperature so that this channel of heat current may even dominate over the phononic heat transport. The idea of a magnetic contribution is also strongly supported by our experimental observation of a highly anisotropic heat transport of $(TMTTF)_2PF_6$ for temperatures > 100 K showing the quasi-one-dimensional character of the system (see right panel of Fig. 7.4). In fact, a magnetic contribution κ_m to κ has been identified in the last few years from experiments on various low-dimensional quantum spin systems, on for example, the spin ladder materials [65, 66].

The remarkably low absolute values observed for κ of these organic materials can be as-

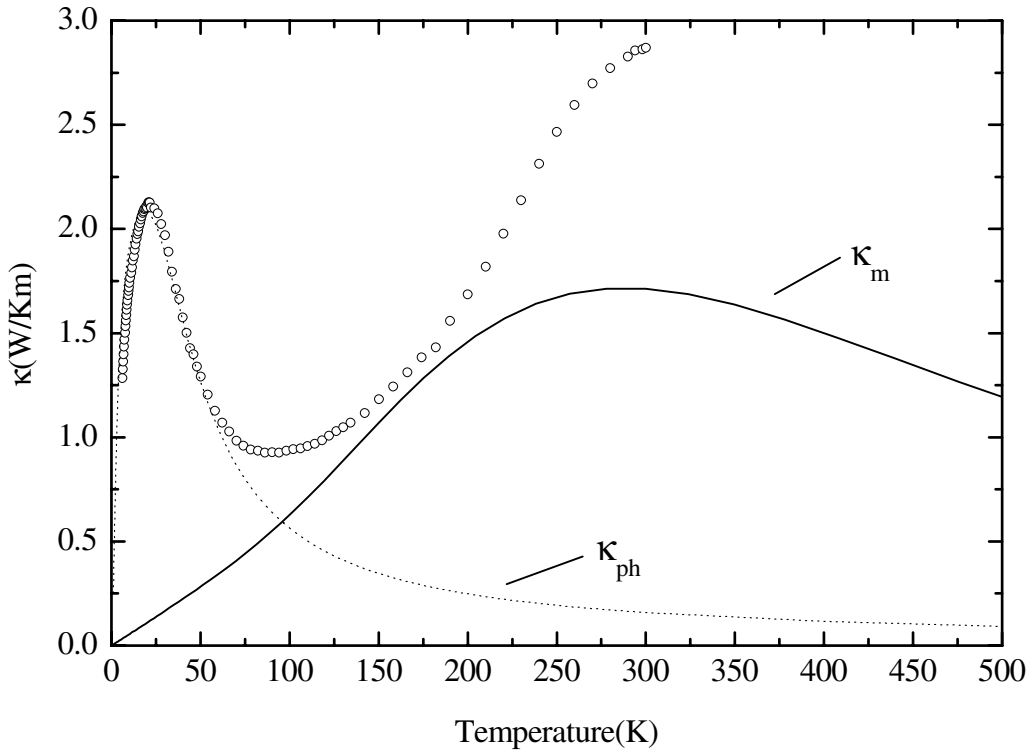

Figure 7.11: Thermal conductivity of $(TMTTF)_2PF_6$ along the a direction (open circles). The hypothetical phonon thermal conductivity κ_{ph} obtained by fitting the low temperature maximum with the standard Debye model is shown by the dotted line. The solid line reflects the estimated magnetic thermal conductivity $\kappa_m \propto c_m v_m l_m$ where c_m is the theoretical magnetic specific heat for a one-dimensional antiferromagnet (see text) [153, 187].

cribed to the large volume V of the unit cell in conjunction with the assumption that only acoustical phonon modes are relevant for the heat transport. I note that with $V = 675.7\mathring{A}^3$ for $(TMTTF)_2PF_6$ and $V = 714.3\mathring{A}^3$ for $(TMTSF)_2PF_6$, the volume is about one order of magnitude larger than, e.g., that of $CuGeO_3$. As the specific heat enters the kinetic formula $\kappa \propto cvl$ in units of J/m^3K both the magnetic and phononic thermal conductivities κ become small for meaningful mean free paths l.
Let us make a crude estimation for the phonon thermal conductivity. Since the Debye temperature is very low it is reasonable to assume the Dulong-Petit value for the acoustical phonon specific heat at room temperature. With the velocity of the phonons of about 3000 m/s and l reasonably chosen to be about $50\mathring{A}$, we obtain for the phononic thermal conductivity a rather small value of about 0.3 W/Km at room temperature.

Now, I show a simple analysis of the measured thermal conductivity of $(TMTTF)_2PF_6$ within the scenario of an additional magnetic contribution in Fig. 7.11. We have fitted the low temperature maximum of κ by a standard Debye model including phonon-Umklapp, point-defect and boundary scattering (see chapter 3). The adjustable parameters P, U, u are given in Table 7.1. The Debye temperature Θ_D is fixed by the value mentioned before [227]. The mean velocity of $(TMTSF)_2PF_6$ was obtained by ultrasonic measurements to be of the order of 3000 m/s [237]. To my knowledge no sound velocities have been determined for

$(TMTTF)_2PF_6$. Thus we assumed for $(TMTTF)_2PF_6$ the velocity to be of approximately the same size due to the very similar crystal structure. The parameter L describing the boundary scattering is one order of magnitude smaller than the smallest dimension of the sample (see Table 7.1). I attribute this to large cracks possibly present in these fragile samples.
With these parameters we obtain κ_{ph} of $(TMTTF)_2PF_6$, as shown by the dotted line in Fig. 7.11. Obviously, at room temperature a second contribution to κ dominates. I use $\kappa_m \approx c_m v_m l_m$ for the magnetic thermal conductivity and assume a constant mean free path l_m. The velocity v_m is determined by the magnetic exchange coupling J. It can be estimated using $v_m \approx (\pi k_B/2\hbar)Ja$ where a is the lattice parameter and J the magnetic exchange coupling constant. For $J \approx 600$ K one obtains $v_m \approx 90000 m/s$ which is very large. For a one-dimensional antiferromagnet spin chain, c_m was obtained theoretically [153, 187]. Obviously, for small but reasonable $l_m \approx 30$ $\mathring{A}$, the behavior of κ_m is consistent with the experimentally obtained steep increase of κ towards higher temperatures and would predict a maximum around 300 K. One should mention that this value of l_m is smaller than the magnetic correlation length ξ (which can be seen as an upper boundary of the mean free path of the magnetic excitations) found in the 2-d system La_2CuO_4 [238]. Unfortunately, no results of the magnetic correlation length ξ of the Bechgaard salts have been published so far.

Now, I turn to the metallic systems. Dumm et al. have pointed out that in spite of the fact that $(TMTSF)_2PF_6$ is a low-dimensional metal down to around 100 K, the temperature dependence of the magnetic susceptibility can be described within the framework of the Hubbard model in the limit of strong Coulomb repulsion [236]. Proceding in the same fashion as for $(TMTTF)_2PF_6$, we obtain the hypothetical magnetic contribution κ_m with a maximum around 700 K, plotted in Fig. 7.12, if we assume a mean free path l_m of about $250\mathring{A}$ and use $J \sim 1400$ K [236]. For the adjustable parameters P, U and u, given in Table 7.1, we find the theoretical phonon thermal conductivity κ_{ph}. The sound velocity was fixed to the value mentioned before where the Debye temperature was calculated via $\Theta_D = v(\hbar/k_B)(6\pi^2 n)^{1/3}$. The boundary scattering length $L = 1.15 \cdot 10^{-4} m$ is close to the smallest sample dimension.
One can also model $(TMTSF)_2ClO_4$ in the same manner, as shown in Fig. 7.13. At room temperature the magnetic susceptibilities of $(TMTSF)_2ClO_4$ and of $(TMTSF)_2PF_6$ are of comparable size. Therefore I assume for the calculation of κ_m of $(TMTSF)_2ClO_4$ a magnetic exchange coupling $J \approx 1400$ K [235]. The remaining parameters are found in Table 7.1.

I give now a posssible interpretation of our results. In a conventional metal one observes the usual (maybe enhanced) Pauli susceptibility of charge carriers, which does not give a sizeable magnetic contribution to the heat current larger than that of the mobile carriers itself. Our thermal conductivity results, in contrast, suggest that in spite of finite dc-conductivity the magnetic contribution to the heat current in the metallic systems is comparable to that of the insulating spin-Peierls system, i.e., the motion of charge carriers does not disturb the spin system. An intriguing interpretation of this finding is possible on the basis of spin/charge separation.
We assume that spin excitations on this spin chain, so called spinons, are mobile and may contribute to the heat current as discussed above.

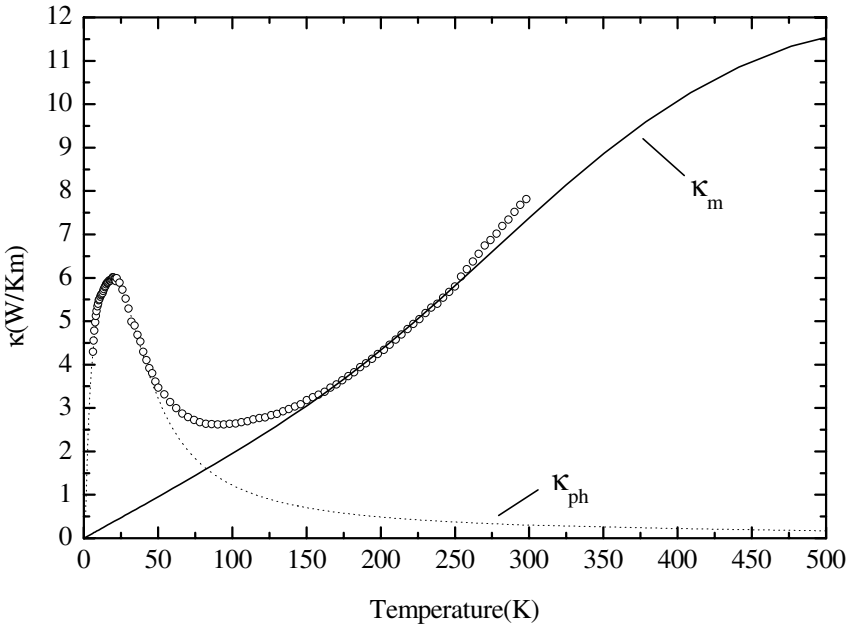

Figure 7.12: Thermal conductivity of $(TMTSF)_2PF_6$ along the a direction (open circles). The hypothetical phonon thermal conductivity κ_{ph} obtained by fitting the low temperature maximum with the standard Debye model is shown by the dotted line. The solid line reflects the estimated magnetic thermal conductivity $\kappa_m \propto c_m v_m l_m$. The magnetic specific heat c_m for a one-dimensional antiferromagnet was obtained theoretically [153, 187].

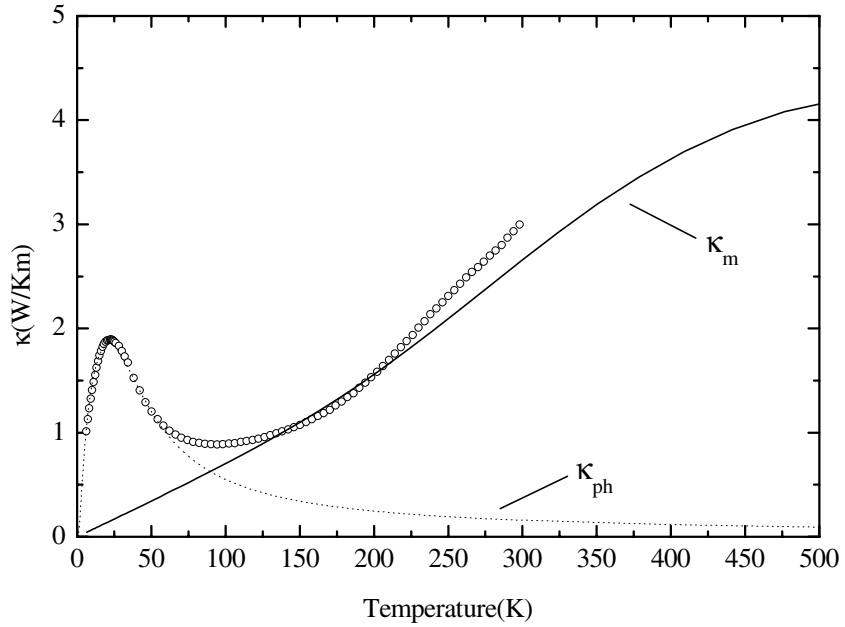

Figure 7.13: Thermal conductivity of $(TMTSF)_2ClO_4$ along the a direction (open circles). The hypothetical phonon thermal conductivity κ_{ph} obtained by fitting the low temperature maximum with the standard Debye model is shown by the dotted line. The solid line reflects the estimated magnetic thermal conductivity $\kappa_m \propto c_m v_m l_m$. The magnetic specific heat c_m for a one-dimensional antiferromagnet was obtained theoretically [153, 187].

Let us now assume that the spin chain is doped with a small concentration p of holes (i.e., that p electrons are removed)[6]. It is known theoretically that in one dimension (for infinite Coulomb repulsion U) a hole doped into the chain separates into a spinless charge excitation (called holon) and a chargeless spin excitation (the spinon) [239]. Remarkably, the charge excitation may move without disturbing the spin configuration on the chain, i.e., without the creation of additional spin excitations. For low doping level the magnetic excitation spectrum, i.e., the number of spinons, will be comparable to that of the undoped chain, while at the same time the holons give rise to dc-conductivity. The number of charge carriers is fixed by the doping level p independent of temperature, whereas the number of spinons increases with temperature just as in the undoped chains. In particular, for small hole doping the number of thermally excited spinons at high temperatures will be much larger than that of holons and therefore one may have a small dc-conductivity and a large spinon heat current at the same time.

	L	P	P^0_{FID}	U	u	J	$\bar{\chi}_s$
	10^{-4}	10^{-41}	10^{-42}	10^{-29}	-	-	10^{-4}
	[m]	$[s^3]$	$[s^3/T]$	$[s^2/K]$	-	[K]	[emu/mole]
$(TMTTF)_2PF_6$	0.2	6.3	5.0	1.55	1.0	600	4.0
$(TMTSF)_2PF_6$	1.15	4.0	3.3	1.4	1.1	1400	1.6
$(TMTSF)_2ClO_4$	0.1	5.8	4.0	1.8	1.35	1400	1.6

Table 7.1: Compilation of the fitting parameters. L, P, P_{FID}, U and u denote the characteristic sample length, the parameters for point defect, field induced point defect (FID), and Umklapp scattering, respectively. J stands for the magnetic exchange coupling constant and $\bar{\chi}_s$ for the average spin susceptibility.

Magnetic Field Dependence

I turn now to the magnetic field dependence of κ observable from the lowest temperatures up to about 100 K that is in all systems essentially the same. The magnetic field dependence of the low temperature maximum, common to all systems, is highly unusual. A possible way to understand this magnetic field dependence of the low temperature maximum is the formation of field induced structural defects giving rise to an additional scattering channel for phonons. I sketch the basic idea. It is known that applying a magnetic field leads to the creation of $s = 1$ excitations[7] on the quasi-one-dimensional spin chains. An associated local lattice distortion can then be expected if a finite coupling between the spin and the phonon-system is present. A second important point supporting our idea is that the Debye temperatures are very small for all Bechgaard salts, meaning the lattices are "soft". Hence appreciable local distortions may be created by the spin excitations. Phonons may be scattered by these local distortions whose number increases with increasing magnetic field leading to the suppression of κ.
Let us check whether these possible structural defects may become important with respect to

[6]This can be achieved by interchain single electron transfer between chains leading to "selfdoping" of individual chains, as discussed by Vescoli and coworkers [220].

[7]In 1-d these $s = 1$ excitations decay into two spinons each carrying spin $s = 1/2$.

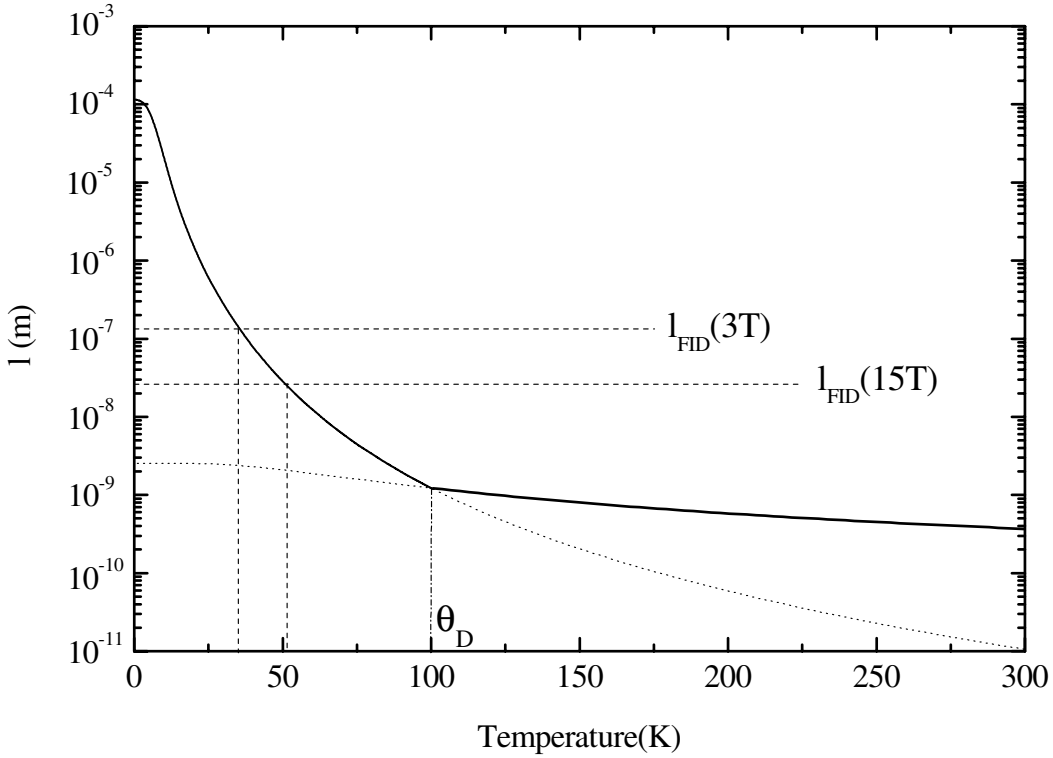

Figure 7.14: Estimated average mean free path l_{tot} (solid curves) using Eq. 7.1. The dotted curves are the completion of the solid curves to the higher and lower temperature regions separated by the Debye temperature Θ_D. The average distances of the field induced lattice defects for magnetic fields of 3 and 15 T are marked by the broken horizontal lines (see text).

the heat transport. An impact of the field induced defects (H > 0 T) on κ from the lowest temperatures up to about 100 K can only be expected if l_{FID}, which stands for the average distance between the distortions, is smaller than the overall scattering length l_{tot} which is the sum of boundary, point-defect and Umklapp-scattering lengths (and maybe others). Now, in the paramagnetic U-phase, l_{FID} can be estimated applying Eq. 2.27 in chapter 2 and $l_{FID} = \pi/\Delta k$. I use average values for the magnetic spin susceptibilitiy χ_s of $4 \cdot 10^{-4}$ and $1.6 \cdot 10^{-4} emu/mole$ for $(TMTTF)_2PF_6$ and $(TMTSF)_2PF_6$ respectively, which are obtained by ESR measurements [235, 236]. For a magnetic field of one Tesla one finds for l_{FID} values of $1 \cdot 10^{-6} m$ and $4 \cdot 10^{-7} m$ for $(TMTTF)_2PF_6$ and $(TMTSF)_2PF_6$ respectively. In order to make plausible that field induced defects may hamper the heat transport I compare l_{FID} with l_{tot}, given by

$$l_{tot} = v \cdot \tau, \text{ where } \tau^{-1} = \frac{v}{L} + P \cdot \omega^4 + U \cdot T\omega^3 exp(-\Theta_D/uT) \ . \tag{7.1}$$

The parameters L, P, U, and u for $(TMTTF)_2PF_6$ and $(TMTSF)_2PF_6$ and $(TMTSF)_2ClO_4$ are summarized in Table 7.1. There is, however, a difficulty – one has to deal with a single phonon frequency ω. In order to calculate l_{tot}, I approximate ω by $k_B/\hbar T$. This is justified for temperatures $T < \Theta_D$, but for higher temperatures one has to be cautious as all phonon frequencies are already excited. Thus I set $T = \Theta_D = 100$ K for $T > \Theta_D$. From this assumption it is clear that the results obtained have to be seen as crude estimations.
The analysis, representatively conducted on $(TMTSF)_2PF_6$ for all samples, is reasonable, as

illustrated in Fig. 7.14. The solid line represents the relevant scattering length l_{tot}. Let us compare l_{tot} with l_{FID} calculated for 3 and 15 Tesla (denoted by the horizontal lines $l_{FID}(3T)$ and $l_{FID}(15T)$). Obviously, for lower temperatures the mean free path of the phonons is limited by l_{FID}, whereas for higher temperatures l_{tot} dominates. From this we expect a sizeable magnetic field dependence below around 30 K (50 K) and no or only a weak impact of the magnetic field at higher temperatures for the 3(15)-Tesla curves. This is consistent with the experiment.
With these results and the assumption that the field induced structural defects behave like ordinary point defects I show now that even a quantitative description of the magnetic field dependence succeeds. I use the parameters of the zero magnetic field phonon fits, given in Table 7.1, and an extended point defect scattering rate (see also chapter 5) of the form

$$\tau_{pt}^{-1} = P\omega^4 + P_{FID}(H)\omega^4 \ , \tag{7.2}$$

with $P_{FID}(H) = P_{FID}^0 \cdot H$. P_{FID}^0 is a constant representing the scattering strength for field induced defects and H the magnetic field strength. The linearity in the magnetic field dependence accounts for the linear increase of the number density of field induced structural defects (see Eq. 2.27 in chapter 2).
The results are illustrated in Fig. 7.15. It is important to note that P_{FID}^0 is a fixed quantity (see Table 7.1) which was optimized in order to get the best fits of all the measurements in different fields. We see that our theoretical curves describe the magnetic field dependences of the low temperature maximum for all three samples very well. Note that the maxima of κ at 20 K do not vary linearily with magnetic field but rather saturate at higher fields. This is exactly reproduced by the calculations (best seen for $(TMTSF)_2PF_6$).
The parameter P_{FID}^0 should scale with the absolute value of $\bar{\chi}_s$ since P_{FID}^0 is proportional to the number density of field induced structural defects and these in turn are proportional to $\bar{\chi}_s$ evident from Eq. 2.27 in chapter 2. This is met for $(TMTTF)_2PF_6$ and $(TMTSF)_2PF_6$. There is unfortunately only a room temperature spin susceptibility available for $(TMTSF)_2ClO_4$, which makes in this case any conclusions questionable.

It is clear that our considerations are actually only valid above the transitions occuring in the samples at different temperatures. Below the spin-Peierls and the spin density wave transition the spin susceptibility χ_s and hence the number of magnetic excitations goes down if one lowers the temperature further. In view of our model we would thus expect a weaker field dependence of the thermal conductivity below the transitions because of the extinctions of the scattering centers. Interestingly, the data do not indicate a weaker magnetic field dependence of κ below the transition temperatures.
In conclusion, we have to admit that our model does not account for the heat transport at the lowest temperatures. Nevertheless, a close interpretation and a quantitative model for all systems was given in terms of a low temperature maximum and a high temperature maximum generated by magnetic excitations. Furthermore, a successful description of the magnetic field dependence of the low temperature phonon maximum in the framework of phonon- scattering on field induced local distortions is achieved, although a question mark has to be put over the conclusions considering the lowest temperatures.

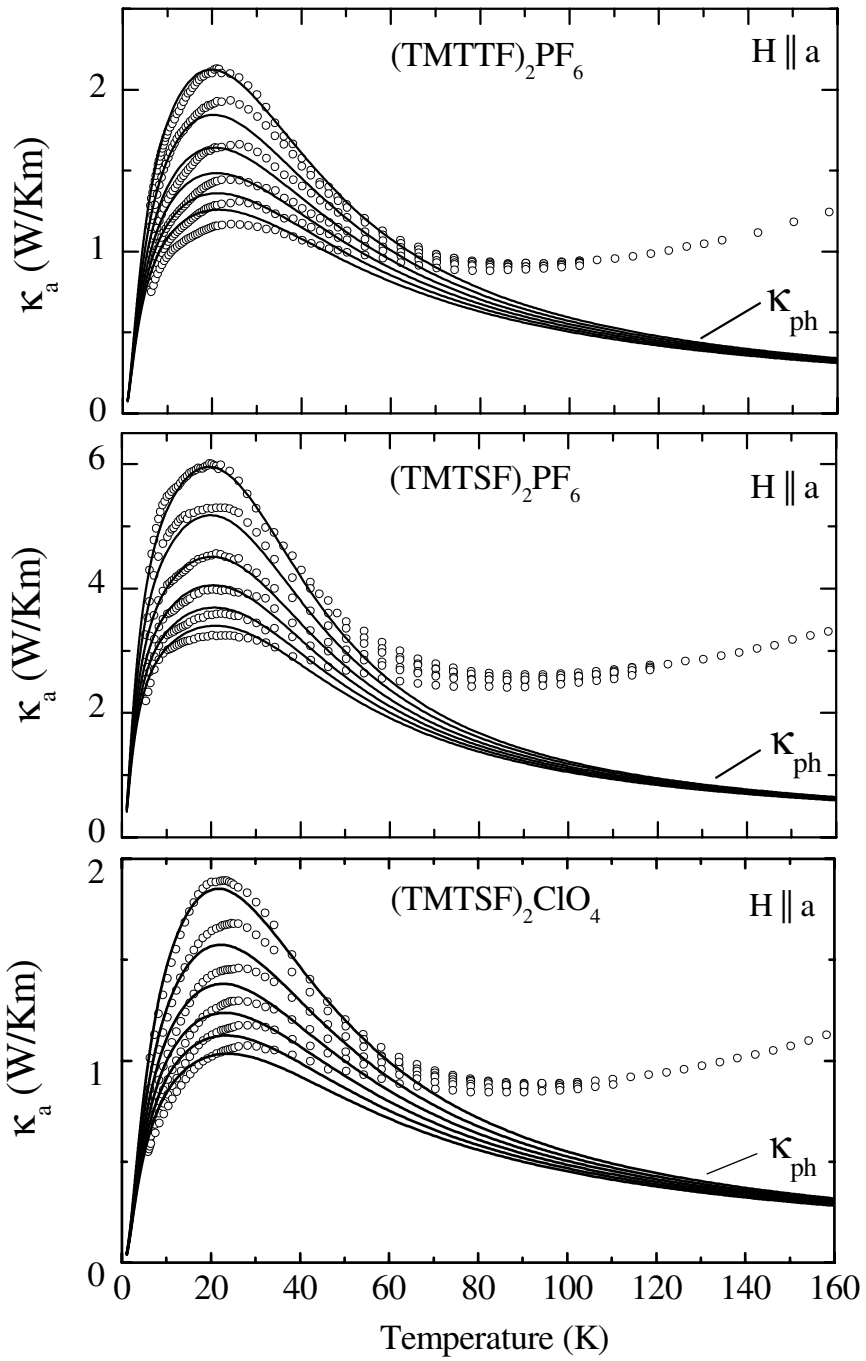

Figure 7.15: Thermal conductivity of $(TMTTF)_2PF_6$, $(TMTSF)_2PF_6$ and $(TMTSF)_2ClO_4$ for magnetic fields $(3, 6, 9, 12, 15\ T)$ aligned along the a direction. The lines are theoretical curves calculated for the same magnetic fields according to the standard Debye model with an extended point defect scattering rate given in Eq. 7.2.

Chapter 8

The Insulating Cuprate $Sr_2CuO_2Cl_2$

In this chapter a brief discussion of the heat transport of the quasi-two-dimensional spin system $Sr_2CuO_2Cl_2$ will be given. Whereas a large magnetic thermal conductivity seems to be established in several one-dimensional systems, the situation is less clear in two-dimensional systems. These are, nevertheless, of particular importance due to their relevance for high temperature superconductors and the nature of their magnetic excitations spectrum is currently under intensive debate [240–244].

8.1 Introduction

Remarkably, in insulating cuprates – as in the one-dimensional spin systems – the rare studies of the thermal conductivity performed so far reveal a characteristic double peak structure of the in-plane thermal conductivity comparable to that in one-dimensional systems [1, 2].
This is best seen in La_2CuO_4, the parent compound of high-T_C-superconductors. In Fig. 8.1 thermal conductivity measurements of undoped (x=0) and doped La_2CuO_4 are shown [1]. I will focus here on the anisotropy of κ_{ab} and κ_c in the x=0 curves. Both, κ_{ab} and κ_c

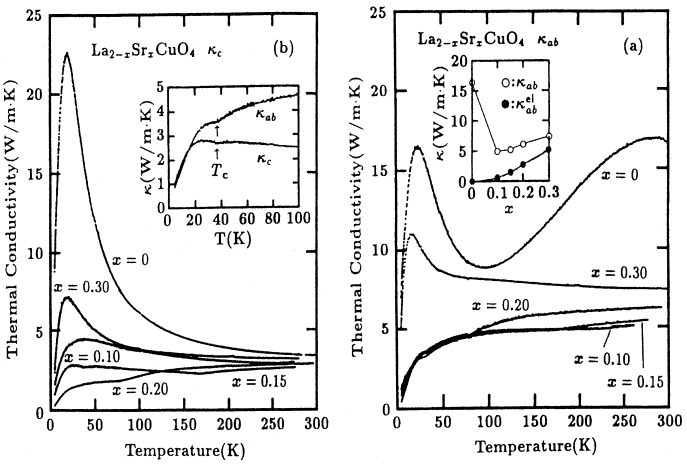

Figure 8.1:
In-plane and out-of-plane thermal conductivity of $La_{2-x}Sr_xCuO_4$ versus temperature. Inset (a) shows the doping dependence of κ_{ab} at 250 K. The increase of both, κ_{ab} and κ_c at T_c is plotted in inset (b). According to Nakamura et al. [1].

show pronounced maxima at around 20 K. These maxima can be addressed to conventional phonon heat transport (see also chapter 3) [1]. But at $\sim 300\ K$ κ_{ab} shows an additional broad maximum not found in κ_c. It has been claimed that this indicates a sizeable magnetic contribution to the heat current of the in-plane thermal conductivity κ_{ab} [1]. However, it has also been proposed that anomalous damping of the in-plane heat carrying phonons resulting from a structural instability could explain the experimental results. Thus, the interpretation of heat transport in insulating cuprates and the possibility of unusual magnetic contributions to the thermal conductivity in two dimensions have to be considered as open problems.

8.2 Experimental Results

In order to clarify the picture, I conducted measurements of the in-plane thermal conductivity of $Sr_2CuO_2Cl_2$, which is isostructural to La_2CuO_4. This material is believed to provide the best realization of the two-dimensional Heisenberg-model. Moreover, the material is free from complications related to doping or structrual instabilities associated with the buckling of the CuO_2-planes. Therefore, an anomalous damping of the phonon heat current is not expected, which predestines $Sr_2CuO_2Cl_2$ to scrutinize the findings in La_2CuO_4.
The single crystal of $Sr_2CuCl_2O_2$ used in this study is of rectangular form with dimensions $1 \times 3 \times 4\text{mm}^3$, where the short direction is along the crystallographic c direction. It was grown by the traveling solvent floating zone method [245]. The thermal conductivity was measured with the heat current along the long direction (within the CuO_2-planes) by the conventional steady state method[1].

In Fig. 8.2 the in-plane thermal conductivity of $Sr_2CuO_2Cl_2$ is plotted as a function of temperature. We identify two maxima in the temperature dependence of κ at $T_L \approx 30$ K and $T_H \approx 250$ K. The absolute value of κ at the low temperature maximum of about 35 W/Km indicates a good crystal quality. For comparison, the in-plane thermal conductivity of a single crystal of La_2CuO_4 measured by Nakamura et al. is also shown [1]. These data of La_2CuO_4 clearly reveal the double peak structure of the thermal conductivity where the high temperature maximum of is even more pronounced than the low temperature maximum. The absolute value of κ of the low temperature maximum is with ~ 15 W/Km smaller than that of $Sr_2CuO_2Cl_2$. The reason is most probably that La_2CuO_4 is much more sensitive to defects, resulting perhaps from oxygen loss, which introduces lattice defects and hole doping, and thus reduces the low temperature mean free path of the heat carrying excitations.

[1] We note that in our first experiments on $Sr_2CuO_2Cl_2$ we had some problems due to the fact that this compound is strongly hygroscopic. Exposure to air for an hour results in a blue surface layer. The corresponding 'phase' has a thermal conductivity distinctly different from that of bulk $Sr_2CuO_2Cl_2$. At low temperatures such samples show a rather pronounced magnetic field dependence which is, however, not reproducible. All measurements presented here are free from such complications.

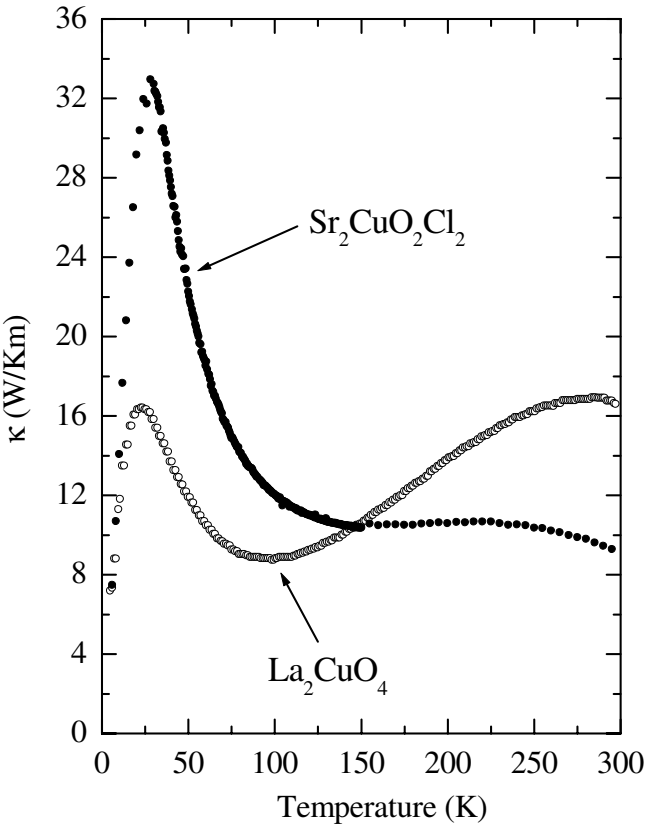

Figure 8.2:
In-plane thermal conductivity κ versus temperature for single crystals of $Sr_2CuO_2Cl_2$ and La_2CuO_4, respectively. The data for La_2CuO_4 have been taken from Nakamura et al. [1].

8.3 Discussion

In an insulator the heat is usually carried by phonons. The typical phonon thermal conductivity κ_{ph} of a crystalline insulator shows one maximum at low temperatues, as shown in Fig. 3.1 in chapter 3.
It is highy unlikely that the double peak structure of the thermal conductivity found here can be attributed to conventional phononic heat transport: (i) Assuming that the low temperature maximum is due to κ_{ph}, the decrease of κ above T_L has to be attributed to a decrease of the mean free path of the phonons. It is unreasonable to assume that l and thus κ should increase again at high temperatures. (ii) The out-of-plane thermal conductivity of La_2CuO_4 measured with the heat current perpendicular to the CuO_2-planes does not show any indication of a high temperature maximum, but is consistent with a usual phononic scenario with one low temperature maximum approximately around T_L. Such a strong anisotropy of κ is not expected for a purely phononic thermal conductivity[2].

A possible explanation of a double peak structure of κ_{ph} involves an additional scattering of phonons mostly active in a narrow temperature range close to the minimum of κ_{ph}. This scenario has recently been discussed in the context of resonant scattering of phonons by magnetic excitations in $SrCu_2(BO_3)_2$ (see chapter 5). Such strong additional damping of phonons

[2]Because the $Sr_2CuO_2Cl_2$ sample has the form of a little tile measuring the out-of-plane thermal conductivity of $Sr_2CuO_2Cl_2$has not been successful so far.

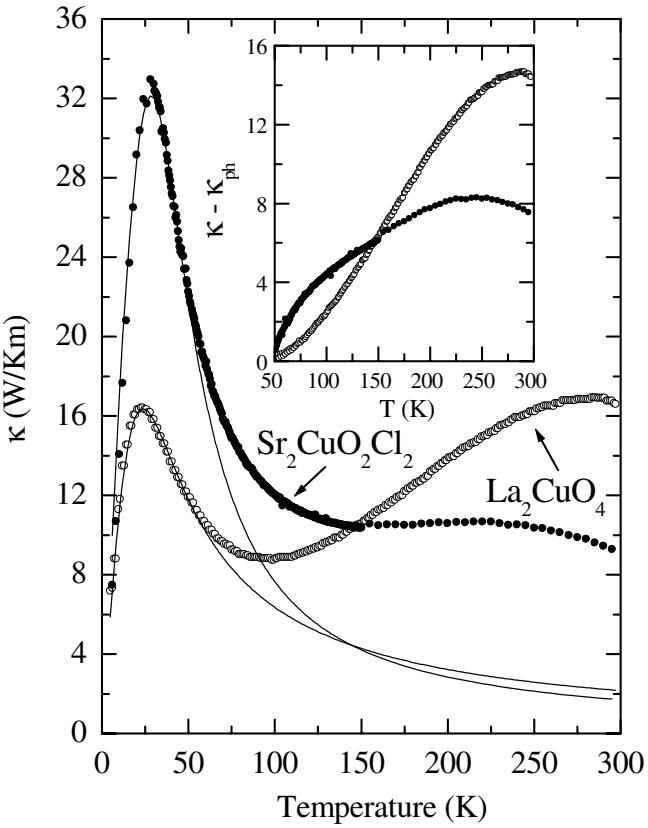

Figure 8.3:
In-plane thermal conductivity κ versus temperature for single crystals of $Sr_2CuO_2Cl_2$ and La_2CuO_4. The data for La_2CuO_4 have been taken from Nakamura et al. [1]. The solid lines represent fits to the low temperature maxima of $Sr_2CuO_2Cl_2$ and La_2CuO_4 using a Debye model for the phonon contribution. Inset: Difference between κ and κ_{ph} for $Sr_2CuO_2Cl_2$ and La_2CuO_4.

may also arise from phonon-phonon scattering near a structural instability. However, no structural instability is present in $Sr_2CuO_2Cl_2$. Moreover, the comparison of $Sr_2CuO_2Cl_2$ and La_2CuO_4 shows that the height of the low temperature maximum varies rather independently from that of the high temperature maximum. This suggests that the high temperature maximum is due to an additional non-phononic channel of heat transport.

In a 2-d Heisenberg system with large magnetic coupling constant J, a natural candidate for an additional channel of heat transport is a magnetic contribution κ_m to the thermal conductivity. In order to extract κ_m from the data we need to know κ_{ph}. Assuming that the low temperature peak is mostly due to phonons, we obtain κ_{ph} by fitting the low temperature

	P $[10^{-43}s^3]$	U $[10^{-30}s^2/K]$	u	D $[10^{-17}s]$
$Sr_2CuCl_2O_2$	6.7	3.5	2.4	4.2
La_2CuO_4	20	2.5	4.9	7.4

Table 8.1: Compilation of the fitting parameters for the phonon thermal conductivity. Good fit of the low temperature peak is achieved only, when in addition to the conventional scattering rates scattering of phonons by sheet-like faults is included. This can possibly be linked to the anisotropy of the system. However, the high temperature behavior of the calculated curves is essentially unaffected by this additional scattering channel.

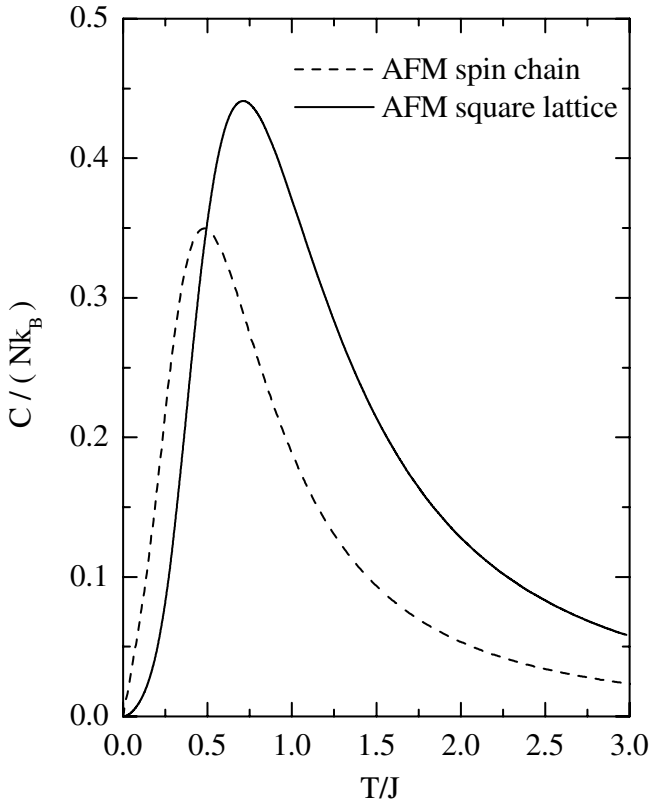

Figure 8.4:
Specific heat c of an antiferromagnetic spin chain and of an antiferromagnetic square lattice [111, 187].

data using a standard Debye model for phonon thermal conductivity (see chapter 3). For La_2CuO_4 the Debye temperature is given by $\Theta_D \simeq 280$ [246]. The sound velocity v is then straightforwardly calculated [7]. For $Sr_2CuO_2Cl_2$, no experimental value for Θ_D is available. Thus the fitting procedure for $Sr_2CuO_2Cl_2$ was conducted with the same Θ_D and v as used for La_2CuO_4. The remaining parameters are given in table 8.1.
Extrapolating κ_{ph} to higher temperatures we identify an additional contribution to the heat current, given by $\kappa_m = \kappa - \kappa_{ph}$, shown in the inset of Fig. 8.3 for both, La_2CuO_4 and $Sr_2CuO_2Cl_2$. Remarkably, the two additional contributions are of comparable magnitude, roughly of the order of 10 W/Km. The maximum of κ_m is around 250 K for $Sr_2CuO_2Cl_2$ and around 280 K for La_2CuO_4.

Is a magnetic contribution of magnitude 10 W/Km reasonable in La_2CuO_4 and $Sr_2CuO_2Cl_2$? In order to answer this question we attempt to estimate the mean free path of the magnetic excitations in $Sr_2CuO_2Cl_2$. We use $\kappa_m = (1/2)c_m v_m l_m$ for the magnetic contribution to κ. The velocity of long wavelength spin waves at low temperatures is obtained from neutron scattering experiments and amounts to $v_m \approx 1.3 \cdot 10^5$ m/s [247].
For the magnetic specific heat c_m we make use of theoretical results. In Fig. 8.4 the calculated magnetic specific heat of the two-dimensional Heisenberg antiferromagnet [111] and for a one-dimensional spin chain [187] is plotted. The largest value of the magnetic specific heat of the AFM square lattice amounts to $\sim 0.45 N_A k_B$. For $Sr_2CuO_2Cl_2$, this corresponds to $c_m^{max} \approx 4.9 \cdot 10^4 \mathrm{J/Km^3}$. Inserting the obtained values for v_m and c_m in the above equation for κ_m yields for the mean free path of the magnetic excitations $l_m \approx 29$Å. The magnetic exchange coupling constant J is around 1200 K for $Sr_2CuO_2Cl_2$. Hence, the maximum of

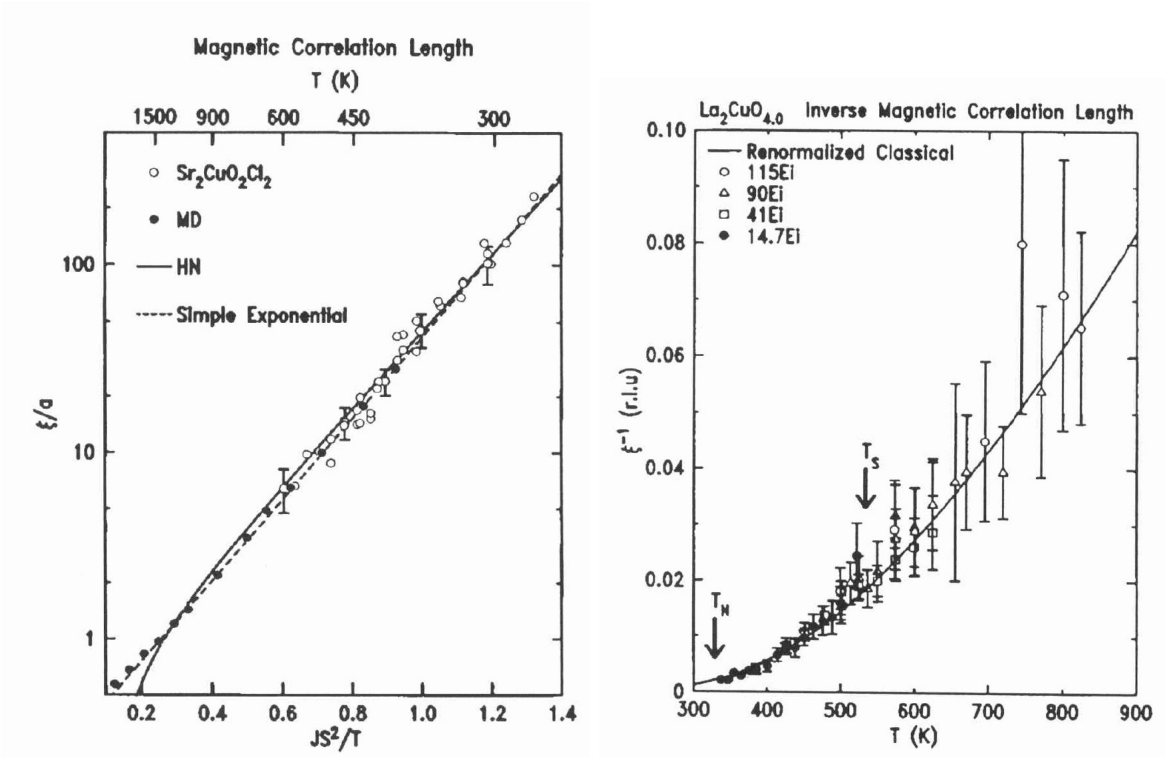

Figure 8.5: Left: Reduced magnetic correlation length in a semilogarithmic plot as function of J/T. The data points (open circles) are obtained using $J = 125meV$ in combination with the lattice constant a. A rather good agreement is achieved between various theoretical predictions, e.g., Monte Carlo simulations (MD), the nonlinear sigma model (HN) and the simple exponential form suggested by Maviki and Ding. Right: Inverse magnetic correlation length of La_2CuO_4 in reciprocal lattice units as function of temperature. The solid curve corresponds to a theoretical calculation with $J = 135meV$. T_N and T_S mark the Néel and structural transition, respectively [238].

the magnetic specific heat c_m is at around 850 K (see Fig. 8.4). As c_m is about a factor of 5 smaller than c^{max} at 300 K, we obtain $l(300K) \approx 145$Å in the relevant temperature range. This value of the mean free path is rather small, rendering a magnetic contribution to the heat current possible.

An upper limit of l_m is given by the magnetic correlation length ξ. Obviously, in the antiferromagnetically ordered state $\xi \to \infty$. Above T_N the magnetic correlation length is still large ($\xi/a \approx 100$ at 300 K in $Sr_2CuO_2Cl_2$, where a is the lattice spacing, see Fig. 8.5). However, with increasing temperature ξ/a drops strongly, approximately exponentially, yielding $\xi/a \approx 20 - 30$ at 400 K and $\xi/a \approx 1$ at the maximum of c_m [248, 249]. This strong decrease of ξ implies a corresponding strong decrease of l_m above the Néel temperature. Therefore the maximum of κ_m is expected to occur at much lower temperatures than the maximum of the magnetic specific heat.

We conclude, an in-plane magnetic contribution to the heat current can be present, even above the Néel-temperature, due to the still sizeable magnetic correlation length.

	T_H (K)	J (K)	J/T_H
$YBa_2Cu_3O_6$	200	1125	5.6
$Sr_2CuCl_2O_2$	230	1200	5.2
La_2CuO_4	270	1400	5.2

Table 8.2: Position T_H of the high temperature maximum of κ, magnetic coupling constant J and the ratio J/T_H for three insulating cuprates. The values of J are taken from Ref. [238]. The data of κ in $YBa_2Cu_3O_6$ and La_2CuO_4 are from Refs. [1] and [2], respectively.

I turn at this point to a comparison of my results to those found in other insulating cuprates. A double peak structure of κ has also been reported for $YBa_2Cu_3O_6$ [2]. The main feature of this data is a high temperature maximum of κ around 200 K. As in La_2CuO_4, this high temperature maximum of κ is absent for the out-of-plane thermal conductivity. In addition the maximum is strongly dependent on oxygen content. In so far, the experimental results of $YBa_2Cu_3O_6$ strongly resemble those of La_2CuO_4 and $Sr_2CuO_2Cl_2$.
We compare in Tab. 8.2 the peak position and the magnetic coupling constants for all three different insulating cuprates. Obviously, the peak position increases with J, which suggests that in all three materials the high temperature structure can be related to the magnetic excitations.

In summary, I have presented experimental data of the thermal conductivity of $Sr_2CuO_2Cl_2$, that clearly shows a double peak structure. Since there is no structural instability in this material, an explanation in terms of additional phonon damping can be excluded. The broad high temperature maximum makes a sizeable magnetic contribution to the heat current possible, comparable to the phononic contribution at 300 K. The temperature dependence and the absolute size of this contribution is consistent with what is expected from the specific heat and magnetic correlation length. A comparison to other insulating cuprates suggests that the large magnetic contribution can be an intrinsic feature of the mono-layer cuprates, if not of all insulating cuprates.

Chapter 9

Summary

In this thesis the thermal conductivity κ of low-dimensional spin systems was systematically investigated.
A device for high accuracy measurements of the thermal conductivity, using the standard steady state method, has been set up. The system permits measurements of κ as a function of temperature and/or as a function of the magnetic field. Depending on the cryomagnetic system it is possible to operate in a temperature range from ~ 2.2 Kelvin up to ~ 300 Kelvin and in magnetic fields up to 17 Tesla. The measurement insert can also be operated in high field cryomagnetic systems, e.g., in the High Field Laboratory of Nijmegen (The Netherlands) where magnetic fields up to 30 Tesla can be generated. The system is computer controlled which enables the running of different measuring programs, the automatic data acquisition and data analysis.
As the temperature differences are detected by thermocouples a procedure permitting the precise calibration of the AuFe-Chromel-P and Constantan-Chromel-P thermocouples, was worked out. This is necessary for an accurate measurement of κ. To verify the procedure, several test measurements of κ on quartz glass (SiO_2) were conducted. Since κ of SiO_2 is "universal" and does not depend on the magnetic field it is most suitable to calibrate thermocouples in magnetic fields. A comparison to previous measurements on quartz glass confirms our calibration method and verifies the reliability of the measurement device (see chapter 4).

The following low-dimensional spin systems have been studied: the spin-Peierls system $CuGeO_3$, the Bechgaard salts $(TMTSF)_2PF_6$, $(TMTTF)_2PF_6$ and $(TMTSF)_2ClO_4$, the spin dimer system $SrCu_2(BO_3)_2$, and the 2-d Heisenberg antiferromagnet $Sr_2CuO_2Cl_2$. The thermal conductivity of the low-dimensional quantum spin systems, summarized above, is very remarkable. Our detailed experimental studies show anomalous heat transport in all systems investigated. In each compound one finds instead of one low temperature maximum of κ, that is observed in "conventional" crystalline solids, unexpected additional maxima. Furthermore, a strong magnetic field dependence of the thermal conductivity in all samples, besides $Sr_2CuO_2Cl_2$, is found. This field dependence backs the idea that magnetic excitations heavily effect the heat transport.

In the 2-d spin liquid system $SrCu_2(BO_3)_2$, the thermal conductivity parallel (κ_a) and perpendicular (κ_c) to the magnetic planes has a characteristic double-peak structure with

two maxima. For both directions the low temperature maxima have a pronounced magnetic field dependence. A significant magnetic contribution to the heat current can, however, be excluded, because the double peak structure is not anisotropic and because the magnetic excitations are (almost) localized.
A quantitative analysis in terms of resonant scattering of phonons by magnetic excitations, performed with the collaboration of G.S. Uhrig, explains the double peak structures and their magnetic field dependence very well and gives evidence for strong spin-phonon coupling. I want to emphasize that spin-phonon coupling in conjunction with spin conservation has to be taken into account in order to describe our results. Moreover, the inclusion of bound triplets and bound singlets is necessary for a correct description of the magnetic field dependence of κ. In addition, our model allows a good description of the magnetic field dependent specific heat data of $SrCu_2(BO_3)_2$, with the same parameter set used for the calculated thermal conductivity.

The systematic study of the heat transport in the spin-Peierls system $CuGeO_3$ has left us with a complex picture. In pure $CuGeO_3$ a double peak structure of the thermal conductivity along the c and b direction, i.e., parallel and perpendicular to the spin chains, is observed. Along these directions the low temperature maximum around 5 K is strongly suppressed in applied magnetic field. Along the a direction only one maximum is detected and no magnetic field dependence is observed. Regarding the magnetic excitation spectrum a magnetic contribution to the heat current is thinkable along the b and c directions. Along the a direction the magnetic exchange coupling is so weak that no magnetic contribution is expected. Unfortunately, we cannot assign the single maximum of κ_a at $\simeq 32$ K to either of the maxima found in κ_c and κ_b that are located at about 5 K and 15 K. This and the similar temperature dependence of κ_b and κ_c prevent a clear identification of a possible additional magnetic contribution and we are left with at least three scenarios.
1.) The low temperature peak is due to phonons and a magnetic contribution causes the high temperature maximum. The magnetic field dependence of the low temperature maximum can then be attributed to the closing of the spin gap with increasing magnetic field. This leads to an increase of the number of magnetic excitations on which phonons can be scattered. This scenario was also proposed by Ando et al. [63].
2.) The low temperature maximum can be attributed to a magnetic contribution and the high temperature peak can be assigned to the conventional phonon heat transport. At first sight this is amazing because below T_{SP} a gap opens and the magnetic excitations die out rapidly, i.e., the number density and hence the magnetic specific heat vanishes. From this one would expect no or little magnetic contribution to the heat current below T_{SP}. However, when we consider scattering among the magnetic excitations as the most important scattering mechanism, the relaxation rate and hence the mean free path l of the magnetic excitations may become larger. The increase of the mean free path may even overcompensate the decrease of the number of excitations leading to an overall increase of κ_m. The suppression of κ with increasing magnetic field follows then from the enhancement of the "magnon-magnon" scattering by closing the spin gap due to Zeeman splitting. An analogous scenario is realized, e.g., in ^{3}He and in the *High-T_c* superconductor $YBa_2Cu_3O_7$.
3.) There is only one maximum caused by phonons and/or "magnons" which is suppressed in a narrow temperature range close to T_{SP} due to anomalous phonon/"magnon" scattering in the vicinity of the phase transition. As T_{SP} shifts to lower temperatures with increasing magnetic field the low temperature peak is further suppressed. A similar scenario involving,

however, phonon scattering on magnetic excitations, is successfully applied to the two-dimensional spin dimer system $SrCu_2(BO_3)_2$.
In order to work out the microscopic mechanisms of the anomalous heat transport in $CuGeO_3$ we studied systematically the influence of Mg and Zn doping on the heat transport along the crystallographic b and c directions. Both Mg and Zn doping drastically effect the thermal conductivity behavior. The most striking feature, however, is the occurrence of a third maximum in both, κ_b and κ_c of $Cu_{0.992}Mg_{0.008}GeO_3$ around 85 K and 150 K, respectively. The analysis of the thermal conductivity data, including the experimental findings on $Cu_{1-x}Zn_xGeO_3$ (x=0.7, 1.4 and 2.2%) suggests the high temperature structure to be most probably caused by an additional scattering of phonons on magnetic excitations in a narrow temperature range around 40 K.
Unfortunately, we cannot extract further information from the low temperature measurements of κ on $Cu_{0.992}Mg_{0.008}GeO_3$ and on $Cu_{1-x}Zn_xGeO_3$ (x=0.7, 1.4 and 2.2%) as no drastic changes of the heat transport can be detected, i.e., the double peak structure still exists and the ratio κ_b/κ_c is roughly the same as for pure $CuGeO_3$.
First numerical calculations of magnetic contributions to κ based on a kinetic approach gives us hope for a deeper understanding of the heat transport in $CuGeO_3$. We can model a magnetic contribution to κ that shows a sizeable maximum around 5 K, assuming reasonable parameters for the boundary scattering length and the "magnon-magnon" mean free path. The model also produces the correct anisotropy ratio and shows qualitatively the correct magnetic field dependence. In contrast, it is not possible to reproduce the correct anisotropy when we try to reproduce the maximum of κ at 15 K. Therefore, one might favor the interpretation where the 5 K maximum is of magnetic origin and the 15 K maximum is of phononic origin. However, in this field many interesting questions are still to be answered, i.e., the frequency dependencies of the various scattering scenarios, namely of "magnon-magnon" Umklapp-scattering, of the "magnon"-scattering on point defects and others.

An anomalous thermal conductivity is also observed in the Bechgaard salts. The electrical insulator $(TMTTF)_2PF_6$, the spin density wave system $(TMTSF)_2PF_6$, and the superconductor $(TMTSF)_2ClO_4$ show the same features: First, we observe a low temperature maximum around 20 K which is strongly suppressed by a magnetic field. This effect is independent of the material and of the orientation of the sample with respect to the magnetic field direction. Second, a steep increase of κ above about 100 K is found. The increase is smaller in the spin-Peierls system $(TMTTF)_2PF_6$ saturating at about 300 K, while for the spin density wave system $(TMTSF)_2PF_6$ and the superconductor $(TMTSF)_2ClO_4$ no saturation at room temperature is apparent.
Regarding the magnetic excitation spectrum, a quite natural explanation for the high temperature maximum of κ can be given for the spin-Peierls system, if an additional magnetic contribution to κ is assumed. Due to the strong electronic correlations the material corresponds to a one-dimensional Mott-Hubbard chain, i.e., a one-dimensional antiferromagnetic insulator. We attribute the low temperature maximum to a phonon contribution to κ and the high temperature "maximum" to a magnetic contribution. In the metallic samples one expects that the thermal conductivity has a phononic and electronic contribution which add to the total thermal conductivity. However, applying the Wiedemann-Franz law we find that the electronic contribution cannot account for the temperature and magnetic field dependence of κ. Therefore we suggest that a magnetic contribution, comparable to that

found in the organic spin-Peierls system $(TMTTF)_2PF_6$, is also present in the metallic systems. This points to the scenario of spin/charge separation, discussed intensively for 1-d metals.
The magnetic field dependence of the low temperature maximum is understood in the framework of phonon scattering on field induced structural defects. We suggest that the application of an external magnetic field leads to the creation of $s = 1$ excitations on these quasi-one-dimensional spin chains. An associated local lattice distortion can be expected if a finite coupling between the spin and the phonon system is present. A second important point supporting this idea is that the Debye temperatures are very small for all Bechgaard salts indicating the softness of the lattice. Hence appreciable local distortions may be created by the spin excitations. Phonons may be scattered by these local distortions whose number increases with increasing magnetic field leading to the suppression of κ. Using a conventional Debye model of phonon thermal conductivity, in conjunction with an extended point defect scattering rate, we are even able to model very well the magnetic field dependence of the low temperature maximum of κ.

The thermal conductivity of La_2CuO_4, the parent compound of the high-temperature superconductors shows a pronounced double peak structure of κ with one maximum at about 20 K and a high temperature maximum at $\simeq 270$ K [1]. Perpendicular to the CuO_2-planes the high temperature maximum is absent. The interpretation of the thermal conductivity results is, however, controversial because structural instabilities and oxygen-non-stoichiometries are present in this material. An interpretation in terms of phonon damping due to structural instabilities is given by Cohn et al. [2]. However, an interpretation in terms of an additional magnetic contribution to the heat current at high temperatures is also possible.
In $Sr_2CuO_2Cl_2$, we also find a double peak structure of κ. A damping of the phonon contribution to κ can be excluded because no structural instabilities and no oxygen-non-stoichiometries are present in this material.
The comparison to La_2CuO_4 and $YBa_2Cu_3O_6$ reveals that the high temperature maxima are evident in these compounds. There are essentially three reasons making a magnetic contribution to the heat current at high temperatures possible. First, the magnetic exchange coupling constant J is very large (of the order of 1000–1500 K). This implies that the maximum of the magnetic specific heat is also located at high temperatures (roughly at $2/3J$). Second, the mean free paths l necessary to account for a magnetic contribution of this size is of a reasonable magnitude, and, in particular, smaller than the in-plane magnetic correlation length. This suggests that a large magnetic contribution can be an intrinsic feature of the mono-layer cuprates, if not of all insulating cuprates.

In conclusion, anomalous behavior of the thermal conductivity is observed in all low dimensional spin systems studied in this thesis. In $SrCu_2(BO_3)_2$ we address the unusual temperature and magnetic field dependence to the scattering of phonons on magnetic excitations. No magnetic contribution to κ is present here.
In $CuGeO_3$ we suggest that the high temperature structure of κ arises from phonon scattering by magnetic excitations. However, the double peak structure at low temperatures is puzzling. No clear identification of a magnetic contribution can be given. Possibly, one deals here with coupled magnetoelastic modes. This idea is supported by the fact that in $CuGeO_3$ a strong spin-phonon coupling is present [130]. In addition the energy scales of the phonon system, characterized by the Debye temperature ($\Theta_D \approx 300$ K), and the magnetic system

characterized by the exchange coupling constant ($J \approx 160$ K) are of similar size. Possibly, this makes an unambiguous discrimination of a phonon and "magnon" thermal conductivity in $CuGeO_3$ unfeasible.
In the Bechgaard salts the energy scales of the phonon system ($\Theta_D \approx 100$ K) and the magnetic system ($J \approx 1000$ K) are distinctly different. Apparently, one can discriminate the phonon and the "magnon" contribution to the total heat current. We suggest the high temperature maxima of κ arises in all three systems from an additional magnetic contribution. The low temperature maxima, located at the same temperature for the three systems, is addressed to phonons scattered by field induced lattice deformations.
Likewise, a double peak structure of the thermal conductivity is found in the 2-d spin system $Sr_2CuO_2Cl_2$. The maximum at high temperatures is most probably due to an additional magnetic contribution to κ. We suggest the low temperature peak to be purely phononic. Here, no magnetic field dependence of κ is observed. As in the Bechgaard salts, the phonon and "magnon" energies are of distinctly different size ($\Theta_D \approx 280$ K and $J \approx 1200$ K) in $Sr_2CuO_2Cl_2$. This most probably allows also a distinct separation into phonon and "magnon" contributions to κ in this compound.

Bibliography

[1] Y. Nakamura, S. Uchida, T. Kimura, N. Motohira, K. Kishio and K. Kitazawa. *Phys. Rev.* B **55**, 1409 (1991).

[2] J. L. Cohn, C.K. Lowe-Ma and T. A. Vanderah. *Phys. Rev.* B **52**, R13134 (1995).

[3] R. Desquiotz, M. Hofmann and E. Dormann. *Europhysical Journal* B **16**, 403 (1999).

[4] W. Brütting, P. H. Nguyen, W. Rieß and G. Paasch. *Phys. Rev.* B **51**, 9533 (1995).

[5] S. Kagoshima, H. Nagasawa and T. Sambongi. *One-Dimensional Conductors, Springer Series in Solid State Science 72.* Springer, Berlin 1988.

[6] D. Reidel. *Physics and Chemistry of Materials with Low-dimensional Structures Series A: Layered Structures (General Ed. E. Moses), Dordrecht: D.Reidel Publ., Vols. 1-6.* V.J. Emery, World Scientific Publishing 1979.

[7] N.W. Ashcroft and N.D. Mermin. *Solid State Physics.* Saunders College Publishing 1976.

[8] M.J. Rice and S. Strässler. *Sol. State Commun.* **13**, 125 (1973).

[9] G.A. Toombs. *Physics Reports* **40**, 181 (1978).

[10] P. A. Lee, T. M. Rice and P. W. Anderson. *Phys. Rev. Lett.* **31**, 462 (1973).

[11] M.J. Rice and S. Strässler. *Sol. State Commun.* **13**, 1389 (1973).

[12] B. Horovitz, H. Gutfreund and M. Weger. *Phys. Rev.* B **12**, 3174 (1975).

[13] P. Monceau. *Electronic Properties of Inorganic Quasi-One-Dimensional Compounds (I+II).* Reidel, Dordrecht 1985.

[14] L.G. Caron H.J. Schulz in: D. Jérome. *Low-Dimensional Conductors and Superconductors.* Plenum, New York 1985.

[15] C. Math, W. Brütting and W. Rieß. *Europhys. Lett.* **35**, 221 (1996).

[16] G. Grüner. *Rev. Mod. Phys.* **60**, 1129 (1988).

[17] L. Gorkov and G. Grüner. *Charge Density Waves in Solids.* North Holland, Amsterdam 1989.

[18] John Bardeen. *Phys. Rev.* B **39**, 3528 (1989).

[19] G. Grüner. *Density Waves in Solids, Frontiers in Physics Series 89.* Addison-Wesley 1994.

[20] P. Fazekas. *Electron Correlation and Magnetism.* World Scientific 1999.

[21] A. W. Overhauser. *Phys. Rev.* **128**, 1437 (1962).

[22] L.P. Le et al. *Europhys. Lett.* **15**, 547 (1991).

[23] M. Braden, B. Hennion, W. Reichardt, G. Dhalenne and A. Revcolevschi. *Phys. Rev. Lett.* **80**, 3634 (1998).

[24] M. Cross and D.S. Fisher. *Phys. Rev.* B **19**, 402 (1979).

[25] E. Pytte. *Phys. Rev.* B **10**, 4637 (1974).

[26] J.W. Bray. *Sol. State Commun.* **26**, 771 (1978).

[27] J.W. Bray. *Sol. State Commun.* **35**, 853 (1980).

[28] L.N. Bulaevskii, A.I. Buzdin and D.I. Khomskii. *Sol. State Commun.* **27**, 5 (1978).

[29] A.I. Buzdin, M.L. Kulic and V.V. Tugushev. *Sol. State Commun.* **48**, 483 (1983).

[30] M. Fujita and K. Machida. *J. Phys. Soc. Japan* **53**, 4395 (1984).

[31] Y. Lépine. *Sol. State Commun.* **57**, 189 (1986).

[32] M.C. Cross. *Phys. Rev.* B **20**, 4606 (1979).

[33] M. Abramovitz and J.A. Stegun. *Handbook of Mathematical Functions.* Dover, New York 1964.

[34] S.M. Bhattacharjee, T. Nattermann and C. Ronnewinkel. *Phys. Rev.* B **58**, 2658 (1998).

[35] R. Chitra, Swapan Pati, H. R. Krishnamurthy, Diptiman Sen and S. Ramasesha. *Phys. Rev.* B **52**, 6581 (1995).

[36] G. Castilla, S. Chakravarty and V. J. Emery. *Phys. Rev. Lett.* **75**, 1823 (1995).

[37] K. Okamoto and K. Nomura. *Physics Lett.* **A169**, 433 (1992).

[38] S. Eggert. *Phys. Rev.* B **54**, R9612 (1996).

[39] C.K. Majumdar and D.K. Gosh. *J. Math. Phys.* **10**, 1388 (1969).

[40] C.K. Majumdar. *J. Phys. C – Solid State Phys.* **3**, 911 (1970).

[41] B.S. Shastry and B. Sutherland. *Phys. Rev. Lett.* **47**, 964 (1981).

[42] P. Debye. *Vorträge über die kinetische Theorie der Materie und Elektrizität.* Teubner, Leibzig and Berlin 1914.

[43] J.M. Ziman. *Electrons and Phonons.* Oxford at the Clarendon Press 1960.

[44] P.G. Klemens. *Thermal Conductivity and Lattice Vibrational Modes, in Solid State Physics.* H. Ehrenreich, F. Seitz and D. Turnbull (Academic, NewYork), Vol. 7 1958.

[45] P. Carruthers. *Rev. Mod. Phys.* **33**, 92 (1962).

[46] J. Callaway. *Phys. Rev.* **113**, 1046 (1959).

[47] J. Callaway. *Phys. Rev.* **122**, 787 (1961).

[48] Baxter H. Armstrong. *Phys. Rev.* B **23**, 883 (1981).

[49] Baxter H. Armstrong. *Phys. Rev.* B **32**, 3381 (1985).

[50] Neelmani and G. S. Verma. *Phys. Rev.* B **6**, 3509 (1972).

[51] J.M. Ziman. *Principles of the Theory of Solids.* Cambridge University Press 1972.

[52] E. Grüneisen. *Ann. Phys.(Leibzig)* **16**, 530 (1933).

[53] Y.S. Toulouhian. *Thermophysical properties of Matter, Vol. 2, Thermal Conductivity Nonmetallic Solids, pp 193.* Plenum Data Corp., New York 1970.

[54] J. B. Hartmann. *Phys. Rev.* B **15**, 273 (1977).

[55] D. L. Huber, J. S. Semura and C. G. Windsor. *Phys. Rev.* **186**, 534 (1969).

[56] D. L. Huber and J. S. Semura. *Phys. Rev. Lett.* page 602 (1969).

[57] D. A. Krueger. *Phys. Rev.* B **3**, 2348 (1971).

[58] D. J. Sanders and D. Walton. *Phys. Rev.* B **15**, 1489 (1977).

[59] D. J. Sanders and D. Walton. *Phys. Rev.* B **16**, 4998 (1977).

[60] L.É. Gurevich and G.A. Roman. *Sov. Phys. Solid State* **8**, 2102 (1967).

[61] B. Zeini, A. Freimuth, B. Büchner, R. Gross, A. P. Kampf, M. Kläser and G. Müller-Vogt. *Phys. Rev. Lett.* **82**, 2175 (1999).

[62] O. Baberski, A. Lang, O. Maldonado, M. Hücker, B. Büchner and A. Freimuth. *Europhys. Lett.* **44**, 335 (1998).

[63] Yoichi Ando, J. Takeya, D. L. Sisson, S. G. Doettinger, I. Tanaka, R. S. Feigelson and A. Kapitulnik. *Phys. Rev.* B **58**, R2913 (1998).

[64] A. N. Vasil'ev, V. V. Pryadun, D. I. Khomskii, G. Dhalenne, A. Revcolevschi, M. Isobe and Y. Ueda. *Phys. Rev. Lett.* **81**, 1949 (1998).

[65] A. V. Sologubenko, K. Giannó, H. R. Ott, U. Ammerahl and A. Revcolevschi. *Phys. Rev. Lett.* **84**, 2714 (2000).

[66] C. Hess, C. Baumann, U. Ammerahl, B. Büchner, F. Heidrich-Meisner, W. Brenig and A. Revcolevschi. *Phys. Rev.* B **64**, 184305 (2001).

[67] H. Miike and K. Hirakawa. *J. Phys. Soc. Japan* **38**, 1279 (1995).

[68] M. Köppen, M. Lang, R. Helfrich, F. Steglich, P. Thalmeier, B. Schmidt, B. Wand, D. Pankert, H. Benner, H. Aoki and A. Ochiai. *Phys. Rev. Lett.* **82**, 4548 (1999).

[69] A. V. Sologubenko, K. Giannò, H. R. Ott, A. Vietkine and A. Revcolevschi. *Phys. Rev.* B **64**, 54412 (2001).

[70] C. Zobel. PhD thesis, Universität zu Köln in preparation.

[71] T.M. Tritt. *Recent Trends in Thermoelectric Materials Research I, in Semiconductors and Semimetals Vol. 69.* Academic Press, London 2001.

[72] T.M. Tritt. *Recent Trends in Thermoelectric Materials Research II, in Semiconductors and Semimetals Vol. 70.* Academic Press, London 2001.

[73] D.G. Cahill. *Rev. Sci. Instrum.* **61**, 802 (1990).

[74] David G. Cahill and R. O. Pohl. *Phys. Rev.* B **35**, 4067 (1987).

[75] S. Uhlenbruck. PhD thesis, Universität zu Köln 2000.

[76] H. Kierspel. PhD thesis, Universität zu Köln 1996.

[77] Landolt-Börnstein. *New Series III/15c, Metals: Electronic Transport Phenomena, pp 154 and 240.* Springer Verlag Berlin 1991.

[78] R. Berman, P.G. Klemens, F.E. Simon and T.M. Fey. *Nature* **166**, 864 (1950).

[79] A. Sala. *Radiant Properties of Materials.* Elsevier, New York 1986.

[80] Lakeshore. *Temperature Measurement and Control (catalogue).* Lakeshore Cryotronics Inc. 1995.

[81] R. Berman and J. Kopp. *J. Phys. F: Metal Phys.* **1**, 457 (1971).

[82] A. von Middendorff. *Cryogenics* **4**, 318 (1971).

[83] C. K. Chiang. *Rev. Sci. Instrum.* **45**, 985 (1974).

[84] The Pascal program Interpol.pas is used in the LabView routine kSR.vi, written by C. Zobel. For details see C. Zobel – thesis, in preparation.

[85] W.H. Press, B.P. Flannery, S.A. Teukolsky and W.T. Vetterling. *Numerical Recipes in Pascal.* Cambridge University Press 1994.

[86] Mu-Yong Choi, P. M. Chaikin and R. L. Greene. *Phys. Rev.* B **34**, 7727 (1986).

[87] D. Durek, M. Prester, D. Jérome and K. Bechgaard. *J. Phys. C – Solid State Phys.* **15**, L669 (1982).

[88] B. Sriram Shastry and Bill Sutherland. *Physica* B **108**, 1069 (1981).

[89] K. Sparta, G.J. Redhammer, P. Roussel, G. Heger, G. Roth, P. Lemmens, A. Ionescu, M. Grove, G. Guentherodt, F. Huening, H. Lueken, H. Kageyama and Y. Ueda K. Onizuka. *preprint, cond–mat/0012383* (2000).

[90] S. Miyahara and K. Ueda. *Phys. Rev. Lett.* **82**, 3701 (1999).

[91] S. Miyahara and K. Ueda. *Phys. Rev.* B **61**, 3417 (2000).

[92] C. Knetter, A. Bühler, E. Müller-Hartmann and G. S. Uhrig. *Phys. Rev. Lett.* **85**, 3958 (2000).

[93] E. Müller-Hartmann, R. R. P. Singh, C. Knetter and G. S. Uhrig. *Phys. Rev. Lett.* **84**, 1808 (2000).

[94] Z. Weihong, C. J. Hamer and J. Oitmaa. *Phys. Rev.* B **60**, 6608 (1999).

[95] H. Kageyama, K. Yoshimura, R. Stern, N. V. Mushnikov, K. Onizuka, M. Kato, K. Kosuge, C. P. Slichter, T. Goto and Y. Ueda. *Phys. Rev. Lett.* **82**, 3168 (1999).

[96] H. Kageyama, K. Onizuka, T. Yamauchi, Y. Ueda, S. Hane, H. Mitamura, T. Goto, K. Yoshimura and K. Kosuge. *J. Phys. Soc. Japan* **68**, 1821 (1999).

[97] P. Lemmens, M. Grove, M. Fischer and G. Güntherodt. *Phys. Rev. Lett.* **85**, 2605 (2000).

[98] H. Nojiri, H. Kageyama, K. Onizuka, Y. Ueda and Mitsuhiro Motokawa. *J. Phys. Soc. Japan* **68**, 2906 (1999).

[99] H. Kageyama, M. Nishi, N. Aso, K. Onizuka, T. Yosihama, K. Nukui, K. Kodama, K. Kakurai and Y. Ueda. *Phys. Rev. Lett.* **84**, 5876 (2000).

[100] Y. Sasago, M. Hase, K. Uchinokura, M. Tokunaga and N. Miura. *Phys. Rev.* B **52**, 3533 (1995).

[101] M. Nishi, O. Fujita and J. Akimitsu. *Phys. Rev.* B **50**, 6508 (1994).

[102] K. Kodama, H. Harashina, H. Sasaki, Y. Kobayashi, M. Kasai, S. Taniguchi, Y. Yasui, M. Sato, K. Kakurai1, T. Mori and M. Nishi. *J. Phys. Soc. Japan* **66**, 793 (1997).

[103] Y. Sasago, K. Uchinokura, A. Zheludev and G. Shirane. *Phys. Rev.* B **55**, 8357 (1997).

[104] B. Leuenberger, A. Stebler, H. U. Gdel, A. Furrer, R. Feile and J. K. Kjems. *Phys. Rev.* B **30**, 6300 (1984).

[105] H. Kageyama. *J. Phys. Soc. Japan* **69**, 65 (1999).

[106] H. Kageyama et al. *Sov. Phys. JETP* **90**, 129 (2000).

[107] R. Berman. *Thermal Conduction in Solids.* Clarendon Press, Oxford 1976.

[108] S. Zherlitsyn, S. Schmidt, B. Wolf, H. Schwenk, B. Lüthi, H. Kageyama, K. Onizuka, Y. Ueda and K. Ueda. *Phys. Rev.* B **62**, R6097 (2000).

[109] V. Roundy and D. L. Mills. *Phys. Rev.* B **1**, 3703 (1970).

[110] G.A. Toombs and F.W. Sheard. *J. Phys. – Condens. Matter* **6**, 1467 (1973).

[111] G.S. Uhrig. private communication.

[112] R. O. Pohl. *Phys. Rev. Lett.* **8**, 481 (1962).

[113] C.T. Walker and R. O. Pohl. *Phys. Rev.* **131**, 1443 (1963).

[114] R. Orbach. *Phys. Rev. Lett.* **8**, 393 (1962).

[115] C. Knetter, E. Müller-Hartmann and G. S. Uhrig. *J. Phys. – Condens. Matter* **12**, 9069 (2000).

[116] W.H. Korving, G.J. Kramer, R.A. Steeman, H.B. Brom, L.J. de Jongh, M. Fujita and K. Machida. *Physica* B **145**, 299 (1987).

[117] M. Hase, I. Terasaki and K. Uchinokura. *Phys. Rev. Lett.* **70**, 3651 (1993).

[118] X. Zotos, F. Naef and P. Prelovšek. *Phys. Rev.* B **55**, 11029 (1997).

[119] J. Takeya, I. Tsukada, Yoichi Ando, T. Masuda and K. Uchinokura. *Phys. Rev.* B **61**, 14700 (2000).

[120] J. Takeya, I. Tsukada, Yoichi Ando, T. Masuda and K. Uchinokura. *Phys. Rev.* B **62**, R9260 (2000).

[121] J. Takeya, I. Tsukada, Yoichi Ando, T. Masuda, K. Uchinokura, I. Tanaka, R. S. Feigelson and A. Kapitulnik. *Phys. Rev.* B **63**, 214407 (2001).

[122] H. Völlenkle, A. Wittmann and H. Nowotny. *Monatsh. Chemie* **98**, 1352 (1967).

[123] J.P. Pouget, L.P. Regnault, M. Ain, B. Hennion, J.P. Renard, P. Veillet, G. Dhalenne and A. Revcolevschi. *Phys. Rev. Lett.* **72**, 4037 (1994).

[124] K. Hirota, D.E. Cox, J.E. Lorenzo, G. Shirane, J.M. Tranquada, M. Hase, K. Uchinokura, H. Kojima, Y. Shibuya and I. Tanaka. *Phys. Rev. Lett.* **73**, 736 (1994).

[125] B. Roessli, P. Fischer, J. Schefer, W. Bührer, A. Furrer, T. Vogt, G. Petravovskii and K. Sablina. *J. Phys. – Condens. Matter* **6**, 8469 (1994).

[126] M. Braden, G. Wilkendorf, J. Lorenzana, M. Ain, G.J. McIntyre, M. Behruzi, G. Heger, G. Dhalenne and A. Revcolevschi. *Phys. Rev.* B **54**, 1105 (1996).

[127] J.B. Goodenough. *Magnetism and the Chemical Bond.* John Wiley & Sons, New York 1963.

[128] W. Geertsma and D. Khomskii. *Phys. Rev.* B **54**, 3011 (1996).

[129] D. Khomskii, W. Geertsma and M. Mostovoy. *Czech. J. Phys.* **46**, Suppl. S6, 3239 (1996).

[130] T. Lorenz. PhD thesis, Universität zu Köln 1998.

[131] W. Geertsma and D. Khomskii. *preprint, cond–mat/0007421* (2000).

[132] S. Oseroff, S-W. Cheong, A. Fondado, B. Aktas and Z. Fisk. *J. Appl. Phys.* **75**, 6819 (1994).

[133] H. Ohta, S. Imagawa, H. Ushiroyama, M. Motokawa, O. Fujita and J. Akimitsu. *J. Phys. Soc. Japan* **63**, 2870 (1994).

[134] C.K. Majumdar and D.K. Gosh. *J. Math. Phys.* **10**, 1399 (1969).

[135] S. Sahling, J.C. Lasjaunias, P. Monceau and A. Revcolevschi. *Sol. State Commun.* **92**, 423 (1994).

[136] T.C. Kobayashi, A. Koda, H. Honda, C.U. Hong, K. Amaya, T. Asano, Y. Ajiro, M. Mekata and T. Yosida. *Physica* B **211**, 205 (1995).

[137] X. Liu, J. Wosnitza, H.v. Löhneysen and R.K. Kremer. *Z. Physik B – condensed matter* **98**, 163 (1995).

[138] Y.-K. Kuo, F. Figueroa and J.W. Brill. *Sol. State Commun.* **94**, 385 (1995).

[139] S.B. Oseroff, S-W. Cheong, B. Aktas, M.F. Hundley, Z. Fisk and L.W. Rupp jr. *Phys. Rev. Lett.* **74**, 1450 (1995).

[140] T. Lorenz, U. Ammerahl, R. Ziemes, B. Büchner, A. Revcolevschi and G. Dhalenne. *Phys. Rev.* B **54**, R15610 (1996).

[141] T.C. Kobayashi, A. Koda and K. Amaya. *Physica* B **216**, 304 (1996).

[142] S. Kleefisch. Master's thesis, Universität zu Köln 1996. (unpublished).

[143] R. Ziemes. Master's thesis, Universität zu Köln 1996. (unpublished).

[144] M. Hiroi, T. Hamamoto, M. Sera, H. Nojiri, N. Kobayashi, M. Motokawa, O. Fujita, A. Ogiwara and J. Akimitsu. *Phys. Rev.* B **55**, R6125 (1997).

[145] M. Nishi, O. Fujita, J. Akimitsu, K. Kakurai and Y. Fujii. *Physica* B **213&214**, 275 (1995).

[146] O. Fujita, J. Akimitsu, M. Nishi and K. Kakurai. *Phys. Rev. Lett.* **74**, 1677 (1995).

[147] O. Fujita, M. Nishi, J. Akimitsu, H. Okumura, K. Kakurai and Y. Fujii. *Physica* B **213&214**, 281 (1995).

[148] L.P. Regnault, M. Ain, B. Hennion, G. Dhalenne and A. Revcolevschi. *Physica* B **213&214**, 278 (1995).

[149] L.P. Regnault, M. Ain, B. Hennion, G. Dhalenne and A. Revcolevschi. *Phys. Rev.* B **53**, 5579 (1996).

[150] J-G. Lussier, S.M. Coad, D.F. McMorrow and D.McK Paul. *J. Phys. – Condens. Matter* **8**, L59 (1996).

[151] M. Ain, J.E. Lorenzo, L.P. Regnault, G. Dhalenne, A. Revcolevschi, B. Hennion and Th. Jolicoeur. *Phys. Rev. Lett.* **78**, 1560 (1997).

[152] J. Riera and A. Dobry. *Phys. Rev.* B **51**, 16098 (1995).

[153] K. Fabricius, A. Klümper, U. Löw, B. Büchner, G. Dhalenne, T. Lorenz and A. Revcolevschi. *Phys. Rev.* B **57**, 1102 (1998).

[154] D.E. Moncton, R.J. Birgeneau, L.V. Interrante and F. Wudl. *Phys. Rev. Lett.* **39**, 507 (1977).

[155] O. Kamimura, M. Terauchi, M. Tanaka, O. Fujita and J. Akimitsu. *J. Phys. Soc. Japan* **63**, 2467 (1994).

[156] G. Els, P.H.M. van Loosdrecht, P. Lemmens, H. Vonberg, G. Güntherodt, G.S. Uhrig, O. Fujita, J. Akimitsu, G. Dhalenne and A. Revcolevschi. *Phys. Rev. Lett.* **79**, 5138 (1997).

[157] P.H.M. van Loosdrecht, J. Zeman, G. Martinez, G. Dhalenne and A. Revcolevschi. *Phys. Rev. Lett.* **78**, 487 (1997).

[158] H. Kuroe, T. Sekine, M. Hase, Y. Sasago, K. Uchinokura, H. Kojima, I. Tanaka and Y. Shibuya. *Phys. Rev.* B **50**, 16468 (1994).

[159] P.H.M. van Loosdrecht, J.P. Boucher, G. Martinez, G. Dhalenne and A. Revcolevschi. *Phys. Rev. Lett.* **76**, 311 (1996).

[160] P.H.M. van Loosdrecht, S. Huant, G. Martinez, G. Dhalenne and A. Revcolevschi. *Phys. Rev.* B **54**, R3730 (1996).

[161] P. Lemmens, B. Eisener, M. Brinkmann, L.V. Gasparow, G. Güntherodt, P. van Dongen, W. Richter, M. Weiden, C. Geibel and F. Steglich. *Physica* B **223&224**, 535 (1996).

[162] G.S. Uhrig and H.J. Schulz. *Phys. Rev.* B **54**, 9624 (1996).

[163] C. Gros, W. Wenzel, A. Fledderjohann, P. Lemmens, M. Fischer, G. Güntherodt, M. Weiden, C. Geibel and F. Steglich. *Phys. Rev.* B **55**, 15048 (1997).

[164] J.C. Bonner and H.W.J. Blöte. *Phys. Rev.* B **25**, 6959 (1982).

[165] J. Riera and S. Koval. *Phys. Rev.* B **53**, 770 (1996).

[166] G.S. Uhrig. *Phys. Rev. Lett.* **79**, 163 (1997).

[167] W. Brenig. *Phys. Rev.* B **56**, 14441 (1997).

[168] M. Saint-Paul, P. Monceau and A. Revcolevschi. *Sol. State Commun.* **93**, 7 (1995).

[169] G.S. Uhrig. *Phys. Rev.* B **57**, R14004–R14007 (1998).

[170] C. Gros and R. Werner. *Phys. Rev.* B **59**, 14356 (1999).

[171] A.D. Bruce and R.A. Cowley. *Structural phase transitions.* Taylor & Francis LTD, London 1981.

[172] J. Mertsching and H.J. Fischbeck. *phys. stat. sol. (b)* **103**, 783 (1983).

[173] M. Braden, E. Ressouche, B. Büchner, R. Keßler, G. Heger, G. Dhalenne and A. Revcolevschi. *Phys. Rev.* B **57**, 11497 (1998).

[174] H. Winkelmann, E. Gamper, B. Büchner, M. Braden, A. Revcolevschi and G. Dhalenne. *Phys. Rev.* B **51**, 12884 (1995).

[175] T. Lorenz, H. Kierspel, S. Kleefisch, B. Büchner, E. Gamper, A. Revcolevschi and G. Dhalenne. *Phys. Rev.* B **56**, 501 (1997).

[176] H. Yokoyama and Y. Saiga. *J. Phys. Soc. Japan* **65**, 3617 (1997).

[177] T. Lorenz, B. Büchner, P.H.M. van Loosdrecht, F. Schönfeld, G. Chouteau, A. Revcolevschi and G. Dhalenne. *Phys. Rev. Lett.* **81**, 148 (1998).

[178] J. K. Hulm. *Proc. R. Soc. London, Ser. A.* **204**, 98 (1950).

[179] C. Uher. In D. M. Ginsberg, editor, *Physical Properties of High Temperature Superconductors III* page 160. World Scientific 1992.

[180] D. Vollhardt and P. Wölfle. *The superfluide phases of Helium 3.* Taylor & Francis LTD, London 1990.

[181] D. D. Osheroff, R. C. Richardson and D. M. Lee. *Phys. Rev. Lett.* **28**, 885 (1972).

[182] R. Balian and N. R. Werthamer. *Phys. Rev.* **131**, 1553 (1963).

[183] P. W. Anderson and P. Morel. *Phys. Rev.* **123**, 1911 (1961).

[184] P. Nozieres. *Theory of interacting Fermi systems.* Benjamin, New York 1964.

[185] D. Pines and P. Nozieres. *Theory of quantum liquids.* Benjamin, New York 1966.

[186] M. Saint-Paul, G. Reményi, N. Hegman, P. Monceau, G. Dhalenne and A. Revcolevschi. *Phys. Rev.* B **55**, 6121 (1997).

[187] A. Klümper. *Euro. Phys. J. B* **5**, 667 (1998).

[188] G. S. Uhrig and B. Normand. *Phys. Rev.* B **58**, R14705 (1998).

[189] M. Troyer, Hirokazu Tsunetsugu and Diethelm Würtz. *Phys. Rev.* B **55**, 13515 (1994).

[190] H. Hori, M. Furusawa, S. Sugai, M. Honda, T. Takeuchi and K. Kindo. *Physica* B **211**, 180 (1995).

[191] K. Takehana, M. Oshikiri, G. Kido, A. Takazawa, M. Sato, K. Nagasaka, M. Hase and K. Uchinokura. *Physica* B **216**, 355 (1996).

[192] F. Schönfeld. PhD thesis, Universität zu Köln 1998.

[193] J A H M Buijs and W J M de Jonge. *J. Phys. C – Solid State Phys.* **82**, 6631 (1982).

[194] B. Grenier, J.-P. Renard, P. Veillet, C. Paulsen, G. Dhalenne and A. Revcolevschi. *Phys. Rev.* B **58**, 8202 (1998).

[195] B. Büchner, T. Lorenz, R. Walter, H. Kierspel, A. Revcolevschi and G. Dhalenne. *Phys. Rev.* B **59**, 6886 (1999).

[196] Y. Sasago, N. Koide, K. Uchinokura, M.C. Martin, M. Hase, K. Hirota and G. Shirane. *Phys. Rev.* B **54**, R6835 (1996).

[197] M.C. Martin, M. Hase, K. Hirota, G. Shirane, Y. Sasago, N. Koide and K. Uchinokura. *Phys. Rev.* B **56**, 3173 (1997).

[198] P.E. Anderson, J.Z. Liu and R.N. Shelton. *Phys. Rev.* B **57**, 11014 (1997).

[199] L.P. Regnault, J.P. Renard, G. Dhalenne and A. Revcolevschi. *Europhys. Lett.* **32**, 579 (1995).

[200] K.M. Kojima, Y. Fudamoto, M. Larkin, G.M. Luke, J. Merrin, B. Nachumi, Y.J. Uemura, M. Hase, Y. Sasago, K. Uchinokura, Y. Ajiro, A. Revcolevschi and J.-P. Renard. *Phys. Rev. Lett.* **79**, 503 (1997).

[201] K. Hirota, M. Hase3, J. Akimitsu, T. Masuda, K. Uchinokura and Shirane. *J. Phys. Soc. Japan* B **67**, 645 (1998).

[202] M. Mostovoy, D. Khomskii and J. Knoester. *Phys. Rev.* B **58**, 8190 (1998).

[203] S. Inagaki and H. Fukuyama. *J. Phys. Soc. Japan* **52**, 2504 (1983).

[204] H. Fukuyama, T. Tanimoto and M. Saito. *J. Phys. Soc. Japan* **65**, 1182 (1996).

[205] M. Mostovoy and D. Khomskii. *Z. Physik B – condensed matter* **103**, 209 (1997).

[206] K. Manabe, H. Ishimoto, N. Koide, Y. Sasago and K. Uchinokura. *Phys. Rev.* B **58**, R575 (1998).

[207] T. Masuda, I. Tsukada, K. Uchinokura, Y. J. Wang, V. Kiryukhin and R. J. Birgeneau. *Phys. Rev.* B **61**, 4103 (2000).

[208] John W. Schwartz and Charles T. Walker. *Phys. Rev.* **155**, 969 (1967).

[209] M. Braden. private communication.

[210] T.H.K. Baron, J.G. Collins and G.K. White. *Adv. in Phys.* **29**, 609 (1980).

[211] K. Bechgaard, C.S. Jacobson, K. Mortensen, H.J. Pedersen and N. Thorup. *Sol. State Commun.* **33**, 1119 (1980).

[212] J.P. Pouget and S. Ravy. *J. Phys.I (France)* **6**, 1501 (1996).

[213] J.P. Pouget. *In Low-Dimensional Conductors and Superconductors.* D. Jérome and L.G. Caron, NATO ASI Ser. B, Physics 155 (Plenum Press, New York), p.17 1958.

[214] A.T. Zheleznyak and V.M. Yakovenko. *Europhys. J.* B **11**, 385 (1999).

[215] J. Moser, M. Gabay, P. Auban-Senzier, D. Jerome, K. Bechgaard and J.M. Fabre. *Europhys. J.* B **1**, 39 (1998).

[216] P. Fertey, M. Poirier and P. Batail. *Europhys. J.* B **10**, 305 (1999).

[217] G. Mihály, I. Kézsmárki, F. Zámborszky and L. Forró. *Phys. Rev. Lett.* **84**, 2670 (2000).

[218] P. Wzietek, F. Creuzet, C. Bourbonnais, D. Jérome, K. Bechgaard and P. Batail. *J. Phys.I (France)* **3**, 171 (1993).

[219] Julien Favand and Frédéric Mila. *Phys. Rev.* B **54**, 10425 (96).

[220] V. Vescoli, L. Degiorgi, W. Henderson, G. Grüner, K. P. Starkey and L. K. Montgomery. *Science* **281**, 1181 (1998).

[221] H.J. Schulz. *Int. J. Mod. Phys.* B **5**, 57 (1991).

[222] S. P. Strong, David G. Clarke and P. W. Anderson. *Phys. Rev. Lett.* **73**, 1007 (1994).

[223] D. Jérome and H.J. Schulz. *Adv. Phys.* **31**, 299 (1982).

[224] G. M. Danner, W. Kang and P. M. Chaikin. *Phys. Rev. Lett.* **72**, 3714 (1994).

[225] Lev. P. Gor'kov and Mogus Mochena. *Phys. Rev.* B **57**, 6204 (1998).

[226] S. Belin and K. Behnia. *Phys. Rev. Lett.* **79**, 2125 (1997).

[227] C. Coulon, P. Dehaes, S. Flandrois, R. Lagnier, E. Bonjour and J.M. Fabre. *J. Phys.I (France)* **43**, 1059 (1882).

[228] C. L. Kane and Matthew P. A. Fisher. *Phys. Rev. Lett.* **76**, 3192 (1996).

[229] G.M. danner, S. McKernan, X.D. Shi, W. Kang, S.T. Hannahs and P.M. Chaikin. *Synthetic Metals* **70**, 731 (1995).

[230] E. I. Chashechkina and P. M. Chaikin. *Phys. Rev.* B **56**, 13658 (1997).

[231] T. Ishiguro and K. Yamaji. *Organic Superconductors, Springer Series in Solid State Sciences 72.* Springer Verlag, Berlin 1990.

[232] T. Osada, A. Kawasumi, S. Kagoshima, N. Miura and G. Saito. *Phys. Rev. Lett.* **66**, 1525 (1991).

[233] W. Kang, S. T. Hannahs and P. M. Chaikin. *Phys. Rev. Lett.* **69**, 2827 (1992).

[234] T. Takahashi, D. Jérome and K. Bechgaard. *J. Phys. (France) Lett.* **43**, L565 (1982).

[235] M. Dumm, A. Loidl, B. W. Fravel, K. P. Starkey, L. K. Montgomery and M. Dressel. *Phys. Rev.* B **61**, 511 (2000).

[236] M. Dumm, A. Loidl, B. Alavi, K. P. Starkey, L. K. Montgomery and M. Dressel. *Phys. Rev.* B **62**, 6512 (2000).

[237] P.M. Chaikin, T. Tiedje and A.N. Bloch. *Sol. State Commun.* **41**, 739 (1982).

[238] M. A. Kastner, R. J. Birgeneau, G. Shirane and Y. Endoh. *Rev. Mod. Phys.* **70**, 897 (1998 and references therein).

[239] H.J. Schulz. *Interacting Fermions In One Dimension: From Weak To Strong Correlation, in Correlated Electron Systems, Vol.9.* V.J. Emery, World Scientific Publishing 1993.

[240] M. Grüninger, D. van der Marel, A. Damascelli, A. Erb, T. Nunner and T. Kopp. *Phys. Rev.* B **62**, 12422 (2000).

[241] Chang-Ming Ho, V. N. Muthukumar, M. Ogata and P. W. Anderson. *Phys. Rev. Lett.* **86**, 1626 (2001).

[242] G. Aeppli et al. *phys. stat. sol. (b)* **215**, 519 (1999).

[243] A. W. Sandvik and Rajiv R. P. Singh. *Phys. Rev. Lett.* **86**, 528 (2001).

[244] R. B. Laughlin. *Phys. Rev. Lett.* **79**, 1726 (1997).

[245] Single crystals provided by A.A. Menovski, Van der Waals-Zeeman Laboratorium, Universiteit van Amsterdam, 1018 XE Amsterdam, The Netherlands.

[246] Y. P. Feng, A. Jin, D. Finotello, K. A. Gillis, M. H. W. Chan and J. E. Greedan. *Phys. Rev.* B **38**, 7041 (1988).

[247] G. Aeppli, S. M. Hayden, H. A. Mook, Z. Fisk, S.-W. Cheong, D. Rytz, J. P. Remeika, G. P. Espinosa and A. S. Cooper. *Phys. Rev. Lett.* **62**, 2052 (1989).

[248] M. Greven, R.J. Birgeneau, Y. Endoh, M.A. Kastner, M. Matsuda and G. Shirane. *Z. Physik B – condensed matter* **96**, 465 (1995).

[249] R.J. Birgeneau, A. Aharony, N.R. Belk, F.C. Chou, Y. Endoh, M. Greven, S. Hosoya, M.A. Kastner, C.H. Lee, Y.S. Lee, G. Shirane, S. Wakimoto, B.O. Wells and K. Yamada. *J. Chem. Phys.* **56**, 1913 (1995).

Ich versichere, daß ich die von mir vorgelegte Dissertation selbständig angefertigt, die benutzten Quellen und Hilfsmittel vollständig angegeben und die Stellen der Arbeit - einschließlich Tabellen, Karten und Abbildungen -, die anderen Werken im Wortlaut oder Sinn nach entnommen sind, in jedem Einzelfall als Entlehnung kenntlich gemacht habe; daß diese Dissertation noch keiner anderen Fakultät oder Universität zur Prüfung vorgelegen hat; daß sie - abgesehen von unten angegebenen Teilpublikationen - noch nicht veröffentlicht worden ist, sowie daß ich eine solche Veröffentlichung vor Abschluß des Promotionsverfahrens nicht vornehmen werde. Die Bestimmungen dieser Promotionsordnung sind mir bekannt. Die von mir vorgelegte Dissertation ist von Herrn Prof. Dr. A. Freimuth betreut worden.

Liste der Teilveröffentlichungen

1. *Strong Damping of Phononic Heat Current by Magnetic Excitations in* $SrCu_2(BO_3)_2$,
   M. Hofmann, T. Lorenz, G. S. Uhrig, H. Kierspel, O. Zabara, A. Freimuth, H. Kageyama, and Y. Ueda,
   Phys. Rev. Lett. **87**, 47202 (2001).

2. *Heat transport in* $SrCu_2(BO_3)_2$ and $CuGeO_3$,
   M. Hofmann, T. Lorenz, A. Freimuth, G. S. Uhrig, H. Kageyama, Y. Ueda, G. Dhalenne, and A. Revcolevschi,
   cond–mat/0108488, (2001); appears in the proceedings of the SCES2001 (Physica B).

Tagungsbeiträge auf den Frühjahrstagungen der Deutschen Physikalischen Gesellschaft, Arbeitskreis Festkörperphysik, 1999 bis 2001.

Tagungsbeitrag auf der General Conference of the Condensed Matter Division, European Physical Society, 2000.

Danksagung

An erster Stelle möchte ich mich bei Prof. A. Freimuth recht herzlich für die Ermöglichung und Betreuung dieser Arbeit bedanken. Er hatte stets ein offenes Ohr für meine Fragen. Mit seinem Ideereichtum und seinen Anregungen hat er wesentlich zum Gelingen dieser Arbeit beigetragen.

Ganz besonders möchte ich mich auch bei meinem Betreuer Dr. T. Lorenz bedanken, zum einen für die freundschaftliche Zusammenarbeit, zum anderen für die hilfreichen Diskussionen, für die Mühe des Korrekturlesens und für die Geduld, die er mit mir hatte.

Ohne die gute Zusammenarbeit mit der Theorie wären viele Fragen zum Wärmetransport offen geblieben. Daher gilt mein ganz besonderer Dank Priv. Doz. Dr. Götz S. Uhrig für die Beiträge zu den Berechnungen der resonanten Streuzeiten, bzw. des magnetischen Wärmetransports und für die stets anregenden Diskussionen.

Dr. Markus "Physikus" Grüninger möchte ich für seine hilfreichen Diskussionsbeiträge danken. Dr. H. Kierspel danke ich für die ausgezeichnete Versorgung mit Helium.

Ein Dankeschön an Prof. M. Dressel, Prof. A. Revcolevschi, Dr. H. Kageyama und Dr. A.A. Menovsky für die Versorgung mit exzellenten Einkristallen.

... nicht zu vergessen:

C. Zobel, M. Zittartz, A. Reichl, S. Kiele und M. *Kardinal* Kriener danke ich für die 'entspannende' Atmosphäre und eine schöne Zeit – ergo bibamus!

Allen weiteren Mitgliedern des II. Physikalischen Instituts, die zum Gelingen dieser Arbeit beigetragen haben und hier nicht namentlich erwähnt wurden, sei ebenfalls gedankt.

Meinen Elterm möchte ich herzlich für die uneingeschränkte Unterstützung danken. Ein herzliches Dankeschön an Elisabeth und Pedro Hastedt für die aufmunternden Worte und die moralische Unterstützung.
Besonders bedanken möchte ich mich bei meiner Frau Inés, ohne deren liebevolle Unterstützung ich diese Arbeit nicht geschafft hätte.

Abstract

The goal of this thesis is the systematic investigation of the thermal conductivity κ on low-dimensional spin systems. Both, measurements of κ and numerical calculations that model the data, have been conducted.
A device for high accuracy measurements of the thermal conductivity, using the standard steady state method, has been set up. The system permits measurements of κ as a function of temperature and/or as a function of the magnetic field. Depending on the cryomagnetic system it is possible to operate in a temperature range from $\sim$ 2.2 Kelvin up to $\sim$ 300 K and in magnetic fields up to 17 Tesla. The system is computer controlled which enables the running of different measuring programs, the automatic data acquisition and data analysis.

The following low-dimensional spin systems have been studied: the inorganic spin-Peierls system $CuGeO_3$, the Bechgaard salts $(TMTSF)_2PF_6$, $(TMTTF)_2PF_6$ and $(TMTSF)_2ClO_4$, the spin dimer system $SrCu_2(BO_3)_2$, and the 2-d Heisenberg antiferromagnet $Sr_2CuO_2Cl_2$. Our detailed experimental studies show anomalous heat transport in all systems investigated. In each compound one finds at least two pronounced maxima of κ, what is very unusual because in conventional crystalline solids only one maximum at low temperatures is expected. Furthermore, a strong magnetic field dependence of the thermal conductivity in all samples, besides $Sr_2CuO_2Cl_2$, is found. This field dependence backs the idea that magnetic excitations heavily effect the heat transport.
In $SrCu_2(BO_3)_2$ we address the unusual temperature and magnetic field dependence to the scattering of phonons by magnetic excitations. No magnetic contribution to κ is present here. A model, based on resonant scattering of phonons by magnetic excitations, describes both κ and the specific heat very well.
In $CuGeO_3$ we suggest that the high temperature structure of κ arises from phonon scattering by magnetic excitations. However, the double peak structure of κ at low temperatures is puzzling. No clear identification of a magnetic contribution can be given. Possibly, one deals here with coupled magnetoelastic modes. This idea is supported by the fact that in $CuGeO_3$ a strong spin-phonon coupling is present.
In the Bechgaard salts one finds, irrespective of whether the system in question is an electrical insulator or an electrical conductor similar behavior of κ: a magnetic field dependent low temperature maximum and an unusual increase of κ towards higher temperatures. We suggest the enhancement of κ at high temperatures to arise in all three systems from an additional magnetic contribution. The suppression of the low-temperature maxima, located at the same temperature for the three systems, is addressed to phonons scattered by field induced lattice deformations. A numerical calculation to model κ by means of an extended Debye model backs this idea.
Likewise, a double peak structure of the thermal conductivity is found in the 2-d spin system $Sr_2CuO_2Cl_2$. The maximum at high temperatures is most probably due to an additional magnetic contribution to κ. We suggest a phononic low-temperature peak. Here, no magnetic field dependence of κ is observed.

Zusammenfassung

In dieser Arbeit wurden systematische Messungen der Wärmeleitfähigkeit (WLF) und numerische Rechnungen zum Wärmetransport an niedrigdimensionalen magnetischen Spin Systemen durchgeführt.
Es ist von mir eine Wärmeleitfähigkeits-Messapparatur aufgebaut worden. Sie ermöglicht die Messung der WLF in einem Temperaturbereich von 2.2 Kelvin bis ca. 300 Kelvin. Abhängig vom Cryomagnetischen System kann im II. Physikalischen Institut der Universität zu Köln in Magnetfeldern bis ca. 17 Tesla gemessen werden. Der Probeneinsatz ist so konstruiert, dass auch in verschiedenen Hochfeldlabors (z.B. im Hochfeld-Labor in Nijmegen, Niederlande) die WLF bestimmt werden kann. Somit ist die Möglichkeit gegeben in extrem hohen Feldern (z. Zt. bis zu 30 Tesla) κ zu untersuchen. Das System ist computergesteuert, was eine vollautomatische Erfassung und Auswertung der Meßwerte erlaubt.
An folgenden niedrigdimensionalen Spin Systemen wurden Wärmeleitfähigkeits-Messungen, mit dem Ziel den Einfluss der magnetischen Anregungen auf den Wärmetransport zu studieren, durchgeführt: am Spin-Peierls System $CuGeO_3$, an den Bechgaard Salzen $(TMTTF)_2PF_6$, $(TMTSF)_2PF_6$ und $(TMTSF)_2ClO_4$, am Shastry-Sutherland System $SrCu_2(BO_3)_2$ und am zweidimensionalen Heisenberg-Antiferromagneten $Sr_2CuO_2Cl_2$. Die gefundenen Wärmeleitfähigkeiten sind sehr bemerkenswert. In jedem System findet man mindestens zwei Maxima in der WLF als Funktion der Temperatur. Das ist sehr außergewöhnlich, da man in einem kristallinen Festkörper nur ein Maximum bei tiefen Temperaturen erwartet.
Zusätzlich sind in allen Substanzen, $Sr_2CuO_2Cl_2$ ausgenommen, starke Magnetfeldabhängigkeiten der WLF zu beobachten. Das führen wir auf den starken Einfluss der, in diesen Systemen vorhanden, magnetischen Anregungen auf den Wärmetransport zurück.
Die Ergebnisse lassen sich wie folgt zusammenfassen:
Das Auftreten von zwei Maxima in der WLF von $SrCu_2(BO_3)_2$ lässt sich durch einen rein phononischen Wärmetransport erklären. Ein Modell, welches unsere Beobachtungen hervorragend beschreibt, basiert auf der resonanten Streuung von Phononen an magnetischen Anregungen. Numerische Rechnungen modellieren sowohl die magnetfeldabhängige WLF als auch die zugehörige Spezifische Wärme im Rahmen des gleichen Modells.
Das Verhalten der WLF von $CuGeO_3$ ist außerordentlich komplex. Wir führen die ungewöhnliche WLF in $CuGeO_3$ auf die starke magnetoelastische Kopplung in diesem Material zurück. Dennoch können hier verschiedene Modelle zur Erklärung herangezogen werden.
In den Bechgaard Salzen findet man, unabhängig davon ob es sich um elektrische Leiter oder Isolatoren handelt, im wesentlichen das gleiche Verhalten in der WLF: ein magnetfeldabhängiges Tieftemperaturmaximum und ein untypisches Ansteigen der WLF zu höheren Temperaturen. Eine Beschreibung der anomalen WLF kann im Rahmen des Tomonaga-Luttinger Bildes, mit dem Phänomen der Spin/Ladungstrennung, erfolgreich gegeben werden. Die Magnetfeldabhängigkeit des Tieftemperaturmaximums wird durch ein erweitertes Debye-Modell, welches Streuung an magnetfeldinduzierten strukturellen Defekten berücksichtigt, sehr gut wiedergegeben.
In $Sr_2CuO_2Cl_2$ findet man zwar eine magnetfeldunabhängige WLF, aber ebenfalls zwei Maxima. Ein Vergleich mit der isostrukturellen Substanz La_2CuO_4 und $YBa_2Cu_3O_6$ lässt das Auftreten eines magnetischen Beitrages zur WLF bei hohen Temperaturen in den zweidimensionalen Kupraten plausibel erscheinen.